Primordial Magnetic Fields: Evolution and Signatures

Salome Mtchedlidze

A dissertation thesis was submitted to the Faculty of Natural Sciences and Medicine of Ilia State University in accordance with the requirements for the degree of Doctor of Philosophy in Physics

Doctoral Program in Physics and Astronomy

Supervisors: Prof. Tina Kahniashvili, Prof. Jens Niemeyer

Ilia State University
Tbilisi, 2023

Statement

As an author of the dissertation presented, I state that the dissertation represents my original work and does not include material already published, submitted for publication or presented as a PhD thesis by other authors, unless mentioned or cited in accordance with proper rules.

Salome Mtchedlidze
03/03/2023

აბსტრაქტი

მაგნიტური ველები განჭოლავენ სამყაროს სხვადასხვა მასშტაბებზე; ისინი დაიკვირვება როგორც “პატარა”, ვარსკვლავებისა და პლანეტების ასევე კოსმოლოგიურ, გალაქტიკებისა და გალაქტიკური კლასტერების მასშტაბებზეც. სხვადასხვა დაკვირვებითი მეთოდები (მაგ., რომლებიც იყენებენ ფარადეის ბრუნვის ეფექტს ან/და დიფუზურ რადიო გამოსხივებას გალაქტიკური კლასტერების მასშტაბებზე) აჩვენებენ, რომ მაგნიტური ველების სიდიდე მიკროგაუსის რიგისაა და მათი კორელაციური სიგრძე აღწევს ათეულ კილოპარსექს გალაქტიკურ კლასტერებში.

ითვლება რომ ასეთი დიდმასტაბოვანი (ე.ი., კოსმოლოგიურ მასშტაბებში არსებული) მაგნიტური ველები წარმოიქმნა სუსტი, ჩანასახოვანი მაგნიტური ველების (“seed magnetic fields”) გაძლიერების შედეგად. ეს ჩანასახოვანი ველები კი შეიძლება დაგენერირებულიყო ასტროფიზიკური ან კოსმოლოგიური (იგივე “პირველადი”, “primordial”) გენერაციის მექანიზმით და შემდგომ უნდა გაძლიერებულიყო დიდმასშტაბოვანი სტრუქტურის ფორმირებისას (რათა მიეღწია დაკვირვებად, მიკროგაუსის სიდიდისთვის მაგ. გალაქტიკურ კლასტერებში). ბლაზარების სპექტრების ბოლოდროინდელი დაკვირვებები თავსებადია არანულოვან მაგნიტური ველების არსებობასთან კოსმოსურ სიცარიელეებში (cosmic voids). ეს კი თავის მხრივ ინტერესს აღრმავებს მაგნიტური ველების წარმოშობის და ევოლუციის საკითხთან დაკავშირებით; კერძოდ, შესაძლებელია რომ მაგნიტური ველები დაგენერირებულიყო ლოკალურად, პირველი სტრუქტურების (ე.ი., პირველი ვარსკვლავები, გალაქტიკები, ა.შ.) წარმოშობისას პატარა მასშტაბებში (ასტროფიზიკური მექანიზმი) და შემდგომ “გადატანილიყო” ასეთ დიდ მასშტაბებზე? თუ მოსალოდნელია რომ მაგნიტური ველები არსებობდა ადრეულ სამყაროშივე (გენერაციის კოსმოლოგიური მექანიზმი) და შემდგომ ევოლუცირებდნენ სამყაროს ევოლუციასთან ერთად? ბლაზარების სპექტრის დაკვირვებები თანხმობაშია პირველადი მაგნიტური ველების არსებობასთან, ე.ი., ველებისა რომლებიც დაგენერირდა ადრეულ სამყაროში და რომელთაც პირველად მაგნიტურ ველებსაც უწოდებენ (primordial magnetic fields).

პირველადი მაგნიტური ველების კვლევა საინტერესოა იმ მხრივაც რომ ასეთი კვლევები შესაძლოა დაგვეხმაროს სტანდარტული კოსმოლოგიური მოდელის მიღმა არსებული თეორიების შემოწმებაში. თეზისში წარმოდგენილ კვლევებში შევისწავლეთ პირველადი მაგნიტური ველების ევოლუცია სამყაროს დიდმასშტაბოვანი სტრუქტურის ფორმირებისას კოსმოლოგიური, მაგნეტოჰიდროდინამიკური (მჰდ) კოდის ENZO-ს გამოყენებით. ჩვენს შრომაში ასევე გავითვალისწინეთ მაგნიტური ველების ევოლუცია რეკომბინაციამდელ ეპოქაში (ე.ი., მათი ევოლუცია მჰდ ტურბულენტურ რეჟიმში). ამ მეთოდის მიზანია პირველადი მაგნიტური ველების ევოლუციის სრული სურათის დანახვა ძალიან ადრეული სამყაროდან დღემდე. ჩვენ შევისწავლეთ ისეთი პირველადი მაგნიტური ველები, რომლებიც შეიძლება დაგენერირებულიყო ინფლაციის ან ფაზური გადასვლების ეპოქაში. ჩვენმა სიმულაციებმა აჩვენა, რომ მაგნიტური ველები ევოლუცირებენ განსხვავებულად იმის მიხედვით თუ როგორია

მათი საწყისი სტრუქტურა (განაწილება) დიდ მასშტაბებში. კერძოდ, თუ ველები ინფლაციურია და გააჩნიათ დიდი კორელაციური სიგრძეები მაშინ მათი გაძლიერება სტრუქტურის ფორმირებისას უფრო ეფექტურად ხდება იმ ველებთან შედარებით რომელთა კორელაციური სიგრძეები გალაქტიკური კლასტერების მასშტაბის რიგისაა.

მიმდინარე და მომავალი დაკვირვებები საშუალებას მოგვცემს შევადაროთ ჩვენი თეორიული შედეგები დაკვირვებებს და ვეძებოთ პირველადი მაგნიტური ველების გენერაციის კვალი დღევანდელი მაგნიტური ველების განაწილებაში. თეზისში წარმოდგენილი შედეგები მნიშვნელოვანია სწორედ ამ მხრივ, ე.ი., პირველადი მაგნიტური ველების დაკვირვებითი ანაბეჭდების შესასწავლად მაგალითად ბლაზარების სპექტრზე (მომავალი Cherenkov Telescope Array-ს (CTA) მონაცემების გამოყენებით) და გალაქტიკური კლასტერების ფარადეის ბრუნვის მონაცემებზე (Square Kilometre Array (SKA)-ს დაკვირვებების გამოყენებით).

Abstract

Magnetic fields permeate our Universe on all cosmic scales: from planets and stars to the large-scale fields found in galaxies and galaxy clusters. Different observational methods, such as the ones using the Faraday rotation effect as well as the diffuse radio emission (detected in the form of radio halos and radio relics), infer a field strength of the order of microGauss and coherence scales reaching a few tens of kpc in galaxy clusters. It is commonly assumed that the observed fields today are originated from either astrophysical or cosmological (primordial) magnetic seeds. The observations of blazar spectra by the Fermi Gamma Ray Observatory provide an intriguing possibility of detecting very weak magnetic fields in cosmic voids. This poses an exciting avenue for studying the generation mechanisms and evolution of observed large-scale-correlated magnetic fields. Notably, blazar spectra observations favour primordial magnetogenesis. In the primordial scenario, magnetic fields originating in the early Universe, i.e., Primordial Magnetic Fields (PMFs) can have volume filling fractions close to unity and thus, are good candidates for explaining the possible magnetisation of cosmic voids.

Primordial magnetogenesis has gained a lot of attention in the last decades as a potential probe of physics beyond the Standard Model. In our research, we combined our current understanding of the generation scenarios and pre-recombination evolution of PMFs with state-of-the-art magnetohydrodynamic (MHD) cosmological simulations to study their evolution during structure formation. Our brand new approach aims at reconstructing a whole picture of the evolution of inflation- and phase-transition-generated PMFs from the very early Universe till the current epoch. Our simulations reveal the distinctive amplification nature of initially small-scale, phase-transitional and large-scale, inflationary fields during the formation of massive structures. Our studies argue in favour of distinguishing between different primordial magnetogenesis scenarios on galaxy-cluster as well as on filaments and cosmic voids' scales.

Current and future radio and gamma-ray astronomy are promising for constraining the magnetogenesis scenarios assuming we have a comprehensive study of PMFs that projects their evolution history into the present-day observational signatures. The observational imprints of PMFs found in the research works of this thesis are relevant for the forthcoming large surveys, such as the ones with the Square Kilometre Array (SKA) and Cherenkov Telescope Array (CTA, in tandem with the Fermi Gamma-ray space telescope). The results of our research program will have implications for many areas of research, including the early Universe physics, high-energy astrophysics, MHD cosmological simulations, and large-scale structure formation.

Acknowledgements

I would like, first of all, to thank my supervisors Tina Kahniashvili and Jens Niemeyer for their guidance and very useful discussions and corrections. Thank you for letting me be in the Lehmann Haupt International Doctoral Program (LHIDP), for allowing me to work on exciting research projects, and for never questioning my abilities. I am grateful for all networking, conference, and research trip opportunities you provided for me; participation in schools and conferences gave me a possibility to better understand how the science and scientific community work. I am thankful to Tina for motivating me to apply for grants and fellowships, and to prepare talks that taught me how to present research works. I value all of her effort in making her group inclusive and for including me in scientific collaborations. I am thankful to Jens for being a great host at Goettingen University and for making sure that I was following the research plan; I was also really inspired by his lectures on Cosmology, and by our meetings. I am also thankful to everyone at the National Astrophysical Observatory of Georgia, at the Ilia State and Göttingen Universities, and to my Thesis Advisory Committee (TAC; Doddy Marsh and Ansgar Reiners) for their interesting questions and discussions during our TAC meetings. I especially thank Axel Brandenburg for hosting me at NORDITA, and in general, for his guidance, support, and motivation throughout my Ph.D., for answering my questions, and for his invaluable feedback on our papers. His expertise in the field and passion for science have always been inspiring to me. I thank Alexander Tevzadze for making my master and bachelor studies exciting and for advising me to join the LHIDP program.

I feel honoured and privileged to be a participant of the LHIDP, the unprecedented program that allowed twelve amazing, interested, and motivated researchers from different fields to deepen their knowledge, be involved in international scientific collaborations, and explore their piece of the Universe. I gratefully acknowledge financial support from the Shota Rustaveli National Science Foundation of Georgia, the Volkswagen Foundation, and the German Academic Exchange Service (DAAD); without their support, we would not be able to work on our research projects. I also wish to express sincere thanks to everyone in the LHIDP; I thank participants for sharing their experiences and research-related challenges with me, for creating such a friendly atmosphere, and for spending time together. I also thank all professors who have been mentoring the participants and supporting the research in Georgia. I sincerely appreciate all the hard work that is being done by the program coordinators (Aleksandra Bovt, Vakhtang Pataridze, Martin Piazena).

I am more than happy that I have worked with amazing collaborators, Xiaolong Du and Paola Domínguez-Fernández. Thank you for being such great teachers to me, without your help and encouragement I would not be able to dedicate myself to the projects. My earnest thanks to you for providing stimulating scientific discussions and hands-on advising, for making me feel that it was worth what I had been doing, and for never leaving me alone. I am thankful to Xiaolong for being a good example for me and always patiently answering my questions. I am thankful to Paola for her friendly attitude and for

thorough checks and editing of the paper. Both of you gave me the biggest motivation during my Ph.D. and made this path to be one of the most interesting paths of my life.

I am grateful to my big family for their love and for giving me an education in those hard years; I am also thankful to all of our family friends who have been supporting me. I always wish all the best for all of you. Needless to say, without the support of my sisters Sofi and Tamar, and my friends, Nika, Nini, Irina, Ana, I would not be able to make this piece of work. I thank Nika for his kindness, for helping me to make the decision of continuing my studies, and for everything he has done for me. I would also like to thank Øyvind for boosting my life and for teaching me to live even during the stressful periods of the Ph.D. I thank all of my beautiful peers during bachelor and master studies, colleagues from my previous job for their help and support, and all teachers of my life.

I thank Franco Vazza for sharing the `Enzo` initial setup for our projects and for inviting me in Bologna. I appreciate useful discussions and comments from Rafael Alves Batista, Emma Clarke, Klaus Dolag, Sayan Mandal, Sergio Martin-Alvarez, Alberto Roper Pol, Günter Sigl, and Chiara Stuardi. I gratefully acknowledge publicly available `Enzo` code (https://enzo-project.org), which is the product of a collaborative effort of many independent scientists from numerous institutions around the world. Their commitment to open science has helped make this work possible. I also acknowledge the *yt* toolkit (https://yt-project.org), which was used as the analysis tool for our projects, and the support from the whole *yt* team. The simulations presented in this thesis made use of computational resources on Norddeutscher Verbund für Hoch- und Höchstleistungsrechnen (HLRN).

Contents

List of Figures

List of Tables

Chapter 1

Introduction

1.1 Overview

Our Universe appears to have a spider web-like structure on cosmological scales. This pattern of the Universe, known as the cosmic web, is a complex network of giant bubble-like voids, sheets, and filaments where the latter itself is a collection of galaxies and galaxies clusters that occupy the nodes of the large-scale structure. According to the most accepted paradigm, the cosmic web has formed from tiny density perturbations that is observed in the relic, Cosmic Microwave Background Radiation (CMBR)[1] coming from the early Universe. These primordial density fluctuations then turned into observed structures through hierarchical structure formation.

It turns out, that the cosmic web from small (i.e., planets and stars, [30, 31]) to large scales (galaxies and galaxy clusters, [32, 33]) is permeated by coherent magnetic fields. Different observational techniques show the ordered, large-scale morphology of these fields with the strengths of $\mu\mathrm{G}$ and correlation lengths reaching a few tens of kpc in galaxy clusters (see e.g., Refs. [34, 35]).

Most of what we know about such large-scale-correlated, extragalactic magnetic fields (EGMFs) comes through the detection of radio waves. Recently, diffuse radio emission, visible through synchrotron radiation, has also been detected in the region connecting the pairs of galaxy clusters [1, 2, 36, 37]. These observations show the magnetisation of the shortest filamentary structures. At even larger scales, in cosmic voids, such measurements are difficult because of the low density of these regions. However, the new technique that uses the observations of high-energy γ-rays from distant blazars is most promising for probing the magnetisation of cosmic voids. The idea of this new technique is that sufficiently strong magnetic fields in voids modify the low-end tail (GeV range) of the blazar spectrum by affecting the trajectories of charged particles (deposited in the intergalactic medium (IGM), along the LOS from the source to the observer). The observed deficit in the GeV emission in the spectra of some of the blazars has imposed a lower bound (of the order $10^{-16}\,\mathrm{G}$) on the strength of magnetic fields in these rarified cosmic regions.

Understanding the origin of cosmic magnetism is one of the challenging questions of modern astrophysics and cosmology. It is commonly assumed that the observed large-scale fields results from the amplification of weak seed magnetic fields. Two broad classes of seed magnetic field generation are generally considered: (1) an astrophysical, or bottom-up scenario, where the observed magnetic fields have their origin in an initial weak seed field produced within local sources (e.g., within first stars), and then amplified and transferred to larger scales [38, 39]; and (2) a primordial (cosmological), or top-down scenario, where a seed magnetic field is generated in the early Universe, during epochs preceding the structure formation [40]. Regardless of the magnetogenesis scenario, magnetic fields must have been significantly amplified to reach the observed strengths in galaxies and galaxy clusters; the physical mechanisms of the amplification of weak seed fields during structure formation are the adiabatic contraction and turbulent small-scale dynamo. The latter is a preferred the mechanism for explaining the efficient amplification of the fields on galaxy (see e.g., [41–43]) and galaxy cluster scales (see e.g., [44–47]). It is also plausible that the amplification of weak seed fields occurred via the combined effect of these two.

It is apparently difficult to create magnetic fields in the classical magnetohydrody-

[1] We note that basic cosmological concepts including CMBR, redshift, homogeneity and isotropy of the Universe as well as the short description of notable events of the Universe are described in Chapter 2.

namic (MHD) limit since the plasma does not provide a source term for the magnetic field generation; i.e., if magnetic field is zero at initial time, it will be zero at all later times. In the earlier works of Biermann [48] and Harisson [49] this limitation has been evaded by taking into account the fact that positively and negatively charged particles do not have identical properties. These so-called cosmic battery mechanisms fall under the category of astrophysical scenarios of the seed field generation (although, Biermann's mechanism has also been applied in the early Universe setting). It should be noted that astrophysical seed magnetic fields, i.e., generated locally on small scales, require additional mechanisms of magnetic field transport into larger scales in order to explain the large coherence scales of the observed fields. These transfer mechanisms usually include star formation and outflows from an active galactic nuclei (AGN, see e.g., Refs. [50–53]).

In the primordial scenario, on the other hand, magnetic fields originating in the early Universe, i.e., PMFs, could be generated during or after inflation. The inflationary magnetogenesis assumes that vacuum fluctuations of an electromagnetic field give rise to a weak seed field which then grows (see Refs. [54, 55] for pioneering work). The coherence scale of the quantum-mechanically produced PMF can be stretched on superhorizon scales whilst breaking the conformal invariance of electromagnetic action. Inflationary PMFs with large coherence scales might have a scale-invariant spectrum (i.e., most of the magnetic energy is concentrated on large scales) or they can be uniform, constant fields as predicted by Mukohyama model [56]. In the post-inflationary scenario, PMFs with smaller coherence scales (limited by Hubble horizon scale), could be generated during phase transitions through e.g., collision and nucleation of bubbles of different phases if the phase transitions are of the first order. This can be translated onto realisation of the seed magnetic field having a sharply peaked magnetic power spectrum where the peak, or the characteristic length-scale is set by the phase transition bubble size; see, e.g., Ref. [57]. Both generation scenarios, inflationary and phase-transitional, could generate helical PMFs [58]. Magnetic helicity, being a measure of twist and linkage of magnetic field lines, has proven to be a helpful tool for understanding the field evolution in the turbulence-dominated flow (see below). The relevance of a primordial, helical magnetic field is that, if ever detected, it will be a direct indication of parity (mirror symmetry) violation in the early universe and can in turn explain the matter-antimatter asymmetry [59, 60].

The extensive presence of magnetic fields in high redshift galaxies [61] and galaxy clusters [62] as well as an intriguing possibility of having very weak magnetic fields in cosmic voids [7] tip the scale in favour of a primordial magnetogenesis scenario. We notice that e.g., inflationary PMFs have volume filling fraction close to unity, i.e., permeating the whole observable Universe, and can naturally explain the large coherence scales of extragalactic fields, as well as the presence of magnetic fields (if detected) in the voids of the Universe.

Apart from the generation physics, PMF studies also focus on the *evolution* and *signatures* of these fields. The signatures of PMFs include their effects on Big Bang Nucleosynthesis (BBN); in particular, the presence of stochastic PMFs during BBN can potentially reduce the ^{7}Li abundance, providing a better agreement with observations; see e.g., Ref. [63]). In addition, the scalar-vector-tensor decomposition of the energy-momentum tensor of PMFs (in Fourier space) is a powerful approach for analysing the effect of PMFs on cosmological perturbations, and therewith, on CMBR (see e.g., Refs. [64–66]). For example, it has been shown that PMF-induced perturbations can be dominant on small angular scales (see e.g., Ref. [67] and references therein). Furthermore, PMFs drive com-

pressional and rotational perturbations affect the matter power spectra on small scales, corresponding to dwarf galaxy scales (see Refs. [68–70] for seminal work; and [71–73] and [74] for recent studies). Interestingly, recently PMFs were also considered as a potential possibility to relax the Hubble tension [75].

The *evolution* of PMFs have been studied in the radiation-dominated and post-recombination epochs. In the *pre-recombination epoch*, transition of the Universe from inflation to reheating phase leads to the production of charged particles. A subsequent increase in plasma conductivity makes magnetic fields coupled to the primordial plasma. If PMFs are dynamically strong enough they can lead to development of turbulent motions. If they are weak the presence of MHD primordial turbulence is still well justified by the phase transition dynamics. Therefore, one can study the pre-recombination evolution of PMFs in the MHD turbulence regime.

Studies using MHD-only simulations (i.e., without gravity and cosmology) have explored characteristics of PMFs in the radiation domination (see e.g., [22,57,76]) or across the recombination epochs [77] in a "freely decaying turbulence" regime. The MHD evolution of both inflationary (large-scale-) and phase-transitional (small-scale-correlated) fields show a decay along with an efficient increase of magnetic coherence scales in the phase-transitional cases. For instance, the typical strength and correlation length obtained for the phase-transitional fields at the recombination epoch are of the order of $10^{-6}\,\mathrm{nG}$–$0.3\,\mathrm{nG}$ and 10^{-3}–$30\,\mathrm{kpc}$, respectively [24]. Particularly noteworthy is the largest coherence scales that are obtained for the helical PMFs.

The PMF is expected to freeze and retain its characteristic spectral profile from the moment of recombination until reionisation. The formation of massive structures, such as galaxy clusters, and subsequent amplification of PMFs on the corresponding scales (see e.g., [78]) is studied with *cosmological MHD* simulations. Even though achieving a large dynamical range in such simulations still remains a challenge, sufficiently high (high enough to reach the non-linear growth of magnetic fields) resolution has been achieved in some large cosmological suites. Notable examples are the MAGNETICUM project (www.magneticum.org), the Illustris TNG [79] and Chronos++ suite presented in Ref [53]. Several other simulations have also been successful to reproduce the observed magnetisation ($\sim\ \mu\mathrm{G}$) of the Universe on large cosmological scales ($\sim\ \mathrm{Mpc}$), such as e.g., on galaxy cluster scales (see e.g., [45, 46, 80]). However, building a self-consistent picture of the evolution of PMFs from the very early Universe until the current epoch is far from trivial. The difficulty lies not only in the modeling of the vast range of astrophysical scales across different cosmological epochs but also in obtaining realistic initial conditions. The initial velocities and densities used in cosmological simulations often neglect any effects from PMFs (i.e., the effects on the initial matter power spectrum) as well as MHD decay effects (coming from the evolution of PMFs in the radiation-dominated epoch). Nonetheless, cosmological MHD simulations still remain our main guiding tool for interpreting the existing observations of cosmic structures, for exploring the origin of cosmic magnetic fields and constraining primordial magnetogenesis scenarios.

In this thesis, we use cosmological MHD simulations and study PMF evolution during structure formation. We hope our work is a step further in understanding the physics of PMFs and in employing more realistic MHD cosmological simulations in order to search for the primordial magnetism imprints. In the following sections, we overview the observed large-scale magnetisation of the Universe in a bit more detail while in Section 1.3 we present the structure and aim of the thesis.

1.2 Large-scale magnetisation of the Universe

The forthcoming large surveys, such as the ones with the SKA and its precursors and pathfinders [81–83], and the CTA, in tandem with the Fermi Gamma-ray space telescope will play a crucial role in answering the key questions about cosmic magnetism. The observed large-scale magnetisation of the Universe is the primary motivation for studying the PMFs. Below we discuss some of the observational techniques that are used for inferring the magnetic field strength on galaxy cluster scales and in the rarefied cosmic regions. We focus on synchrotron emission and Faraday rotation as probes of cluster and intercluster magnetic fields, and blazar spectra observations as probes of the magnetisation of rarefied cosmic regions (such as cosmic voids and the IGM).

1.2.1 Galaxy clusters and filamentary structure?

Galaxy clusters, the largest gravitationally bound structures of the Universe with a total (baryonic and dark matter, DM) mass of $\sim 10^{14} M_{\odot}$ – $10^{15} M_{\odot}$, reveal the existence of large-scale magnetic fields in the dilute plasma between galaxies known as the intracluster medium (ICM). The most of the baryonic mass of galaxy cluster is contained in the ICM which is mainly composed of ionised hydrogen with $\sim 10^{-3}\,\mathrm{cm}^{-3}$ electron number densities at 10^7—$10^8\,\mathrm{K}$ temperature. We observe ICM through *X-ray* and *radio emission*. At the ICM temperatures, the primary emission for a gas is the thermal bremsstrahlung which results from free-free electron-ion collisions and it is detected at X-ray wavelengths. The morphology of X-ray emission along with other parameters of the cluster can be used to identify the dynamical state of galaxy clusters (see e.g., Ref. [84]); i.e., whether it is a relaxed cluster or it is undergoing a merger with another cluster (so-called merging clusters). The radio emission, on the other hand, results from relativistic electrons gyrating along magnetic field lines producing **synchrotron emission**. This is an extended, diffuse emission which is not directly associated to any source (i.e., galaxy) in galaxy clusters and it rather traces the ICM magnetic fields and relativistic electrons.

Radio sources are now being detected in nearby as well as distant galaxy clusters thanks to the advancements of radio telescopes. These sources are divided into *radio halos* and *radio relics* (see Ref. [85] for a recent review) where the former is usually found in the centre of merging clusters (200-1500 kpc in sizes), following approximately the X-ray emission, while the latter is a $\sim$ Mpc-sized source with elongated structures located in the cluster periphery; see Figure 1.1 for such an example. In dynamically relaxed clusters one also finds smaller-size ($100\,\mathrm{kpc}$) radio sources called *radio mini-halos*. Interestingly, the recent LOw Frequency ARray (LOFAR; observations at frequencies of < 200 MHz) observations have detected clusters whose radio halos are embedded in a much more extended diffuse radio emission, referred to as *"megahalos"*. The intensity of the megahalos is lower compared to the radio halos but they point to the existence of magnetic fields (along with relativistic electrons) far beyond the regions of radio halos. This makes them interesting objects for unveiling the nature of relativistic electrons and magnetic fields in the outskirts of galaxy clusters. More importantly, radio emission has also been detected on scales larger than galaxy clusters [1, 2, 36, 37], i.e., extending over filamentary scales. Such regions are now referred to as "radio bridges" (similarly to the so-called bridge, a term which has been applied to the detected intercluster matter between galaxy clusters [86] and that has motivated a search of this diffuse radio emission between galaxy clusters, i.e., the radio bridge). In Figure 1.2 we show the radio (blue) and X-ray

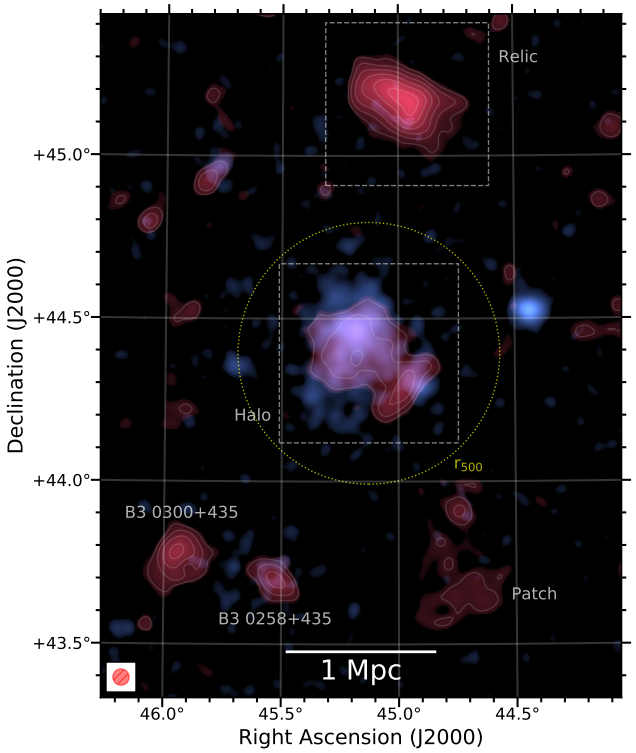

Figure 1.1: Composite radio (LOFAR 120168 MHz, red) + X-ray (X-ray telescope ROSAT, 0.12.4 keV, blue) image of the Ant Cluster showing radio halo and radio relic. Figure credit: Ref. [1].

(red) emission (LOFAR observations) in a galaxy cluster pair of Abell 399 and Abell 401 from Ref. [2]. As the figure shows, the space connecting these two merging clusters is permeated by magnetic fields traced by synchrotron emission. Furthermore, Ref. [62] has recently claimed the detection of radio halos in high redshift ($z \sim 0.6$–0.9) galaxy clusters which requires the fast and efficient amplification of seed magnetic fields within the few Gyr timescale during cluster formation (regardless of magnetogenesis scenario).

Even though detected synchrotron emission gives us evidence for the existence of the ICM magnetic fields, it does not allow an unambiguous determination of the field strength. One usually has to make an assumption, such as e.g., the minimisation of the total energy of the source in order to estimate the volume averaged magnetic field strength. The total energy of the source ϵ_T, is the sum of magnetic field energy (ϵ_B) and the relativistic particles' (electrons and protons, ϵ_e, ϵ_p) energy: $\epsilon_T = \epsilon_B + \epsilon_e + \epsilon_p$. It can be shown that ϵ_T is a function of synchrotron luminosity and magnetic field strength (along with other parameters; see e.g., Section 3 in Ref. [87]). Then one assumes equipartition between particle and magnetic energies since this approximately happens for the magnetic field value where the total energy has a minimum (see e.g., Figure 2 in Ref [87]). The magnetic field value determined with this method is referred to as equipartition value $B_{\mathrm{eq}} = 24\pi\epsilon_{\mathrm{min}}$ where ϵ_{min} is the minimum energy density and it can be expressed in terms of observable quantities, such as e.g., source brightness at certain frequency. This method has been used to estimate magnetic field strengths in galaxy clusters (see e.g., [88, 89], see also Table 3 in Ref. [87]). Moreover, B_{eq} has also been estimated for the intercluster medium in the recent work [16]. The authors used a nondetection of radio ridge between colliding galaxy clusters (Abell 3391, Abell 3395) to put an upper bound of the order of $0.1\,\mu\mathrm{G}$ on the magnetic field strength. Another recent work [17] has used equipartition argument for

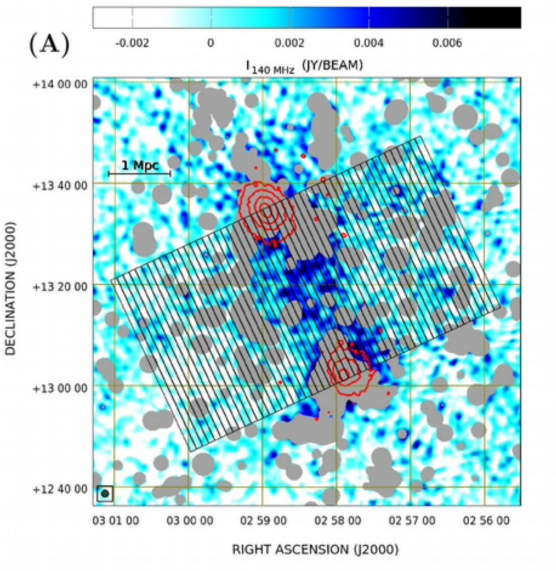

Figure 1.2: The X-ray and radio (LOFAR observations) emission detected from Abell 0399 and Abell 0401 are shown in red and blue colors, respectively. Sources not related to radio bridge are shown in grey. See the text and Ref. [2] for more details. Figure credit: Ref. [2].

deriving the field strength (to be of the order of 30—$60\,\mathrm{nG}$) in cosmic web filaments; in this case, authors used a novel technique of stacking the multiple radio and X-ray maps of physically close luminous red galaxies to search for the synchrotron emission from the filamentary structure.

Another probe of the EGMF is the **Faraday rotation effect**. Faraday rotation of linearly polarised emission helps us understand magnetic fields on a vast range of astrophysical scales. Polarised radio emission from distant sources is affected by an intervening magnetised plasma which rotates the intrinsic polarisation plane of emission. This happens due to the different phase velocities that are gained by the left and right-circular polarisation states of a wave when traversing the foreground magnetised region.

In order to understand why the Faraday rotation effect takes place, following the Ref. [90], we first consider the magnetised plasma with characteristic $w_{\rm p} = \sqrt{\frac{4\pi n_{\rm e} e^2}{m_{\rm e}}}$ frequency,[2] where $n_{\rm e}$, e and $m_{\rm e}$ are the electron number density, electron charge and electron mass, respectively. Another characteristic frequency of such medium is the electron gyration frequency: $w_{\rm e} = \frac{eB}{m_{\rm e}c}$ with B being the magnetic field strength. Next, we consider the propagation of a linearly polarised electromagnetic wave (such as the synchrotron radiation) in the magnetised plasma. We assume that the electric field vector $\mathbf{E}_l$ oscillation frequency is much larger than the mentioned characteristic frequencies of the plasma, i.e., $\omega >> w_{\rm e}, w_{\rm p}$, We also note that a linearly polarised wave is the superposition of a right and a left circularly polarised modes (with the same frequency); that is $\mathbf{E}_l = \mathbf{E}_R + \mathbf{E}_L$, where $\mathbf{E}_l$ and $\mathbf{E}_R$ are the right (R) and left (L) circularly polarised modes, respectively. They rotate in opposite senses, symmetrically with respect to the polarisation orientation.

[2]This is a frequency that is caused by the Coulomb force which acts as a restoring force on the electrons (e.g., when they undergo small displacements in the ion-electron gas).

Finally, we discuss the case when the wavevector $\mathbf{k}$ ($k = |\mathbf{k}|$) of the emission matches the magnetic field direction, $\mathbf{k}||\mathbf{B}$. In such case, the dispersion relation (derived from the Maxwell equations; see e.g., Ref. [90] and its Appendix A) takes the form:

$$\omega^2 = c^2k^2 + \omega_{\rm e}^2 \pm \frac{w_{\rm p}^2\omega_{\rm e}}{\omega}.^{3} \tag{1.1}$$

In the latter equation $\pm$ sign corresponds to the R and L circularly polarised modes, respectively. One can rewrite this relation in terms of the phase velocity:

$$V_\Theta \equiv \frac{w}{k} = c\left(1 + \frac{\omega_{\rm p}^2}{2\omega^2} \pm \frac{w_{\rm p}^2\omega_{\rm e}}{2\omega^2}\right), \tag{1.2}$$

where we see that, indeed, the R and L modes have different phase velocities ($V_{\Theta,R} > V_{\Theta,L}$). In the calculations below, we adopt the definition of the phase of a wave as

$$\Theta = \omega t - \int_0^l k dl', \tag{1.3}$$

noticing that at the source ($l = 0$) there is no difference between the phases of the L and R modes. The difference in the phase of L and R modes arises during the propagation of a wave in the magnetised plasma (see the nice illustration, Figure 2 in Ref. [90]). Then we expect the following difference in the phases of the L and R modes [90]:

$$\Delta\Theta = \Theta_{\rm R} - \Theta_{\rm L} = -\int_0^l \Delta k dl' = \int_0^l \frac{\Delta V_\Theta}{V_\Theta} k dl' = \int_0^l \frac{w_{\rm p}^2 w_{\rm e}}{w^3} k dl'. \tag{1.4}$$

One can also show that the angle by which the wave polarisation plane is rotated during its propagation in the magnetised medium is half of the phase difference between the L and R modes:

$$\Delta\psi_\lambda = \frac{1}{2}\Delta\Theta = \frac{1}{2}\int_0^l \frac{w_{\rm p}^2 w_{\rm e}}{w^3} k dl' = \left(\frac{e^3}{2\pi m {\rm e}^2 c^4}\int_0^l n_{\rm e} B dl'\right)\lambda^2. \tag{1.5}$$

The latter equation can also be written in terms of the rotation measure (RM):

$$\Delta\psi_\lambda \equiv \psi_\lambda - \psi_0 = {\rm RM}\lambda^2, \tag{1.6}$$

where

$${\rm RM} = \frac{e^3}{2\pi m_{\rm e}^2 c^4}\int_{\rm source}^{\rm observer} n_{\rm e} B_l dl, \tag{1.7}$$

and ψ_λ and ψ_0 are the polarisation plane angles at the observer location and at the source, respectively. The subscript l in B_l indicates that magnetic field is directed toward the observer. By convention, a positive (negative) RM implies a magnetic field pointing toward (away from) the observer. For a source at cosmological distance and redshift z, RM is modified to

$$\begin{aligned} {\rm RM} &= \frac{e^3}{2\pi m_{\rm e}^2 c^4}\int_0^l (1+z)^{-2} n_e(z) B_l(z) dl(z) \\ &= 0.812 \int_0^l (1+z)^{-2}\left(\frac{n_e}{\rm cm^{-3}}\right)\left(\frac{B_l}{\mu\rm G}\right)\left(\frac{dl}{\rm pc}\right)\ \frac{\rm rad}{\rm m^2}, \end{aligned} \tag{1.8}$$

[3] Note that here the electrons' thermal motion is not taken into account; i.e., the plasma is assumed to be "cold".

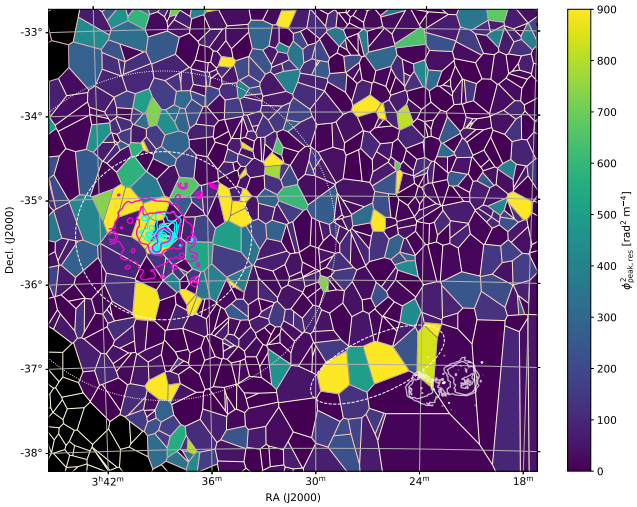

Figure 1.3: The morphology of $\psi^2_{\rm peak,res}$ (frequently referred also to as RM) in Fornax galaxy cluster as revealed by Australian Square Kilometre Array Pathfinder (ASKAP) observations. Light blue and pink contours show X-ray emission as seen by Chandra in 0.3–$1.5\,{\rm keV}$ bandpass [3] and ROSAT 0.1–$2.4\,{\rm keV}$ bandpass [4], respectively. The white dotted lines shows a virial radius of Fornax cluster ($705\,{\rm kpc}$); the white dashed lines show the region outside X-ray emitting ICM where the enhancement of $\psi^2_{\rm peak,res}$ values has been found (see Ref [5] for more details). Figure credit: Ref. [5].

where $(1+z)^{-2}$ factor accounts for the dilution of the electromagnetic waves due to expansion of the Universe (see Section 2.2).

As we can see from the definition, measurements of ${\rm RM}$ can provide information on the LOS magnetic field strength, weighted by electron number density. Although, it should be noted that, in general, Equation (1.8) defines the Faraday depth $\psi(L')$ (see below) where L' is a location of a source. Faraday depth [91, 92] coincides the definition of RM in the ideal case when the rotation is caused by only one, non-emitting Faraday screen.

Various methods exploiting the Faraday rotation effect have been used to understand the strength and structure of the magnetic field in the ICM. A traditional way has been to estimate RM as a slope from a linearly-fitted $\psi_\lambda(\lambda^2)$ relation where ψ has been measured for different wavelengths, λ. See e.g., Refs. [18, 93] where this method has been used to constrain the Coma cluster and the Coma relic magnetic field strengths (derived to be $\sim 5.4\,\mu{\rm G}$ and $2\,\mu{\rm G}$, respectively).

The wide-band data which is becoming available through SKA precursors/pathfinders makes it possible to use other methods for tracing the properties of large-scale magnetic fields. For instance, Faraday tomography, offering a tomographic reconstruction of magnetised structures along the LOS [94], seems to become a powerful tool in near future. This method uses the Rotation Measure Synthesis (RMS) technique to calculate the Faraday depth [91, 92]. The results from the RMS technique have been presented in several recent works (see e.g., [5, 20]). Figure 1.3 shows the results from Ref. [5] mapping the $\psi^2_{\rm peak}$ for the low mass ($\sim 6\times10^{14}M_\odot$) Fornax galaxy cluster (contribution from Galactic magnetic field has been subtracted; see below). The Faraday depth is obtained through: $\psi^2_{\rm peak} = {\rm argmax}(|\mathbf{F}(\psi)|)$ where the function $\mathbf{F}(\psi)$ is determined from the Faraday dispersion spectrum, $\mathbf{P}(\lambda^2)$. Here, $\mathbf{P}(\lambda^2) = \int \mathbf{F}(\psi)e^{2i\psi\lambda^2}d\psi$ (see Ref. [5] for more details on the technique). Figure 1.3 illustrates that magnetised medium extends beyond the X-ray

emitting ICM, thus, again, showing that magnetic fields are present outside dense environments, specifically, in moderately-dense components of the Warm-Hot Intergalactic Medium (WHIM; plasma with $T \sim 10^5$–$10^7\,\mathrm{K}$, and $n_e \sim 10^{-6}$–$10^{-4}\,\mathrm{cm}^{-3}$, and that is thought to be formed during structure formation).

Finally, we note that all magnetised regions along the LOS contribute to the Faraday rotation effect. Here, for simplicity we refer to RM which is conveniently decomposed into components [95]:

$$\mathrm{RM} = \mathrm{RM}_{\mathrm{source}} + \mathrm{RM}_{\mathrm{Gal}} + \mathrm{RM}_{\mathrm{IGM}}, \tag{1.9}$$

where $\mathrm{RM}_{\mathrm{source}}, \mathrm{RM}_{\mathrm{Gal}}$ and $\mathrm{RM}_{\mathrm{IGM}}$ are the contributions from the magnetised medium of the source itself, of our own Galaxy and the IGM, respectively. In Section 6.6 we will also describe a novel approach that has been used recently to isolate the contribution from the IGM. RM observations of extragalactic radio sources are fundamental in further constraining the properties of large-scale magnetic fields in the near future and for discriminating between (primordial) magnetogenesis scenarios.

1.2.2 Rarefied cosmic regions

Observations of high-energy gamma rays from blazars provide an intriguing possibility of detecting very weak magnetic fields in the IGM of voids. Although these observations have not yet led to the measurements of void magnetic fields, they have been used to put a lower limit on the field strength. Blazar spectra observations are most promising for measuring the magnetisation of cosmic voids since this technique is immune to the effects coming from the source (i.e., blazar) or Galactic magnetic fields which are otherwise difficult to exclude from the RM measurements. Below, we briefly describe the technique underlying the use of blazars as a probe of cosmic magnetism (see pioneering work of Ref. [96]) and its uncertainties while we refer the reader to more detailed reviews on the question (e.g., Refs. [6, 9, 23]).

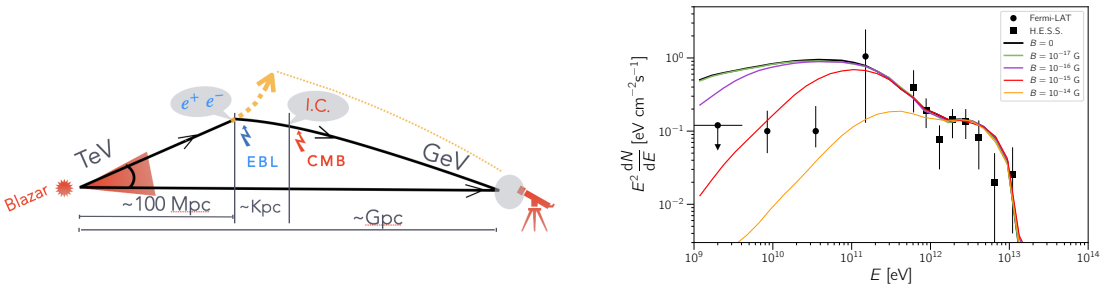

Figure 1.4: *Left panel:* Propagation of high-energy γ-rays (emitted from blazars) that show channelling of TeV emission into GeV cascade emission due to interactions with the EBL and CMB photons. The GeV emission affected by intervening magnetic fields is broadened out of the telescope's point spread function. The sketch adapted from Ref. [6]. *Right panel:* Simulated blazar spectra as they are obtained for different magnetic field strengths in IGM. The amplitude of the magnetic field affects the low-end tail ($< 10^{12}$ eV) of γ-ray spectra. The data points represent measurements by Fermi-LAT [7] and H.E.S.S. [8]. The figure credit: Ref. [9].

In the left panel of Figure 1.4, we show a sketch illustrating the process associated with the propagation of high energy γ-rays. TeV γ-rays, emitted from blazars, interact

with the extragalactic background light (EBL) producing electron-positron pairs ($\gamma\gamma \rightarrow e^+ + e^-$). The pair energy is then channelled into the cascade, GeV emission through inverse-Compton scattering of e^+, e^- with the Cosmic Microwave Background (CMB) photons. The secondary GeV emission propagates along with the primary TeV emission and γ-ray spectrum is expected to have a bump (excess) in the GeV regime. If magnetic fields reside on the largest scales ($\sim 100\,\mathrm{Mpc}$) of the Universe, they can alter the process by bending the trajectories of the pair and broadening the secondary GeV emission out of the telescope's point spread function. The secondary cascades are often referred to as haloes [97] because of their expected halo-alike morphology in the axi-symmetric case; i.e., when the angle between the observer and blazar jet axis is ~ 0 (see also Ref. [9]). The cascade emission might also be not detectable if the signal is delayed with respect to the primary γ-ray propagation time. This again depends on the strength of the IGM magnetic field, and on the distance to the source and duration of emission [98–100].

In the right panel of Figure 1.4, we show the simulated blazar spectra (simulated using the Monte-Carlo simulations; see Ref. [9]) for different magnetic field strengths. As we can see zero magnetic field case, $B = 0$, shows an excess with respect to the $B > 0$ cases. The non-observation of this GeV bump in the blazar spectra (the data points in the figure) along with the modelling of the cascade emission has been used to impose lower bounds on the intergalactic magnetic field strength. The first such analysis has been done in Ref. [101] where authors derived a lower limit on the IGM magnetic field strength to be $\gtrsim 3 \times 10^{-16}\,\mathrm{G}$ on Mpc scales assuming broadening of the cascade emission around the initial point source. The constraints on the magnetic field strength, derived from such analysis, in general, depend on the structure of the field (see e.g., Figure 4.2; see also Section 8.1); thus, this method can help us to test magnetogenesis scenarios. For instance, Ref. [102] has studied the propagation of cascade emission to put constraints on the volume filling factors of large-scale magnetic fields. The authors argue that either magnetic fields have been generated from primordial magnetogenesis scenarios or should have been (very) efficiently transported toward large cosmological scales if they were generated by local processes in the late Universe. Even though the TeV blazar spectra measurements still remain the strongest argument for the proposed relic magnetisation of the Universe it is still unknown whether the void magnetic fields could be effectively polluted by e.g., galactic winds. The recent modelling of the blazar spectra in combination with galactic outflows has shown that the effect of the observed GeV flux suppression should be coming due to magnetic fields residing in cosmic voids [103].

The picture described above may change and production of GeV gamma rays might be inhibited if the pair beam is subject to plasma instabilities [104, 105]; e.g., if the electron-positron pair loses the energy via interactions with the ionised component of the IGM rather than through the inverse Compton scattering of the CMB photons. Various mechanisms of instabilities have been proposed in the literature (see e.g., [106–108]). Even though the effect of plasma instabilities is still under debate the recent work [109, 110] has shown that the weak, small-scale-correlated ($\lesssim$ kpc) magnetic field can reduce the electrostatic instability growth rate and eliminate the suppression of the secondary cascades. If the GeV halo is detected using the future telescopes, such as e.g., the CTA, this will settle the issue confirming that plasma instabilities do not play a role and suppression of secondary cascades is due to large-scale magnetic fields existing in cosmic voids. It should also be mentioned that detection of the GeV halo can give us a hint on the primordial magnetic helicity since helical magnetic fields lead to the unique morphological signatures in the γ-ray-induced electromagnetic cascades [9, 111, 112]. We will briefly

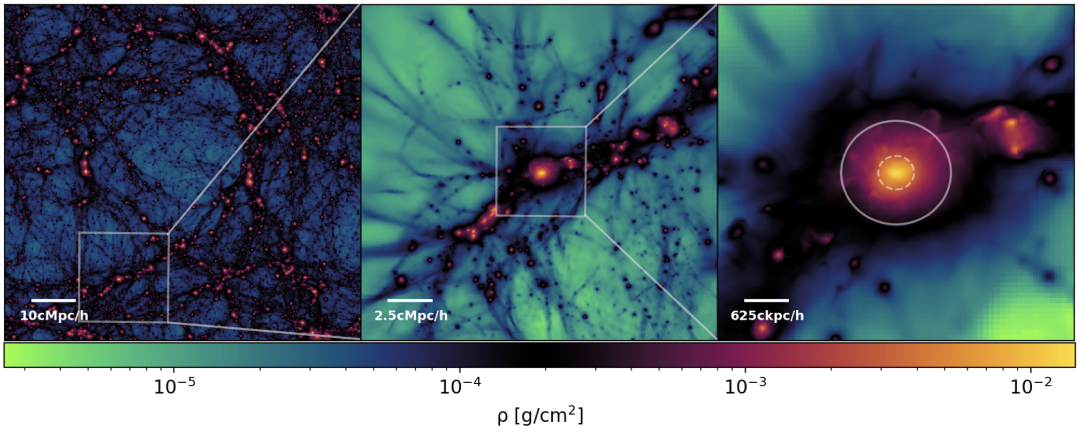

Figure 1.5: Projected density of the simulated volume relevant for the *cosmic web* study (left panel; [10]) and *galaxy cluster* study (middle and right panels; [11]). Left panel shows simulated $(80\ h^{-1}\mathrm{cMpc})^3$ volume with $19.5\ h^{-1}\mathrm{ckpc}$ resolution; *middle* and *right panels* show the simulated cluster with $2.44\ h^{-1}\mathrm{ckpc}$ resolution within $(20\ h^{-1}\mathrm{cMpc})^3$ and $(5\ h^{-1}\mathrm{cMpc})^3$ boxes, respectively. From left to right the zoom-ins of the selected regions are shown. We note that throughout this document we use the 'c' to emphasise comoving units, i.e., comoving with the expansion of the Universe. See Chapter 2 for more details.

discuss this in Section 8.1.

1.3 Aim and structure of the thesis

In our work, we assume that PMFs are good candidates for explaining the magnetisation of large-scale cosmic structures. This thesis is an attempt, for the first time, to combine our current understanding of the PMF generation scenarios and pre-recombination evolution of PMFs to study their evolution during structure formation. Our thesis aims to answer the following questions: (1) is the PMF structure relevant when studying their amplification during the formation of the cosmic web? (2) Are the PMF imprints erased after the non-linear structure formation? (3) What is the initial structure of the PMF which leads to the observed magnetic field strengths and coherence scales in galaxy clusters and cosmic voids?

We study the PMFs that originate during inflation and phase-transition epochs. We model the evolution of these fields during structure formation while taking into account their end-of-recombination spectral characteristics (i.e., taking into account their MHD decay effects in the early Universe). We employ cosmological MHD code `Enzo` [113] to simulate their amplification/decay in the (i) *cosmic web* and in (ii) *galaxy clusters*. In the former project, we also study helical PMFs. As mentioned earlier, study of the helical PMFs can be helpful in constraining the early Universe physics.

In both of our projects, we group PMF models according to their characteristics. We study PMFs that have large and small coherence scales at the start of our simulations, corresponding to the inflation- and phase-transition magnetogenesis scenarios, respectively. In Figure 1.5 we show cosmological volume relevant to our cosmic web and galaxy-cluster studies. In the cosmic web simulations, we study global distribution and properties of PMFs through large-scale structure formation. In the galaxy cluster simulations,

even though they also account for the evolution of the larger-scale cosmic environment, we focus on analysing the "shorter" length scales that cover galaxy clusters and the ICM.

In this thesis, apart from presenting our results from the mentioned works, we will also briefly review the theoretical framework relevant to the PMF studies. We start this in Chapter 2 by giving a short overview of the (ΛCDM) cosmology that is employed in our projects. In Chapter 3, we write down the MHD equations essential for understanding the basic principles of the evolution of (primordial) magnetic fields. In the same chapter, we also give a description of the characteristic scales of PMFs and their amplification mechanisms. In Chapters 4 and 5 we overview the generation and pre-recombination evolution of PMFs, and adopted methods for studying their evolution during structure formation, respectively. In Chapters 6 and 7 we present our results which are based on the following papers:

- Mtchedlidze, S., Domínguez-Fernández, P., Du, X., Brandenburg, A., Kahniashvili, T., O'Sullivan, S., Schmidt, W., Brüggen, M., "Evolution of Primordial Magnetic Fields during Large-scale Structure Formation", *ApJ* 929, 127 (2022),
- Mtchedlidze, S., Domínguez-Fernández, P., Du, X., Schmidt, W., Brandenburg, A., Niemeyer, J., Kahniashvili, T., "Inflationary and phase-transitional primordial magnetic fields in galaxy clusters", *ApJ* 944, 100 (2023)

where we studied the evolution of PMFs in the cosmic web and in galaxy clusters, correspondingly. In these chapters, we also include a more detailed description of the setup of our simulations, physical model, as well as the key findings of the project in summaries. Finally, in Chapter 8 we will discuss future prospects that have been raised by the studies presented in this thesis.

In this document, we mostly use natural units ($c = k_B = 1$; i.e., except Chapters 6, 7), Minkowski metric sign convention (+, –, –, –) in Chapter 2 and (-, +, +, +) convention in Chapter 3. In Chapter 3 we distinguish between the rescaled (comoving) and physical variables; for instance, for the rescaled and physical magnetic field we use $\mathbf{B}^*$ and $\mathbf{B}$ notations, respectively. From Chapter 5 we use only comoving values of the fields (i.e., $\mathbf{B}$ becomes comoving value in the mentioned chapters and stars no longer indicate rescaled values) unless stated otherwise. We also use 'c' to emphasise comoving units (e.g., $h^{-1}\mathrm{ckpc}$ denotes comoving (kpc) length scale).

Chapter 2

Standard model of Cosmology

Λ-Cold Dark Matter[1] (ΛCDM) cosmology or Concordance Model, is the framework in which we study the evolution of PMFs. This model successfully describes the formation and evolution of large-scale structure. Over the past decades, Cosmology has become a data-driven precision science and the ΛCDM model has been tested against various observations. Even though the model has some tensions and unexplained phenomena, concordance cosmology with its standard model of particle physics (describing and classifying all known elementary particles) gives a good agreement between theory and observations. According to this model, tiny density perturbations that are imprinted on CMBR lead to the formation of the cosmic web; the "known" constituents of our accelerated expanding (dark-energy dominated) Universe are the baryonic and dark matter that causes the observed clustering of matter through gravitational attraction. In this chapter, we give a brief overview of the mathematical framework of ΛCDM cosmology and tell a short story of the evolution of the Universe that is based on the mentioned paradigm (or more precisely, on the extension of ΛCDM paradigm which is sometimes referred to as inflationary-ΛCDM). We mostly follow classic textbooks [114–116] on the subject, as well as the lecture notes by Jens Niemeyer.

[1] Λ is standing for the cosmological constant, associated to dark energy and which is thought to cause the accelerated expansion of our Universe. Cold DM is hypothesised to be consisting of weakly interacting massive particles. Cosmologists strive to understand the nature of these components.

2.1 Homogeneous and isotropic Universe

One of the main assumptions of Cosmology, firmly established by observations (and often referred to as Cosmological Principle), is the homogeneity and isotropy of the Universe. According to this principle, there is no preferred scale and direction for the matter distribution on large cosmological scales (at least scales $\gtrsim 1000\,\mathrm{Mpc}$). Another important concept is the expansion of the Universe. Even though it had already been predicted by General Relativity, it was largely accepted only after Edwin Hubble's observations of galaxies and their redshifts [117]. These observations showed that physical separation between gravitationally unbounded systems grows in time.

The homogeneity and isotropy of an expanding Universe implies the corresponding 4-dimensional space-time line-element, describing the geometry of our Universe, to have the form:

$$ds^2 = g_{\mu\nu}dx^\mu dx^\nu = dt^2 - a^2(t)\left[\frac{dr^2}{1-kr^2} + r^2 d\Omega^2\right] \tag{2.1}$$

where $g_{\mu\nu}$ is the metric tensor and dx_i is the 4-dimensional line element; $a(t)$ is the scale factor, carrying the dimension of length, $d\Omega^2 = d\theta^2 + sin^2\theta d\phi^2$, and k determines the spatial curvature of the Universe with $k = 0$, $k > 0$ and $k < 0$ corresponding to the flat (bounded), closed (unbounded) and open (unbounded) Universes, respectively.

The metric expressed with Equation (2.1) is called the Friedmann-Lemaitrie-Robertson-Walker (FLRW) metric [118–121]). It is often written in terms of a conformal time, defined as:

$$\tau = \int \frac{dt}{a(t)}, \tag{2.2}$$

and in terms of a comoving coordinate χ which replaces the radial coordinate r with the following relation:

$$d\chi^2 = \frac{dr^2}{1-kr^2}. \tag{2.3}$$

Note that the comoving distance $\chi = \mathrm{arcsinh}r$ if $k = -1$, $\chi = \mathrm{arcsin}r$ if $k = +1$, and $\chi = r$ for $k = 0$. Using Equations (2.1)–(2.3), FLRW metric will take the form:

$$ds^2 = a^2(\tau)(d\tau^2 - d\chi^2 - \Psi(\chi)(d\theta^2 + sin^2\theta d\varphi^2)), \tag{2.4}$$

where

$$\Psi^2(\chi) = r = \begin{cases} \sinh^2(\chi), & k = -1; \\ \chi^2, & k = 0; \\ \sin^2(\chi), & k = +1. \end{cases} \tag{2.5}$$

It should also be noted that for $k = 0$ metric (Equation (2.4)) is *conformally Minkowski*; that is, there exists a transformation for the metric in the form: $g^{FLRW}_{\mu\nu} = f^2 g^{Min}_{\mu\nu}$, where f is a function of spatial coordinates x^α and $g^{Min}_{\mu\nu}$ is the Minkowski metric.[2]

The comoving spatial coordinate defined in Equation (2.3), (i.e., defined in the Lagrangian coordinate system which is comoving with the expanding hypersurfaces), is

[2] In general, transformations in the form: $g'_{\mu\nu} = f^2 g_{\mu\nu}$ are called *conformal transformations*; such transformations keep the metric signature, sign of the four-vectors and angles between them unchanged.

related with the physical spatial coordinates $\mathbf{R}$ (Eulerian, fixed coordinate frame) by the following relation:

$$\mathbf{R} = a(t)\boldsymbol{\chi}, \tag{2.6}$$

Taking a time derivative of the definition above, we will obtain two components for the physical velocity $\mathbf{V}$:

$$\mathbf{V} = \dot{\mathbf{R}} = \dot{a}(t)\boldsymbol{\chi} + \boldsymbol{\upsilon}, \tag{2.7}$$

where $\boldsymbol{\upsilon}$ is the peculiar velocity which e.g., can be caused due to local gravitational forces; the first term on the right hand side represents the receding velocities due to cosmic expansion and it depends on the time derivative of the scale factor (denoted by dot). An usual way for normalising the scale factor is to take its value at the present time as $a(t = t_0) = a_0 \equiv 1$; hereafter, we will always use the subscript "0" for the present day values of different cosmological parameters. The first term in Equation (2.7) represents the Hubble law: $\mathbf{V} \sim H(t)\mathbf{R}$ with $H(t)$ being the Hubble parameter. The present time value of the Hubble parameter, H_0, is often expressed in terms of the dimensionless Hubble parameter h, $H_0 = 100h$ km s^{-1} Mpc and $h = 0.674 \pm 0.0005$ according to the recent analysis of the Planck data [122].

2.2 Redshift

A helpful quantity associated to an expansion of the Universe is the cosmological redshift z. It is defined as the amount by which the wavelength of an emitted photon stretches when propagating through an expanding space. It is given as:

$$z = \frac{\lambda_{\text{obs}} - \lambda_{\text{em}}}{\lambda_{\text{obs}}}, \tag{2.8}$$

where λ_{em} and λ_{obs} are wavelengths of the emitted and observed photons, respectively. This shift in the wavelength is due to differences between the scale factors at the moment of light emission and at the moment the observer detects it. Therefore, we can express the ratio of the wavelengths of the observed and emitted light as:

$$\frac{\lambda_{\text{obs}}}{\lambda_{\text{em}}} = \frac{a(t_{\text{obs}})}{a(t_{\text{em}})} \tag{2.9}$$

leading to:

$$1 + z = \frac{a_0}{a}. \tag{2.10}$$

The redshift can be used as a measure of distance, and as we will see below it helps us in constraining the cosmological parameters.

2.3 Matter & dynamics

One can assume that cosmic fluid behaves as an ideal gas on large scales. Its stress-energy tensor $T_{\mu\nu}$ then can be written in the form:

$$T_{\mu\nu} = (p + \rho)u_\mu u_\nu + p g_{\mu\nu}, \tag{2.11}$$

with p, ρ, u_μ being the pressure, density, and four-velocity of the fluid, respectively. In the rest frame and in comoving coordinates we have: $u^\mu = (1, 0, 0, 0)$ and $T_{\mu\nu} = diag(\rho, -p, -p, -p)$.

The trace of the energy-tensor, given as $T_{\mu\nu} = \rho - 3p$, is covariantly conserved $\nabla_\mu T^{\mu\nu} = 0$. It should be noted that in its general form, Equation (2.11) must include contributions from the electromagnetic fields (such as e.g., PMFs); see e.g., Equation (2.4) in Ref. [123] for such an example. However, here we only focus on the standard cosmology and we comment on the consequences of the inclusion of PMFs in Equation (2.11) in Chapters 3 and 8.

Conservation of $\mu = 0$ component of $T_{\mu\nu}$ i.e., $\nabla_\mu T^\mu_0 = 0$ yields relationship between the density and scale factor:

$$\frac{\dot{\rho}}{\rho} = -3(1+w)\frac{\dot{a}}{a}, \tag{2.12}$$

where the constant w is defined through an equation of state $p = w\rho$. The solution of Equation (2.12):

$$\rho \propto a^{-3(1+w)}, \tag{2.13}$$

has an important implications for Cosmology. In particular, we see that dynamics of the fluid is determined by its equation of state. For example, we see that i) the collisionless, non-relativistic matter with $w = 0$ (i.e., pressureless fluid, or "*dust*") evolves as $\rho \propto a^{-3}$; ii) the relativistic component (i.e., *radiation*), with $w = 1/3$ scales as $\rho \propto a^{-4}$; that is, the energy density for this component decreases faster than that of the non-relativistic matter; and finally, iii) vacuum energy (or "cosmological constant") with $w = -1$ gives $\rho =$ constant.

In order to see how the scale factor evolves with time we need to turn to the Einstein equations, relating stress-energy tensor (i.e., distribution of mass-energy) with the space-time metrics. They are written in the form:

$$G_{\mu\nu} \equiv R_{\mu\nu} - \frac{1}{2}g_{\mu\nu}R = 8\pi G T_{\mu\nu}, \tag{2.14}$$

where the Einstein tensor $G_{\mu\nu}$ is a function of the Ricci tensor $R_{\mu\nu}$ (*curvature tensor*) and Ricci scalar R (*scalar curvature* of the space), and G is the gravitational constant. The (symmetric) Ricci tensor is constructed from the metric and its first and second derivatives (through Christoffel symbols), while the Ricci scalar is a trace of $R_{\mu\nu}$ with respect to the metric. Solving of the Einstein second order differential equations for the FLRW metrics leads to the so-called Friedmann equations:

$$\left(\frac{\dot{a}}{a}\right)^2 \equiv H^2(a) = \frac{8\pi G}{3}\rho - \frac{k}{a^2}, \tag{2.15}$$

$$\frac{\ddot{a}}{a} = -\frac{4\pi G\rho}{3}(1+3w). \tag{2.16}$$

As we see from the first Friedhmann equation (Equation (2.15)), the Hubble parameter depends on the scale factor and its time derivative. In addition, Equation (2.16) shows that if the Universe is dominated by matter with $w < -1/3$ we get an accelerated expanding Universe. By contrast, both $w = 1/3, w = 0$ cases lead to the decelerated expansion. The exact solution of the Friedmann equations can be found when assuming the flat ($k = 0$) Universe. Then using the solution for the density field (Equation 2.13), we will have:

$$a \propto t^{\frac{2}{3(1+w)}}. \tag{2.17}$$

This gives the following behaviour: i) $a \propto t^{2/3}$ for a matter, ii) $a \propto t^{1/2}$ for a radiation, and iii) $a \propto e^{H_0 t}$ for a vacuum dominated Universes.

Finally, an useful quantity for Friedmann equations, is the critical density of the Universe. It is defined through Equation (2.15) when assuming $k = 0$; that is, we have:

$$\rho_{\text{crit}} = \frac{3H^2(z)}{8\pi G}. \tag{2.18}$$

Using this definition of critical density we can now normalise the density of various cosmic fluids

$$\Omega_i(z) \equiv \frac{\rho_i(z)}{\rho_{\text{crit}}} \tag{2.19}$$

and rewrite the first Friedmann equation as:

$$\Omega_{\text{tot}} - 1 = \frac{k}{H^2 a^2}. \tag{2.20}$$

Here, $\Omega_{\text{tot}} = \sum \Omega_i$ denotes the total density parameter with i referring to different matter/energy components of the Universe. In a similar fashion, we introduce the curvature parameter: $\Omega_{\text{k}}(z) \equiv -k/H^2(z)a^2$. Then using the Equation (2.19) we can define the present day matter, radiation, dark energy and curvature parameters, i.e., $\Omega_{\text{m},0}, \Omega_{\text{r},0}, \Omega_{\text{de},0}, \Omega_{\text{k},0}$, respectively:

$$\Omega_{\text{m},0} = \frac{8\pi G\rho_{\text{m},0}}{3H_0^2}, \quad \Omega_{\text{r},0} = \frac{8\pi G\rho_{\text{r},0}}{3H_0^2}, \quad \Omega_{\text{de},0} = \frac{8\pi G\rho_{\text{de},0}}{3H_0^2}, \quad \Omega_{\text{k},0} = -\frac{k}{H_0^2 a_0^2}. \tag{2.21}$$

For the density fields, we have relationships:

$$\rho_{\text{m},0} = \rho_{\text{m}}\left(\frac{a(t)}{a_0}\right)^3, \quad \rho_{\text{r},0} = \rho_{\text{r}}\left(\frac{a(t)}{a_0}\right)^4, \quad \rho_{\text{de},0} = \rho_{\text{de}} a^{-3(1+w)}. \tag{2.22}$$

The latter equations along with Equations (2.10) and (2.20) can be used to write the Hubble parameter in the following manner:

$$H^2(z) = H_0^2[\Omega_{\text{m},0}(1+z)^3 + \Omega_{\text{r},0}(1+z)^4 + \Omega_{\text{de},0}(1+z)^{3(1+w)} + \Omega_{\text{k},0}(1+z)^2]. \tag{2.23}$$

This latter equation is especially important for testing the current ΛCDM paradigm. It allows us to obtain cosmological parameters and test cosmological models (see below).

2.3.1 Distances and cosmological parameters

Equation (2.4) takes a simple form when considering the light propagation in an isotropic Universe with an observer located at the origin. The light propagates on null geodesics[3], that is, $ds^2 = 0$; then taking a radial trajectory with $\theta, \varphi = \text{const}$, we obtain:

$$d\tau^2 - d\chi^2 = 0, \tag{2.24}$$

with a solution:

$$\chi(\tau) = \pm\tau + \text{const}. \tag{2.25}$$

[3] An extremal world line in four dimensional curved space-time on which particle draws its trajectory [124].

We can now use Equation (2.25) along with Equation (2.2) to define the comoving distance for photons travelling along the LOS:

$$\chi = \frac{1}{a_0}\int_0^z \frac{dz'}{H(z')}. \tag{2.26}$$

This latter equation is useful for defining the *angular diameter distance*, D_A to an object at a comoving distance χ:

$$D_A = a(t)\Psi(\chi(z)), \tag{2.27}$$

and the *luminosity distance*, D_L

$$D_L = \sqrt{\frac{L}{4\pi F}} = a_0\Psi(\chi(z))(1+z)^2 \tag{2.28}$$

to an object with an intrinsic luminosity L and the measured bolometric flux (energy per unit area and per unit time), F. These two distance measures have proven their importance in measurements of cosmological parameters (note that the knowledge of the cosmological parameters leads to identifying the curvature of the Universe; see Equation (2.20)). Although, one needs to have astronomical objects whose luminosities or angular sizes are known (so-called standard candles and standard rulers; see e.g., Ref. [125] for the concise review of different distance measures in Cosmology). In general, finding a reliable standard rulers and candles turned out to be a hard task. Nonetheless, one important standard ruler has been extracted from the observations of CMB. The angular power spectrum of the CMB temperature fluctuations (see Section 2.4) shows peaks (Baryon Acoustic Oscillations, BAO) and valleys, where the position of the first peak is sensitive to the total density parameter at the current epoch $\Omega_{tot,0}$ (and therefore, to the curvature parameter k) and provides a robust geometrical test of cosmology (see e.g., Refs. [122, 126, 127] for recent studies). Based on the recent analysis of BAO and the Planck data following joint constraints are obtained on cosmological parameters [122]:

$$\begin{aligned}
&\Omega_{k,0} = 0.001 \pm 0.002,\\
&\Omega_{m,0} = 0.315 \pm 0.007,\\
&\Omega_{b,0}h^2 = 0.0224 \pm 0.0001,\\
&\Omega_{c,0}h^2 = 0.120 \pm 0.001,
\end{aligned} \tag{2.29}$$

where $\Omega_{b,0}$ and $\Omega_{c,0}$ are the density parameters of baryonic and cold DM, correspondingly. Thus, the current observational data favours **spatially flat Universe**[4] with only $\sim 30\%$ of matter in total, including only $\sim 5\%$ of visible, baryonic matter and $\sim 25\%$ of cold DM.

The rest ($\sim 70\%$) of the energy budget of the Universe is thought be in the form of dark energy. Elucidating nature of dark energy is one of the challenges of Cosmology. One possible form of it is the vacuum energy (see [129] for a review on the question) with an equation of state parameter $w = -1$. This leads to to the accelerated expansion of the Universe, as mentioned in Section 2.3. The type Ia Supernovae (SNe; used as standard candles) measurements indeed showed the **accelerated expansion of the Universe** (see [130, 131] for pioneering works and [122] for a recent study) at the current epoch. The joint analysis of BAO and SNe data is agreement with $w = -1.03 \pm 0.002$.

[4] See, however, Ref. [128] which argues that the closed ($k > 0$) Universe is preferable by recent releases of different observational data.

2.4 Short story of the Universe

CMB. Solutions of Einstein's equations predict growing scale factor regardless of the matter content of the Universe. This makes us think that our Universe should have been expanding since its beginning (usually referred to as Big Bang) and should have been denser and hotter at earlier times. One of the main observational evidence for the existence of such a state comes from the detection of the CMBR [132]. This faint glow of light that fills our Universe is residual heat from the *recombination epoch*, having a nearly perfect black body spectrum and showing imprints of tiny density fluctuations at the last scattering surface. Before recombination, particles of this hot bath (consisting of photons, baryons, electrons, neutrinos, etc.) were continuously scattered. As the Universe was expanding and cooling down particles were decoupling from the plasma. At $T \sim 3650\,\mathrm{K}$ temperatures, as the Universe cools down sufficiently, first neutral hydrogens along with other light elements start to form; this marks the beginning of recombination. After recombination, photons propagate freely, i.e., entering the so-called *free streaming regime*. It is exactly the moment before the free streaming phase that reaches out to us through CMBR and that is referred to as the last scattering surface. The observed fluctuations in the CMBR are quantified through its angular power spectrum (i.e., power spectrum as a function of angular scale) and give us invaluable information about the early Universe. It allows us to test cosmological parameters/models, as mentioned already and to explore extensions of the ΛCDM cosmology. It is also an inarguably powerful tool for studying the imprints of primordial magnetogenesis (see e.g., Ref. [21]).

Inflation. The so-called hot Big Bang picture, outlined above, has difficulties known as *flattness* and *horizon problems*. As we have seen, the current experimental evidence is spatially flat (zero-curvature) space-time. However, if we assume $k \neq 0$ in Equation (2.20) we will see that deviation of $\Omega_{\rm tot}$ from unity is fine-tuned at early times; this is because that we would expect always-decelerating Universe (at earlier times) with $\dot{a}_{in} > \dot{a}_0$ at origin, $t = t_{in}$. Thus, we have (see e.g., Ref. [115]):

$$\Omega_{\rm tot,in} - 1 = (\Omega_{\rm tot,0} - 1)\left(\frac{\dot{a}_0}{\dot{a}_{in}}\right)^2 \leq 10^{-56}. \tag{2.30}$$

That is, the Universe "becomes" flat with implausibly high order accuracy which clearly requires justification. Besides, the horizon problem emphasises that in the standard hot Big Bang scenario, comoving (Hubble) horizon $\chi_H = H^{-1}/a = \dot{a}^{-1}$, e.g., at the time of recombination is much smaller than the observed patch of the Universe (which we "see" through CMB). Nearly constant temperature of the CMB observed from all directions is not justifiable if those patches were not causally connected at early times. These problems are easily evaded by inflationary scenario [133], i.e., if the Universe has undergone an accelerated phase of expansion before entering the decelerating period. The inflation should have lasted long enough to make comoving horizon today much smaller than at the beginning of inflation. Driven by the dynamics of a scalar field (known as the inflaton), inflation requires $w < -1/3$ equation of state. It is widely accepted that this epoch provides primordial perturbations (exhibiting a nearly scale-invariant spectrum) by stretching the quantum fluctuations of the metric beyond the horizon. These fluctuations then serve as seeds for the growth of DM halos and therewith, for structure formation in the late Universe.

Post-inflationary notable events. After inflation, inflaton decays into standard model

particles and thermalises. This so-called *reheating* phase is followed by electroweak (EW) and quantum chromodynamics (QCD) *phase transitions* taking place at $T \sim 100\,\mathrm{GeV}$ and $T \sim 150\,\mathrm{MeV}$ temperatures, respectively. The former phase involves the spontaneous breaking of electroweak symmetry (electromagnetic and weak forces became differentiated) and the generation of masses of fundamental particles, such as quarks, leptons, and gauge bosons through the Higgs mechanism [134, 135]. During QCD phase-transitions, quark-gluon plasma (high-temperature) is transformed into colourless hadrons (lower temperature; see Ref. [136] for a review). Hot Big Bang proceeds by freezing out (decoupling) of particles whose collision timescales are shorter than the temperature change due to the expansion ($\propto H^{-1}$). At later times (~ 3 minute after the Big Bang), the Universe is consisting of relativistic particles (photons, electrons, positrons), decoupled neutrinos, and non-relativistic particles (baryons, composed of quarks). Baryons then start to fuse into nuclei via the process of BBN (see e.g., [137]). Finally, it should be noted, even though the primordial nucleosynthesis and its predictions for the light element (H, ^{3}He, ^{4}He, D) abundances are one of the powerful aspects of the standard model, the model does not explain the excess of baryons to antibaryons (a condition which leads to baryogenesis; see e.g., [138] for a review).

Post-recombination notable events. After becoming neutral (with a low residual ionisation fraction) and transparent for photons, the Universe enters the *dark ages* epoch ($z \lesssim 1000$–$O(10)$) when there are no light sources in the Universe. At this time, the gas temperature still follows the CMBR temperature due to Compton scattering. It is only at $z \sim 120$ (see e.g., Figure 1 in Ref. [139]) when thermally decoupled gas from the CMBR cools down faster than the CMB photons. This is when ($\sim z = 70$) the first (so-called population III) stars form in the DM gravitational potential wells. These DM halos, having masses up to 10^5–$10^7 M_\odot$ and being called mini-halos, are thought to have sufficient H_2 abundance in their constituent gas to allow star formation. The peak of star formation rate is expected to be at $z \sim 30$–20 which was followed by the first galaxy formation (~ 15–10). The radiation emitted from the first stars should have ionised the rest of the gas in the IGM, decreasing the neutral hydrogen abundance and heating the IGM to $T \gtrsim 10^4\,\mathrm{K}$. At this stage, Universe enters the reionisation epoch ($z \sim 15$–6). The end of the reionisation epoch, and in general, the low redshift IGM, is being intensively probed through high-redshift quasar emission. Quasars are used as background sources to study the intervening IGM through hydrogen Lyman-α emission.

Chapter 3

Theoretical framework for PMFs

In the previous chapter, we discussed the FLRW space-time describing a homogeneous and isotropic Universe and neglected the effects of PMFs. In general, the nearly homogeneous and anisotropic magnetic field in the early Universe could cause anisotropic expansion along its direction [140], thus, spoiling the isotropy of FLRW space-time. Isotropic, stochastic distribution of PMFs might still be incompatible with FLRW symmetries if such fields are strong enough, so that they have an impact on space-time symmetries. In that case, as discussed by Ref. [141], cosmological (primordial) electromagnetism should be studied in the perturbed FLRW framework. Nevertheless, since current observations (e.g., isotropy of CMB) supports the homogeneous and isotropic Universe, we can think of PMFs as of weak fields so that they do not generate an anisotropy larger than observed cosmological anisotropy (see e.g., [142]).

The presence of magnetised cosmic plasma suggests that fluid dynamics should be described in terms of magnetohydrodynamics. The generalised form of magnetised fluid equations in FLRW space-time has been derived by several authors [141, 143–145]. An approach that is employed can vary from author to author. Although, the main principle lies in the description of cosmic fluid in a general curved space-time and then focusing on the flat FLRW models. In this chapter, we limit ourselves by describing electromagnetic fields in their general form; then we write down the Maxwell equations in the flat space-time. We also note that equations that are employed in our cosmological simulations are listed in Chapter 5.

In this Chapter, we also introduce magnetic energy spectrum and characteristic scales; the amplification mechanisms of the magnetic field are also touched upon.

3.1 Electromagnetic field and its stress-energy tensor

An electromagnetic action in a space-time with a metric determinant g is given by:

$$S^{\rm EM} = \int d^4x\sqrt{-g}\Big\{ -\frac{1}{4}F_{\mu\nu}F^{\mu\nu} + J^\mu A_\nu \Big\}, \tag{3.1}$$

where

$$F_{\mu\nu} = A_{\mu;\nu} - A_{\nu;\mu} \tag{3.2}$$

is the Faraday tensor (also referred to as field strength tensor or Maxwell tensor) and A_μ, J^μ are the 4-vector potential and 4-current density, correspondingly. We recall that in Minkowski space $A_\mu = (-\phi, \mathbf{A})$ with ϕ and $\mathbf{A}$ being the scalar and vector electromagnetic potentials respectively; the electric field, $\mathbf{E}$ and the magnetic field, $\mathbf{B}$ in Minkowski space are then found from:

$$\mathbf{B} = \nabla \times \mathbf{A}, \qquad \mathbf{E} = -\nabla\phi - \frac{\partial \mathbf{A}}{\partial t}. \tag{3.3}$$

A general form of electric and magnetic fields is obtained from the Faraday tensor. It should be noted that the matrix form of $F_{\mu\nu}$ for the FLRW space-time differs from its Minkowski space representation $F^{Min}_{\mu\nu}$ (see e.g., Sec 3.1.1. in Ref. [145] and references therein). Although, in a first order approximation, $F_{\mu\nu} = a^2 F^{Min}_{\mu\nu}$. In order to define electric and magnetic fields in a general space-time one uses observers who measure electromagnetic fields from a coordinate system owing the four-velocity $u^\mu = dx^\mu/ds$ with $u^\mu u_\nu = -1$ (see Section 3 in Ref. [146]).[1] One also defines an effective spatial metric for these observers where the 4-vector electric field E_μ and magnetic field B_μ are defined through equations:

$$E_\mu = F_{\mu\nu}u^\nu, \qquad B_\mu = \tilde{F}^{\mu\nu}u^\nu, \tag{3.4}$$

with $\tilde{F}^{\mu\nu} = \frac{1}{2}\epsilon^{\mu\nu\lambda\gamma}F_{\lambda\gamma}$ and $\epsilon^{\mu\nu\lambda\gamma}$ being the dual Faraday tensor and the fourth-order Levi-Civita tensor, respectively. From Equation (3.4) we have $E_\mu u^\nu = 0$ and $B_\mu u^\nu = 0$. Thus, in the space orthogonal to u^μ we have only 3-vectors that characterise electric and magnetic fields.

Electromagnetic field is characterised by the stress-energy tensor $T^{\rm EM}$ which is obtained from its action, (Equation (3.1)):

$$T^{\rm EM}_{\mu\nu} = -\frac{2}{\sqrt{-g}}\frac{\delta S^{\rm EM}}{\delta g^{\mu\nu}} = F_{\mu\chi}F^\chi_\nu - \frac{1}{4}g_{\mu\nu}F_{\lambda\sigma}F^{\lambda\sigma}. \tag{3.5}$$

This term contributes to the general form of $T_{\mu\nu}$ in Equation 2.14. PMFs, through this term, could source gravitational waves in the early Universe (i.e., perturbing the space-time metrics). This, in principle, should be imprinted on CMB anisotropies (see e.g., [64, 65, 123]). The stress-energy tensor defined by Equation (3.5) has a vanishing trace: $T \equiv g^{\mu\nu}T_{\mu\nu} = 0$ and in the presence of charges ($J^\mu \neq 0$ in Equation (3.1)) it is not covariantly conserved. From the definition of the stress tensor, one can also construct the energy density, momentum flux, and momentum flux density of an electromagnetic field.

[1] Note that, as mentioned in Section 1.3, in this chapter we use (-, +, +, +) convention with the space-time metric defined as: $ds^2 = -dt^2 + a^2(t)\left[\frac{dr^2}{1-kr^2} + r^2 d\Omega^2\right]$.

Finally, it should be mentioned that the electromagnetic action (again, with $J^{\mu} \neq 0$) is invariant under conformal transformation. This implies that electromagnetic wave equation along with Maxwell equations have the same form in conformally flat FLRW space-time as in the Minkowski space. Although, as it has been argued in Ref. [141] (see also Refs. [143, 144, 147]) the electromagnetic field adds anisotropic stress to FLRW space which is not a conformally flat anymore. Nevertheless, sufficiently weak, background fields can still be described within the FLRW space as already mentioned in the introduction of this chapter.

3.2 Maxwell equations

We obtain the Maxwell equations, governing the evolution of electric and magnetic fields by varying the action (Equation (3.1)) with respect to the metric and vector potential. This procedure leads to the equation system in the form:

$$F^{\mu\nu}{}_{;\mu} = J^{\mu}, \qquad \tilde{F}^{\mu\nu}{}_{;\mu} = \frac{1}{2}\epsilon^{\mu\nu\lambda\gamma}F_{\lambda\gamma;\mu} = 0. \tag{3.6}$$

These equations can, in general, be written in terms of E_{μ}, B_{μ} (Equation 3.4) and without any pre-assumption of the space-time metric. The details of such a procedure is given, for example, in Ref. [148].

We now turn to the Maxwell equations that are written for the flat FLRW Universe. In this case, we can set up a locally inertial frame and define the components of the magnetic and electric field vectors and of the current density in the form (see Section 3.1 in Ref. [146]): $\mathbf{B} = (\bar{B}^1, \bar{B}^2, \bar{B}^3)$, $\mathbf{E} = (\bar{E}^1, \bar{E}^2, \bar{E}^3)$, $\mathbf{J} = (\bar{J}^1, \bar{J}^2, \bar{J}^3)$; we also define the charge density ρ_q. As already noted in Section 3.1, because of the conformal invariance of the electromagnetic action we can use the appropriate rescaling of the fields [149]:

$$\mathbf{B}^* = a^2\mathbf{B}, \qquad \mathbf{E}^* = a^2\mathbf{E}, \qquad \mathbf{J}^* = a^3\mathbf{J}, \qquad \rho_q^* = a^3\rho_q, \tag{3.7}$$

which ensures the Maxwell equations in the flat FLRW space-time will have the same form as that in the Minkowski space-time:

$$\begin{aligned} \nabla_r \cdot \mathbf{B}^* = 0, \quad \nabla_r \times \mathbf{E}^* = -\frac{\partial \mathbf{B}^*}{\partial \tau} \\ \nabla_r \cdot \mathbf{E}^* = \rho_q^*, \quad \nabla_r \times \mathbf{B}^* = \mathbf{J}^* + \frac{\partial \mathbf{E}^*}{\partial \tau}; \end{aligned} \tag{3.8}$$

here $\nabla_{\mathbf{r}}$ denotes the spatial derivative in the Lagrangian coordinates $\mathbf{r}$ which is related to the physical spatial derivative $\nabla_{\mathbf{x}}$ with: $\nabla_{\mathbf{r}} = a\nabla_{\mathbf{x}}$. We omit the subscript $\mathbf{x}$ when using physical spatial derivatives.

The system of Maxwell equations is complemented by the Ohm's law:

$$\mathbf{J}^* = \rho_q^*\boldsymbol{v} + \sigma^*(\mathbf{E}^* + \boldsymbol{v} \times \mathbf{B}^*), \tag{3.9}$$

where $\sigma^* = a\sigma$ with σ being the electrical conductivity. By introducing the magnetic diffusivity as $\eta^* = 1/\sigma^*$ and using the Equations (3.8) and (3.9), we obtain the induction equation:

$$\frac{\partial \mathbf{B}^*}{\partial \tau} = \nabla_r \times [\boldsymbol{v} \times \mathbf{B}^* - \eta^* \nabla_r \times \mathbf{B}^*]. \tag{3.10}$$

This equation describes the evolution of the magnetic field. We see that in the absence of resistivity (i.e., in the high conductivity limit, $\sigma^* \to \infty$) and peculiar velocities ($\boldsymbol{\upsilon} = 0$), the rescaled magnetic field remains constant, $\mathbf{B}^* \equiv$ const; that is, in the local inertial frame, magnetic field decays with the expansion of the Universe: $\mathbf{B} \propto 1/a^2$. It can be shown that the first term (induction term) in Equation (3.10) ensures that the magnetic field evolves as $1/a^2$ even if the peculiar velocities are not zero. This condition is often referred to as *flux freezing* and implies that magnetic flux Φ through a comoving surface S^*, $\Phi = \int_S \mathbf{B}^* \cdot d\mathbf{S}^*$ is conserved.

We can also discuss an opposite limit in Equation (3.10), i.e., assuming $\boldsymbol{\upsilon} = 0$ but $\eta^* \neq 0$. Then we see the Equation (3.10) reduces to the diffusion equation:

$$\frac{\partial \mathbf{B}^*}{\partial \tau} = \eta^* \nabla_r^2 \mathbf{B}^*, \tag{3.11}$$

and the rescaled field $\mathbf{B}^*$ decays on the (comoving) diffusion timescale: $\tau_{\rm diff} = L^2/\eta^*$, where L defines typical variation scale (comoving) for the magnetic field. Using Equation (3.11), we can estimate diffusion length scale for the magnetic field. For this, we again return to physical quantities, so that we have:

$$L_{\rm diff} \sim \sqrt{\frac{t}{\sigma}}. \tag{3.12}$$

The value of σ is unknown but we can calculate it using $\eta \sim 3 \cdot 10^{13} T^{-3/2}$ relation for the physical resistivity η (measured in cm^2/s units; see e.g., Ref. [150]). Assuming $T \sim 10^8\,\mathrm{K}$ for galaxy clusters and $t = t_0$, Equation (3.12) leads to $L_{\rm diff} \sim 4 \cdot 10^{10}\,\mathrm{cm}$. Thus, as we see, magnetic diffusion should be negligible on cosmological scales.

The ratio of the magnetic induction relative to magnetic diffusion defines another important characteristic of magnetised fluids, namely, the magnetic Reynolds number:

$$\mathrm{Re}_M = \frac{\upsilon L}{\eta^*} = \frac{\upsilon l}{\eta}; \tag{3.13}$$

here υ is the velocity on a comoving scale L (the proper scale $l = aL$). The condition $\mathrm{Re}_M \gg 1$, i.e., when the magnetic induction dominates over magnetic diffusion, is of particular importance for the dynamo mechanism that can exponentially amplify weak seed magnetic fields. The onset of the exponential growth of the field depends on the magnetic Reynolds number. We will discuss this mechanism in a bit more detail in Section 3.8.

In a similar fashion, one defines the fluid Reynolds number

$$\mathrm{Re} = \frac{\upsilon l}{\nu}, \tag{3.14}$$

with ν being the viscosity of the fluid, and the Prandtl number Pr,

$$\mathrm{Pr} = \frac{\mathrm{Re}_M}{\mathrm{Re}}, \tag{3.15}$$

being the ratio of the magnetic Reynolds number to the fluid Reynolds number. The onset of the dynamo is also studied in terms of the varying Prandtl number (see e.g., Ref. [151]), while $\mathrm{Re} \gg 1$ is a condition for turbulent flows.

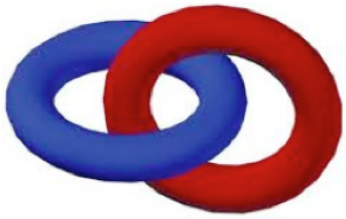

Figure 3.1: Illustration of two interlocked flux tubes. Figure credit: Ref. [12].

3.3 Magnetic helicity

Another conserved quantity in the high conductivity limit of the plasma is magnetic helicity. In the next chapter, we will see that magnetic helicity has a unique imprint on the pre-recombination evolution of PMFs. Furthermore, helicity is related to baryogenesis, and thus to matter-antimatter asymmetry, through the Chern-Simons number which is defined in the electroweak gauge theory (see Refs. [152–154] for pioneering works).

Magnetic helicity measures the linkage, twist, and writhing of magnetic field lines; we can also think of it as a systematic swirling of the field lines, e.g., toward or away from the observer. It is defined as a volume ($V^* = a^3 V$) integral[2] of the dot product of vector potential and magnetic field (see e.g., [156–159]):

$$H = \int \mathbf{A}^* \cdot \mathbf{B}^* dV^*, \tag{3.16}$$

Following Refs. [12, 155], we can see why magnetic helicity is a measure of magnetic linkage. For example, consider two untwisted, thin and interlocked magnetic flux tubes (as shown in Figure 3.1) with cross sectional areas $d\mathbf{S}_1^*$ (tube 1) and $d\mathbf{S}_2^*$ (tube 2). We assume that magnetic fields $\mathbf{B}_1^*$, $\mathbf{B}_2^*$ in both tubes are constants and directed along $d\mathbf{S}_1^*$ and $d\mathbf{S}_2^*$ vectors, respectively; i.e., the field has no component normal to the surface boundary ($\mathbf{B}_i^* \cdot \hat{\mathbf{n}} = 0$ where $\hat{\mathbf{n}}$ is the normal of the surface). Let then $\Phi_1 = \int \mathbf{B}_1^* \cdot d\mathbf{S}_1^*$ and $\Phi_2 = \int \mathbf{B}_2^* \cdot d\mathbf{S}_2^*$ be the magnetic fluxes in the tubes. The magnetic helicity, defined with Equation (3.16) can then be split into contributions of fluxes from these two flux tubes:

$$\int \mathbf{A}^* \cdot \mathbf{B}^* dV^* = \int \int \mathbf{A}_1^* \cdot \mathbf{B}_1^* dl_1^* dS_1^* + \int \int \mathbf{A}_2^* \cdot \mathbf{B}_2^* dl_2^* dS_2^* \tag{3.17}$$

where the line integrals are taken along $\mathbf{B}_1$ and $\mathbf{B}_2$ directions. We recall that we chose these vectors to be constant; therefore, we get:

$$\int \mathbf{A}^* \cdot \mathbf{B}^* dV^* = \oint A_1^* dl_1^* \oint B_1^* dS_1^* + \oint A_2^* dl_2^* \oint B_2^* dS_2^* = \Phi_2 \Phi_1 + \Phi_1 \Phi_2 = 2\Phi_1 \Phi_2; \tag{3.18}$$

here, we used Gauss's theorem to replace: $\int A_1^* dl_1^* = \Phi_2$, $\int A_2^* dl_2^* = \Phi_1$ with Φ_2 and Φ_1 being the magnetic fluxes of tube 2 linked to tube 1 and of tube 1 linked to tube 2, respectively. Generally, the sign of $\Phi_1 \Phi_2$ depends on the relative orientation of the

[2] In general, the requirement for this definition is that there should be a vanishing magnetic field component normal to the surface of the volume. See Ref. [155] for more details.

flux tubes (i.e., on the relative orientation of the magnetic field lines in the flux tubes). Note that helicity would be zero if the tubes are not interlocked (see Refs. [12, 155] and references therein). In a similar way, one can also quantitatively characterise helicity as the measure of the twist and writhe of the magnetic field lines (see examples in Ref. [12]).

The evolution equation of magnetic helicity is derived from the induction equation and its uncurled version $\partial\mathbf{A}^*/\partial\tau = -\mathbf{E}^* - \nabla_{\mathbf{r}}\phi^*$, so one has [155]:

$$\frac{\partial}{\partial\tau}(\mathbf{A}^*\cdot\mathbf{B}^*) = (-\mathbf{E}^*-\nabla_{\mathbf{r}}\phi^*)\cdot\mathbf{B}^*+\mathbf{A}^*\cdot(-\nabla_{\mathbf{r}}\times\mathbf{E}^*) = -2\mathbf{E}^*\cdot\mathbf{B}^*-\nabla_{\mathbf{r}}\cdot(\phi^*\mathbf{B}^*-\mathbf{E}^*\times\mathbf{A}^*); \tag{3.19}$$

integrating the latter equation within the volume V^*, we get:

$$\frac{\partial H}{\partial\tau} = -2\int_{V^*}\mathbf{E}^*\cdot\mathbf{B}^* dV^* - \oint_{\partial V^*}(\phi^*\mathbf{B}^* - \mathbf{E}^*\times\mathbf{A}^*)\cdot\hat{\mathbf{n}}dS^* = -2\eta^* C^*, \tag{3.20}$$

with $C^* = \int_{V^*}\mathbf{J}^*\cdot\mathbf{B}^* dV^*$ being the current helicity. In the volume integral, we have used the Ohm's law: $\mathbf{E}^* = -(\boldsymbol{\upsilon}\times\mathbf{B}^*) + \eta^*\mathbf{J}^*$ where for the first term we have: $\int_{V^*}(\boldsymbol{\upsilon}\times\mathbf{B}^*)\cdot\mathbf{B}^* \equiv 0$. In addition, in the last equality, we assumed that the surface integral vanishes for closed domains.

Equation (3.20) shows that in the non-resistive case ($\eta^* = 0$) helicity is a conserved quantity, $\partial H/\partial\tau = 0$; note that this conservation law is independent of fluid velocities $\boldsymbol{\upsilon}$. That is, the generation/dissipation of helicity is not affected by any type of fluid flow (e.g., flow due to turbulent diffusion, ambipolar drift, etc.). However, care has to be taken in the limit when $\eta^* \to 0$ since current helicity can become large. We will see in the next chapter that it is exactly this property that makes the pre-recombination evolution of helical PMFs distinguishable from that of non-helical fields.

3.4 Magnetised fluid equations

In Section 3.2 we discussed the dynamics of electromagnetic fields based on the induction equation and mentioned the high-conductivity regime during which magnetic field decays with the expansion of the Universe. However, this is a simplified treatment that is applicable only on large length-scales (larger than the characteristic scales of magnetic fields; see Section 3.6). In general, there are various regimes in the PMF evolution and one must solve the full set of MHD equations taking into account the dynamics of baryons. The Euler and continuity equations that account for magnetic fields are obtained from the conservation law of the total stress-energy tensor $T_{\mu\nu}$ (in this case, $T_{\mu\nu}$ includes electromagnetic part of the stress-energy tensor as well). In this case, in addition to the rescaling of the fields provided in Equation (3.7) we should also define the rescaled baryonic density, pressure, and shear viscosity μ in the form

$$p^* = a^4 p, \quad \rho^* = a^4\rho, \quad \mu^* = a^3\mu, \tag{3.21}$$

respectively. Then for the continuity and Euler equations in the non-relativistic limit (see e.g., [23, 123, 145, 149, 160] for derivations and more generalised formulation of these equations) we will correspondingly have:

$$\frac{\partial\rho^*}{\partial\tau} + \nabla\cdot[(\rho^*+p^*)\boldsymbol{\upsilon}] - \mathbf{E}^*\cdot\mathbf{J}^* - \mu^*\nabla\cdot\mathbf{f} = 0, \tag{3.22}$$

$$\frac{\partial}{\partial\tau}[(\rho^*+p^*)\boldsymbol{v}]+(\boldsymbol{v}\cdot\nabla)[(\rho^*+p^*)\boldsymbol{v}]+\boldsymbol{v}\nabla\cdot[(\rho^*+p^*)\boldsymbol{v}]=$$
$$=-\nabla p^*+\mathbf{J}^*\times\mathbf{B}^*+\mu^*[\nabla^2\boldsymbol{v}+\frac{1}{3}\nabla(\nabla\cdot\boldsymbol{v})], \quad (3.23)$$

where $\mathbf{f}=\nabla(\boldsymbol{v}^2/2)-2/3\boldsymbol{v}\nabla\cdot\boldsymbol{v}$. These equations along with the induction equation (Equation (3.10)) are used to study the dynamics of the PMF in the radiation (or across the recombination) era either in the linear approximation or in non-linear regimes. Below, we show simple linear solutions while the non-linear pre-recombination evolution of the PMF is discussed in Chapter 4.

One particular class of solutions which are discussed in the literature in the ideal, non-viscous limit (see e.g., Ref. [123]):

$$\frac{\partial}{\partial\tau}\boldsymbol{v}+(\boldsymbol{v}\cdot\nabla)\boldsymbol{v}=\frac{(\mathbf{B}^*\cdot\nabla)\mathbf{B}^*}{4\pi(\rho^*+p^*)}, \quad (3.24)$$

$$\frac{\partial\mathbf{B}^*}{\partial\tau}+(\boldsymbol{v}\cdot\nabla)\mathbf{B}^*=(\mathbf{B}^*\cdot\nabla)\boldsymbol{v}, \quad (3.25)$$

are the stable solutions, in the form [123]:

$$\boldsymbol{v}=\pm\frac{\mathbf{B}^*}{4\pi(\rho^*+p^*)}, \quad \frac{\partial\boldsymbol{v}}{\partial\tau}=0, \quad \nabla\cdot\boldsymbol{v}=0. \quad (3.26)$$

The exact solutions of Equations 3.26 can be obtained e.g., when magnetic field is decomposed into uniform, constant ($\mathbf{B}_0^*$) and stochastic ($\mathbf{b}^*$) components (see also Ref. [123] and Ref. [146] for a review) and velocity is parallel to the stochastic field. In this case, one finds solution in the form of Alfvén waves propagating along the uniform component at the Alfvén speed: $v_A=b^*/4\pi(\rho^*+p^*)^{1/2}$. Finally, it should be noted that Ref. [123] has also studied an approximate diffusive viscous regime to obtain the nonlinear solutions of Equations (3.10), (3.22) and (3.23).

In the pre-recombination Universe, some of the MHD modes are damped due to radiation viscosity. Around the recombination epoch, modes whose proper lengths are smaller than the mean free path of photons are entering the free streaming regime. In order to understand the evolution of such modes, one has to solve the Boltzmann equations for the photons together with the MHD equations of plasma. Although, Ref. [123] uses a simpler approach, assuming that in the linear regime the modes which are in the free streaming regime are affected by isotropic and homogeneous radiation. The resulting Euler equation then reads [123]:

$$\frac{\partial\boldsymbol{v}}{\partial t}+H(t)\boldsymbol{v}+(\boldsymbol{v}\cdot\nabla)\boldsymbol{v}=\frac{1}{a\rho_b}\nabla p_b+\frac{1}{\rho_b}\mathbf{J}\times\mathbf{B}-\frac{1}{a}\nabla\phi_g-\frac{4\rho_\gamma}{3\rho_b}n_e\sigma_T\boldsymbol{v}, \quad (3.27)$$

where ρ_b is fluid pressure, ϕ_g is the gravitational potential from Poisson's equation (see Section 5.1) and the last term describes the frictional drag force on the baryon fluid due to the radiation energy density ρ_γ. Note that we have written the above equation in the physical quantities (not in the starred variables) and included the gravitational term because of the fact that perturbed modes can now become gravitationally unstable. Equation (3.27) can then be used to discuss the interplay between the baryon and magnetic pressures and estimate the corresponding damping scale of the magnetic field.

3.5 Magnetic energy power spectrum

Primordial density fluctuations that are thought of as seeds of all the structures in the Universe are close to Gaussian distribution. Processes that generate PMFs in the early Universe are also considered to be stochastic and random. In general, as noticed in Ref. [161] one might talk about inherent randomness that echoes the idea of quantum uncertainty, i.e., instead of talking about the precise measurement of, for example, particle position we will speak about the probability of the particle being at a certain location. Similarly, one can introduce the concept of random fields which we can think of as a set of functions each having its probability.

As mentioned in the beginning of this chapter, PMFs are assumed to be the stochastic background in the non-perturbed FLRW space-time and thus, should be described as stochastic, random fields. In addition, they are assumed to have Gaussian distribution (Gaussian field is the simplest type of random field). However, as we will discuss in Chapter 4 PMFs depending on their particular generation mechanism at play might be characterised by different structure (or topology, as we will often call it). They can be either *statistically homogeneous* with a stochastic, isotropic and homogeneous distribution or uniform fields with a constant amplitude and direction at each point of the space. Nevertheless, in this section, we give a general treatment for both of these models by formulating magnetic energy power spectrum that we use as one of the analysis tools for our simulations.

In the statistical framework of random fields, instead of working with probability distribution functions (PDFs) one usually defines two-point correlation functions. For the magnetic field, we define its two-point correlation function in the form:

$$\mathcal{B}_{ij}(\mathbf{x}, \mathbf{x}+\mathbf{r}) \equiv \langle B_i(\mathbf{x}) B_j(\mathbf{x}+\mathbf{r}) \rangle, \tag{3.28}$$

where angle brackets denote ensemble averaging, i.e., averaging over many stochastic realisations of the magnetic field. Equation (3.28) in its most general form, can be written as [162, 163]:

$$\mathcal{B}_{ij}(\mathbf{r}) = M_N(r)\delta_{ij} + [M_L(r) - M_N(r)]\hat{r}_i\hat{r}_j + M_H(r)\epsilon_{ijl}r_l, \tag{3.29}$$

where $\hat{r}_i = r_i/|\mathbf{r}|$ and the normal, $M_N(r)$, longitudinal, $M_L(r)$, and helical, $M_H(r)$, components of the magnetic correlation function are obtained via the equations

$$P_{ij}(\hat{\mathbf{r}})\mathcal{B}_{ij}(\mathbf{r}) = 2M_N(r), \tag{3.30}$$

$$\hat{r}_i\hat{r}_j\mathcal{B}_{ij}(\mathbf{r}) = M_L(r), \tag{3.31}$$

$$\epsilon_{ijl}\hat{r}_l\mathcal{B}_{ij} = 2rM_H(r), \tag{3.32}$$

respectively. In Equation (3.30) $P_{ij},(\hat{\mathbf{r}}) = \delta_{ij} - \hat{r}_i\hat{r}_j$ is the projection operator onto the plane normal to $\mathbf{r}$ and the trace is given by $\mathcal{B}_{ii} = \delta_{ij}\mathcal{B}_{ij(\mathbf{r})} = 2M_N(r) + M_L(r)$. In addition, since the magnetic field is divergence-free we find the relationship between the normal and longitudinal components to be

$$M_N(r) = M_L(r) + \frac{r}{2}\frac{\partial}{\partial dr}M_L(r). \tag{3.33}$$

The 3D magnetic power spectrum is the Fourier transform of the real-space correlation function (see e.g., Appendix A of Ref. [163]):

$$\mathcal{F}_{ij}(\mathbf{k}) = \int d^3\mathbf{r} e^{i\mathbf{kr}} \mathcal{B}_{ij}(\mathbf{r}).^{3} \tag{3.34}$$

Replacing $\mathcal{B}_{ij}(\mathbf{r})$ by $\mathcal{B}_{ii}(\mathbf{r}) = 2M_N(r) + M_L(r) = 1/r^2 d(r^3 M_L)/dr$ (in Equation (3.34) leads to:

$$\begin{aligned} \mathcal{F}_{3D}(k) = \int \frac{1}{r^2}\frac{d(r^3 M_L)}{dr} e^{i\mathbf{kr}} \mathbf{dr} = 2\pi \int \frac{d}{dr}(r^3 M_L) dr \int e^{ikrcos\theta} dcos\theta = \\ = 4\pi \int \frac{d}{dr}(r^3 M_L)\frac{sin(kr)}{kr} dr = 4\pi \int \frac{d}{dr}(r^3 M_L)[1 - k^2 r^2/6 + ...]dr, \end{aligned} \tag{3.35}$$

where in the last step we used a small-angle approximation in $sin(kr)$ term with respect to kr. (see also Ref. [164]). It should be noticed that in the infinity if M_L decreases faster than $1/r^3$ then the first term in the latter equality goes to zero and the overall integral converges into $\propto k^2$. Then the 1D power spectrum (see below) $\propto k^2 \mathcal{F}_{3D}(k) \propto k^4$. We will see in Chapter 4 that these results can also be the outcome of the MHD turbulence in the early Universe. Another outcome of Equation (3.35) is that if the magnetic field correlator falls off as $1/r^3$ the integral goes to a constant and 1D spectrum $\propto k^2$. Both of these spectra have been discussed in the earlier works [165, 166]. Ref. [166] argued that divergence free condition of the magnetic field requires $\propto k^4$ spectrum while Ref. [165] argued in favour of $\propto k^2$ spectrum. For more discussion on this topic see also Ref. [29] and Section 3.5 in Ref. [164].

Finally, in our numerical implementation of the calculation of magnetic energy spectrum (analysis in Chapters 6 and 7) we employ one dimensional spectrum which is defined as:

$$\int E_B(k) dk = \frac{1}{2V} \int \hat{\mathbf{B}} \cdot \hat{\mathbf{B}}^* 4\pi k^2 dk, \tag{3.36}$$

where $\hat{\mathbf{B}}$ denotes the Fourier transform of the magnetic field, with $\hat{\mathbf{B}}^*$ being its complex conjugate, $k = |\mathbf{k}|$ is the norm of the wavenumber vector and V is the volume that normalises the spectrum. We notice that, contrary to the theory, in practice we use volume averaging based on the ergodic assumption (see e.g., [161, 162]); this is due to the fact that in reality, we have only one realisation of the ensemble (i.e., magnetic field distribution in simulations, as well as in cosmic structures).

3.6 Characteristic scales

Having defined the magnetic energy power spectrum, we can also define the *magnetic correlation length* (often referred to as the coherence or the integral scale) as:

$$\lambda_B = \frac{\int_0^\infty dk\, k^{-1} E_B(k,t)}{\int_0^\infty dk\, E_B(k,t)}. \tag{3.37}$$

[3] Note that similar to Equation (3.29) one can also define the generalised form of $\mathcal{F}_{ij}(\mathbf{k})$ with its normal, longitudinal, and helical components in the Fourier space [162, 163].

From Equation (3.37) we see that the magnetic correlation length is the inverse wavenumber weighted by the magnetic energy power spectrum.

The other two characteristic scales that are also associated to the magnetic spectrum are: *the peak scale*, i.e., the inverse wavenumber $L_{E_B(k)} = 1/k_{\rm peak}$ with $k_{\rm peak}$ being the wavenumber where the magnetic energy spectra has a peak, and *the largest energy containing scale* of the magnetic field. The latter is defined as the peak scale of $kE_B(k)$, i.e, the peak scale of the spectral energy per mode [167] and is denoted as $L_{kE_B(k)}$.

In order to characterise the variation of the magnetic field, we also define the characteristic wavenumbers [26]

$$k_{\parallel} = \left(\frac{\langle|\mathbf{B}\cdot\nabla\mathbf{B}|^2\rangle}{\langle B^4\rangle}\right)^{1/2}, \quad k_{\mathbf{B}\times\mathbf{J}} = \left(\frac{\langle|\mathbf{B}\times\mathbf{J}|^2\rangle}{\langle B^4\rangle}\right)^{1/2} \tag{3.38}$$

corresponding to the magnetic-field variation along ($k_{\parallel}$) and across ($k_{\mathbf{B}\times\mathbf{J}}$) itself.

Finally, we study the geometry of the magnetic field lines in terms of the curvature $\mathbf{K}$ defined as [168]:

$$\mathbf{K} = \frac{(\mathbf{B}\cdot\nabla)\mathbf{B}}{|\mathbf{B}^2|} = \frac{1}{\mathbf{B}^2}\left[\frac{1}{2}\nabla\mathbf{B}^2 - \mathbf{B}\times(\nabla\times\mathbf{B})\right]. \tag{3.39}$$

In our simulations, we define the *curvature scale*, λ_K, as the peak scale of the PDF of the absolute curvature, $K = |\mathbf{K}|$. This is the typical bending scale of the field lines where the bulk of the curvature distribution is concentrated at (see Section 7.3.3). We note that our definition of the curvature scale is different from the definition adopted in Ref. [167].

3.7 Bounds on the field strength

Magnetic field topology and coherence scale are of notable importance when deriving constraints on the PMF strength. In Section 1.2 we discussed some of the observational bounds on large-scale magnetic fields that are obtained through Faraday rotation measurements, diffuse radio emission, and blazar spectra observations. More theoretical constraints on PMFs come from analysing their effects e.g., on the BBN and CMB; see e.g., Refs. [169–171] for reviews.

PMFs might alter predictions of BBN by changing the rates of weak (e.g., β-decay of neutrons [172–174]) and nuclear reactions [175], or they could also induce anisotropic expansion, as mentioned earlier. Since the magnetic field increases the overall expansion rate of the Universe (providing additional energy density) neutrons have less time to decay; as a result, one anticipates increased ^{4}He abundance. Such effects can be used to put constraints on the PMF strength. For instance, Ref. [176] included the effects from PMFs on the expansion rate (and in turn, on light element abundances) to derive an upper limit of the order of $2\,\mu$G on the scale-invariant PMF, i.e., for the magnetic energy distribution of PMF that is characterised by the scale-invariant spectrum. Ref. [177], on the other hand, analysed the effects of PMFs on the BBN reaction chain and obtained $1.5\,\mu$G upper limits on the field strength, although with a caution that effects of PMFs on nuclear reaction rates are rather weak (this is in agreement with the results of Ref. [178] who found that PMF effect on BBN through modified expansion rate is predominant over the effects arising from the changed reaction rates).

The anisotropic stress from PMFs induces noticeable effects on smaller scales of the CMB angular power spectrum where the primary fluctuations are suppressed due to Silk

damping[4] (see Ref. [21] and references therein). Limits on the PMF strength derived from the CMB observations depend on the specific effects that are analysed. The effects of PMFs on the CMB angular power spectrum suggest a few nG for the upper bound on the amplitude of stochastic PMFs ($\sim 4.4\,\mathrm{nG}$ assuming zero helicity and $\sim 5.6\,\mathrm{nG}$ for a maximally helical field at a scale of $1\,\mathrm{Mpc}$ and with a power-law power spectrum [21]).

We summarise some of the recent constraints or the obtained field strengths from observations in Figure 3.2. Even though this plot is usually given in B–λ_B parameter space, here, instead, we show the scales for which the constraints have been derived (without specifying it to be the correlation length). The reason for this is that (as it has also been noticed in Ref. [6]) observations use different definitions for the characteristic scales of the magnetic field and therefore, any B–λ_B constraint plot or the plot shown here gives the qualitative understanding of the limits on the field strength.

3.8 Amplification of the magnetic field

As mentioned in Section 3.1, a high Reynolds number leads to the development of turbulent motions in the fluid. That is, according to the Kolmogorov hydrodynamic turbulence model [179], turbulent eddies will cascade from large (injection scale, also referred to as an outer scale) to small scales (the Kolmogorov inner scale) until the viscous-dissipation scale is reached. Assumption of isotropic, homogeneous, and incompressible turbulence leads to $\propto k^{-5/3}$ spectrum for the kinetic energy.

Turbulence is an important precondition for the dynamo which is a generic amplification mechanism applied to the evolution of PMFs in the early and late Universe settings. There have been different types of dynamos discussed in the literature (see Ref. [155] for overview). The more realistic (or more intuitively understandable) dynamo models are based on the idea that in a highly conducting fluid, magnetic field lines can be randomly stretched and bent by turbulent velocity field, the process that amplifies the magnetic field [180–182]. For example, in the Zeldovich "stretch-twist-fold" dynamo model (which is referred to as fast dynamo [155]) each round of velocity-induced stretch, twist and fold of the magnetic field lines increases the field strength by factor of 2; reoccurrence of this process (n times) leads to the growth of the field by a factor of 2^n (see e.g., Figure 4.6 in Ref. [155] and Figure 2 in Ref. [183]). Dynamos are usually divided into large- and small-scale dynamos. While the large-scale dynamos (mean-field dynamo) require anisotropy, the small-scale (turbulent/fluctuation) dynamos are studied in a homogeneous, isotropic setting. The small-scale dynamos can be of main interest for our work on galaxy cluster scales since (1) the growth rate of the field is expected to be larger in this case and (2) turbulence can still source dynamo action in the absence of large scale rotational motions (being necessary for mean-field dynamos).

The idea that a magnetic field can be exponentially amplified by a random flow was initially qualitatively introduced by Batchelor [180]. He discussed that in turbulent flows particles would diffuse apart, stretching the lines along which they move. In a similar way, in a highly conducting, incompressible fluid, if the damping of the magnetic field is less effective compared to the stretching of the magnetic field lines by a random flow, then magnetic energy will grow. This growth is governed by the small-scale part of the

[4]This is a process of damping of the small-scale acoustic oscillations (driven by the pressure gradients associated to the density perturbations) due to photon diffusion towards the end of the recombination epoch.

kinetic energy spectrum. Batchelor made an analogy between the induction and vorticity equations arguing, that after some time, the system reaches an equilibrium state (although as mentioned by the author this is different from the scale-by-scale equipartition between kinetic and magnetic energies; such equipartition has not been observed in MHD simulations of e.g., Ref. [26] either). Later, Kazantsev [184] introduced a more rigorous approach with velocity being a Gaussian, random field; in that case, velocity can be represented in the same (statistical) manner as the magnetic field through Equation (3.29) (although without helical part, i.e., ignoring the last term in Equation 3.29):

$$\mathcal{T}_{ij}(r) = \left(\delta_{ij} - \frac{r_i r_j}{r^2}\right)\mathcal{T}_N(r) + \frac{r_i r_j}{r^2}\mathcal{T}_L(r). \tag{3.40}$$

Using the Equation (3.29) for the magnetic field, from the induction equation one gets (see Ref. [184] for pioneering work and Ref. [155] for a review):

$$\frac{\partial M_L}{\partial t} = \frac{2}{r^4}\frac{\partial}{\partial r}\left[r^4 \eta_T(r)\frac{\partial M_L}{\partial r}\right] + G M_L \tag{3.41}$$

where $\eta_{\rm T}$ is the sum of microscopic and turbulent magnetic diffusivities. the term G includes first and second derivatives of $\mathcal{T}_{ij}$ and sources the generation of the magnetic field by velocity shear. If magnetic energy spectrum is peaked on much larger scales than the viscous scale, then the above equation can be written in Fourier space for scales that are larger than viscous scales [185, 186]:

$$\frac{\partial E_B}{\partial t} = \frac{\gamma}{5}\left(k^2\frac{\partial E_B}{\partial k^2} - 2k\frac{\partial E_B}{\partial k} + 6E_B\right) - 2\eta k^2 E_B \tag{3.42}$$

where $\gamma = -1/6[\nabla^2 \mathcal{T}_{ii}(r)]_{r=0}$ describes shearing by the flow. Without diffusion ($\eta \sim 0$) the equation describes the evolution of the magnetic energy spectrum whose peak moves toward smaller and smaller scales (so-called *forward cascade*) while the energy develops $E_B(k) \propto k^{3/2}$ spectrum and its amplitude grows exponentially (see e.g., Eq. 11 in Ref. [26]). However, note that such a solution is not valid if the peak of the magnetic energy spectrum reaches resistive scales. Even though the Kazantsev theory has been obtained for the non-helical flows, its framework has also been used in Refs. [155, 187], incorporating helical flows [155] and diffusion of the magnetic field (in particular, the ambipolar diffusion which is caused by a Lorentz-force-induced relative velocity between ions and a neutral component of the fluid [187]).

Previously performed MHD simulations have shown that exponential growth of the magnetic field indeed takes place in the forced-turbulence setups. In such setups, Euler equation contains an additional, forcing term that drives turbulent motions in the system. In general, the results of these simulations (and thus, the efficiency of dynamo) depend on different factors, including magnetic and kinetic Reynolds number, Prandtl number, driving force nature (e.g., whether it is solenoidal or compressible), and also, type of turbulence, e.g., its spectrum and whether it is regarded as a subsonic or supersonic (controlled by the Mach number, the ratio of fluid velocity to the local speed of sound). See e.g., Refs. [26, 188–192], and Refs. [155, 183, 193, 194] for reviews. The Kazantsev scaling and exponential growth of the field have been found both in the subsonic [192] and supersonic regimes [189] of turbulence as well as in the incompressible MHD simulations (e.g., [26]). Although as it is noticed in Ref. [26] Kazantsev's scaling can also be a mere coincidence in numerical simulations since there is not a one-to-one

comparison of the model proposed by Kazantsev and the simulation results. The similar scaling/growth (although less efficient than in the pure MHD simulations) of the magnetic field has also been obtained in the MHD simulations taking into account gravity effects, e.g., in the case of isolated spherical collapse (see e.g., Ref. [195]) or during galaxy (see e.g., Refs. [196, 197]) and galaxy cluster formation (see e.g., Refs. [45, 79], and Refs. [78, 194] for reviews). However, one should be aware that such simulations do not take into account any non-ideal MHD effects.

Given the fact that small-scale dynamo is an efficient amplification mechanism of the magnetic field, one might wonder what is the typical timescales required for this process to explain observed μG strength fields found in galaxies and galaxies clusters. As we will see in Section 4.1 the seed magnetic field strength depends on the magnetogenesis scenarios. Assuming inflationary magnetogenesis produces fields with the strengths of $10^{-30} - 10^{-20}\,\mathrm{G}$ then dynamo should operate very efficiently, exponentiating the field strength by a factor of ~ 33 – 57. The growth of the field, as we already mentioned, occurs on turbulent eddy scales. In galaxy clusters, eddy turnover time is ~ 0.1 Gyr (assuming $t_{\rm eddy} = L/v$ with $L = 500\,h^{-1}\mathrm{kpc}$ and $v = 1000$ km s^{-1}). This is much smaller than the galaxy-cluster lifetime ($\sim$ billion years). Although there must have been enough time for the dynamo mechanism to act, it is also possible that the magnetic field reaches saturation quite early on, thus quenching its further amplification or interfering with the large-scale dynamo action; see Refs. [185, 187], and Refs. [155, 183] for reviews. Generally, as it has been discussed in Refs. [155, 198], small-scale dynamos could act in combination with large-scale dynamos. In addition, during the formation of galaxy clusters, magnetic fields can also be amplified due to adiabatic contraction (see below). Thus, all these mechanisms might still lead to efficient growth of an initial weak seed fields on galaxy and galaxy cluster scales.

Finally, it should be mentioned that magnetic field grows during adiabatic contraction of a collapsing object which implies flux freezing of the magnetic field lines (see Section 3.2). For instance, for a spherically and isotropically collapsing gas cloud, conserving its mass (ρR^3) and magnetic field flux ($\propto BR^2$), magnetic field is expected to be amplified as (see Refs. [23, 169] for reviews):

$$\frac{B_{\rm fin}}{B_{\rm in}} = \left(\frac{\rho_{\rm fin}}{\rho_{\rm in}}\right)^{2/3} \tag{3.43}$$

where subscripts "in" and "fin" corresponds to field (magnetic and gas densities) values at the initial and final phase of the gravitational collapse. If we assume that the difference between matter densities of the IGM and galaxies is $\sim 10^6$ then we see that μG fields in galaxies would be obtained if the field strength at the onset of the gravitational collapse was $\sim 10^{-10}\,\mathrm{G}$. In cosmological simulations, one often compares amplification of the field due to pure adiabatic contraction and due to small-scale dynamo action (as an example for galaxy cluster scales see Ref. [45]). However, it should also be noted that if the collapse is not isolated as is the case of galaxy clusters (undergoing a series of mergers) one cannot estimate the growth due to "purely" adiabatic processes.

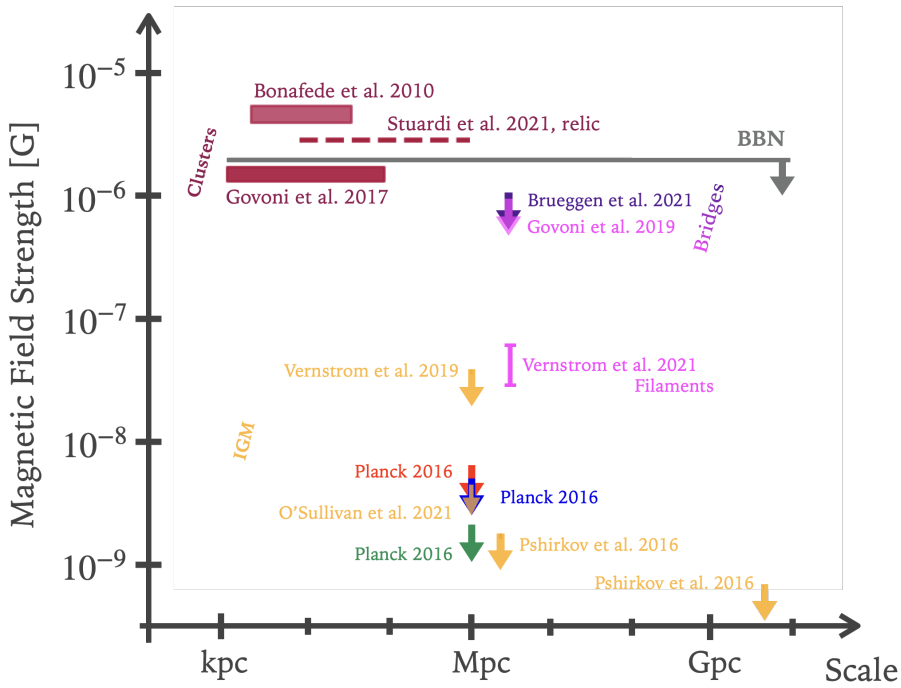

Figure 3.2: Constraints on the magnetic field strength versus scales that have been used as characteristic scales of the magnetic field in the corresponding studies (i.e., when defining the magnetic energy spectrum). The constraints are grouped according to the technique employed in the shown references. For instance, yellow colour shows constraints from the studies focusing on $\mathrm{RM_{IGM}}$ (see Section 1.2; Refs. [13–15]); pink and purple colours refer to estimations on the bridges' scales based on the *equipartition hypothesis* (Refs. [2, 16, 17]); the crimson red shows constraints from the RM measurements in galaxy clusters (including a measurement on the relic scale; Refs. [18–20]). An important caveat the reader should be aware of is that RM measurements in galaxy clusters relies on the assumption of the certain shape of the magnetic energy power spectrum; we show constraints from such measurements with the minimum $(1/k_{\mathrm{max}})$ and maximum $1/k_{\mathrm{min}}$ scales employed in those studies. The red, blue and green arrows from the Planck data analysis [21] corresponds to the constraints for the helical, nonhelical and scale-invariant PMFs (characterised with the scale-invariant spectrum), respectively. In this analysis, the constraints are obtained for the magnetic field amplitude that is smoothed over a comoving scale $L = 1\,\mathrm{Mpc}$.

Chapter 4

Early Universe: generation and evolution of PMFs

PMFs could come from different generation scenarios, involving inflation and phase transition epochs, and recombination. Although this chapter focuses on inflationary and phase-transitional magnetogenesis we note that a number of other proposals have been put forward to explain the generation of PMFs. Regardless of magnetogenesis scenarios, produced "seed" fields should satisfy following criteria: they should be (i) weak enough to preserve spatial anisotropy of our Universe, and (ii) strong enough to seed their subsequent growth during structure formation (in order to be in agreement with the observed strengths in galaxies and galaxy clusters).

In the first part of this chapter, we will overview the main ideas of the inflation and phase-transitional magnetogenesis scenarios and their outcomes in terms of the magnetic field strength and/or the spectrum of the field. In the second part of the chapter, we will present the results from the works where the pre-recombination evolution of PMFs have been studied in the "freely decaying turbulence" regime. Understanding this aspect of PMF physics is of relevance to the novel approach presented in our studies. We also note that this chapter relies on the existing review papers [6, 23, 40, 146, 169, 199] on PMFs where a more detailed description of the topics discussed here can be found.

4.1 Magnetogenesis scenarios

In Introduction we mentioned that magnetic fields cannot be generated from an initially zero magnetic field in the classical limit, i.e., within the strong coupling condition of electrons and protons. This is clear from the induction equation (Equation (3.10)) where the source terms on the RHS of this equation require preexisting magnetic field. However, the source terms for the $\mathrm{B} = 0$ case can be present if we go beyond the MHD limit. For example, magnetic field could be generated if there were charge separation processes in the charge neutral Universe. Such scenarios, for the first time, have been proposed by Biermann [48] and Harrison [49]. The Biermann battery mechanism requires presence of non-parallel temperature and density gradients in the fluid. If this condition is satisfied, electrons are accelerated more than ions because of their smaller mass; this process generates electric currents and if the current vorticity is not zero then magnetic fields are produced through the Ampere law [200]. This seed field generation mechanism has been discussed in the context of PMF generation during phase transitions (see below) as well as e.g., in the context of field production during reionisation [201]. Alternatively, Harrisson's mechanism proposes that Thomson interaction (scattering of photons and charged particles) cross section is more effective for electrons than for protons, leading to generation of currents and then to magnetic field in the presence of rotation (or vortical perturbations) in the plasma. Ref. [202] has shown that the tight-coupling approximation must be broken at first order in order the magnetogenesis to take place in this scenario.

In the next sections we discuss PMF generation during phase-transitions based on the ideas mentioned above while briefly commenting on the generation scenario due to the Higgs field. Inflationary magnetogenesis is discussed in the setting where the conformal invariance of the electromagnetic action is broken. See also some of the recent works [203, 204] discussing whether semiclassical magnetogenesis is possible in a quantum mechanical setting.

4.1.1 Inflationary magnetogenesis

Inflationary magnetogenesis is an attractive scenario for generating large-scale magnetic fields. The coherence scale of the seed field originating from quantum fluctuations of the vector potential can be stretched on scales larger than the Hubble horizon and thus, ensuring magnetisation of the largest scales of the Universe. However, in the standard Maxwell theory, the solution of Maxwell equations (Equation (3.6)) is plane waves and due to conformal invariance of the electromagnetic action the field energy decays as $1/a^4$ in the expanding Universe. The post-inflationary seed field might have amplitudes as low as $\sim 10^{-50}\,\mathrm{G}$ [40] which require unrealistically efficient dynamo growth in the subsequent epochs. It then follows that the conformal invariance of electromagnetism must be broken to give rise to larger-amplitude seed fields. See Refs. [54, 55] for pioneering works and Refs. [23, 40, 146, 170], for reviews. In addition, Ref. [205] discussed that apart from producing tiny fields inflation could also generate the large vector fluctuations at the quantum level which would serve as initial conditions for their classical evolution. Below we will only give examples for the weak seed field generation during inflation, i.e., the former scenario.

Many theories, invoking the breaking of the conformal invariance of electromagnetism, have been proposed in the literature (see Refs. [23, 40, 146, 148, 170, 206] for

a review). In such scenarios, electromagnetic action can be written:

$$S^{\rm EM} = \int d^4x\sqrt{-g}\Big\{ -\frac{1}{4}F_{\mu\nu}F^{\mu\nu} + \text{coupling terms}\Big\}, \tag{4.1}$$

where the coupling terms introduce the coupling of the electromagnetic field to a time dependent background field, such as e.g., inflaton or another coupling that breaks conformal invariance. This form of action ensures that the theory recovers the standard Maxwell theory at later times. One of the most-studied models of inflationary magnetogenesis is the so-called *Ratra model* [55] which uses the coupling term in the form of $\propto e^{\alpha\phi'}F_{\mu\nu}F^{\mu\nu}$ where ϕ' is the scalar inflaton field. Since the scalar field is a time-dependent quantity (slowly varying function of scale factor, $a(t)$), magnetic fields are also treated as time-evolving classical fields. The total action of the system includes the action for the inflation field and the electromagnetic action (Equation 4.1). The equation of motion is then solved for the vector potential perturbation in the Fourier space [55] (see also Eqs. (36-42) in Ref. [23]). The exact solution for the vector potential, $\mathbf{A}(\mathbf{k}, t)$ and therewith, for the magnetic energy density $E_B(k, t)$ depends on the form of the coupling function. If the coupling function is a simple form of the scale factor $\propto a^\alpha$ [207], where α is a parameter, one obtains *the scale invariant spectrum* for the PMF $dE_B(k)/dlog(k) \approx {\chi_{H\rm infl}}^2$ with $\chi_{H\rm infl}$ being the Hubble scale during inflation. Such scenario leads to 10^{-12} G magnetic field strength on large cosmological scales today.

Problems for the Ratra and Ratra-alike models (e.g., Refs. [208–210]) are the back-reaction and strong coupling [211]. The former arises if the magnetic energy density becomes large and can, in turn, affect the inflationary expansion. The strong coupling problem, on the other hand, is related to the time evolution of the coupling function; i.e., if there is a strong coupling between the scalar field and electromagnetic field at the beginning of inflation the perturbative quantum field theory can no longer be used for the evolution equation of the vector potential (see also [212] for a review on the problems). The back-reaction problem can be avoided in the weak coupling mode by a suitable choice of parameters such as e.g., the power law index for the magnetic energy spectrum. In the most admissible case, the magnetic field strength is constrained to be $< 10^{-32}$ G on $\rm Mpc$ scales [211]. In addition, in some extensions of the Ratra model these problems have been evaded (see e.g., [212–214]). For instance, Ref. [212] has shown that by lowering the energy scale of inflation along with a prolonged reheating scenario avoids the back-reaction and coupling problems and leads to $\gtrsim 10^{-13}$ G-strength PMFs on $\rm Mpc$ scales. In the same reference, a more complex coupling function (consisting of piecewise sections with different slopes) has also been used to overcome the mentioned problems.

Apart from the Ratra-like models alternative scenarios of seed field production have also been discussed in the literature. In these scenarios, conformal invariance is broken e.g., by introducing the coupling of electromagnetic action to the curvature (R, [54]), a pseudo-scalar field such as e.g., the dark matter candidate axion [215], or to the scalar-tensor gravity [56]. The latter model generates PMF which is a *uniform, constant field* (see also [216]). In addition, recent works investigate the generation of helical fields (e.g., Refs. [217–221]) during inflation; e.g., Ref. [217] introduces the coupling of electromagnetic action to the parity-violating term which leads to the blue power spectrum ($\sim k$) of the helical magnetic field. On the other hand, the model employed in Ref. [219] leads to generation of *scale-invariant helical fields* with $B \simeq 10^{-15}$ G on $\lesssim$ Mpc scales.

4.1.2 Phase-transitional magnetogenesis

Primordial seed magnetic fields could be generated during EW or QCD phase transitions. The current understanding of these epochs is such that the transitions should be crossovers (i.e., smooth transition between two phases) rather than the first or second-order transitions (see e.g., [222–225]). However, in many modifications of the standard model both EW and QCD phase transitions can still be of the first order [226–228]. In addition, the generation of random seed magnetic fields has been proposed during cross-over phase transitions.

The seed magnetic field generation during first-order phase transitions involves "violent", non-equilibrium processes such as bubble nucleation, collisions, and explosions. A general idea that has been applied to both EW and QCD phase transitions, is that, such a first order phase transition can generate weak seed fields through charge separation processes. Generation of seed fields through the Biermann battery mechanism has been explored in Refs. [165, 229]. During the QCD phase transition a net positive charge, which is due to baryon asymmetry, is balanced by an excess negative charge in leptons. However, pressure gradients generated e.g., during shocks [230] affect the quarks and leptons differently which gives rise to an electric field. Turbulence is produced as a result of bubble collisions on the scales of bubbles' size, L_b and thus, $\nabla \times \mathbf{E} \neq 0$ and magnetic fields could grow. For the QCD epoch, Ref. [229] finds $B_l \sim 5\,\mathrm{nG}$ when the field is correlated on scales one-two orders of magnitude smaller than the Hubble scale, χ_H at the moment of generation. By assuming that on scale L the field amplitude scales as $B_\mathrm{L} = B_\mathrm{l}(l/L)^{3/2}$[1], this will result into $\sim 10^{-17}\,\mathrm{G}$ strength of the field on $\sim 10^{10}\,\mathrm{cm}$ scales at the epoch of recombination. The amplitude is decreased if one considers even larger scales (such as galaxy scales, $\sim 100\,\mathrm{kpc}$) and thus, such a tiny fields (and correlated on small scales) may not be relevant for their growth during structure formation.

Subsequent studies [230–232], using more complex analysis, have also explored scenarios based on the charge separation processes. In these works, it is assumed that dipole charge layers are formed on the surfaces of the phase transition bubble walls whose motion generates electric currents and magnetic fields. For instance, Ref. [232] derives the charge density distribution on bubble walls and argues that hydrodynamic instabilities produced by the expanding bubble walls will generate seed magnetic fields. These instabilities will also lead to the development of turbulence which, in turn, non-linearly amplifies seed fields. In the equipartition phase, authors estimate the order of $10^{-29}\,\mathrm{G}$ and $10^{-20}\,\mathrm{G}$ field strengths on $10\,\mathrm{Mpc}$ scales for the EW and QCD phase transitions, respectively.

The magnetic energy power spectrum, $E_\mathrm{B}(k)$, of the phase transition-generated field is often conveniently split into its large-scale, E_B^LS and small-scale, E_B^SS parts (see also Figure 4.4 in Section 4.3). In general, this formulation also applies to inflationary models; although, in this latter case, transition from the large to small-scale spectrum occurs on much larger scales than the characteristic scale for the phase-transitional scenarios, that is, $k_\mathrm{peak}^\mathrm{infl} \ll k_\mathrm{peak}^\mathrm{PT}$ [163], or alternatively, $L_{E_B(k)}^\mathrm{infl} \gg L_{E_B(k)}^\mathrm{PT}$. The coherence scale of phase transition-generated primordial seed magnetic field is commonly assumed to be the fraction, f_c, of the Hubble horizon; that is, $\lambda_{B,\mathrm{phys}} = f_\mathrm{c}\chi_{H,\mathrm{phys}}$, and for the comoving magnetic correlation length: $\lambda_{B,\mathrm{com}} = \lambda_{B,\mathrm{phys}}(a_0/a)$. In order to calculate $\chi_{H,\mathrm{phys}}$

[1]This is an assumption that a volume $V = L^3$ contains $N = (l/L)^3$ uncorrelated volumes so that the overall amplitude of the field over the volume V is decreased by a factor N; see also discussion in [166] where this scaling has been criticised.

we recall that $\chi_{H,\rm phys} = cH^{-1}$ where $H = 1.66 g_*^{1/2} T^2$ with g_* being the effective degrees of freedom, T measured in $\rm MeV$ and H in $\rm s^{-1}$.[2] Then for the comoving magnetic correlation length we have:

$$\lambda_{B,\rm com} = f_{\rm c} \frac{c}{1.66 g_*^{1/2} T^2} \ {\rm cm}, \tag{4.2}$$

which corresponds to

$$\begin{aligned} \lambda_{B,\rm phys} &\sim 2.6 \cdot 10^{14} f_c \ \ {\rm cm \ \ (EW)} \\ \lambda_{B,\rm phys} &\sim 1.9 \cdot 10^{17} f_c \ \ {\rm cm (QCD)} \end{aligned} \tag{4.3}$$

for the field generated during EW or QCD phase transitions, respectively. One can see that even for the large f_c coherence scale of the phase transition-generated seed field is much smaller than the observed correlation lengths (of the order of few tens of $\rm kpc$) derived from e.g., Faraday rotation measurements (e.g., [34]) in galaxy clusters. As we will see in Section 4.2 this situation can change when one accounts for the MHD decay effects of the generated field in the radiation-dominated epoch.

The large-scale part of the magnetic energy spectrum of the phase transition-generated has been argued in Ref. [166] to fall sharply, satisfying Batchelor spectrum $E_{\rm B}^{\rm LS} \propto k^4$ in order to preserve causality combined with the divergence-free field requirement. However, smoother slopes have also been discussed the literature, such as e.g., the so called Saffman spectrum $\propto k^2$ (i.e., white noise spectrum, [165]). As we shall see in Section 4.2 both of these spectra can emerge during MHD evolution of the generated seed field and the realisation of these spectra depends on the driving nature of the turbulent magnetic field. On the other hand, the small-scale part of the spectrum is usually assumed to quickly converge into Kolmogorov $E_{\rm B}^{\rm SS} \propto k^{-5/3}$ scaling during MHD evolution.

A primordial seed field, with similar properties discussed above, could also be generated directly from the Higgs field (see Ref. [234] for pioneering work, Refs. [235–237] for subsequent studies and Refs. [238, 239] for some recent works). In this case, an electromagnetic field is constructed in a way that is different from its classical representation (Equation (3.2)) and the seed field is generated from the gradients of the Higgs field. As pointed out in Ref. [6] the model can be as robust as the generation of the seed field in the "classical" electromagnetism, especially, after the discovery of the Higgs field. Without further going into details of this model we note that the magnetic energy spectrum is obtained to be $E_{\rm B}^{\rm LS} \propto k^3$ (see section III in Ref. [6] for a more detailed discussion on the expected spectrum and generally, about the Higgs mechanism) and its energy peaks at $L_{E_B(k)}$ scales. Ref. [6] estimates the strength of such a field to be $10^{-18}\,{\rm G}$ on $\rm kpc$ scales.

Various scenarios have been proposed for the generation of helical PMFs (see [6] for reviews). These scenarios include e.g., generation of helicity from a coupling of PMF with axion field [240, 241]. Generally, physical processes associated to EW phase transitions are expected to generate helical PMFs [58, 60, 242]. Production of helical fields is of great relevance for explaining the magnetisation of large scale structure since helical fields lead to larger coherence scales during their evolution in the radiation dominated epoch (see Section 4.2).

[2] We remind the reader that the latter equation comes from the Friedmann equation (Equation (2.15)) where for the radiation dominated epoch the density field $\rho_{\rm r} = \frac{\pi^2}{30} g_* T^4$ (see e.g., [233]). The effective degrees of freedom depends on particle species and temperature. For the EW and QCD phase transitions $g_* = 100$ and $g_* = 60$, respectively.

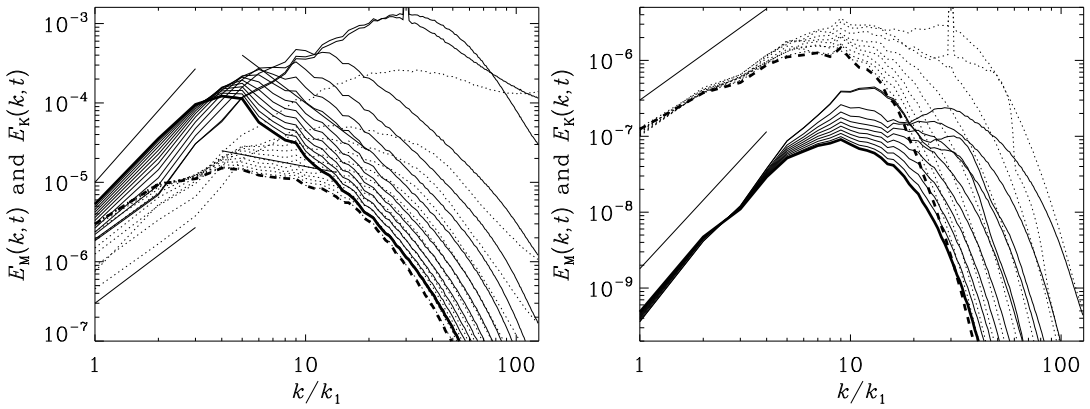

Figure 4.1: Evolution of magnetic (solid lines) and kinetic energy spectra (dashed lines) for the magnetically (left panel) and kinetically dominated turbulence (right panel). Thick line shows spectra at final time. The slopes indicated in the left and right panels are: 3, 2, 2, and $1/2$, and 2 and 3, respectively. The wavenumbers are normalised by $k_1 = k_0/30$ where $k_0 = 2\pi/\lambda_0$ is determined by the largest bubble size λ_0 ($\lambda_0 = f_c\lambda_{\rm H,phys}$. Figure credit: [22].

4.2 Pre-recombination evolution of PMFs

In the previous sections, we discussed the generation of primordial seed magnetic fields during inflation and phase transitions and the expected spectral characteristics of such fields. In this section, we focus on their evolution from the moment of generation until the recombination epoch. As we pointed out in Sections 3.1 and 3.8, in the absence of resistivity, in a high conductivity limit magnetic field decays as $1/a^2$; however, the concept of simple adiabatic dilution has to be abandoned when the effects of turbulence can become important. Turbulence could be generated either during inflation through the inflaton decay to standard model fields, or as discussed in Section 4.1.2 during first-order phase transitions. This motivates us to discuss the pre-recombination evolution of PMFs in the turbulent regime. A detail worth noting is that while the early phase of turbulent small-scale dynamo is required to amplify initially tiny seed fields, generated either during inflationary or phase-transitional magnetogenesis, at later times, the field is expected to decay and its evolution is studied in the so-called "freely decaying turbulence" regime. Thus, in principle, we can think of this regime as a late, saturation/post-saturation phase of small-scale, turbulent dynamo action.

The evolution of magnetic field in the decaying turbulent regime has been studied analytically (see e.g., [76]) as well as by using the direct numerical simulations (e.g., [22]). In the latter case, the whole set of non-linear MHD equations (Equations (3.10), (3.22) and (3.23)) are solved numerically in order to understand the complex evolution and resulting structure of the magnetic field. The exact form of the system equations depends on the problem being addressed and the numerical code being used. Generation of turbulence is usually accounted for by the driving force in the equations; the term corresponding to this force is present in the Euler or induction equations only at initial times until the equipartition between kinetic and magnetic energies is reached and then the free-decay phase of turbulence is studied (see, e.g., [243,244]). In the case of inflationary-generated PMFs, one can think of this driving force as a generation of turbulence after inflation, during an epoch of reheating [216]. In the case of phase-transitional PMFs, Ref. [57] studied two types of the driving forces that mimic the action of bubble-induced

external forces in the plasma. In the first case, the initial velocity of the fluid is zero and magnetic energy is "injected" in the flow; i.e., initial magnetic field has a Dirac delta function power spectrum peaked on the scale that is associated to the turbulent eddy size.[3] This case is called *magnetically dominated turbulence*. In the second case, the magnetic field has a Batchelor spectrum ($\propto k^4$) and instead, kinetic energy is injected into the system (again, with a delta function spectrum); this case is called *kinetically dominated turbulence*.

The evolution of the kinetic and magnetic energy spectrum for the described two scenarios is shown in Figure 4.1. Freely decaying MHD turbulence regime leads to a distinguishable spectrum in magnetically and kinetically dominated cases. In the former scenario, the magnetic field keeps the Batchelor spectrum on large scales $E_{\rm B}^{\rm LS} \propto k^4$, while the former scenario leads to the scaling which is shallower than that for $E_{\rm B}^{\rm LS} \propto k^3$ spectrum [57]. Thus, the slope of the magnetic spectra on large scales can vary between the Saffman ($\propto k^2$) and the Batchelor spectrum. Ref. [243] has also studied the evolution of QCD-generated PMF [245] in a magnetically dominated turbulence regime. Authors confirm the $E_{\rm B}^{\rm LS} \propto k^4$ scaling for the driving force which consists of plane monochromatic waves and fractional helicity, while on small scales $E_{\rm B}^{\rm SS} \propto k^{-5/3}$ is obtained. In addition, the recent work [29] has also shown that, in the kinetically dominated turbulence regime (although with a weak magnetic field; i.e., contrary to the magnetic field used in Ref. [57]) the Batchelor spectrum occurs on scales larger than the energy-containing scale of turbulence and in the kinematic stage of the dynamo, while the Saffman spectrum is obtained in the saturated case [29]. In Table 4.1 we summarise some of the scalings of the magnetic energy spectrum that is expected from the MHD turbulence studies.

Another important result that we see in Figure 4.1 is that not only the final state of turbulence, i.e., the peak of the kinetic energy spectrum, but the spectrum of the magnetic field also shows dependence on the initial driver of turbulence. While the peak of the magnetic energy spectrum shifts towards small wavenumbers for both driving modes (so-called inverse cascade; discussed below), the larger characteristic scale ($L_{E_B(k)}$) of the magnetic field is obtained when turbulence is magnetically dominated. Thus, for the phase transition-generated PMF, its post-recombination spectral characteristics will depend on the physics of phase transitions. On the other hand, if the magnetic field was generated in the earlier epoch, turbulence in the phase-transition epoch might be magnetically dominated; then it will back-react to the evolution of PMF and affect its spectral characteristics. Although the discussed model presented in Ref. [57] is not exhaustive it still gives us an idea of the evolution of phase-transitional-alike PMFs in the pre-recombination Universe.

Numerical MHD simulations have shown that evolutionary trends of phase-transitional PMFs is helicity dependent. This is illustrated in Figure 4.2 where the evolution of magnetic (red lines) and kinetic energy spectra (blue lines) is shown for the magnetically dominated turbulence case with zero (right panel) and non-zero magnetic helicity (left panel). Similarly to the magnetic spectra shown in Figure 4.1, here we again see that magnetic energy decreases on small scales and shows an increase towards large scales. This is known as the *inverse cascade* [76, 163, 246–249], i.e., the process of the energy transferring from small to large scales accompanied by an increase in the magnetic cor-

[3] An alternative of this procedure is simply to take the initial (magnetic/kinetic energy) spectrum which is e.g., Batchelor on large scales and Kolmogorov on small scales. In that case [24], no Dirac delta function is used for mimicking the injection of turbulence. However, since a short period of initial driving with the Dirac delta function also leads to a turbulent spectrum these two methods can be equivalent.

Large-scale spectrum ($E_{\rm B}^{\rm LS}$)	Origin/occurrence in MHD simulations
$k^{3/2}$ (Kazantsev)	• Kazantsev theory [184], Section 3.8. • dynamo ($\mathrm{Pr} \geq 1$) - kinematic phase.
k^2 (Saffman)	• Phenomenological [165], Section 3.5. • dynamo ($\mathrm{Pr} \geq 1$) - saturated phase; • non-helical decaying turbulence.
$\sim k^3$	• Dynamo ($\mathrm{Pr} \geq 1$) - kinematic phase.
k^4 (Batchelor)	• Phenomenological [166], Section 3.5. • dynamo ($\mathrm{Pr} \geq 1$) - kinematic phase; • helical decaying turbulence.

Table 4.1: Large-scale spectrum of the magnetic field expected from theory (the first rows in each cell of the second column) or from the MHD simulations (the rest of the rows in each cell of the second column). As Ref. [29] noticed recently the existence of the Kazantsev spectrum requires the large scale separation between the largest and forcing wavenumbers. On the contrary, for the Batchelor spectrum to be seen in the MHD simulations it is necessary that there is enough scale separation between the smallest and forcing wavenumbers.

relation length. An important feature of the figure is that final characteristic scale of the magnetic field depends on helicity. Helical fields lead to a slowdown of the decay due to conservation of magnetic helicity.[4] This is accompanied by speeding up the growth of the magnetic field coherence scale; i.e., the final peak scale of the magnetic field is larger in the helical scenario than in the non-helical case.

Ref. [24] has shown that the MHD turbulent decay of EW phase transition-generated field in the radiation-dominated epoch leads to an increase of the magnetic correlation length as a function of conformal time τ. If the initial magnetic field is non-helical, the increase is $\lambda_B \propto \tau^{1/2}$, whereas if it is fully helical, the increase is $\lambda_B \propto \tau^{2/3}$. The final coherence scale of the QCD phase transition-generated field can be even larger as a result of larger initial correlation lengths in these models (Equation (4.3)). The decaying turbulence is invariant under rescaling with the correlation length λ_B; this allows to rescale initial magnetic field to any desired epoch based on the initial value of λ_B. Finally, it should also be mentioned that similar values of the field strength and correlation length is found in Ref. [76] where the authors accounted for the dissipative processes (e.g., due to photon-neutrino diffusion and free streaming in the early Universe) in their analysis.

In Figure 4.3 we show the MHD evolution of inflationary PMFs. In the left panel of the figure, the evolution of PMF with a scale-invariant spectrum is shown. As we can see, the magnetic field decays on all scales and develops turbulent $k^{-5/3}$ scaling, although no inverse cascade is observed. In the later work, Ref. [163] has also studied the evolution of an inflationary, scale-invariant field whose spectrum has an infrared cutoff on large scales, $E_{\rm B}^{\rm LS} \propto k^4$ (we remind a reader that in such scenario $k_{\rm peak}^{\rm infl} \ll k_{\rm peak}^{\rm PT}$). In this latter work, authors have shown that for a certain wavenumber range (close to the peak of the spectrum, $k > k_{\rm peak}^{\rm infl}$) the magnetic energy power spectrum still will be characterised by

[4]The latter feature of helical fields itself leads to the so-called realizability condition which implies that helicity is bound by magnetic coherence scale and energy; that is $H \leq 2\lambda_B(\langle \mathbf{B}^2 \rangle/2)$. See Ref. [163] for more details and references therein.

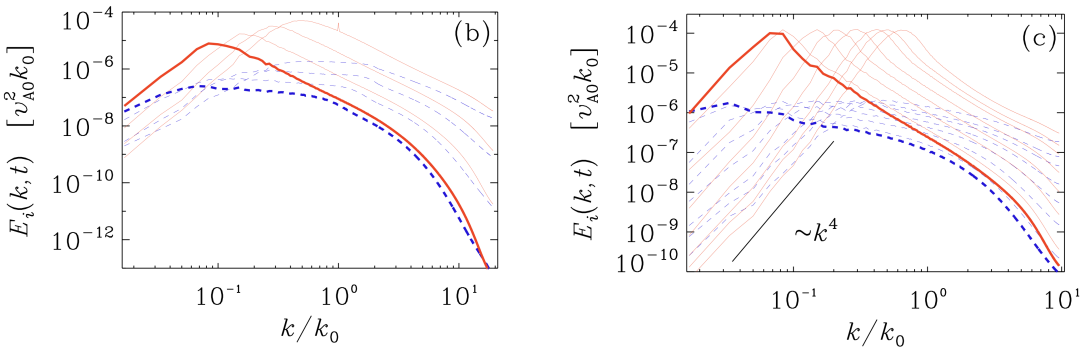

Figure 4.2: Evolution of kinetic (blue) and magnetic energy spectra (red) in the magnetically dominated turbulence regime (resembling the phase-transition magnetogenesis scenario). Thick line shows spectrum at final time. The black solid line shows Batchelor scaling and k_0 indicates the wavenumber associated to the peak of the spectrum at initial time (or driving scale). Figure credit: [22].

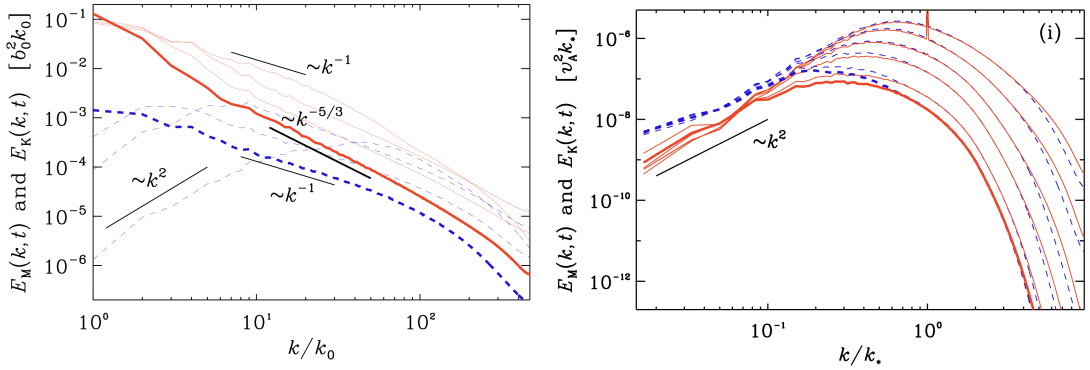

Figure 4.3: MHD evolution of inflationary PMFs characterised by an initial, scale-invariant (*left panel*) or Dirac delta spectrum (uniform distribution). As in Figure 4.2, the red and blue lines indicate magnetic and kinetic energy spectra, respectively. Thick line shows spectrum at final time. Note that left panel can be regarded as magnetically dominated case (see the text; with helicity) while in the right panel initial velocities differ from zero (kinetically dominated case which includes initial forcing; without helicity). k_0 is same as in Figure 4.2; k_* is the driving scale. Figure credit: [22].

the scale-invariant spectrum (see also Figures 4,7 in Ref. [163]).

Inverse cascade is absent for another inflationary scenario, which we refer to as *Mukohyama model*. Contrary to the models discussed above, in this case, the magnetic field is a uniform, constant (rather than stochastic, statistically homogeneous) field that can be considered as a local approximation of a slowly varying background field [216]. As argued in Ref. [216], the MHD evolution of such a field can be quite different from the evolution of the large-scale-correlated, scale-invariant field. The tangling of the uniform field by turbulence leads to Saffman scaling for the magnetic energy spectrum. During this process magnetic coherence scale increases but as pointed out by the authors, this is not due to the real inverse cascade but due to a rather faster decay of the spectrum at larger k compared to the decay of the spectrum at small wavenumbers.

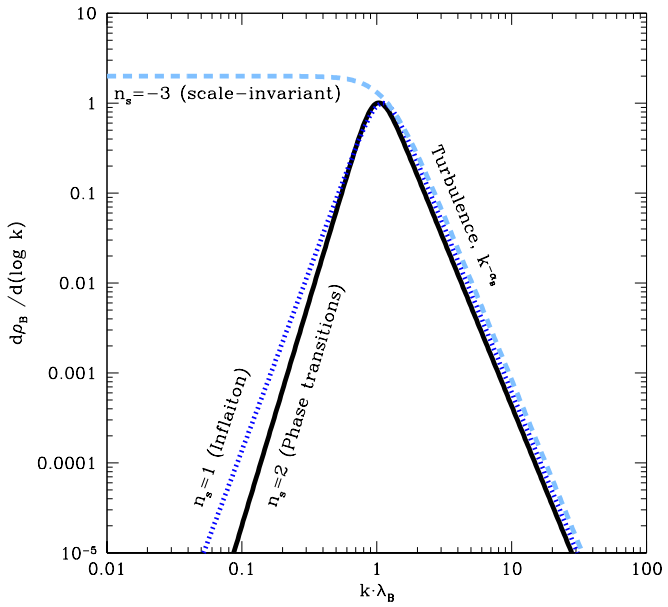

Figure 4.4: *Left panel*: Possible characteristic spectra for inflation- and phase transition-generated PMFs. The figure credit: Ref. [23].

4.3 Summary

Predicted spectrum of the field from primordial magnetogenesis scenarios. We have seen that PMFs could be generated through various magnetogenesis scenarios during inflation and phase transitions. The predicted structure (topology) and amplitude of the generated field may vary from theory to theory. Figure 4.4 shows expected spectral characteristics for some of the inflationary and phase-transitional generation scenarios. Note that the figure shows $d\rho_B/d(logk)$ where ρ_B is related to the magnetic energy power spectrum $E_B(k)$ in our notation through: $E_B(k) = k^2\rho_B(k)$; that is, $n_s = -3$ corresponds to the scale-invariant spectrum $E_B(k) = k^{-1}$. As can be seen from the figure, the largest differences in the shape of the power spectrum of inflationary and phase-transitional fields are expected on the largest scales of the Universe when inflationary and phase-transitional magnetogenesis leads to the scale-invariant and Batchelor ($n_s = 2$) magnetic energy spectra, respectively. We will see that this is the case even for the late evolution of PMFs, during structure formation (Chapters 6 and 7). On smaller scales, it is expected that the initial shape of the spectrum is irrelevant since the turbulence will lead to Kolmogorov forward cascade with $\alpha_B = -11/3$ scaling (or $-5/3$ scaling for our notation; see below).

Evolution in the radiation-dominated epoch. The evolution of PMF proceeds as "freely decaying turbulence" in the radiation-dominated epoch. The pre-recombination evolution of inflationary and phase-transitional PMFs have been studied with MHD simulations assuming inflation leads to scale-invariant magnetic energy spectrum and phase transition-generated fields have blue spectrum (i.e., most of the magnetic energy concentrated on smaller scales; [57, 163]). It has been shown that the correlation length of the small-scale (phase-transitional) as well as the large-scale correlated (inflationary) primordial field increases, although much more efficiently in the former case due to an inverse cascade.

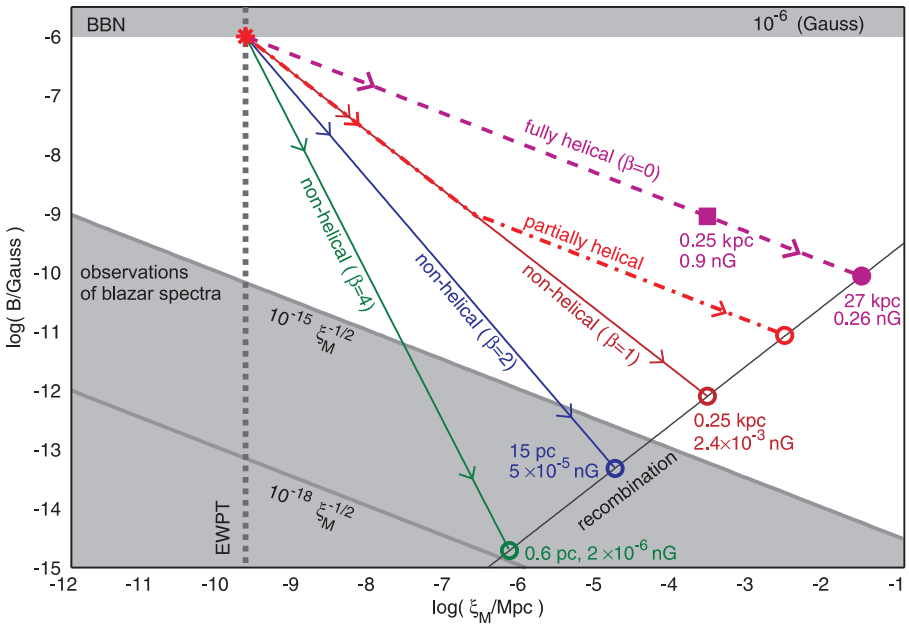

Figure 4.5: Dependence of the magnetic field amplitude on coherence scale. Different color lines show turbulent evolution of $B_{\rm rms}$ in the non-helical, helical or fractionally helical cases. Circles indicate the final characteristics of phase transition-generated PMFs at recombination. Figure credits: Refs. [23, 24].

The slope of the large-scale spectrum of phase transition-generated PMFs (after their MHD decay) depends on the underlying nature of turbulence during phase transitions; e.g., whether the turbulence is magnetically or kinetically dominated and $E_B^{\rm LS}$ can commonly be approximated either by Batchelor or Saffman spectrum. In addition, the phase-transitional helical field attains a larger coherence scale than the phase-transitional non-helical field. These evolutionary trends of EW phase transition-generated helical and non-helical fields are summarised in Figure 4.5. We see that if a magnetic field is generated at the horizon scale with a strength limited by BBN, a fully helical (non-helical) field reaches a (comoving) magnetic field strength of $0.3\,{\rm nG}$ ($3\times10^{-3}\,{\rm nG}$) at a scale of $30\,{\rm kpc}$ ($0.3\,{\rm kpc}$) at the epoch of recombination. Thus, we see that inverse cascade is an efficient process, increasing magnetic correlation length by orders of magnitude from the moment of generation till the recombination epoch. It turns out that both EW and QCD phase transition-generated seed magnetic fields can reach even larger coherence scales if one applies BBN bounds not to the time of generation of the seed field, but to the later times, at the epoch of BBN (see the constraint plot, Figure 1 in Ref. [250]). Ref. [250] have shown that QCD phase-transition generated magnetic field reaches $\sim 300\,{\rm ckpc}$ coherence scales (if the field is fully helical) by accounting for the decaying nature of turbulent sources between the time of generation and BBN. Finally, it should be noted that for the phase-transitional field generated from the Higgs field helical PMF reaches $10^{-11}\,{\rm G}$ strengths on $10\,{\rm kpc}$ scales at the recombination epoch [6].

The structure of the PMF at the recombination epoch is distinguishable for different inflationary models as well. An imposed (uniform) field develops a characteristic peak during its MHD decay, while the scale-invariant model will still be characterised by the largest power at the largest scales [216]. Even though no inverse cascade has been observed for such models the correlation length of inflationary PMF is expected to be larger than those of phase transition-generated PMFs (due to the fact that their post-generation

coherence scales are not bounded by the Hubble horizon scale).

Thus, in general, we can conclude that PMF characteristics such as the amplitude and coherence scale of the field at the recombination epoch will depend on (i) details of the particular magnetogenesis model and (ii) evolutionary trends in the pre-recombination Universe. We will see that these characteristics are of notable relevance for their evolution in the post-recombination Universe, during structure formation (see Chapters 6 and 7).

Evolution across recombination-epoch and during dark ages. Finally, one should mention what is the fate of PMFs across the recombination epoch and dark ages. It should be noted that the freely decaying turbulence regime is terminated when the damping term in Equation (3.23) becomes important on magnetic coherence scales. In the free streaming regime, there are Alfvén and compressible modes that are still damped. In the post-recombination Universe, on the other hand, damping is subdominant compared to the expansion damping. In this epoch, the decaying turbulence regime is not relevant anymore because the baryonic fluid becomes neutral (i.e.., no strong coupling between fluid and magnetic fields any more); then the comoving amplitude, spectral shape, and helicity of the magnetic field is expected to remain unchanged until reionisation ($z \sim 15$; see Ref. [76] and Section 6.4 Ref. [146] for more discussion on this) and structure formation.

Chapter 5

Methods: cosmological simulations

MHD simulations help us understand the complex evolution of PMFs in the early Universe, as we already outlined in the previous chapter. Cosmological MHD simulations, on the other hand, advance our understanding of the amplification and sustenance of PMFs during structure formation, reproducing the magnetisation of galaxies and galaxy clusters. They have also been used to understand the PMF effects on the first star [251] and dwarf galaxy formation [73] in the simulated $(250\,h^{-1}\mathrm{ckpc})^3$ and $(3\,h^{-1}\mathrm{cMpc})^3$ cosmological volumes, respectively. In the former case, MHD simulations resolve mini-halo scales (resolution of ~ 400 astronomical units); in the latter case, no magnetohydrodynamics is involved in simulations, although initial matter power spectrum includes effects from PMFs. PMF-induced density perturbations have been accounted for in the matter power spectra of the simulations presented in Ref. [74]. The authors studied the impact of PMFs on galaxy formation and on the evolution of IGM during the epoch of reionisation in a $(5\,h^{-1}\mathrm{cMpc})^3$ cosmological volume. The other class of cosmological simulations are those which study the evolution of PMFs even in larger volumes (e.g., in $(100\,h^{-1}\mathrm{cMpc})^3$ volume, see e.g., Ref. [252, 253] to understand the impact of the initial structure of the PMF on the final distribution of magnetic fields in the IGM. Our cosmic-web simulations (Chapter 6) also fall under the latter category. Our galaxy-cluster study (Chapter 7), on the other hand, is among the pioneering work where the impact of the initial topology of the field has been studied on the ICM scales (see also [254]).

Nowadays, many of the cosmological codes include different methods for solving the MHD equations. Examples of such codes are GADGET [255], RAMSES [256, 257], Athena [258], `Enzo` [113], AREPO [259], MASCLET [260]. The comparison some of these codes have also been done in several works (see e.g., Refs. [261, 262] for such examples). In our projects we use the `Enzo` code which is a well-tested and maintained tool for studying various astrophysical/cosmological problems. In this chapter we will briefly review the main methods that we used in `Enzo` and that applies to both of the presented projects in this thesis. The project-specific methods can be seen in Sections 6.2 and 7.2 for the cosmic-web and galaxy-cluster studies, respectively.

5.1 Equations solved by Enzo

Cosmological simulations imply the modelling of the formation of the large-scale structure by taking into account the dynamics of all species of matter across a vast range of spatial and temporal scales. The whole set of system equations (see below), formulated in discrete space, are solved numerically either by grid-based, Eulerian schemes or Lagrangian, particle-based schemes. In the Eulerian viewpoint, gas is discretised on the grid where each grid cell represents the fluid elements. In the Lagrangian solvers, on the other hand, fluid elements are particles that move along with the flow. Tracking the inter-particle forces then allows tracking the dynamics of the fluid. Apart from these two methods, a new approach has also been developed in recent years. In this approach, the computational mesh is unstructured and is defined according to a set of discrete points that can move arbitrarily. Thus, the method combines the grid and particle-based discretisation schemes (see more details on this method based on the technique used in the AREPO code [259]).

The Enzo code is Eulerian, grid-based code in terms of solving fluid equations and Lagrangian, particle-based code in terms of solving the dynamics of collisionless components of the fluid, such as e.g., the dark matter particles. The whole set of ideal MHD equations that are solved in our simulations (in a comoving coordinate system) is as follows [113]:

$$\frac{\partial \rho}{\partial t} + \frac{1}{a}\boldsymbol{\nabla}\cdot(\rho \boldsymbol{v}) = 0, \tag{5.1}$$

$$\frac{\partial \rho \boldsymbol{v}}{\partial t} + \frac{1}{a}\boldsymbol{\nabla}\cdot\left(\rho \boldsymbol{v}\boldsymbol{v} + \mathbf{I}p^* - \frac{\mathbf{B}\mathbf{B}}{a}\right) = -\frac{\dot{a}}{a}\rho\boldsymbol{v} - \frac{1}{a}\rho\boldsymbol{\nabla}\phi_g, \tag{5.2}$$

$$\frac{\partial \mathcal{E}}{\partial t} + \frac{1}{a}\boldsymbol{\nabla}\cdot\left[(\mathcal{E}+p^*)\boldsymbol{v} - \frac{1}{a}\mathbf{B}(\mathbf{B}\cdot\boldsymbol{v})\right] = -\frac{\dot{a}}{a}\left(2\mathcal{E} - \frac{B^2}{2a}\right) - \frac{\rho}{a}\boldsymbol{v}\cdot\boldsymbol{\nabla}\phi_g \tag{5.3}$$

$$\frac{\partial \mathbf{B}}{\partial t} - \frac{1}{a}\boldsymbol{\nabla}\times(\boldsymbol{v}\times\mathbf{B}) = 0 \tag{5.4}$$

where ρ, $\mathbf{v}$, B, $\mathcal{E}$, $\mathbf{I}$ are the comoving density, peculiar velocity, comoving magnetic field and comoving energy density, and identity matrix, respectively. Contrary to previous chapter, hereafter comoving values are denoted without stars and we always refer to comoving values unless stated otherwise. The comoving total energy density and pressure are given by:

$$\mathcal{E} = e + \frac{\rho v^2}{2} + \frac{B^2}{2a}, \tag{5.5}$$

where e is the comoving thermal energy density. The total comoving isotropic pressure p^* is given by

$$p^* = p + \frac{B^2}{2a}, \tag{5.6}$$

with an equation of state

$$e = \frac{p}{(\gamma-1)}, \tag{5.7}$$

and Possion's equation for the gravitational potential ϕ_g:

$$\nabla^2\phi_g = \frac{4\pi G}{a}\left(\rho_{\rm total} - \rho_0\right) \tag{5.8}$$

which closes the set of the equations solved by Enzo. Here, ρ_0 is the mean density, and $\rho_{\rm total}$ includes a contribution from gas and dark matter densities. Accelerated expansion of

the Universe is accounted for in the second Friedmann (Equation (2.16)) which is used for solving the evolution of $a(t)$. The dark matter particle dynamics are modelled by N-body approach using Newton's equations:

$$\frac{d\mathbf{x}}{dt} = \frac{1}{a}\boldsymbol{v}, \tag{5.9}$$

$$\frac{d\boldsymbol{v}}{dt} = -\frac{\dot{a}}{a}\boldsymbol{v} - \frac{1}{a}\boldsymbol{\nabla}\phi_g. \tag{5.10}$$

Dark matter particles are coupled with the fluid by gravitational potential (through Poisson's equation). Generally, these latter equations are also used to solve the dynamics of stars while physics associated to radiative cooling and heating, or thermal conduction is included through corresponding terms in Equation (5.2) (see Equation (3) in [113]). In addition, in `Enzo`, one can also include the evolution of chemical species, such as e.g., H, H^+, He, He^+, etc. In our cosmic web and galaxy-cluster studies, we restricted ourselves to understanding the effects of magnetic amplification due to adiabatic processes. Thus, we neglected radiative gas cooling, chemical evolution, and star formation or feedback from AGN.

Numerical methods that are used by ENZO for solving the Equation system 5.1-5.4 are based on Godunov's conservative numerical scheme. In its basic form, Godunov's scheme is first-order accurate and might not be appropriate for describing the system that exhibits shocks, discontinuities, or large gradients. In our works, we used MUSCL-based (Monotone Upstream-centered Schemes for Conservation Laws; [263]) scheme combined with the Dedner hyperbolic divergence cleaning algorithm [264]. Specifically, we used the second-order accurate piecewise parabolic (PLM) method for the reconstruction of spatial variables and the second-order Runge-Kutta (RK) scheme [265] for the time integration. A few different solvers are also available in `Enzo` for solving the Riemann problem. The Riemann problem is posed when there is a discontinuity at the interface between two finite-volume cells. In our setups, fluxes at cell interfaces are calculated using the Harten–Lax–van Leer (HLL) Riemann solver. In Appendix 9.2.2 we also test another solver of ENZO, namely the local Lax-Friedrichs, (LLF, [266]). See also Sections 6.7 and 7.5 and Section 4.1.2 in Ref. [113].

In a similar fashion, to solve the dynamics of dark matter particles Equations (5.9) and (5.10) are finite differenced with the same timestep that is used for solving the fluid equations. The particle positions are first interpolated on the grid and then Poisson's equation is solved on the (triply) periodic grid using the Fast Fourier Transform technique. Once the forces between particles are calculated they are interpolated back to the particle positions.

5.2 Divergence cleaning and Dual Energy Formalism

The solenoidal property of the magnetic field has been ensured by Dedner divergence cleaning in our works, as we mentioned above. Generally, maintaining the divergence-free constraint on the magnetic field is one of the most challenging tasks for the MHD codes. As outlined in Ref. [267] (for more recent work, see Ref. [268]) numerical discretisation can lead to errors in keeping divergence of the field zero even if it is zero initially. That is, spatial, δx, and temporal, δt, discretisation steps have an impact on the equation [268]:

$$\partial/\partial t(\nabla \cdot \mathbf{B}) = 0 + \mathcal{O}[(\Delta x)^m, (\Delta t)^n]$$

where, $m, n >= 1$. This itself can lead to nonphysical effects and instabilities in MHD equations. To compensate for numerical errors the hyperbolic divergence cleaning method introduces hyperbolic correction or divergence wave which is included in the induction and $\nabla \cdot \mathbf{B} = 0$ equations (i.e., by providing additional scalar field).

The Constrained Transport (CT) technique is another method for maintaining the divergence-free magnetic field, although more strictly, to machine round-off error precision. CT uses staggered mesh for defining the magnetic field components at the cell interfaces while electric fields are defined at the zone edges [269] (see e.g., Figure 4.1 in Ref. [268]). In our future works, we plan to employ this method for the projects presented in this thesis in order to see how/if our results are altered. Meanwhile, in Sections 6.7 and 7.5 we comment on possible uncertainties in our results from the divergence cleaning algorithm.

In our works, we additionally used another feature of the `Enzo` code, namely the dual energy formalism (DEF). In cosmological simulations, one often encounters the problem when thermal energy is a small fraction of the kinetic energy, e.g., in supersonic flows. This leads to the disastrous numerical situation when thermal pressure (proportional to the total energy subtracted a kinetic energy, $\propto \mathcal{E} - \mathcal{E}_k$) is a difference between two large numbers. Even though this occurs only in some regions where pressure is small we still used DEF method to ensure the correct temperature profile in such regions. In that case, `Enzo` code will solve the internal energy equation separately for updating the temperature profile of those regions. The code will exclude the contribution of this internal energy in gas dynamics.

5.3 Initial conditions

As already mentioned in Chapter 2, according to the ΛCDM paradigm structure formation is driven by initial tiny perturbations in the density field that must be also reflected in the initial conditions of our simulations. We generate initial conditions by the *inits* program which is provided by `Enzo` collaboration. *inits* sets up desired volume of particle-mesh grid and generates initial positions and velocities of dark matter particles as well as gas density and velocity distribution according to the adopted matter power spectrum (using periodic boundary conditions). In both studies, we use an initial matter power spectrum $P(k)$ which results from a primordial, scale-invariant spectrum $P_i(k)$ by taking into account the (linear) evolution of post-inflationary perturbations. Evolution of these perturbations is captured by the transfer function $T(k)$. $T(k)$ is related to the matter power spectrum through equation:

$$P(k) = T^2(k) P_i(k) \tag{5.11}$$

where $P_i(k) \propto k^n$ with $n = 1$ (so-called Harisson-Zeldovich spectrum) is the spectrum predicted by the inflationary theory. In the early Universe, each species of particles are expected to have a separate transfer function. However, since in the post-recombination Universe baryons quickly become pressureless, they follow cold dark matter perturbations and have the same transfer function (see e.g., Ref. [270]). In our works, we used the Eisenstein & Hu [270] transfer function which includes case of one massive neutrino. We assumed ΛCDM cosmology (as in Ref. [122]) with the following parameters: $h = 0.674$, $\Omega_m = 0.315$, $\Omega_b = 0.0493$, $\Omega_\Lambda = 0.685$, and $\sigma_8 = 0.807$. Here σ_8 is the parameter measuring the amplitude of (linear) power spectrum on the scale of $8\,h^{-1}\mathrm{Mpc}$. The main influence on the power spectrum comes from Ω_m and h parametres while σ_8 affects power

spectrum in a certain wavenumber range.

Once the initial matter power spectrum is provided, *inits* calculates dark matter and gas density fluctuations from the corresponding Gaussian random fields (see Ref. [271] for more details). Particle positions and velocities are then calculated from the Zel'dovich approximate (i.e., based on the first-order Lagrangian perturbation theory).

We note that the adopted matter power spectrum neglects any effects from PMFs. PMFs are expected to affect the clustering of matter on intermediate and small scales, smaller than galaxy cluster scales [71, 73, 171, 272, 273]. In particular, PMFs provide a source term in Equation (2.11) and produce gravitational instabilities, scalar (density), vector (vorticity), and tensor (gravitational waves) modes. The effects on the initial matter power spectrum have been discussed in the pioneering works [68–70]. Although, all these studies have neglected the PMF decay effects, assuming a frozen-in magnetic field with an unchanged spectral profile from the moment of generation until recombination. In our projects, we neglect PMF effects on the matter power spectrum while emulating the spectrum of the field according to the magnetogenesis and pre-recombination evolution scenarios. Thus, we do not expect that the presence of PMF-induced density perturbations in the early Universe will have a significant impact on the results presented in Chapters 6 and 7.

Magnetic initial conditions for our projects are generated with the PENCIL CODE and are described in Chapters 6 and 7 for the cosmic web and galaxy cluster studies, respectively. In brief, our magnetic initial conditions are divided into inflationary and phase-transitional-alike ones, i.e., resembling the characteristics of inflation- and phase-transition-generated PMFs. For each scenario, we study two different initial conditions differing from each other by magnetic energy power spectrum (while having the same total magnetic energy).

5.4 Adaptive Mesh Refinement (AMR)

The modeling of nonlinear structure formation should ideally encompass the formation and evolution of (proto-) stars and galaxies, and clusters of galaxies into filamentary structures, thus, requiring to resolve scales spanning from a few solar radii to hundreds of Mpc. One might strive to use a large number of grid cells and particles (e.g., in the hybrid codes, such as the `Enzo` code) to accurately model the processes inside the collapsed structures in large cosmological boxes. At the same time, care must be taken not to waste computational resources on the modelling of low-density regions, such as e.g., cosmic voids where the lower resolution will still suffice. In the Lagrangian codes, e.g., Smooth Particle Hydrodynamics (SPH) method [274–276] naturally leads to high resolution in high-density/collapsed regions. However, drawbacks of this method are the poorer resolution in the low-density regions compared to the Eulerian, grid-based codes as well as the fixed particle mass and poorer shock-capturing capabilities. The structured Adaptive Mesh Refinement (AMR, or also referred to as SAMR) technique, introduced by Berger and Collela [277], provides a means for adaptively increasing the resolution in the regions of interest, such as e.g., the gravitationally collapsing objects. Thus, this method complements the grid-based codes by providing improved spatial (and temporal) resolution where it is required [261, 278, 279].

AMR technique used by `Enzo` is well documented in method papers (e.g., Ref. [113]). Here, we shortly describe the main idea and refinement criteria offered by the code. The basic principle of AMR lies in constructing the hierarchy of grids within the targeted

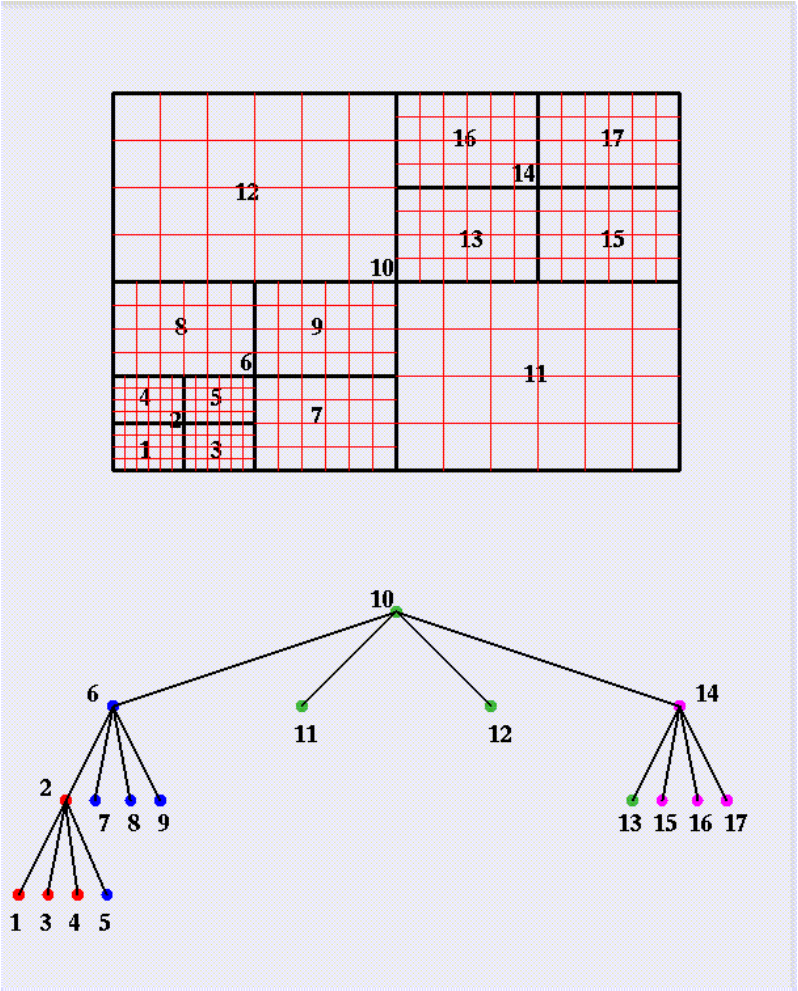

Figure 5.1: Representation of AMR structure: 2D grid structure where certain cells, triggered by the refinement criterion, are subdivided into smaller-size cells. The tree structure on the bottom panel illustrates the AMR hierarchy. Figure credit: Ref. [25].

regions. The target region can be a small part of the whole simulating domain which consists of uniformly sampled grid points, referred to as the root grid. As the AMR is activated, triggered by certain refinement criterion (see below), subgrids are built on the root grid. Each subgrid results from dividing the cells of its parent, coarser grid by an integer number (typically used 2 or 4) so that the resolution of this child grid is increased by the same factor (see Figure 5.1 for illustration of AMR technique). The hierarchy advancement process (i.e., the process of building the subgrids) continues until the refinement criterion is met; see section 3 in Ref. [113] for more details. An important parameter during the grid reconstruction process is the time step by which the grid is advanced. This time step itself satisfies various stability and accuracy criteria which is also documented in Ref. [113] (see Section 9).

AMR technique is of particular importance for cosmological applications since it enables us to define the refinement criteria that best suit the problem being simulated. The `Enzo` code provides various options for the refinement criteria that are necessary for activating the AMR. Examples of such criteria are flagging of computational domain cells according to the gas and dark matter density thresholds, pressure and velocity gradients, and second derivatives of fields. In the latter case, a cell is refined when the ratio of the second and first derivatives of the user-provided field exceeds a certain threshold. Refine-

ment according to pressure and velocity jumps is used for identifying the shocks in the simulations. This latter criterion is based on the pressure and velocity difference across adjacent cells. Several works have studied the refinement strategies and their suitability for resolving the turbulence in galaxy clusters (see e.g., Refs. [280–282]). Studying such refinement techniques was also important for our galaxy-cluster study. In Section 7.2 we describe the strategy employed in our "zoom-in" simulations of galaxy clusters. Cosmological zoom-in simulations are good examples of achieving high resolution in individual objects within the cosmic web using AMR. Such simulations usually comprise two sets of simulations: one where the region of interest is identified and the other one where this region is studied with higher resolution and tailored AMR refinement factors.

Chapter 6

PMFs during large-scale structure formation

In this chapter, we are interested in the global properties of PMFs and their signatures on the RM; we describe our results of the cosmic web study based on our publication:

- Mtchedlidze, S., Domínguez-Fernández, P., Du, X., Brandenburg, A., Kahniashvili, T., O'Sullivan, S., Schmidt, W., Brüggen, M., "Evolution of Primordial Magnetic Fields during Large-scale Structure Formation", *ApJ* 929, 127 (2022).

I confirm the sole contribution to the paper and responsibility for the following: participation in the study conception and design, running of simulations and data analysis, interpretation of the results and the draft manuscript preparation.

6.1 Physical model

We first start by discussing the physical motivation for studying the chosen primordial magnetogenesis models and statistical characteristics for these scenarios. The statistical characteristics of each PMF are determined by the generation mechanism. First, in the case of a uniform, homogeneous PMF (the Mukohyama model) that is generated during the inflationary stage, the correlation length λ_B is undetermined (well above the horizon scale at the generation moment). Indeed, such a PMF might be described as a monochromatic field at $k = 0$. Such a field has zero helicity, and no spectrum can be associated to it[1] (i.e., the realisation in Fourier space is a Dirac delta function). If a statistically homogeneous field has been generated through some mechanism after inflation, its peak scale $L_{E_B(k)}$ and therefore its correlation length must be limited by the size of the Hubble horizon at the moment of generation, $H_\star^{-1}$. In this case, we can still use a monochromatic field at a nonzero wavenumber $k_{\rm peak}$. Correspondingly, the PMF in Fourier space will be approximated by a Dirac delta function as $\delta(k - k_{\rm peak})$. This is a common description when referring to the lower limits of the magnetic field through blazar spectra observations [100]. The energy density associated with a homogeneous PMF is simply given through $B^2/(8\pi)$, regardless of whether the field has finite or infinite correlation length.

In the case of causally generated magnetic fields after inflation, under the standard description of a PMF generated during the electroweak phase transitions through bubble collisions, the physical correlation length is determined by the bubble length scale. A length scale of around one-hundredth of the Hubble horizon scale is commonly assumed, with 100 bubbles within a linear Hubble scale. For the QCD phase transitions, the bubble size is commonly assumed to be one-sixth of the Hubble scale (see e.g., Ref. [283]).

We focused on studying two subcases of inflationary and phase-transitional magnetogenesis scenarios. In the inflationary case, we study (i) a uniform, homogeneous and (ii) a stochastic, scale-invariant initial magnetic field (see Section 6.2.1). In the latter case, we take into account the development of a turbulent forward cascade in the radiation-dominated epoch [284]. That is, the inflation-generated, scale-invariant k^{-1} spectra result in a Kolmogorov $k^{-5/3}$ spectrum by the end of recombination (see Figure 4.3). In the phase-transitional case, we study (iii) a helical and (iv) a nonhelical initial magnetic field. These cases correspond to a turbulent, causally generated magnetic field with a characteristic scale of $\sim 2.6\,h^{-1}\,{\rm Mpc}$ and $\sim 1.26\,h^{-1}\,{\rm Mpc}$, respectively. Toward larger scales, the magnetic energy spectrum is proportional to k^4 (*Batchelor spectrum*; see Section 4.2). On smaller scales, a turbulent magnetic cascade with an energy spectrum proportional to $k^{-5/3}$ (*Kolmogorov spectrum*) is expected. These spectra are obtained quite generically even when turbulence is driven monochromatically at one wavenumber [285].

As we discussed in Section 4.3, phase transitional fully helical (non-helical) magnetic fields are expected to reach a (comoving) magnetic field strength of $0.3\,{\rm nG}$ ($3 \times 10^{-3}\,{\rm nG}$) at a scale of $30\,{\rm kpc}$ ($0.3\,{\rm kpc}$) at the epoch of recombination (see Figure 4.2). Our selected initial characteristic scales for models (iii) and (iv) are larger than these predictions due to our limited resolution of $132\ h^{-1}\,{\rm kpc}$. It is therefore important to stress that our initial stochastic, helical and nonhelical spectra are intended only to emulate the shape that is ex-

[1] It is important to emphasise that such magnetic fields are qualitatively different from the small-scale fields that are obtained by tangling of a uniform (imposed) one. This is because, in periodic domains, such a field constitutes a separate component that can never change. This has dramatic consequences for the evolution of the magnetic field on all smaller scales; see Ref. [216] for examples.

Scenario	Model	Norm. (nG)	Sim. ID	$\langle B_0^2 \rangle$ (nG)^2	$\langle B_0 \rangle$ (nG)	$k_{\rm peak}$ $h\,{\rm Mpc}^{-1}$	$L_{E_B(k)}$ $h^{-1}\,{\rm Mpc}$
Inflationary	(i) Uniform	0.1	u01	0.0072	0.085	—	—
		0.5	u05	0.180	0.390	—	—
		1	u1	0.719	0.804	—	—
	(ii) Scale-invariant	0.1	s01	0.0072	0.079	0.02	45
		0.5	s05	0.180	0.395	0.02	45
		1	s1	0.719	0.790	0.02	45
Phase-transitional	(iii) Helical	0.1	h01	0.0072	0.080	0.4	2.6
		0.5	h05	0.180	0.402	0.4	2.6
		1	h1	0.719	0.781	0.4	2.6
	(iv) Nonhelical	0.1	nh01	0.0072	0.085	0.8	1.26
		0.5	nh05	0.180	0.424	0.8	1.26
		1	nh1	0.719	0.848	0.8	1.26

Table 6.1: Initial conditions for the magnetic field; the characteristic wavenumber and scale of the magnetic spectra is denoted by $k_{\rm peak}$ and $L_{E_B(k)}$ accordingly, and $\langle B_0^2 \rangle$ and $\langle B_0 \rangle$ are the mean of the initial magnetic field energy and the initial magnetic field strength respectively.

pected theoretically. In the helical case, we selected a correlation length that is larger than the one in the nonhelical scenario since this is also expected from theory as a consequence of the inverse cascade that helical fields undergo in the radiation-dominated epoch.

6.2 Simulations

We simulated $(67.7h^{-1}\,{\rm Mpc})^3$ comoving volume with static uniform grid of 512^3 cells with 512^3 DM particles, each of mass $m_{\rm DM} = 2.53 \times 10^8 M_\odot$. Our grid resolution is 132 $h^{-1}\,{\rm kpc}$. The chosen box size is of the same order as the scales where the Universe is assumed to be homogeneous and isotropic. Therefore, it is suitable for studying the global properties of the PMF evolution in the cosmic web. The resolution, on the other hand, has been chosen to reduce the computational resources since we are not aiming at resolving turbulence amplification in galaxy clusters; although, this resolution still allows us to resolve the amplification of the field due to adiabatic dynamics. We note that our setup is a first step in describing the evolution of more realistic PMFs than what was done previously (using the uniform seed field only; see, e.g., Refs. [252, 286]). The ΛCDM cosmology parameters that we use are as follows, $h = 0.674$, $\Omega_m = 0.315$, $\Omega_b = 0.0493$, $\Omega_\Lambda = 0.685$, and $\sigma_8 = 0.807$.

6.2.1 Initial conditions

We consider four different scenarios for the initial magnetic seed field (see Table 6.2 and Section 6.1 for the validity of the models):

(i) Uniform (spatially homogeneous) field: we study an initial seed magnetic field with

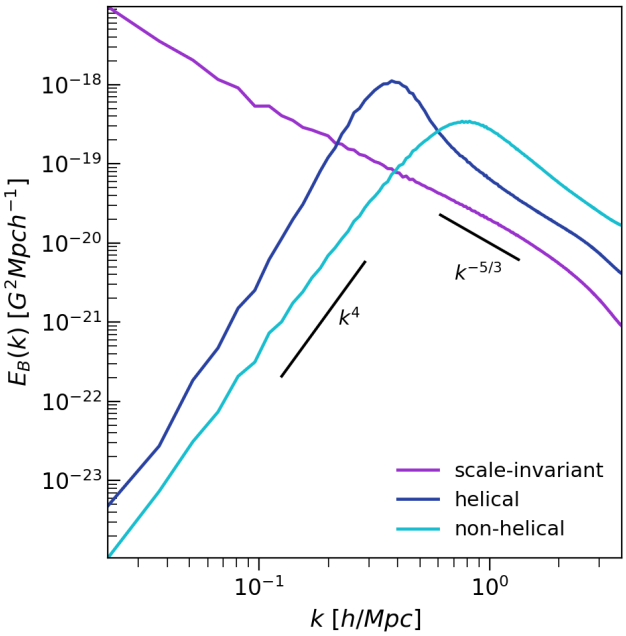

Figure 6.1: The initial magnetic power spectra for the stochastic setups.

a constant strength across the whole computational domain. The magnetic field is directed along the diagonal. This case corresponds to the Mukohyama model [56].

(ii) Scale-invariant field: this is a setup for a stochastic, statistically homogeneous PMF with no helicity. This case corresponds to an inflationary scenario.[2]

(iii) Nonhelical field: a stochastic, phase-transitional PMF with no helicity.

(iv) Helical field: the same stochastic setup as (iii), but with helicity.

As we noted in Section 4.3, any power-law decay/growth of the magnetic field and its correlation length on small scales is expected to virtually freeze at the end of the radiation-dominated epoch [76], while the large-scale evolution of PMFs during dark ages as well as after the reionisation epoch is primarily dominated by the expansion of the Universe. [3] Therefore, we initialise the simulation at $z = 50$ without loss of generality since no significant changes at the cosmological scales of interest for this work are expected between the recombination epoch and $z = 50$ redshift.

The seed magnetic field conditions (ii)–(iv) were preproduced with the PENCIL CODE [288]. These were then used as initial conditions for the `Enzo` code. We normalised the mean magnetic energy density in all four cases (at initial redshift $z = 50$) to the same value corresponding to a mean (*effective*) magnetic field strength. The reader is referred to Appendix 9.1 for a detailed description of the generation of the initial magnetic conditions (ii)–(iv), including the setup for the helical field, as well as their normalisation.

In Section 6.3, we discuss the results of three different normalisations: 0.1 nG, 0.5 nG, and 1 nG (see Table 6.2) for the uniform, scale-invariant, helical, and nonhelical models,

[2] We note that we call this model "scale-invariant" even though it has a turbulent spectra with $k^{-5/3}$ scaling; see Section 6.1.

[3] See, however, Ref. [287], who recently claimed a faster decay of PMFs than expected by the expansion of the Universe.

model	Normalisation (nG)	$\langle B \rangle_{z=0.02}$ (nG)
Uniform	0.1	0.15
	0.5	0.69
	1	1.29
Scale-invariant	0.1	0.15
	0.5	0.69
	1	1.27
Helical	0.1	0.09
	0.5	0.42
	1	0.79
Nonhelical	0.1	0.08
	0.5	0.39
	1	0.74

Table 6.2: Mean of the magnetic field strength at $z = 0.02$ achieved for all our models (see also Table 6.2). Note that the mean value is computed in the whole cosmological box.

respectively. In the remainder of this chapter, we only discuss the results of the 1 nG normalisation (which is below the upper limit from the CMB bounds;see Ref. [21]).

We show the initial magnetic power spectra for the stochastic setups considering a 1 nG normalisation in Figure 6.1. In our work, as already mentioned in Chapter 5, we consider the MHD decay effects while neglecting the initial matter power spectrum modifications. The self-consistent derivation of the initial linear magnetised perturbation is beyond the scope of the project. Recent numerical works [73, 74] have shown that PMF effects on matter power spectrum are mainly at the high end tail of the spectrum (small scales). Such effects should not significantly impact the results presented in this work since our initial magnetic conditions are better suited for studying the evolution of magnetic fields on larger scales and higher-mass haloes. The main novelty of our approach lies in the fact that we adopt a magnetic field from a self-consistent turbulence simulation where the field displays an approximately self-similar decay. In particular, the field contains coherent structures over all length scales.

6.3 Dependence on the magnetic field strength

We start our analysis by studying the effects of the initial magnetic field strength on the final distribution of magnetic fields in different cosmic environments. In this section, we discuss the results from three different initial magnetic strengths: 0.1 nG, 0.5 nG, and 1 nG (see Table 6.2).

In Figure 6.2, we show the median of the magnetic field and temperature distributions with respect to the gas density distribution for the different models at $z = 0.02$. In the same figure we also show a 2D histogram, i.e., we overplot the gas mass (for the helical case) falling into each bin. The distributions differ according to the different regions of the cosmic web, i.e., voids, filaments, bridges, and clusters. We identified bridges in our simulations by visual inspection. The typical range of the overdensity in this environment is given in Figure 6.2. Notably, we define bridges in a way so that they also include the

outskirts of galaxy clusters. It is important to distinguish this environment from large-scale filaments, because currently bridges are the most promising way to observationally detect large-scale warm–hot gas filaments (see e.g., [2, 289]).

The resulting differences between magnetic seedings in each cosmic environment observed in Figure 6.2 can be summarised as follows:

Clusters. As we can see from the top panel of Figure 6.2 the variation of the initial magnetic field strength does not affect the normalised[4] magnetic field distributions in galaxy clusters; although each model leads to higher final mean values for the higher initial magnetic field realisation (see Table 6.3). The highest median values are observed from the inflationary seedings where the uniform seeding shows a magnetic field strength twice as large as the scale-invariant model. On the other hand, the phase-transitional seedings show the lowest magnetic field strengths within these regions. In particular, the nonhelical case is the model that shows the lowest amplification in galaxy clusters. Interestingly, different seed magnetic fields, as well as the variation of the seed field strength, do not alter the temperature distribution in these regions (see for comparison Ref. [253]).

Bridges. Similarly to clusters, the highest magnetic fields in these regions are seeded by the inflationary scenarios. However, the differences in the magnitude of the uniform and scale-invariant cases are reduced in comparison to cluster regions, while for phase-transitional models they are slightly enlarged. Finally, the temperature distribution is again unaffected by different primordial scenarios.

Filaments. The different initial magnetic field strengths do not alter the normalised magnetic field or temperature trends in this region. However, the final distribution of the magnetic field is affected by the initial topology of the seed field. The seed fields with initial larger characteristic scales lead to larger magnetisation levels in filaments. The uniform and scale-invariant cases show amplification due to adiabatic contraction. In the helical and nonhelical models, where the magnetic power of the large-scale modes is smaller (see Figure 6.1), the amplification due to adiabatic compression is less efficient. Previous work that focused on filaments (see e.g., [286]), have argued that the magnetic amplification within these regions is less dependent on resolution and possible dynamo action even at high Reynolds numbers. This can happen because compression are expected to be dominant in filaments and suppress small-scale twisting of magnetic structures. Finally, it seems that the differences between the inflationary and phase-transitional models are not reflected in the temperature distribution. Similar trends have been found in Ref. [290], where the different seeding scenarios show significant imprints on final magnetic field distributions but only mild differences in the temperature trends (pronounced mostly at high densities).

Voids. These regions are assumed to be most promising for discriminating among different magnetogenesis scenarios (see e.g., Refs. [51, 291]). We see that differences between the models in the temperature profiles are revealed only for the higher initial magnetic field realisations (i.e., only for the $0.5\,\mathrm{nG}$ and $1\,\mathrm{nG}$ initial magnetic field strengths). However, the differences between the uniform and scale-invariant models are negligible, while the helical and nonhelical cases show the largest discrepancies. In addition, we see that stochastic (scale-invariant, helical, or nonhelical) seedings lead to the highest magnetic field strengths, and consequently highest temperatures within these regions. This highlights the fact that

[4]Normalised by the corresponding mean field value of the model; see Table 6.3.

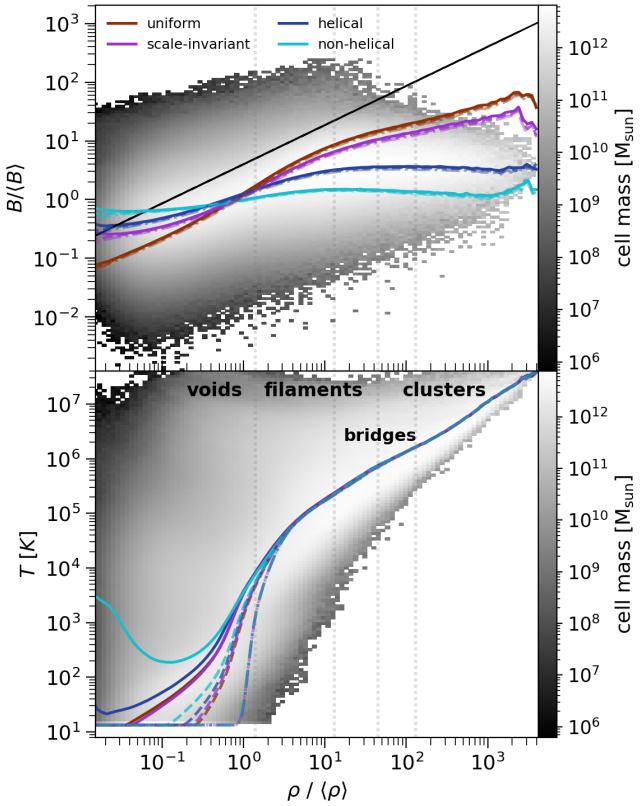

Figure 6.2: Dependence of the median magnetic field and temperature on density for all of our simulations. The x-axis shows the gas density normalized by the mean density field. The solid, dashed, and dashed-dotted lines correspond to the 1 nG, 0.5 nG, and 0.1 nG, normalizations, respectively. The black solid lines show the expected density scaling of the magnetic field strength based on the adiabatic contraction only ($\propto \rho^{2/3}$). The additional color coding (black–white palette) shows the mass of gas (for the helical case) falling into each bin. Vertical dotted lines indicate the characteristic densities in filaments and bridges.

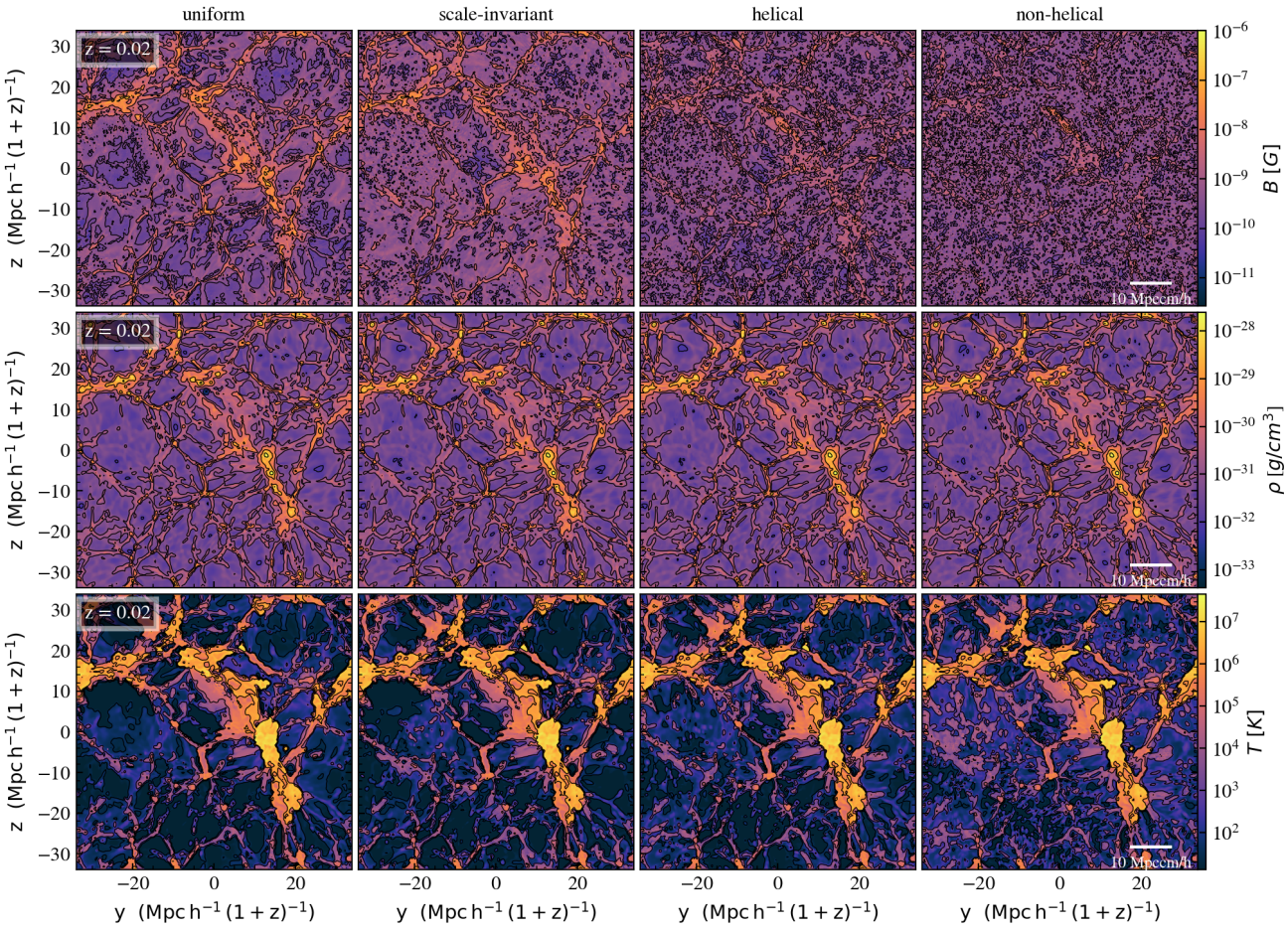

Figure 6.3: Contoured slices through the centre of the simulated box at $z = 0.02$. The top, middle, and bottom panels show the magnetic field, density, and temperature slices correspondingly. The overplotted contour lines mark the regions with a certain field strength, and the range of the field values are set according to the minimum and maximum of the annotated fields.

initial stochastic turbulent motions could cause local heating. Similar trends were obtained in Ref. [253] where only models with an initial power-law magnetic spectrum were considered. Therefore, initial magnetic fluctuations could be important for the local heating. In particular, PMFs can heat up the hydrogen and helium in the IGM by, for example, decaying turbulence (see e.g., Refs [272, 292]) and this can be reflected in the 21 cm signal [293–295]. Strong absorption spectra of the global signal detected by the EDGES experiment suggest that IGM was colder than expected from the standard cosmological scenario [296]. In the recent work of Ref. [287] it has been shown that heating of IGM due to PMFs along with DM–baryon interactions [297] can be used for constraining the strength of PMFs. Hence, the observed temperature differences in Figure 6.2 could be used to probe the strengths of both inflationary as well as phase-transitional models in cosmic voids.

We can conclude that the amplification of the initial magnetic field due to adiabatic contraction is subdominant in the stochastic turbulent cases at our resolution. Conversely, the uniform model can be well fitted by the simple $\rho^{2/3}$ relation (expected from adiabatic contraction only) in the filaments and low-density regions (see also Appendix 9.2.1). As

expected, the differences between models become larger at the galaxy-cluster scales due to our limited resolution. While we expect that these differences should persist (although to a lesser degree) with higher resolution, only future work focusing on these regions can demonstrate it.

In the next sections of this chapter we will focus on the PMF scenarios with an initial 1 nG normalisation (see Table 6.2). The resulting mean magnetic field strengths from this normalisation are more in agreement with current observations; see, e.g., Refs. [298, 299] for the 0.1–1 μG magnetic field strengths found in galaxy clusters based on the inverse Compton measurements from radio haloes, and [35] for the strengths as high as 1–7 μG based on the likelihood analysis of Faraday rotation measures.

6.4 General properties

We show slices of the final ($z = 0.02$) magnetic field, density, and temperature in the 67.7 $h^{-1}\mathrm{cMpc}$ box in Figure 6.3. As we can observe in the top panels of Figure 6.3, the stochastic seeding fills the voids more efficiently than the uniform case, while the uniform and scale-invariant magnetic seedings show the largest spatial correlation with the filamentary structures. This is not surprising because the initial magnetic power spectrum of the uniform seeding does not have a characteristic scale, and the characteristic scale of the scale-invariant spectrum is larger than that of the helical and nonhelical cases. We also observe that nonhelical initial magnetic fields tend to create more substructures than helical ones. This is an expected trend in MHD simulations of helically and nonhelically driven turbulence because of the magnetic helicity (and thereby magnetic energy) transfer to large scales. In a recent study of turbulent dynamos driven by isotropic forcing in isothermal MHD [300], helical and nonhelical cases were compared. The authors found that an initially Gaussian magnetic field (with a magnetic energy spectrum $\propto k^2$) develops a magnetic energy spectrum with a characteristic scale (peak spectrum) in both cases. Nonetheless, the helical case attains a large-scale nature (more power at k smaller than the peak scale), while the nonhelical case is still characterised by a small-scale structure.

The density (middle row in Figure 6.3) and temperature (bottom row in Figure 6.3) contours show a spatial correspondence between the densest structures ($\sim 10^{-28}\,\mathrm{g\,cm^{-3}}$) and the highest temperatures ($\sim 10^7\,\mathrm{K}$) in all four cases. The low-density regions ($\sim 10^{-32}$–$10^{-31}\,\mathrm{g\,cm^{-3}}$) enclose higher temperatures in the nonhelical case than in all the other cases. This is a direct consequence of having smaller magnetic substructures in the nonhelical model at the initial and final redshifts, which leads to extra turbulent dissipation in the voids region.

In Figure 6.4 we show the volumetric PDFs of the magnetic field for all our models. The PDFs are shown for two epochs: $z = 40$ (dotted lines) and $z = 0.02$ (solid lines). The final PDFs show a broadening in all the models. The low-end tail of the distribution (values below $6 \times 10^{-10}\,\mathrm{G}$) is very similar for all the models. By contrast, the high-end tail of the distribution (values above $4 \times 10^{-9}\,\mathrm{G}$) differs in the inflationary and phase-transitional models. Both inflationary models produce higher magnetic field values than the phase-transitional models. It should also be noted that the PDFs for both scenarios deviate from the Gaussian trend (more evidently seen for the inflationary models) and the peak of the distribution in the inflationary case is shifted toward lower values. For example, in the uniform case, the peak is shifted from $8 \times 10^{-10}\,\mathrm{G}$ to $2 \times 10^{-10}\,\mathrm{G}$. We can see that the main differences in the distributions come from the regions where the magnetic field strength is of the order of 4×10^{-9}–$5 \times 10^{-7}\,\mathrm{G}$.

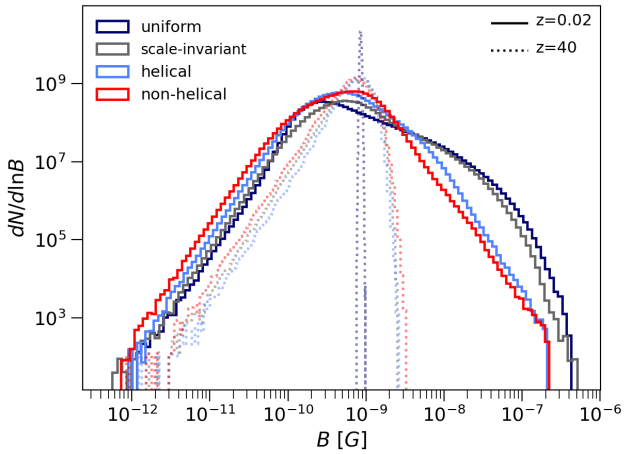

Figure 6.4: PDFs for the different magnetic seedings at $z = 40$ (dotted lines) and $z = 0.02$ (solid lines).

Finally, the evolution of thermal, kinetic, and magnetic energies over a time span of $13.5\,\mathrm{Gyr}$ is shown in Figure 6.5. The thermal $\mathcal{E}_T$, kinetic $\mathcal{E}_K$, and magnetic $\mathcal{E}_B$ energies are defined as

$$\int nk_B T dV, \quad \int \frac{\rho \mathbf{v}^2}{2} dV, \quad \int \frac{\mathbf{B}^2}{8\pi} dV, \tag{6.1}$$

where n is the gas number density, $\mathbf{v}$ the velocity, k_B the Boltzmann constant, and V the volume. The growth of kinetic and thermal energies achieved in all four models is of the order of $\sim 10^5$ by the end of the simulation. The thermal energies show variations between the models at earlier redshifts (see $z \gtrsim 6$, where stochastic phase-transitional cases show larger thermal energies). This indicates that more dissipative processes are present in these scenarios. Although we find that the extra heating shown in Figure 6.5 is independent of the Riemann solver, we cannot rule out a numerical origin. However, we also see that the thermal-energy evolution converges to the hydrodynamic case for redshifts $z \lesssim 6$ (see also Appendix 9.2.2). For this reason, it is unlikely that our analysis at lower redshifts is affected by the initial transient. Moreover, spurious heating will be suppressed by radiative cooling in a more advanced model.

The final thermal and kinetic energies (for $z \gtrsim 6$) show no difference between the four models. However, differences in the magnetic energies arise at a redshift as early as $z \sim 40$. At $z = 0.02$ it is evident that the magnetic energy in the inflationary models is roughly one order of magnitude larger than the magnetic energy in the phase-transitional models. Overall, the magnetic energy growth throughout the evolution is observed to be by a factor of ~ 10 in the uniform and scale-invariant cases, and by a factor of ~ 2–4 in the nonhelical and helical cases, respectively.

6.5 Evolution of magnetic power spectra

In this section, we focus on the properties of the magnetic power spectra (Equation (3.36)) for the different primordial magnetic seedings. We remind a reader that as we have seen in Section 4.2 pre-recombination evolution of magnetic energy spectra is affected by turbulence; the final topology of the field at the recombination epoch shows dependence on the initial conditions as well as on the nature of turbulence. In this section, we will see that

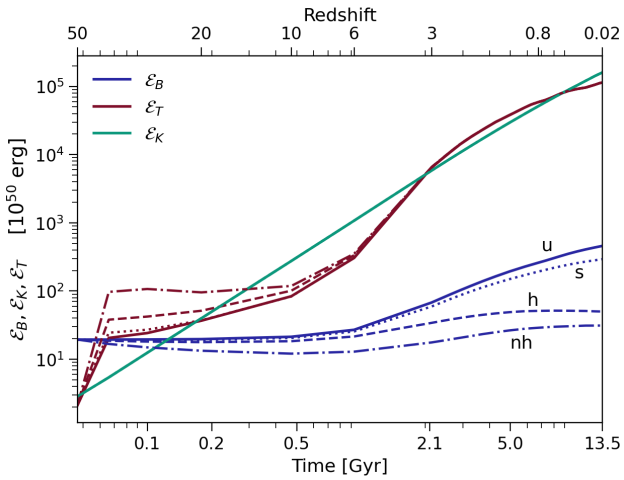

Figure 6.5: Evolution of magnetic, thermal, and kinetic energies for the different magnetic seedings. The solid, dotted, dashed, and dashed-dotted lines correspond to uniform, scale-invariant, helical, and nonhelical cases, respectively.

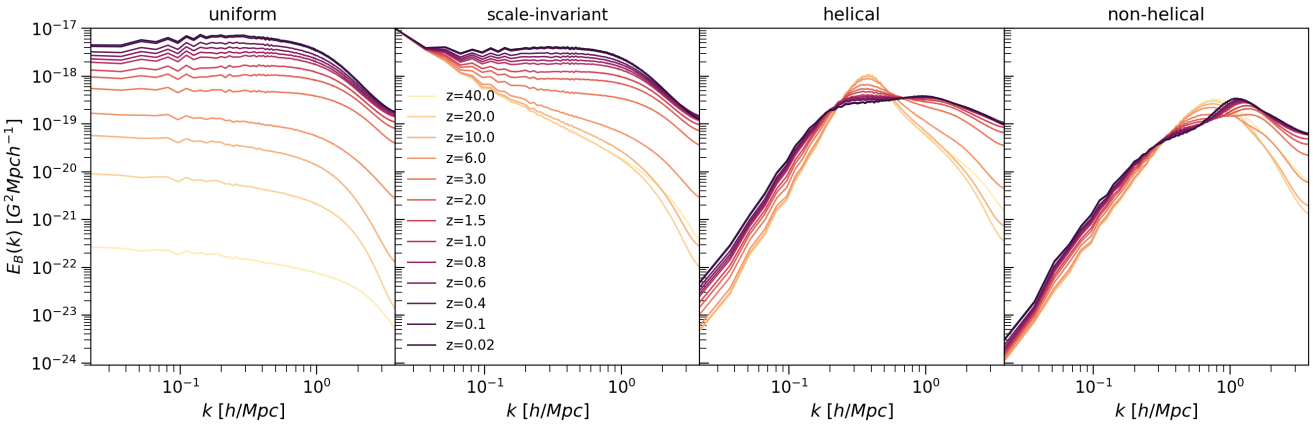

Figure 6.6: Redshift evolution of magnetic power spectra. From left to right: the uniform, scale-invariant, helical, and nonhelical seedings.

field topology after structure formation (at the current epoch) would still differ according to different magnetogenesis scenarios.

In Figure 6.6 we show the evolution of the magnetic power spectra of the inflationary (uniform and scale-invariant) and phase-transitional (helical and nonhelical) cases. Notable features of this figure are as follows:

a) *Inflationary seeding*. The magnetic power spectrum in the uniform and scale-invariant cases reaches higher values at the final redshift than that of the cases with helical and nonhelical seeding. In particular, the uniform seeding shows how the magnetic energy builds up at all scales in a similar fashion from early redshift ($z = 40$). This emphasises how the magnetic field follows the growth of the density perturbations. On the other hand, the amplitude of the power spectrum in the scale-invariant case starts increasing only from $z = 10$, but the final distribution achieved in this case is similar to that in the case of the uniform seeding.
The obtained trends for these two subcases of an inflationary scenario seem to be different from the results of a recent study by Ref. [216], where the MHD evolution with imposed and scale-invariant initial fields has been compared in the radiation-dominated epoch. They showed that even if small-scale turbulent forcing is applied, the uniform (imposed) field always decays faster than the field with the scale-invariant spectrum. Subsequent studies revealed that the apparent difference between the two types of simulations is caused by the fact that in the present cosmological simulations there is always a large-scale velocity field, which was not the case in the simulations of Ref. [216]. However, repeating their simulations with a large-scale velocity field characterised by an initial k^{-2} spectrum produces the rapid growth of the magnetic field also on large scales; see Appendix 9.2.3, where we demonstrate the tangling of a homogeneous magnetic field by an initial turbulent velocity field with a k^{-2} spectrum. Thus, there is no conflict between these two types of simulations if comparable initial velocity fields are used in both cases.

b) *Phase-transitional seeding*. The initial characteristic scale $L_{E_B(k)}$ in these cases makes the magnetic power spectra evolve in a very different way. Overall, the total amplitude is smaller than in the inflationary cases, as can be observed in Figure 6.6. Nevertheless, the most interesting result is how the characteristic scale defines the evolution at large and small scales. On large scales ($k \lesssim 1\,h\,\mathrm{Mpc}^{-1}$), the magnetic field growth is moderate. The helical seeding shows stronger magnetic growth than the nonhelical seeding. This happens because in the former case the initial magnetic perturbations are correlated on larger scales (see Figure 6.1). It is also possible that helicity leads to larger power on these scales. This is an expected trend in MHD simulations of decaying turbulence where the larger growth is observed for large length scales due to the inverse transfer from small to larger scales; see, e.g., Ref. [76] and Ref. [301]. On the other hand, scales smaller than the characteristic scale, i.e., $k \gtrsim 0.4\,h\,\mathrm{Mpc}^{-1}$ for the helical case and $k \gtrsim 0.9\,h\,\mathrm{Mpc}^{-1}$ for the nonhelical case, respectively, can grow and reach magnetic levels comparable to the inflationary cases. Additionally, we observe that there is a shift of the peak spectra toward smaller scales (at $z \sim 5$) in both cases as more substructure is building up on galaxy-cluster scales ($\sim 1\,\mathrm{Mpc}$).[5] Finally, we also observe magnetic power decay on the peak scales and on the smallest scales at early redshifts ($z > 10$) in both the

[5]It should be noted that after the first shift of the peak, the peak again gradually moves from smaller to larger scales (from $z = 3$); this behaviour is similar to the aforementioned inverse cascade. This trend is more evident for the nonhelical case.

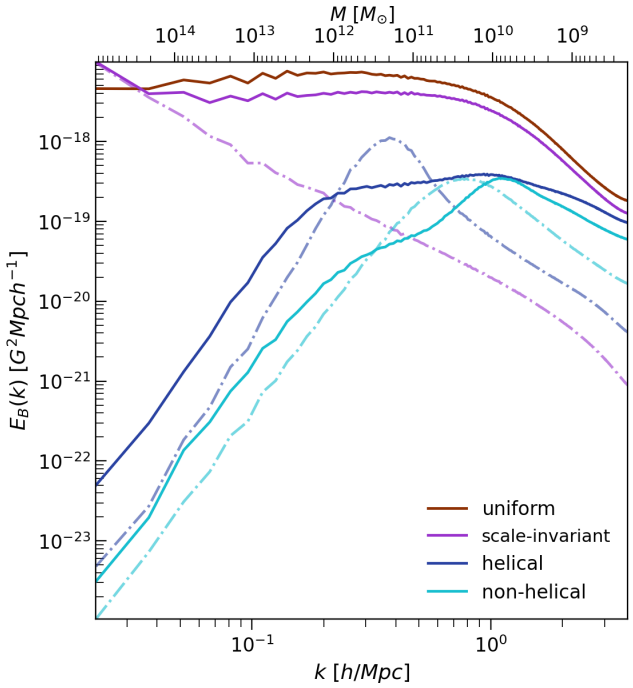

Figure 6.7: Magnetic power spectra for the uniform and stochastic cases. The dashed-dotted lines show the corresponding power spectra at the initial redshift ($z = 50$) and the solid lines at the final, $z = 0$ redshift.

helical and nonhelical cases. In these cases, most of the magnetic energy is initially contained toward small scales while the matter (and density) power spectrum has most of its power contained on larger scales. This limits, for example, the magnetic energy growth in the two cases at early redshifts (see also the discussion at the end of this section).

We compare the initial and final magnetic power spectra with the corresponding linear mass scales for all the models in Figure 6.7. Note that these mass scales should not be interpreted as the masses of the massive objects (e.g., galaxy clusters) since they can only be accepted as an estimation of masses at certain radii that are still in the linear regime (i.e., these would be the largest scales in our simulations, $k \lesssim 0.5\,h\,\mathrm{Mpc}^{-1}$). The difference between the amplitudes of the inflationary and phase-transitional magnetic power spectra is more evident at small wavenumbers. As we mentioned above, in Figure 6.7 the spectra peak of the two stochastic seedings are shifted toward larger wavenumbers. In addition, we see that different phase-transitional seedings are expected to be harder to distinguish at masses $M \lesssim 10^{10}\,M_\odot$, whereas the magnetisation at masses $M \gtrsim 10^{12}\,M_\odot$ is distinguishable for the inflationary and phase-transitional models. The reader may note that the behaviour of the magnetic amplification at different scales is strongly affected by the spectrum peak (or by the coherence scale) at the initial redshift. The role of the peak position will be considered in future work.

The differences between the uniform and scale-invariant spectra for all mass scales is remarkably small. It is only at $3 \times 10^{14}\,M_\odot$ that the amplitude of the scale-invariant spectra is higher than that of the uniform model. Overall, we discern these differences in the amplitude of the power spectrum between the inflationary and phase-transition models to be increased on larger scales ($M \gtrsim 2 \times 10^{10}\,M_\odot$) reaching order of 10^5 difference on mass scales $\gtrsim 10^{14}\,M_\odot$.

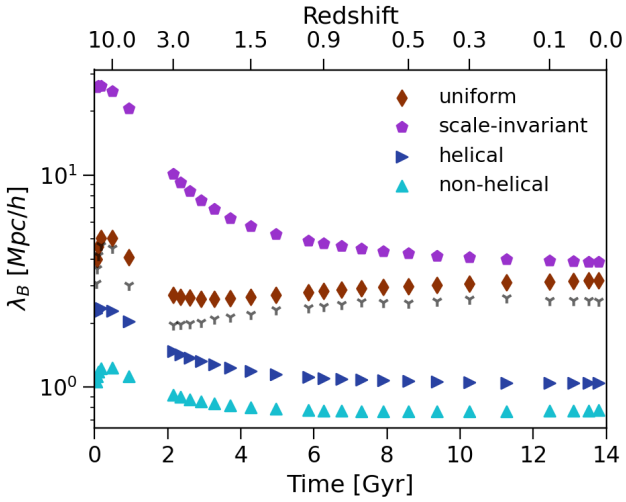

Figure 6.8: Evolution of magnetic correlation length obtained from different magnetic seeding. Gray points show the correlation length computed from the density power spectrum.

In a collapsing magnetised region, field amplification mainly occurs via adiabatic contraction. However, if that region contains a randomly oriented magnetic field, there are two additional things to consider: 1) the cancellation of opposite-polarity fields can reduce the magnetic flux, and/or 2) there could be extra field amplification by turbulent dynamo if the growth rate is faster than the gravitational compression rate (see also Ref. [302] and Appendix A in Ref. [303] for a comparison between uniform and stochastic models in idealised MHD simulations). In our study, shocks that originate during structure formation can additionally affect the magnetic amplification since they can destroy coherence small-scale structures. This can also contribute to decreasing power of the peak scales of helical and nonhelical cases at early redshifts. All these effects explain why in the helical and nonhelical cases we see less efficient amplification on both small and large scales (see Figure 6.6). While all our four cases are affected by the not-well-resolved turbulent motions within the collapsing regions of the cosmic web, the lower magnetic power increase observed in the two phase-transitional cases could be partly attributed to field cancellation (see also discussion below on the correlation length). On the other hand, the stochastic, scale-invariant case develops a nonzero mean field (due to an initial larger correlation length in this case) which makes its evolution very similar to that of the uniform case and less subject to field-cancellation effects. Hence, we observe a larger magnetic field amplification in this case.

Finally, we show in Figure 6.8 the evolution of the magnetic correlation length (Equation (3.37)). It should also be emphasised that for inflationary, uniform magnetic fields, the correlation length at the initial redshift can be ill-defined, because the numerator of Equation (3.37) diverges for $k \to 0$, so this point needs to be excluded. For our nearly scale-invariant field, however, the spectral energy goes to zero for $k \to 0$, and thus the integral does not diverge; see [163] for details.

In all four models, we see an increasing trend at initial redshifts which mostly follows the evolution of the density correlation length. In unigrid Eulerian cosmological simulations, the density power spectrum tends to be more damped at small scales since the gravity forces are smoothed at the grid scale, as noted in Ref. [304]. This slower growth of the smallest scales leads to the increase of the magnetic and density correlation length

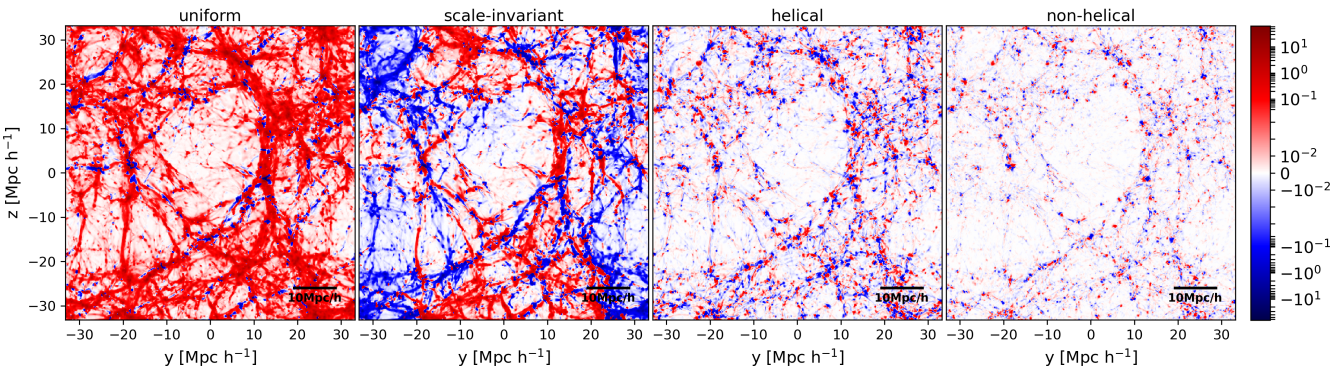

Figure 6.9: Faraday rotation maps from the simulated cosmic web at $z = 0.02$. From top to bottom: uniform, scale-invariant, helical, and nonhelical cases respectively. The color bar shows values in [rad/m^2] and it is linearly scaled in the range $[-0.04, 0, 04]$.

at $z > 10$ in Figure 6.8.

The correlation-length evolution is followed by a decrease ($z \lesssim 10$) in both density and magnetic correlation lengths for all four models. This results from the small-scale modes entering the nonlinear regime of the growth of density perturbations. At this stage, power is transferred from large to small scales. A final increase of magnetic correlation length is only noticeable in the uniform seeding case at $z \lesssim 1.75$. The density correlation length shows a similar trend as the magnetic correlation length in the uniform case, although it shows a slower increase. It should be noted that the latter trend could also be affected by the damped growth of perturbations at small scales because of our limited resolution.

Finally, we see that the correlation length in the uniform case is about twice as large as in the helical and nonhelical cases, and the scale-invariant model shows the largest final correlation length ($\sim 4\ h^{-1}\mathrm{cMpc}$). This is in line with our previous discussion on the discrepancies in magnetic amplification of inflationary and phase-transitional cases.

6.6 Faraday rotation measures

We discussed in Section 1.2.1 that one of the main observational tool for the large-scale magnetic fields is the RM. The total observed RM includes contributions from various magnetised regions along the LOS (see Equation (1.9)), including contribution from the magnetised regions of our own Galaxy. In the recent years, effort has been put into constraining the extragalactic RM, $\mathrm{RM_{IGM}}$ (see e.g., Refs. [14, 15, 305, 306]). Such observations are especially important for constraining the magnetogenesis scenarios.

In Figure 6.9 we show the RM maps of the simulated cosmic web at $z = 0.02$ for different primordial seeding cases. In this section, we use physical quantities, such as physical magnetic field strength, electron number density, and physical length scales. We also note that in our calculation we did not include the Galactic contribution [307]. These maps have been obtained by integrating Equation (1.8) along the x-axis. We checked that the selected axis of projection does not produce differences in the results described in this section. We observe significant differences in the RM maps for the different primordial seeding models. First, we observe more coherent structures in the uniform and scale-invariant seeding cases than in the helical and nonhelical cases. Second, the RM values are highest for the inflationary scenarios and lowest in the helical and nonhelical ones.

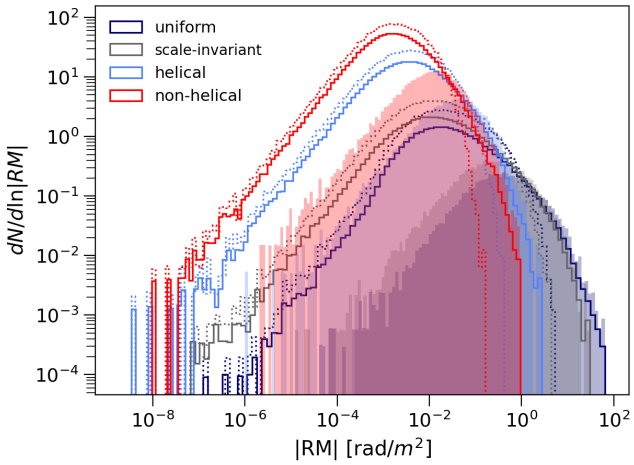

Figure 6.10: Distribution functions of the absolute RM for different seeding models. The dotted lines show the contribution to the total PDF from the regions excluding galaxy clusters while the filled histograms represent contributions from galaxy clusters ($\rho/\langle\rho\rangle \geq 1.3 \times 10^2$).

This result is a consequence of the RM being an integrated quantity. The sum of coherent magnetic fields will give rise to a strong RM signal, which is the case in the uniform and scale-invariant models (see first and second panels of Figure 6.9). On the other hand, the sum of stochastic magnetic fields can cancel out and weaken the RM signal (see third and fourth panels of Figure 6.9). In addition, the RM maps are determined by the total level of magnetisation at this epoch (see Table 6.3). The helical and nonhelical seedings lead to lower magnetisation levels in filaments, as was discussed in Sections 6.5 and 7.3.1. Therefore, this adds to the discrepancy observed between inflationary and phase-transitional models. We also note that uniform seeding leads to higher Faraday rotation than the scale-invariant seeding. This seems to be in agreement with the results that are given in Ref. [253], where the authors explored also a uniform seed field and various seeds described by power laws. Nevertheless, our inflationary results cannot be directly compared to this recent work since they applied a subgrid dynamo model for further magnetic amplification.

In Figure 6.10 we show the corresponding PDFs for the absolute value of RM at $z = 0.02$. We additionally show the PDF for the regions excluding galaxy clusters (dotted lines), and for galaxy clusters with the overdensity criterion $\rho/\langle\rho\rangle \geq 1.3 \times 10^2$ (filled histograms). These criteria were applied before computing the integral defined in Equation (1.8). The distributions accounting for the whole $67.7\,(\,h^{-1}\mathrm{cMpc})^3$ region, as well as distributions excluding galaxy clusters, peak at 1.6×10^{-3}, 4×10^{-3}, 1.2×10^{-2}, and 1.7×10^{-2} rad m^{-2} for the nonhelical, helical, scale-invariant, and uniform cases, respectively. When considering only the highly ionised regions (clusters; $T > 10^6$ K), the PDFs peak at 1.5×10^{-2}, 4.5×10^{-2}, 0.3, and 0.5 rad/m^2 for the nonhelical, helical, scale-invariant, and uniform cases, respectively. We see that the highest RM values are obtained at these highly ionised regions for the four models. As can also be seen in Figure 6.9, the highest values of RM tend to follow the collapsed structures. Similar trends have been observed in other cosmological simulations (see e.g., [252]). In line with Figure 6.9, we find that the highest RM values are observed for the two inflationary models.

In the following, we extend the analysis to a range of redshifts. In Figure 6.11 we show the redshift evolution of the mean and rms statistics of |RM| within different en-

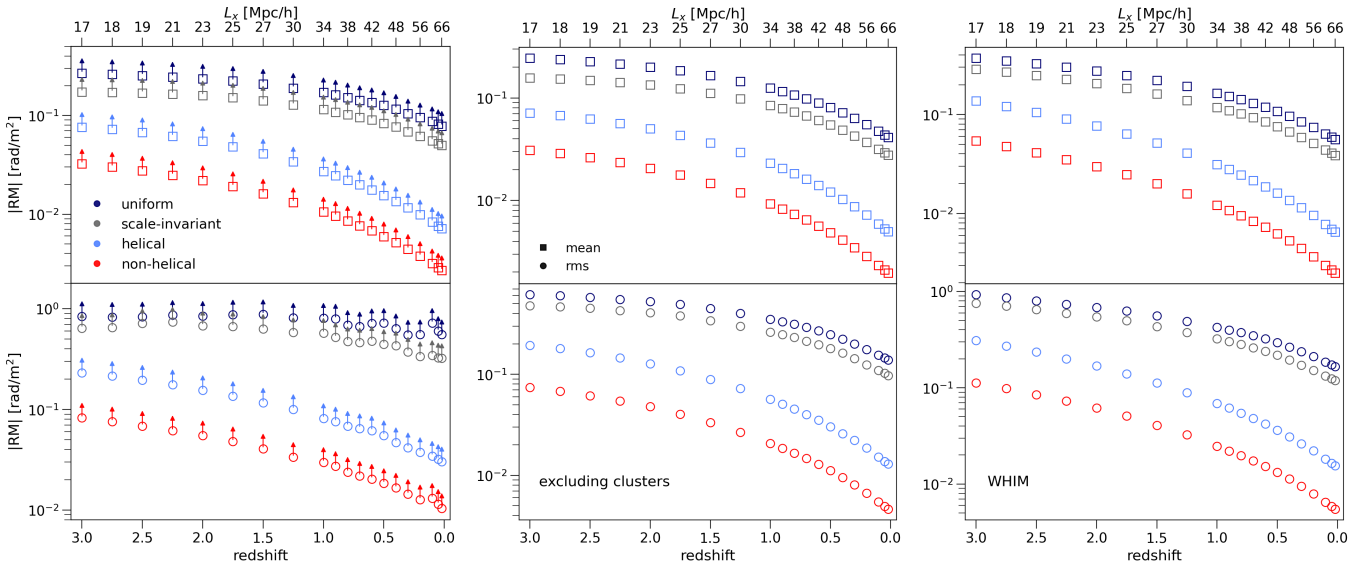

Figure 6.11: Redshift evolution of the mean and rms statistics of the absolute |RM| for the whole simulating volume (first column), for the regions excluding galaxy clusters ($\rho/\langle\rho\rangle < 1.3 \times 10^2$; second column) and for the regions satisfying the criteria for WHIM ($10^5 \leq T \leq 10^7$, $\rho/\langle\rho\rangle < 1.3 \times 10^2$; third column). The upper panels show the mean values and the lower panels show the rms values. Statistics of all these regions exclude the lowest-density regions (satisfying the $\rho/\langle\rho\rangle < 2 \times 10^{-2}$ criterion).

vironments and for different seeding scenarios. We analysed a total of 20 cosmological boxes (corresponding to 20 redshift bins) in a redshift range of $3 \leq z \leq 0.02$. This range is particularly relevant, for example, for the upcoming WEAVE-LOFAR survey [308], where one expects to obtain spectroscopic redshifts for all polarised radio sources detected in the LOFAR Two-meter Sky Survey (LoTSS, [309]) up to $z < 1$. In the first column of Figure 6.11, we show the statistics from the whole simulating box while the second and third columns show the RM statistics in the regions excluding galaxy clusters and in the warm-hot intergalactic medium (WHIM), respectively. The regions excluding galaxy clusters imply the same criterion as in Figure 6.10, while for the WHIM region we additionally set the temperature criterion $10^5\,\mathrm{K} \lesssim T \lesssim 10^7\,\mathrm{K}$. Due to the cosmological expansion, it is expected that the mean and rms RM will decrease with time. This is in particular true for the lowest-density regions of the cosmic web where there is almost no turbulent amplification (see the second and third columns of Figure 6.11). As we can see, the highest rms and mean |RM| values are obtained when including cluster environments and in the WHIM, which are the densest regions. The first is consistent with previous numerical work, where it has been found that the resulting RM is dominantly contributed by the density peaks along the LOS (see e.g., Refs. [310, 311]). Note that in these regions our reported RM values are lower than the typical observed values due to our limited resolution (see discussion in Section 6.7). RMs of hundreds rad m^{-2} have been observed in clusters (see Ref. [312] for a sample of galaxy clusters). Since clusters are especially underresolved in our simulations, the RM values in these regions should be interpreted only as lower limits.

We characterise the $|\mathrm{RM}|_{\mathrm{rms}}$ evolution by fitting the data to the following equation: $|\mathrm{RM}|_{\mathrm{rms}} = \mathrm{RM}_0(1+z)^{\alpha}$. We show the fitted values for each environment for the four models in Table 7.3.4. Since the definition of RM (see Equation 1.8) includes the proper

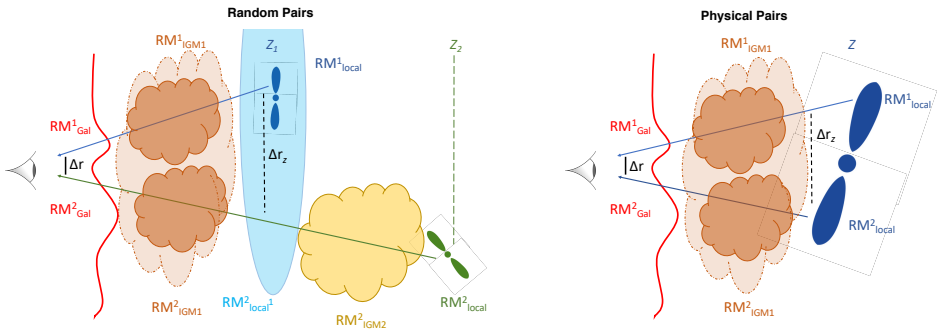

Figure 6.12: Simple illustration of random and physical pairs used in the RM measurements [14, 15]. The $\mathrm{RM_{Gal}}$ denotes the contribution to the total RM from the rotation effect caused by Galactic magnetic field. The $\mathrm{RM_{local}}$ denotes the Faraday rotation contribution that is caused by the source magnetic field itself. The figure credit: Ref. [14].

values of the electron density, magnetic field, and integration path length, we expect it to scale as RM$\sim (1+z)^2$, with $\alpha = 2$. However, as we can see from Table 7.3.4, $\alpha < 2$ for all environments in the uniform and scale-invariant case; i.e., the decrease of RM values with redshift will be slower in these scenarios. This means that magnetic fields along with density do not only decrease in these regions, as it is expected by the expansion of the Universe but are subject to amplification.

Recently, Ref. [14] and Ref. [15] presented a new approach in order to isolate the extragalactic RM variance. The method relies on comparing pairs of extragalactic radio sources and computing the difference in the ΔRM between two types of pairs. Following Refs. [14, 15], the statistical results come from computing the $\Delta\mathrm{RM} = \mathrm{RM}_1 - \mathrm{RM}_2$ for sources at the same redshift (named as physical pairs), e.g., double-lobed radio galaxies, and from sources at different redshifts (named as random pairs). Here, RM_1 and RM_2 are the total RMs that are measured for each source being within the physical or random pair. Figure 6.12 illustrates contributions in the total RM from the intervening IGM for the random pairs (left panel) and physical pairs (right panel). Since random pairs are background sources at different redshifts, one expects larger ΔRM between such sources. After analysing the difference between physical and random pairs, the authors of Ref. [15] concluded that the excess Faraday rotation contribution found for the random pairs has an upper limit of 1.9 rad m^{-2}; they placed an upper limit of 4 nG for a PMF. A similar analysis at 1.4 GHz and in a redshift range of $0 < z < 1$ was done in Ref. [14], where the authors obtained an excess contribution for the random pairs of 10.3 rad m^{-2}. In this case, the authors placed an upper limit of $\sim 37\,\mathrm{nG}$.

In order to compare our simulation results with the results of these recent work, we would have to carry out a careful study of stacking cosmological boxes (see Ref. [313] and Ref. [314], for pioneering work) and defining light cones before integration (see Refs. [253, 311] in the context of RM). Such a study is out of the scope of this project and we leave it for future work. Nevertheless, we can give a first-order estimate on the RM difference by using the information in Figure 6.11.

We considered the $|\mathrm{RM}|$ distribution function of the simulation box to be representative of each redshift. In this way, we select the variance of the distribution to be the representative value at each redshift. We analysed a total of 20 redshift bins up to $z = 3$, where we obtained 190 different combinations of redshift pairs. Note that here we do not

take into account the spatial distribution of possible sources within each simulation box. Instead we assume the PDF statistics to be representative of the simulation box at that redshift. We refer the reader to Appendix 9.2.4 for a word on the distribution of sources as a function of redshift.

We compute the variance in the environment where we exclude the regions of galaxy clusters (see second column of Figure 6.11) and the WHIM environment (see third column of Figure 6.11). These two environments are less affected by our low resolution. We are also interested in these environments because LOFAR is not expected to detect polarised sources from intervening clusters [315]. As a second step, we compute the average variance between each selected redshift (random) pair, i.e. taking into account all redshift bins in between the pair. Once this is done for all the 190 pairs, we compute the rms of all the variances. This procedure yields an rms upper limit in the WHIM of 0.7, 0.6, 0.3, and 0.2 rad m^{-2} for the uniform, scale-invariant, nonhelical, and helical cases, respectively. The environment where we only exclude galaxy clusters gives similar values: 0.6, 0.5, 0.3, and 0.2 rad m^{-2}, respectively. These RM values are marginally lower than the results reported at 144 MHz in Ref. [15] or in Ref. [14]. After analysing the difference between physical and random pairs, the authors concluded that the excess Faraday rotation contribution between random pairs has an upper limit of 1.9 rad m^{-2}. This work places an upper limit of 4 nG for a PMF. A similar analysis at 1.4 GHz and in a redshift range of $0 < z < 1$ was done in Ref. [14], where the authors obtained an excess contribution between random pairs of 10.3 rad m^{-2}. In this case, the authors placed an upper limit of $\sim 37\,\mathrm{nG}$. Our rms RM values suggest that an initial magnetic seed larger than $1\,\mathrm{nG}$ for the four different seedings is required to meet these particular observational RM upper limits. We can give crude estimates of the initial magnetic field strength by asking ourselves which initial magnetic field strength is needed to reach the upper limit of 1.9 rad m^{-2} for all our models: the results of the uniform, spatially homogeneous field (the Mukohyama model) and the scale-invariant, inflationary field would suggest an initial magnetic field strength of $\sim 3\,\mathrm{nG}$. This is comparable to LOFAR results and remains below the upper limits obtained in Ref. [15] and in Ref. [14]. Nevertheless, this crude approach alone cannot strictly rule out the $\sim 1\,\mathrm{nG}$ normalisation (see discussion below); the phase-transitional models would allow for an even larger initial magnetic seed, namely a magnetic field strength of a primordial stochastic seed (helical or nonhelical) ~ 6 nG. These values could be in agreement with CMB constraints of helical ($\sim 5.6\,\mathrm{nG}$) and nonhelical ($\sim 4.4\,\mathrm{nG}$) PMFs (see e.g., [21]). Yet, these high values conflict with recent Planck, Atacama Cosmology Telescope (ACT) and South Pole Telescope (SPT) constraints of a $\sim 0.05\,\mathrm{nG}$ PMF [316]. It is important to stress that a one-to-one comparison with these recent RM observations is not strictly possible since the reported upper limits are also influenced by environmental selection effects. In this sense, we can only conclude that our first-order approximation RM analysis favours more inflationary PMFs than phase-transitional PMFs. While future simulations with a more sophisticated RM analysis could improve our predictions, future observations that will better isolate the RM signal from the diffuse WHIM and/or voids and filaments will play a decisive role in discriminating PMF models.

We expect great advances with LOFAR in the coming years. There has been significant progress in overcoming challenges in observations by using the ionospheric RM correction errors techniques (see e.g., Ref. [317]. These techniques have significantly improved and will be crucial for the accurate calibration of not only the next LOFAR surveys but also for the SKA. Indeed, the SKA-Low and SKA-Mid (see Ref. [318] and references therein) is expected in coming years to provide stronger constraints on the magnetisation

Model	Environment	RM_0 (rad/m^2)	α
Uniform	Exc. clusters	0.15	1.12
	WHIM	0.17	1.26
	All	0.59	0.31
Scale-invariant	Exc. clusters	0.11	1.20
	WHIM	0.12	1.36
	All	0.34	0.61
Helical	Exc. clusters	0.01	2.03
	WHIM	0.02	2.21
	All	0.03	1.15
Nonhelical	Exc. clusters	0.01	2.07
	WHIM	0.01	2.22
	All	0.01	1.52

Table 6.3: Fitted values of $|\mathrm{RM}|_{\mathrm{rms}} \propto \mathrm{RM}_0(1+z)^{\alpha}$ of Figure 6.11 for different environments of our simulations.

of the Universe. The increased expected number of polarised sources and knowledge of spectroscopic redshifts will enable us to make better comparisons with cosmological simulations. We expect that these advances can further help us to distinguish between the possible origins of cosmic magnetism. The present work shows that a scale-invariant and phase-transitional helical and nonhelical models still cannot be rejected. In future work, we will study a more extended range of initial conditions in parallel with the stacking technique and definition of light cones to put more stringent constrains.

6.7 Numerical aspects

The spatial resolution adopted in the present simulations place limitations on our results. Our resolution is not sufficient to resolve, for example, the additional magnetic amplification within galaxy clusters [44, 45, 47]. Nevertheless, in Appendix 9.2.1 we show that our results are robust at least on scales $\gtrsim 1\,\mathrm{Mpc}\,h^{-1}$. We have checked the convergence of the magnetic energy power spectrum in the whole simulation box with increasing resolution (see Figure 9.1 in Appendix 9.2.1). As expected, increasing the resolution results in higher power at higher wavenumbers. On the other hand, we have also checked the trends of the magnetic field compared to the density for the phase-transitional helical and inflationary uniform cases at different resolutions (see Figure 9.2 in Appendix 9.2.1 and corresponding discussions). In the uniform scenario, there is no substantial change in the overall trends at higher resolution. On the other hand, the phase-transitional helical case shows subtle differences in filaments and voids, while the main differences are observed in the overdensity regions corresponding to galaxy clusters. This seems to indicate that our results on the global properties of the filament and void regions, as well as the differences between the primordial models in those regions, are robust for the present goal of this work.

We also tested the dependence of our RM results on the adopted spatial resolution in

the Appendix 9.2.1. We show the distribution of RM at $z = 0.02$ at different resolutions for the uniform scenario in Figure 9.3. At double resolution, the |RM| values converge for the environment excluding clusters, while for the cluster environments we still see higher (lower) RM values at the high-end (low-end) tail of the distribution. We expect the same follows for the stochastic scenarios.

The Dedner cleaning algorithm used in our work has an intrinsic dissipation compared to the CT scheme (see Section 5.2). This reduces the magnetic spectral bandwidth to keep the numerical divergence under control (see Ref. [319]). The Dedner formalism has been tested to be robust, accurate and to converge quickly to the right solution for most idealised test problems (see e.g., Refs. [113, 320, 321] and for other more realistic astrophysical applications Refs. [322–324], as long as the resolution is conveniently increased.

As mentioned in Section 5.3, we neglected physical processes associated with radiative gas cooling, chemical evolution, stellar and AGN feedback. In this way, we can solely focus on the effects of different primordial magnetic seeding through LSS formation. However, these unaccounted processes, are known to pollute the rarefied regions of the cosmic web and, thus, they can potentially lower the possibility of detecting the imprints of different PMFs (see e.g., Ref. [252]). We refer the reader to Ref. [53] for a comparison between the predictions of primordial and astrophysical seeding scenarios of magnetic fields with the `Enzo` code.

In addition, as an important caveat, we note the effect of different Riemann solvers on our results. The most diffusive Riemann solver LLF [266] of `Enzo` affects the evolution of magnetic energy in the tested nonhelical case and decreases it by factor of 2 at final redshifts (see Appendix 9.2.2 for more details). Consequently, the magnetic field and temperature distributions in the void regions also show lower values at $z = 0.02$ for the phase-transitional cases. In the uniform case, on the other hand, we do not observe changes in temperature and magnetic fields due to the LLF solver. We also checked the effect of the DEF used in our simulations, which controls thermal energy in highly supersonic bulk flows. We verified that the DEF does not affect the magnetic field distribution neither in the uniform case nor in the stochastic, nonhelical case. This holds for both Riemann solvers, LLF and HLL. Nevertheless, the DEF affects the temperature distribution, as expected. We caution the reader on the interpretation of the regions where shocks and discontinuities are created by the extreme gravitational forces. However, we do not expect these regions to be statistically significant to modify the obtained trends from our simulations.

The initial conditions used in the simulations, do not account for the effect of magnetised perturbations on the initial matter power spectrum (see, e.g., Refs. [72–74], where the authors have taken this effect into account), which would give us a self-consistent view of the cosmological initial conditions. Nevertheless, it has been recently shown that such effects will only have an impact on smaller haloes and on scales $\sim k > 1\,h$ Mpc^{-1}. Therefore, we would not expect significant changes in our results at the largest and most massive components of the cosmic web.

Finally, in our work we have excluded the nonideal MHD processes, meaning that the viscous and resistive dissipation are not modelled realistically and, therefore, the magnetic Prandtl number, i.e., the ratio of kinematic viscosity and magnetic diffusivity, is effectively unity. This approach is reasonable enough given the existing uncertainties and the difficulties in the characterisation of galaxy clusters (see e.g., Refs. [325, 326]) and larger cosmological scales. Furthermore, the ideal MHD description allows us to easily

compare our work with previous work (see e.g., Refs. [79, 253, 327]). Studying higher Prandtl numbers is out of the scope of this work.

6.8 Conclusions

In this work we have investigated the evolution of PMFs through the formation of LSS. For the first time, we have compared inflationary and phase-transitional initial seed magnetic fields with cosmological MHD simulations. We have explored four types of initial magnetic seeds: (i) spatially homogeneous (uniform) and (ii) statistically homogeneous (scale-invariant) magnetic fields generated in an inflationary epoch, and (iii) helical and (iv) nonhelical magnetic fields representing a phase-transitional scenario. In the latter three models the initial magnetic spectra reflect the physics of the early Universe when the magnetic seed develops Kolmogorov-like turbulent spectra through its MHD decay, while the former case mimics a primordial magnetogenesis according to the Mukohyama model [56].

The main results of our work can be summarised as follows:

- *The role of the initial magnetic field strength*. A higher normalisation of the initial magnetic field leads to higher magnetic field values at later redshifts. However, the overall trend of the distribution of final magnetic fields in different cosmic environments is not affected by the amplitude of the initial seed field. Regarding the temperature distribution, we note that phase-transitional seedings (nonhelical case) may lead to extra heating in the void regions as a result of possible turbulent decay of these fields. In addition, the higher (initial $\geq 0.5\,\mathrm{nG}$) magnetic field realisation reveals larger differences between the inflationary and phase-transitional models. This suggest that an impact of the stronger initial seed fields will be imprinted on rarefied cosmic regions. Hence, both the strength and topology of the seed fields will be of notable relevance for the studies accounting for the effects of magnetic fields on the reionization history of the Universe [272, 292].
- *Traces in the cosmic web*. Phase-transitional and inflationary scenarios lead to variations in the final magnetic field distribution of the cosmic web. The magnetic amplification in the inflationary models tends to follow the law of adiabatic gas contraction in voids (partially) and filaments, while a deviation from this law is evident in the phase-transitional models. The overall magnetisation of galaxy clusters and bridges as well as of voids in the inflationary models can be orders of magnitude higher than in the phase-transitional scenarios, although the differences between the models on the galaxy clusters' and bridges' scales will be a subject of our future study (and should be confirmed with higher resolution runs). Discernible differences (with a lower magnitude) between the seeding scenarios are also observed in filamentary structures, where again inflationary seed fields show the largest magnetic amplification.
- *Possible inverse cascade*. The characteristic peak of the magnetic power spectra in the phase-transitional helical and nonhelical cases shifts toward small scales at late redshifts, $z < 6$. This means that, during this epoch, preferred scales due to structure formation would initially quench the energy transfer from small to large scales. At later stages, $z < 3$, we observe a shift of the peak spectrum from small to large scales in the nonhelical case without an increase of correlation length, though. Therefore, our results cannot unambiguously confirm the existence of an inverse cascade.

- *Magnetic correlation length*. The final correlation length in the inflationary seedings is larger than that in the phase-transitional seedings (reaching ~ 3, 4, 1, and $0.8\,\mathrm{Mpc}\,h^{-1}$ in the uniform, scale-invariant, helical, and nonhelical models, respectively). Previous modelling of PMFs in the early Universe (in the radiation-dominated epoch) showed the same trend: inflationary, scale-invariant scenarios lead to coherent magnetic structures on larger scales than in the phase-transitional cases [24, 163, 216]. We found that the final magnetic correlation length in the phase-transitional cases is strongly correlated with the initial peak spectrum, limiting the magnetic growth at selected scales of the cosmic web.
- *Uniform versus stochastic inflationary models*. The late ($z > 6$) evolution of spectral magnetic energy of an inflationary, scale-invariant case at scales $\lesssim 10\,\mathrm{Mpc}\,h^{-1}$ shows similar amplification as the inflationary uniform case. A uniform, homogeneous seed magnetic field that is customary to use in cosmological MHD simulations is a good representation of a scale-invariant magnetic field on scales smaller than $\sim 29\,\mathrm{Mpc}\,h^{-1}$ at $z = 0.02$.
- *Nonhelical versus helical phase-transitional models*. The spectral evolution of the phase-transitional helical and nonhelical models are similar at all wavenumbers. However, the helical model exhibits more amplification as a result of larger initial correlation length and power on a characteristic scale than in the nonhelical scenario. We have shown that, within the limitations of our modelling, it will be hard to distinguish observationally between helical and nonhelical scenarios.
- *RM predictions*. Significant differences are observed in Faraday rotation measure maps for different PMF models. These differences arise both in the collapsed objects and in the low-density regions of the cosmic web. We computed the rms |RM| excess coming from random redshift pairs ($z \leq 3$) for the regions excluding galaxy clusters and the WHIM. RM values for all the models are lower than expected from the recent observations reported at 144 MHz [15]. Our RM analysis favors inflationary seed fields with larger magnetisation levels in filamentary structures.
- *Non-Gaussianity*. We find non-Gaussian trends in the magnetic field PDFs for both inflationary and phase-transitional seedings. This is also imprinted on the distribution functions of the absolute RM, where all models show deviation from a log-normal distribution. The low-end tail ($10^{-12} - 10^{-10}$ G) of the magnetic field PDFs is similar for all models; on the contrary, we observe larger differences between the models in the RM distribution function for both the low- ($10^{-8} - 10^{-5}$ rad m^{-2}) and high-end tails ($10^{-1} - 10^{2}$ rad m^{-2}) of the PDFs.

In summary, our results indicate that phase-transitional and inflationary PMFs lead to different realisations of the magnetised cosmic web (retaining the information of magnetic initial conditions on the largest scales of the Universe). The differences can potentially be probed observationally. The Faraday rotation measures from our simulations manifest the traces of the initial magnetic seeding. A stronger and more correlated RM signal is expected from inflationary scenarios as a result of larger initial correlation lengths and higher final magnetisation levels in filaments from these scenarios. In future work we will complement our analysis by stacking the cosmological boxes and producing light cones to give more realistic estimates of RMs. Future observations (e.g., SKA) will detect the RM signal over a large extent of the sky and have the potential of unravelling the origin of magnetic fields on filamentary scales. Then the results of future work can be readily compared to those observations probing the large-/small-scale nature of the seed magnetic fields.

Finally, future numerical work related to high-energy gamma-ray propagation in cosmic voids (for relevant studies, see, e.g., Refs. [53, 102, 327] and Ref. [103] for a recent work) will be relevant to probe the seed magnetic fields studied in our work. It is not clear a priori what kind of topology of void magnetic fields is responsible for the suppression of the secondary gamma-ray flux [101]. Therefore, studying inflationary and phase-transitional scenarios in the context of the magnetisation of cosmic voids could help to more stringently discriminate between the competing magnetogenesis scenarios. This, in turn, will help us understand the effects of such fields on the reionization history of the Universe and first structure formation (see e.g., Refs. [251]). Our work gives a first step and a novel approach in the search for the origin of cosmic magnetic fields. Future effort in combining state-of-the-art MHD cosmological simulations and more realistic initial magnetic field conditions will be needed to explore the role of the primordial fields on galaxy-cluster scales and down to smaller scales.

Chapter 7

PMFs in Galaxy Clusters

In this chapter we study the evolution of PMFs on galaxy cluster scales. We are interested in the non-linear growth of the field and whether it can erase the imprints of different PMFs in the ICM. We show results from our paper:

- Mtchedlidze, S., Domínguez-Fernández, P., Du, X., Schmidt, W., Brandenburg, A., Niemeyer, J., Kahniashvili, T., "Inflationary and phase-transitional primordial magnetic fields in galaxy clusters", *ApJ* 944, 100 (2023).

I confirm the sole contribution to the paper and responsibility for the following: participation in the study conception and design, running of simulations and data analysis, interpretation of the results and the draft manuscript preparation.

7.1 Physical model

In this work, we explore two phase-transition-generated PMFs characterised by a Saffman and a Batchelor spectrum, and two inflationary-generated PMFs characterized by a turbulent spectrum and by a Dirac delta function (in Fourier space, corresponding to a uniform magnetic field). The latter model serves as a comparison to our simulations with other cosmological simulations where a uniform seed magnetic field is commonly assumed as an initial condition (see, e.g., Refs. [45, 252, 254]). Nevertheless, as already discussed before, the physical generation of a uniform seed magnetic field in the early Universe has been predicted to be plausible under specific conditions by Ref. [56]. We again refer to this model as the Mukohyama model.

We adopt these models as our initial magnetic conditions despite our relatively low initial resolution of $312.5\ h^{-1}\mathrm{ckpc}$ (see below). We note that this initial resolution may not be enough for resolving the magnetic field coherence scales expected from theory or small scales dominated by the turbulent spectra (see Section 4.2).

7.2 Simulations

In this study, we simulated the formation of a galaxy cluster employing the AMR technique of `Enzo` (see Section 5.4) We followed two steps for solving the galaxy cluster: (1) a *global* AMR simulation, where we identified a list of fairly resolved haloes and (2) a *local* AMR or 'zoom-in' simulation, where we applied several levels of AMR in a selected region where the cluster forms. In both setups the refinement is triggered based on baryon, $f_{\rm b}$, and dark matter, $f_{\rm DM}$, overdensity thresholds. These parameters ensure refinement when the gas (DM) mass in a cell reaches a factor of $f_{\rm b}$ ($f_{\rm DM}$) times the mean baryonic (DM) mass expected in a cell at the root grid level [113]. In this study, we use a nominal refinement factor of 2 between the parent grid and its subgrid which is the commonly used value for cosmological simulations (see Ref. [113] for more details). In the global AMR simulations, we set $f_{\rm b} = f_{\rm DM} = 4$ and we use 4 levels of refinement activated in the whole, $(80\ h^{-1}\mathrm{cMpc})^3$ simulating box. We used a root grid of 256^3 cells and 256^3 dark matter (DM) particles each of mass $m_{\rm DM} = 3.34 \times 10^9 M_\odot$. The initial and final spatial resolutions are $312.5\ h^{-1}\mathrm{ckpc}$ and final $19.5\ h^{-1}\mathrm{ckpc}$, respectively. Based on this simulation, we produced a halo catalog using the *yt* halo finder [328]. The halo finder identifies groups of linked DM particles based on the Eisenstein and Hut [329] algorithm. The galaxy cluster selected for the present work is among the most massive clusters from our halo catalog (see Section 7.2.2 for a detail description of the cluster). Next, we re-simulated the selected galaxy cluster in the $(80\ h^{-1}\mathrm{cMpc})^3$ simulation box by centering our simulation box where the galaxy cluster forms. We selected a volume of $(20\ h^{-1}\mathrm{cMpc})^3$ and used 7 levels of refinement. In this case, the refinement was triggered on $f_{\rm b} = 0.1$ and $f_{\rm DM} = 4$ refinement factors giving us a final maximum spatial resolution of $2.44\ h^{-1}\mathrm{ckpc}$.

The selection of the overdensity factors, f_i (where 'i' indicates baryons or DM), is important and depends on the problem being addressed. In this work, the grid refinement thresholds are chosen in order to solve the turbulent motions in the ICM which are crucial for the seed magnetic field amplification. Mergers and accretion events driven by gravitational dynamics are the main agents of turbulence in the ICM. Therefore, low overdensity thresholds for both gas and DM ensure resolving low-mass gas substructures and DM halos (as discussed in Ref. [261]) and thus, can maintain turbulence in the ICM [280]. Note

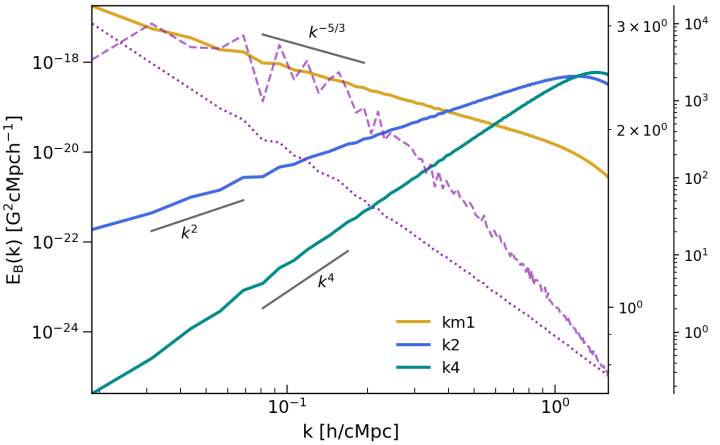

Figure 7.1: The initial magnetic power spectra for the stochastic setups and velocity (purple dotted) and density (purple dashed) spectra shown for the run with the uniform model. The first and second secondary axis showed on the right correspond to the density and velocity spectra in $(10^{63}\,\mathrm{g/\,cm^3})^2\,h^{-1}\mathrm{cMpc}$ and $10^8\,\mathrm{cm^2/\,s^2}\,h^{-1}\mathrm{cMpc}$ units, respectively. The initial power spectra of the baryon and DM perturbations are nearly indistinguishable at the scales resolved by our resolution. The only difference between these two spectra is in their amplitude.

Scenario	Model	Simulation ID	$\langle B_0^2\rangle$ (nG)^2	$\langle B_0\rangle$ [nG]	$B_{1\mathrm{Mpc}}$ [nG]	λ_B h^{-1} cMpc
inflationary	(i) uniform	u	0.99	0.99	—	—
	(ii) scale-invariant	km1	0.99	0.92	0.92	33.04
phase-transitional	(iii) Saffman	k2	0.99	0.92	0.92	1.07
	(iv) Batchelor	k4	0.99	0.92	0.92	0.85

Table 7.1: Initial conditions for the magnetic field. The correlation length and mean value of the smoothed (smoothed on $1\,h^{-1}\mathrm{cMpc}$ scale) magnetic field are denoted by λ_B and $B_{1\mathrm{Mpc}}$ accordingly, and $\langle B_0^2\rangle$ and $\langle B_0\rangle$ are the mean of the initial magnetic field energy and the initial magnetic field strength respectively

that lower refinement factors significantly increase the number of refined grids and one has to compromise between the final resolution and the computational cost. For this purpose, we used a higher value of the f_{DM} compared to the f_{b} factor. This selection closely follows [45], where the authors have proven that the impact of an increased DM resolution is only minor on the final magnetic field distribution (see Figure 17 in Ref. [45]). Indeed, we will show in Section 7.2.2 that the chosen refinement thresholds result in large turbulence filling factors in our simulated ICM.

7.2.1 Initial conditions

We study four different realisations of the simulated galaxy cluster. Our simulations differ only in the initial magnetic field configuration. We assume only non-helical magnetic fields (at the initial redshift $z = 50$) that have the same total magnetic energy (see Table 7.2). The four models are:

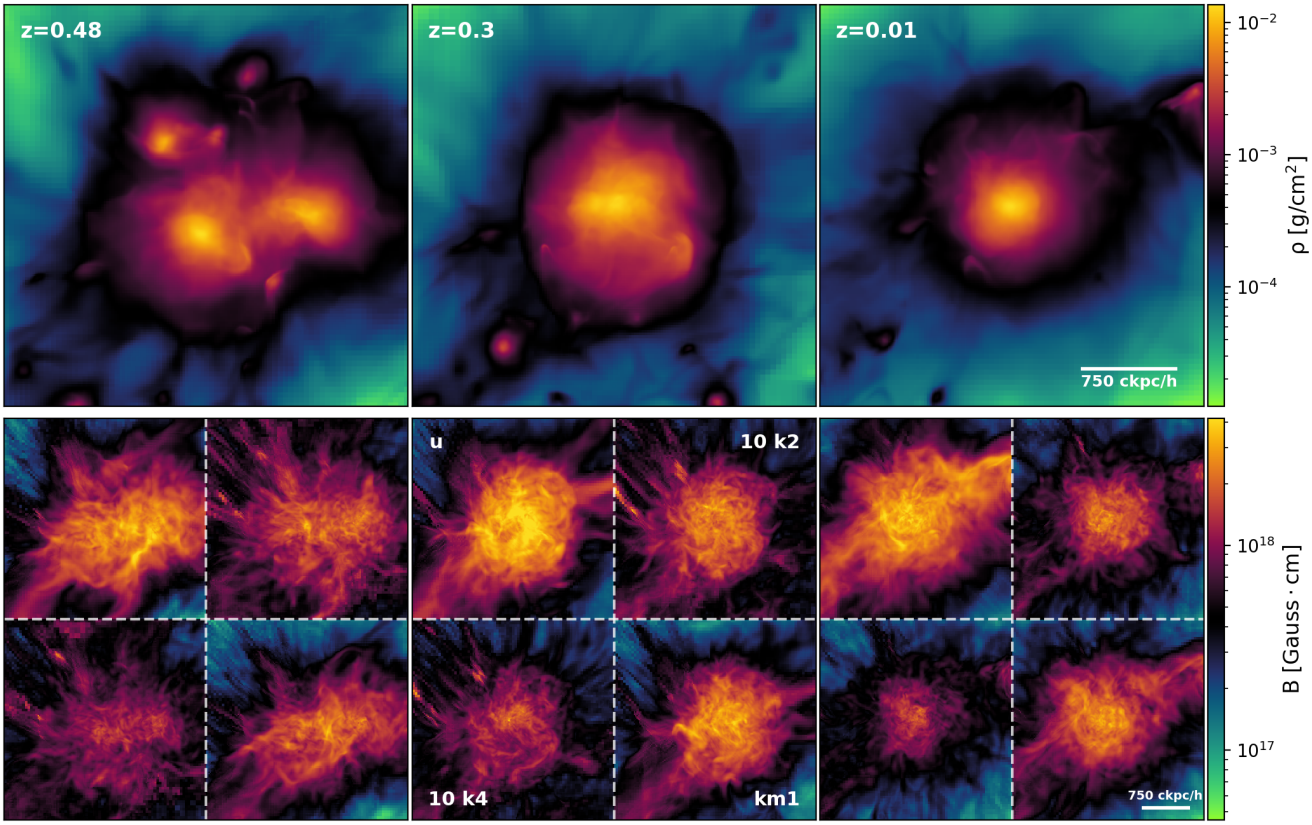

Figure 7.2: Projected maps of gas density (top panel) and magnetic field from a $(3\,h^{-1}\mathrm{cMpc})^3$ box for different seeding scenarios (bottom panel) and at different stages of the cluster evolution. Left, middle, and right panels show projected fields at the merging ($z = 0.48$), post-merger ($z = 0.3$) and relaxing ($z = 0.01$) states, correspondingly. Magnetic field projections for the Batchelor and Saffman models are normalised by a factor of 10.

(i) Uniform (spatially homogeneous; constant) field; corresponding to an inflationary magnetogenesis scenario (the Mukohyama model [56]).

(ii) Scale-invariant field: stochastic, statistically homogeneous PMF (with a turbulent spectrum) corresponding to an inflationary scenario.

(iii) Saffman model: a stochastic, phase-transition generated PMF which has a Saffman spectrum.

(iv) Batchelor model: the same stochastic setup as (iii), but with a Batchelor spectrum.

The initial conditions (ii)–(iv) were again produced with the PENCIL CODE [288]. Even though magnetic initial conditions in this study are different from what have been used in Chapter 6, the procedure of producing them is the same. See Appendix 9.1. The initial magnetic power spectra for these stochastic setups are shown in Figure 7.1.

7.2.2 Selected cluster

The selected cluster from our two-step simulations can be seen in Figure 7.2. The total mass of our cluster, $2.39 \cdot 10^{14} M_\odot$, is comparable to the masses of some observed galaxy

Radius $[h^{-1}\mathrm{cMpc}]$	Mass $[10^{14} M_\odot]$	$E_{\mathrm{tot}} = E_{\mathrm{kin}} + E_{\mathrm{th}}$
$R_{500} = 0.50$	1.14	0.15
$R_{100} = 1.01$	1.86	0.16
$R_{\mathrm{vir}} = 1.54$	2.39	0.16

clusters such as Abell 3527 (see e.g., Ref. [330]) or the recently studied Ant cluster [1]. We summarise the most important parameters of our simulated cluster in Table 7.2.2.

The formation history of a galaxy cluster fully determines the amount of amplification of the seed magnetic field. Our selected cluster undergoes a series of mergers and its evolution can be characterised by three phases: (1) at the early stage of formation, $z \lesssim 0.7$, it continuously grows by several accreting minor merger events; (2) in the redshift range 0.7 to 0.3, a major merger takes place with a mass ratio of 1.2 between the main and secondary clusters (within R_{500} radius), and (3) at late redshifts, i.e., $z < 0.3$, it enters into a relaxing state. In Figure 7.3 we show the mass accretion history of the cluster in the redshift range $1.5 > z > 0$. The mass of the cluster is computed within R_{vir} and we show its evolution for the uniform model. We indicate the major merger phase with a shaded grey area ($\sim 2\,\mathrm{Gyr}$ timescale) in Figure 7.3. During this phase, we observe a steep growth of the total mass increasing by a factor of ~ 2.

Mergers of clusters play a key role in shaping the properties of the ICM by injecting turbulence. To characterise the turbulence in our simulated galaxy cluster, we followed the recipe proposed by Ref. [282]. In that work, the authors used the vorticity modulus as an indicator of the velocity fluctuations and its volume filling factor f_ω as a proxy for the turbulent state of galaxy clusters. In detail, the procedure consists of flagging a cell as "turbulent" if it satisfies the criterion (see Ref. [282, 331] and references therein)

$$\omega_{\mathrm{vort},i} > N/t_{\mathrm{age}}, \tag{7.1}$$

where $\omega_{\mathrm{vort},i}$ is the vorticity in the ith cell, t_{age} is the age of the Universe at redshift z, and N is the number of eddy turnovers, respectively. Following [282], we set $N = 10$. Finally, the volume filling factor f_ω is the volume fraction satisfying Equation (7.1). The authors find that f_ω is substantial both in the core and outskirts of their simulated galaxy cluster reaching $f_\omega > 90\%$ and $f_\omega > 60\%$, respectively. In the bottom panel of Figure 7.3, we show the evolution of the volume filling factors computed for the core and outskirt regions of our simulated galaxy cluster. The volume filling factors are shown to be also substantial, with percentages larger than 90% in the core region and 60% in the outskirts. We note that we obtain similar results as Ref. [282], even though our numerical setups differ. For example, their simulations use 8 AMR levels triggered by spatial derivatives of the velocity field to reach a final maximal resolution of $7.8\,h^{-1}\mathrm{cMpc}$. Additionally, they make use of a subgrid scale model that is based on the Germano [332] formalism to account for unresolved turbulent motions in the ICM; see also Ref. [333]. Thus, our volume filling factors along with high final resolution of $2.44\,h^{-1}\mathrm{ckpc}$, show that our numerical setup is adequate for capturing turbulent motions in the simulated galaxy cluster.

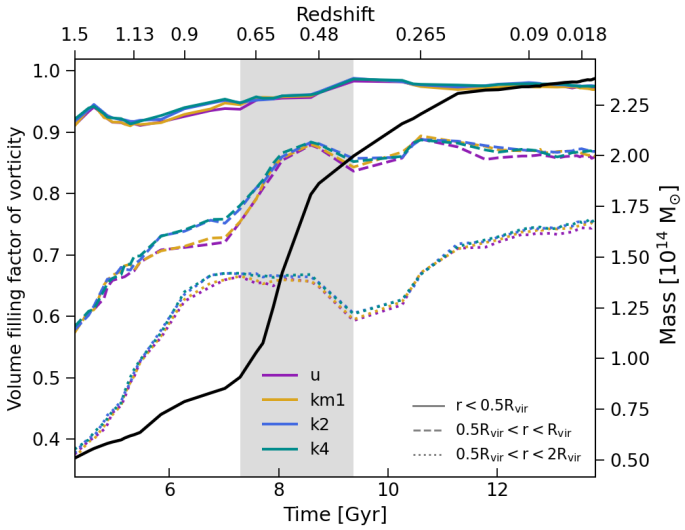

Figure 7.3: Time evolution of the total virial ($r = R_{\rm vir}$) mass (black solid line) and vorticity volume filling factor for the cluster core (solid lines) and the outskirts enclosing a spherical shells in: $0.5\,R_{\rm vir} < r < R_{\rm vir}$ (dashed lines) and $0.5\,R_{\rm vir} < r < 2\,R_{\rm vir}$ (dotted lines).

7.3 Results

7.3.1 General properties

We start our analysis by giving a qualitative view of the density and magnetic field distribution in the simulated galaxy cluster. In Figure 7.2 we show the projected density and corresponding magnetic field distribution for different seeding scenarios. The projections are extracted from a $(3\,h^{-1}{\rm cMpc})^3$ simulation box for three different epochs: merging ($z = 0.48$), post-merging ($z = 0.3$), and relaxing ($z = 0.01$) phases. As we will further discuss below, a different initial magnetic structure leads to a different final strength in the simulated galaxy cluster. In order to better visualise the spatial differences between our models in the projected magnetic field distribution, we normalise in Figure 7.2 the distributions for the Batchelor and Saffman models by a factor of 10. These two models, being correlated initially on smaller scales, reach the lowest magnetic field strengths already at early redshifts, $z \sim 10$ (before the cluster forms), and later on all stages of the cluster evolution.

In Figure 7.4, we compare the mean magnetic energy density evolution to the evolution of thermal, kinetic, and small-scale (turbulent) kinetic energy densities of the cluster within a comoving box of side length $1.5\ h^{-1}{\rm cMpc}$. We compute the turbulent energy by filtering out motions at large scales. At each component of the three-dimensional velocity, we subtract the mean velocity smoothed on two different scales of our selection. Here, we selected $25\ h^{-1}{\rm ckpc}$ and $100\ h^{-1}{\rm ckpc}$ as the fiducial smoothing scales (for a more elaborated multi-filtering technique see, e.g., Ref. [334]). The magnetic energy density growth in the uniform and scale-invariant cases is correlated with the growth rates of thermal and kinetic energy densities. For example, the approximate power-law growths of thermal, kinetic, and magnetic energies in the redshift range $z = 3$–0.65 are found to be $\sim t^{2.6}$, $t^{3.29}$, and $t^{2.77}$, respectively. By contrast, the magnetic energy density evolution of the Batchelor and Saffman models show a less pronounced growth than the aforementioned trends. These models evolve as $\sim t^{0.38}$ and $\sim t^{0.1}$, respectively. In addition, we

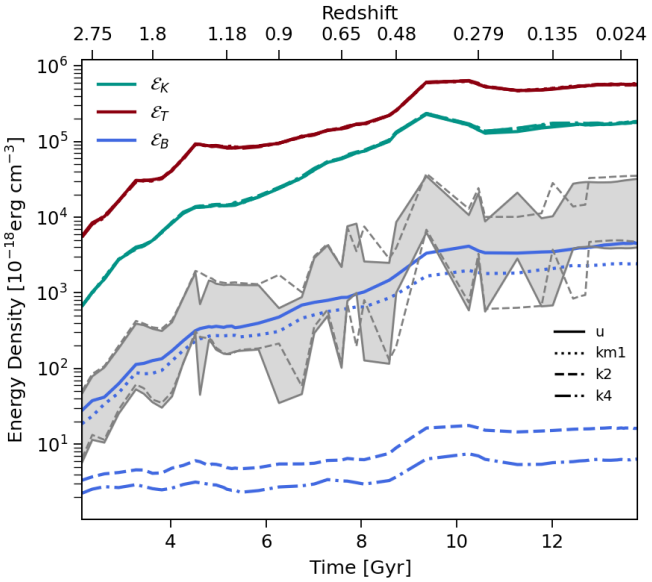

Figure 7.4: Evolution of thermal, kinetic, turbulent kinetic, and magnetic energy densities obtained from the comoving box with a side length of $1.5\ h^{-1}\mathrm{cMpc}$. The solid, dotted, dashed, and dashed-dotted lines correspond to uniform, scale-invariant, Saffman, and Batchelor models, respectively. The gray shaded area covers the turbulent energies having the smoothing scales between $25 - 100\ h^{-1}\mathrm{ckpc}$ and indicated with the lower and upper gray lines, respectively. The solid gray line corresponds to the uniform case and the dashed line to the Saffman model.

see that the magnetic energy of the cluster reaches similar levels as the turbulent energy at all times only in the uniform and scale-invariant models. Overall, we observe the total growth of turbulent, kinetic, and thermal energy densities with respect to $z = 3$ to be ~ 700, 270, and 100, respectively. On the other hand, the magnetic energy density of the uniform, scale-invariant, Saffman, and Batchelor models grows during the same $\sim 12\,\mathrm{Gyr}$ time-span by a factor of 160, 130, 5, and 3, respectively.

7.3.2 Radial profiles

The radial profiles of our cluster are shown in Figure 7.5. In the top panel, we show the magnetic field profiles along with the expected trend from adiabatic flux freezing ($\propto r^{-4/3}$) and the slope profiles. As previously mentioned, we observe that those initial conditions with more magnetic power at large scales, such as the uniform and scale-invariant models, show the largest field strengths. Conversely, as shown in the bottom panel of Figure 7.5, neither in the trends of the slope nor in the radial temperature and density profiles do we observe significant differences.

A commonly used proxy for relating the magnetic field and density distributions is to combine their radial dependencies. In the outskirts ($r > 150\,h^{-1}\mathrm{ckpc}$), this leads to $B_{\mathrm{uni}} \propto \rho^{0.43}$, $B_{\mathrm{inv}} \propto \rho^{0.50}$, $B_{\mathrm{Saff}} \propto \rho^{0.54}$, and $B_{\mathrm{Batch}} \propto \rho^{0.49}$ for the studied models. These trends are similar to those inferred from the radio observations of the massive $M_{200} \sim 1.8 \times 10^{15} M_{\odot}$ [335] Coma cluster [18], but are smoother than the slopes found, e.g., in the observations of the less massive cluster $M_{200} \sim \times 10^{14} M_{\odot}$ [336], or Abell 194 [19]. It should also be noted that the strength of the magnetic field in the core of the Coma cluster is found to be higher ($4.7\,\mu\mathrm{G}$) than the obtained values from our simulations.

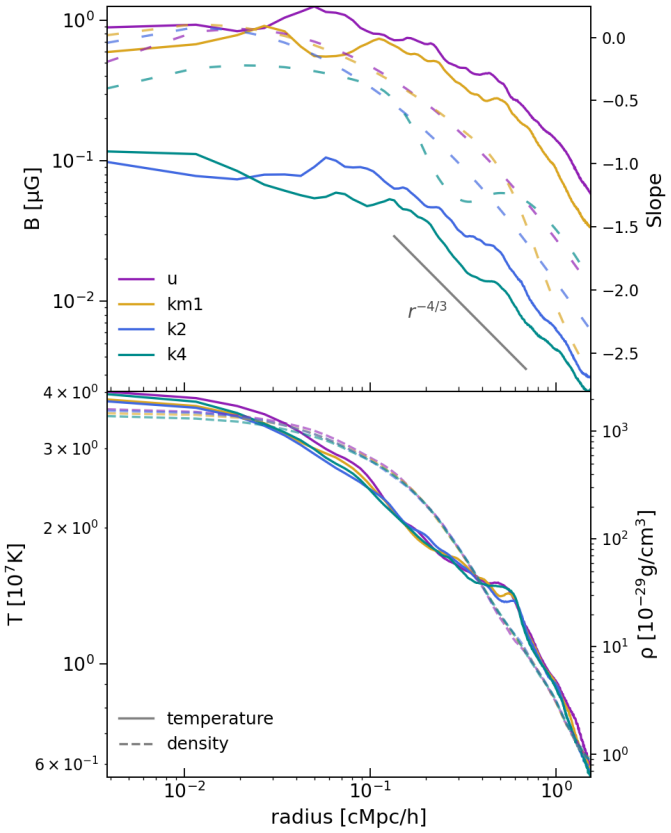

Figure 7.5: Radial profiles of the magnetic field (*top panel*) with the corresponding linear fits (*dotted lines*) for each magnetic seeding model and density and temperature fields (*bottom panel*). All profiles are calculated in a sphere having $r = R_{\rm vir}$ radius. In the outskirts magnetic field scales as $r^{-1.19}, r^{-1.39}, r^{-1.5}, r^{-1.34}$ for the uniform, scale-invariant, Saffman and Batchelor models, respectively.

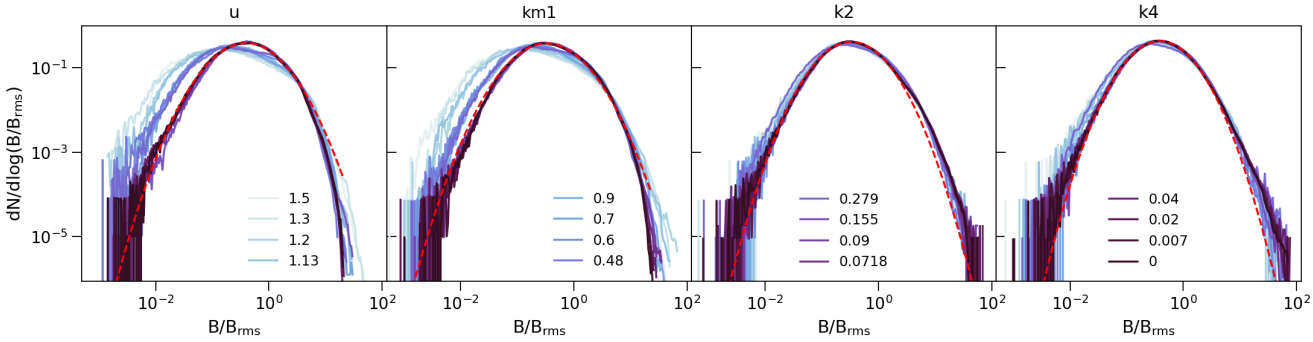

Figure 7.6: Redshift evolution of PDF. From left to right: the uniform, scale-invariant, helical and non-helical seedings. PDFs are obtained within the sphere having $R_{\rm vir}$ radius. The red dashed line shows lognormal fit for each model.

This can be explained by the fact that the simulated galaxy cluster in our work is still dynamically young (see, e.g., Ref. [52], who finds that dynamically older relaxed clusters have larger magnetic field strengths in the ICM [52]. In general, we find these trends to be in good agreement with the results of Refs. [45, 46], where the authors have studied the dynamo amplification in the simulated galaxy clusters using also AMR.

7.3.3 Probability distribution function and curvature

The distribution of magnetic fields has been the subject of several works. It follows from the induction equation that in the diffusion free regime and the kinematic stage of the dynamo (weak-field limit), the magnetic field is characterized by a lognormal PDF (see, e.g., Refs. [26, 155, 337, 338]). The log-normality of the magnetic PDFs is qualitatively understood in terms of the central limit theorem which is applied to the induction equation (without the diffusion term). A more rigorous derivation of this result involves the Kazantsev-Kraichnan dynamo model [184, 339]. Following this model, it is possible to predict the evolution of the mean and the dispersion (see, e.g., Equations (5) and (6) in Ref. [337]) of the lognormal distribution of the magnetic field. The spread of the PDF of $\log B$ both at low- and high-tails of the distribution is an important characteristic of a log-normal distribution which means that a fluctuating magnetic field possesses a high degree of intermittency, i.e., the fluctuations tend to become more sparse in time and space and on smaller scales (see, e.g., Ref. [340]). In the saturated state of dynamo, this intermittency is partially suppressed and the PDF develops an exponential tail (see, e.g., Ref. [26] and recent simulations in Ref. [302]).

In the following, we check whether dynamo action is present in our simulations. A comprehensive criterion for dynamo action in the presence of gravity is still missing; see Ref. [183] for some attempts.[1] We follow the diagnostics presented in [26] that has also been used in [45] and [47].

In Figure 7.6 we show the evolution of the normalized magnetic field ($B/B_{\rm rms}$) PDF for all four models. In the kinematic stage of a dynamo, [26] find that the magnetic PDF converges onto a single stationary profile, referred to as self-similarity of the field strength. In our simulations, we find that the PDFs of the Saffman and Batchelor models resemble the stationary profile, while the large-scale models (uniform and scale-invariant) do not show the same behavior towards the low-end tail of the PDF. The dispersion of the PDF of the latter two cases decreases (although not significantly), while the dispersion of phase-transition-generated models stays mostly constant. At the final redshift, we overplot a lognormal fit in Figure 7.6 and show that the low- and high-end tails of the distribution are reasonably well fitted by a lognormal distribution for all PMF models. Finally, we computed the kurtosis at $z = 0$ and obtained the values: 12, 13, 31, and 68 for the uniform, scale-invariant, Saffman, and Batchelor models, respectively. These values confirm that all our models exhibit super-Gaussian profiles.

The geometry of the magnetic field lines can be studied in terms of the curvature, defined in Equation 3.39. In Figure 7.7, we show the dependence of the magnetic field on the absolute curvature, $K = |\mathbf{K}|$ (top panel) and the curvature distribution (bottom panel) at $z = 0$. In small-scale dynamo theory, turbulent amplification of the field proceeds by stretching and bending of field lines by turbulent eddies, which results in folded structures (see, e.g., Figures 1 and 2 in Ref. [337]). Due to flux conservation arguments, it is expected that the magnetic field strength is larger in the stretched segments of field lines, while in the bends the strength remains small, i.e., the field strength and its curvature are expected to be anti-correlated. This is similar to an earlier finding that stronger flux tubes are also more straight [346]. The top panel of Figure 7.7 is a good illustration of this hypothesis. We observe a declining profile of the magnetic field strength with increasing curvature of the field. This anti-correlation is confirmed by calculating the cor-

[1] We refer here to earlier papers [341–345], who study the turbulent dynamo in the context of the formation of the first stars.

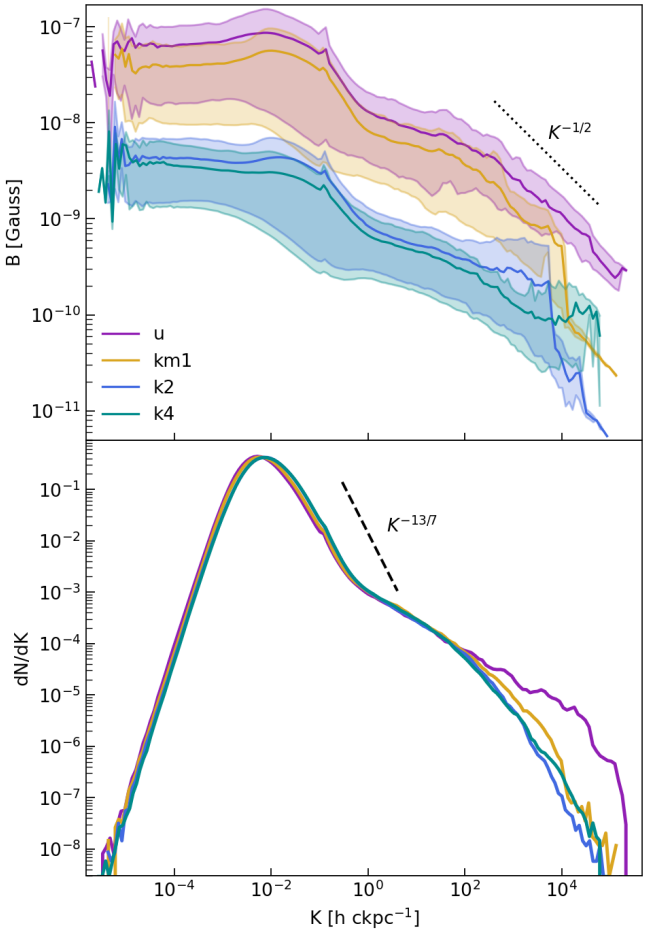

Figure 7.7: Profile of the magnetic field versus curvature ($|\mathbf{K}|$) and curvature PDF calculated from $(3.0\,h^{-1}\mathrm{cMpc})^3$ box at $z = 0$. The dotted and dashed lines in the panels indicate scalings expected from theoretical estimations [26]. Shaded regions for each model cover the distribution points between the 16th and 84th percentiles.

relation coefficient between the curvature and the magnetic field $C_{K,B}$ (see Equation (26) in Ref. [26]). For all our models at $z = 0$, we obtain $C_{K,B} \sim -0.999$, which is practically its minimum possible value. We also note that this anti-correlation is observed already from earlier redshifts in our simulations. At $z = 0$, we obtain slopes: -0.32 (-0.46), -0.42 (-0.39), -0.35 (-0.47), and -0.25 (-0.34) for the $(1.5\,h^{-1}\mathrm{cMpc})^3$ region ($(3\,h^{-1}\mathrm{cMpc})^3$ region) corresponding to the uniform, scale-invariant, Saffman, and Batchelor models, respectively. Another interesting feature that we see in the top panel of Figure 7.7, is the flattening of the magnetic field profile towards extremely low curvatures. From the bottom panel of Figure 7.7, we see that this happens for $K \lesssim 7 \times 10^{-3}\,h\,\mathrm{ckpc}^{-1}$ where we observe a steep decrease ($\sim K^{2.5}$) of the curvature PDFs. The bulk of the curvature distribution is concentrated at the peak values corresponding to: 192, 175, 140, and $143\,h^{-1}\mathrm{ckpc}$, i.e., on curvature scales, λ_K, for the uniform, scale-invariant, Saffman, and Batchelor models, respectively. As we shall see in Section 7.3.4, λ_K is comparable to the scale containing the largest magnetic energy. We find that the peak of the curvature PDF shifts to the right for all our models during the major merging phase, i.e., λ_K decreases. This shows that mergers tend to further compress the existing folded structure instead of elongating it. Finally, we also observe a distinctive difference between the uniform and stochastic models with the former exhibiting the largest curvatures.

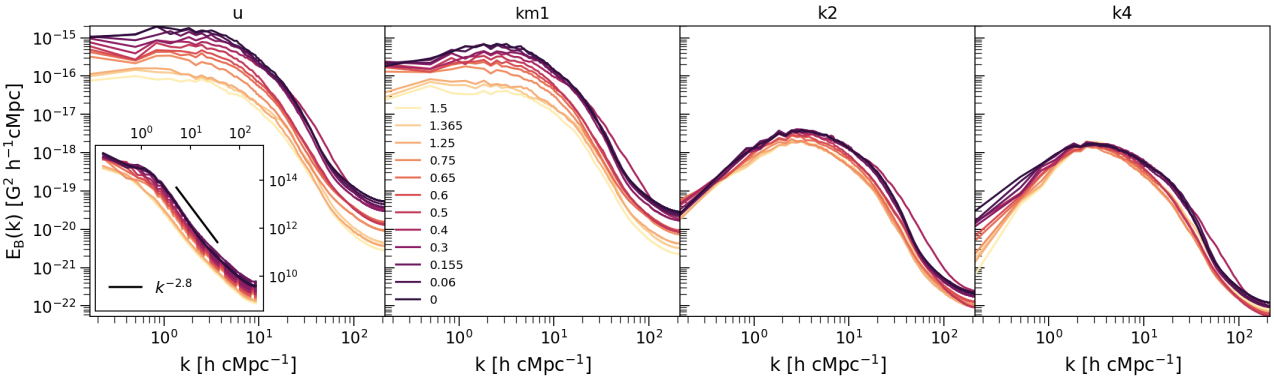

Figure 7.8: Redshift evolution of magnetic and kinetic (inset in the left panel) energy spectra. From left to right: the uniform, scale-invariant, Saffman, and Batchelor models. The energy spectra are calculated from the $(3.0\,h^{-1}\mathrm{cMpc})^3$ box at the 7th level of AMR using the *yt* interpolation method [27]. For additional effects on the shape and amplitude of the magnetic energy spectra, we refer the reader to Appendix 9.2.1. The axis units in the inset are $\mathrm{cm}^2\,\mathrm{s}^{-2}\,h^{-1}\mathrm{cMpc}$ and $h\,\mathrm{cMpc}^{-1}$ for the specific kinetic energy and wavenumber, respectively.

In summary, (1) all PMF scenarios attain intermittent structures (log-normality of the PDFs) during their evolution even though the growth of magnetic energy is relatively lower for the Saffman and Batchelor models (see Figure 7.4). (2) There is an anti-correlation between the field strength and the curvature for all models; however, curvature scales are different for the large- and small-scale correlated fields. As a result, different growth rates in the PMFs, i.e., possible suppression or excitation of the dynamo, may leave imprints on the scale where further stretching and bending of the field lines is counteracted by the stronger fields.

7.3.4 Spectral evolution

In observations, previous knowledge of the magnetic energy spectrum is required to get more information about the general characteristics of magnetic fields in the ICM (see e.g., Refs. [19,20,34,347]). In Figure 7.8 we show the evolution of the magnetic energy spectra of our four models and specific kinetic energy spectrum for the uniform model in the inset of the first panel. The magnetic spectrum is again computed using Equation (3.36) for different time snapshots in a $(3\,h^{-1}\mathrm{cMpc})^3$ simulation box that follows the cluster centre as it evolves. From the figure, one can see the differences between the spectra of the inflation- and phase-transition generated seed fields arise both in the amplitude and shape of the magnetic power spectra. The differences observed in the shape are more pronounced toward the largest scales ($\gtrsim 0.5\,h^{-1}\mathrm{cMpc}$) of the simulated galaxy cluster. In particular, at these scales the spectra corresponding to the uniform and scale-invariant models is flatter than the spectra corresponding to the Saffman and Batchelor models. A similar result has also been presented in Chapter 6. We will further discuss the shape of the magnetic energy spectrum in Section 7.3.4, where we parameterise our four cases. On the other hand, we note that the kinetic energy spectra (the inset in the left panel of Figure 7.8) in our simulations do not show differences between different PMF models. The spectra follow a k^{δ} profile where δ changes between ~ -2.3 and -2.8 at small scales ($\lesssim 0.5\,h^{-1}\mathrm{cMpc}$) in the $9.5\,\mathrm{Gyr}$ time span.

In order to understand the differences in the magnetic field amplitudes between different models, we recall that at early times ($10 \lesssim z \lesssim 50$), *before the cluster forms*, only the uniform field model shows amplification homogeneously on all scales (see Figure 6.6),[2] i.e., in the absence of gravitational accretion and induced turbulent motions, the stochastic models mostly stay frozen-in or show an insignificant decay. At late times, *as the cluster forms*, the large-scale stochastic model (i.e., the scale-invariant) shows a similar trend as the uniform model and the amplitude of the power spectrum grows on all scales. This happens because the magnetic power is concentrated on the largest scales similarly to the power corresponding to the density and velocity fields (this can be seen in Figure 7.1, in which we show our selected initial density and velocity power spectra, as well as in the inset in the first panel of of Figure 7.8). In addition, when turbulence develops, it first produces large-scale eddies that stretch and bend the field lines of those models where the large-scale magnetic component is present. In the stochastic small-scale models, magnetic amplification happens after turbulence cascades down to scales comparable to the corresponding magnetic coherence scales. Therefore, the magnetic energy of these models (Saffman and Batchelor) is prone to less efficient and slower growth. Furthermore, as Ref. [168] pointed out, a chaotically tangled field will decay toward a folding state at a rate comparable to the rate of the magnetic energy growth. Thus, the initial slower growth in the Saffman and Batchelor models will further suppress the folding of the field lines, leading to overall a lesser amplification degree in these models.

We note that different growth rates (see also Figure 7.4) for large- and smaller-scale magnetic fields obtained in our simulations are at odds with the results of driven-turbulence simulations; see e.g., Ref. [348] and Ref. [302] who compare the evolution of uniform (imposed) and random (stochastic) fields in incompressible and compressible MHD turbulence setting, respectively. Although, these authors also find a delay of the onset of the linear growth for low initial field strengths (uniform field case [348]) or a decay during the initial transient phase (random field case [302]). In the latter work, the uniform model does not decay and shows rapid growth during this phase; this trend is similar to the results presented in our work. Contrary to the results of driven-turbulence MHD simulations (see e.g., Refs. [26, 301]), our study does not clearly indicate forward or inverse cascading either. However, we must bare in mind that the ICM is a complex system where mergers might alter the mentioned trends as we have already discussed above.

Characteristic scales

A clearly visible characteristic of the magnetic energy spectrum is the peak scale $L_{E_B(k)}$ corresponding to 1200 and $400\,h^{-1}\mathrm{ckpc}$ for the uniform and scale-invariant models, respectively and to $316\,h^{-1}\mathrm{ckpc}$ scales for the Saffman and Batchelor models. The $L_{kE_B(k)}$ scales are $222\,h^{-1}\mathrm{ckpc}$ for the uniform and scale-invariant models and 171, $154\,h^{-1}\mathrm{ckpc}$ for the Saffman and Batchelor models. We also find that the peak scales of the density, $L_{kP_\rho(k)}$, and velocity, $L_{kE_v(k)}$ spectral energy per mode are the same: $\sim 857\,h^{-1}\mathrm{ckpc}$. In the inflationary and phase-transitional models, $L_{kE_B(k)}$ is $\sim 1/4$ and $\sim 1/5$ of $L_{kE_\rho(k)}$

[2] A similar result has also been shown by Ref. [302], where the authors found that even in the case of a non-active small-scale dynamo, a uniform seed magnetic field is still linearly amplified due to the tangling of the large-scale field (see also discussion in the Appendix of Ref. [303] and Section 6.5). We remind a reader that in this latter work, and generally in small-scale dynamo studies, contrary to the cosmological simulations, the magnetic and velocity spectra are concentrated at the same scales.

and $L_{kE_v(k)}$, respectively. A similar result has also been found in the MHD simulations of Ref. [167] where the authors find a $\sim 1/5$ ratio at saturation between $L_{kE_B(k)}$ and the driving (injection) scale of turbulence.[3] Therefore, our results suggest that most of the magnetic energy resides on scales that are smaller than the gravity-induced scale or the peak scale of the density and velocity power spectra.

In top panel of Figure 7.9 we show the evolution of the magnetic correlation length for different PMF models. We computed the correlation length throughout the 12 Gyr period focusing on a $(1.5\ h^{-1}\mathrm{cMpc})^3$ region (as in Figure 7.4). We also did the same analysis in a $(3.0\ h^{-1}\mathrm{cMpc})^3$ region since the correlation length can depend on the box size under consideration. *During merger events* (shown as vertical shaded areas in Figure 7.9), the magnetic correlation length decreases for all four models. This happens mainly because compression becomes dominant as the infalling gas clump crosses the cluster center.[4] The same effect has also been observed in other cosmological MHD simulations, e.g. in Ref. [46] where the authors found that major merger events shift the magnetic power towards smaller scales. It is *after each merger event* that the magnetic correlation length increases again for all four models.

Finally, as the cluster enters its *relaxing phase* at $z \lesssim 0.135$, the correlation lengths for all models converge to 260–410, 240–330, 180–230, and 170–240 $h^{-1}\mathrm{ckpc}$ for the uniform, scale-invariant, Saffman and Batchelor models, respectively. These values are one order of magnitude larger than what is obtained and typically referred to as coherence scale (few tens of kpc) from radio observations (see e.g., Refs. [34,35,85]). The strongest differences in the magnetic correlation length between the models are better seen at earlier redshifts where the scale-invariant model shows a coherence length that is larger than those of the Saffman and Batchelor models by a factor of ~ 2. We note that while the differences between the uniform and scale-invariant models and between the Batchelor and Saffman models decrease after the merger events, we still observe larger correlation lengths in the inflationary cases than in the phase-transitional scenarios throughout the evolution of galaxy cluster in this 12 Gyr period.

In the bottom panel of Figure 7.9 we show the evolution of $\lambda_{\parallel}, \lambda_{\mathbf{B}\times\mathbf{J}}$, scales corresponding to the inverse $k_{\parallel}$, $k_{\mathbf{B}\times\mathbf{J}}$, characteristic wavenumbers, respectively. In small-scale dynamo theory, it has been argued that generally $k_{\mathbf{B}\times\mathbf{J}} > k_{\parallel}$ since the shear flows can more rapidly stretch and reverse the field lines in the plane transverse of the field line itself [see][and references therein]Schekochihinetal2002b. In other words, the growth of the typical fluctuation wavenumber $k = \sqrt{k^2_{\mathbf{B}\times\mathbf{J}} + k^2_{\parallel}}$ should be mostly due to the increase of $k_{\mathbf{B}\times\mathbf{J}}$. It has been shown that in both, the MHD dynamo [26] and the plasma dynamo [351], the $k_{\mathbf{B}\times\mathbf{J}} > k_{\parallel}$ ordering is satisfied in the initial, rapid growth phase and persists in the kinematic and nonlinear regime of a dynamo (during saturation). As we can see from Figure 7.9, the condition $k_{\mathbf{B}\times\mathbf{J}} > k_{\parallel}$ is satisfied for $z < 3$ in the simulated cluster for all four magnetic cases. We find a maximum ratio of $k_{\mathbf{B}\times\mathbf{J}}/k_{\parallel} \sim 2-3$ during the 12 Gyr period. The ordering of these characteristic scales seems to be consistent with the arrangement of a magnetic field in folded structures; see also Figure 23(a) of Ref. [26]. This result, along with the log-normality of the PDFs and curvature results, would be compatible with the kinematic stage of a dynamo in our simulations.

[3] See also Ref. [349] and Ref. [350], who studied the dependence of different characteristic scales on magnetic Prandtl number.

[4] We note that merger events add additional power as they enter the analysing box, and therefore, this can also contribute to the decrease of magnetic correlation length.

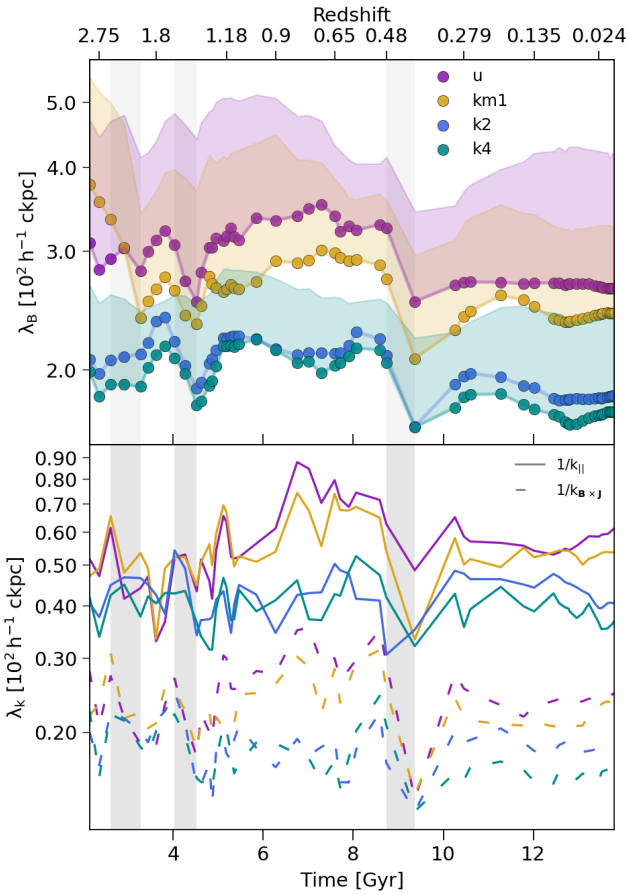

Figure 7.9: Evolution of magnetic correlation length (top panel) and characteristic parallel and perpendicular scales (bottom panel) for the simulated galaxy cluster. The vertical shaded regions show merging phases during the evolution of galaxy cluster. The horizontal shaded areas in the top panel are delimited according to the analyzed region; lower (upper) lines correspond to a $(1.5\,h^{-1}\mathrm{cMpc})^3$ ($(3.0\,h^{-1}\mathrm{cMpc})^3$).

Parameterised magnetic energy spectra

In order to discriminate among magnetic field models we characterised the magnetic energy spectra in the $(3\ h^{-1}\mathrm{cMpc})^3$ box. We considered two different fitting functions. First, we use the equation:

$$E_B(k) = Ak^{\beta}\left\{1 - \mathrm{erf}\left[B\,\ln\left(\frac{k}{C}\right)\right]\right\}, \tag{7.2}$$

where A gives the normalisation, B is related to the width of the spectra, C is a characteristic wavenumber of the magnetic field, and β is the slope of the spectrum at small wavenumbers. This fitting function has been used in Ref. [46] to study the evolution of magnetic energy spectra for a set of highly resolved galaxy clusters, assuming a uniform magnetic field seeding. The large-scale slope used by the authors satisfies the Kazantsev [184, 185] scaling, $\beta = 3/2$. We use a similar approach by fitting Equation (7.2) to the magnetic energy spectra of our simulated cluster and obtaining the best-fit parameters A, B, and C. In our case, we fix the initial β at each time-step separately. That is, as a first-step, we determine the large-scale slope of the spectra, β, and, as a second step, we fix this value in the fitting equation.

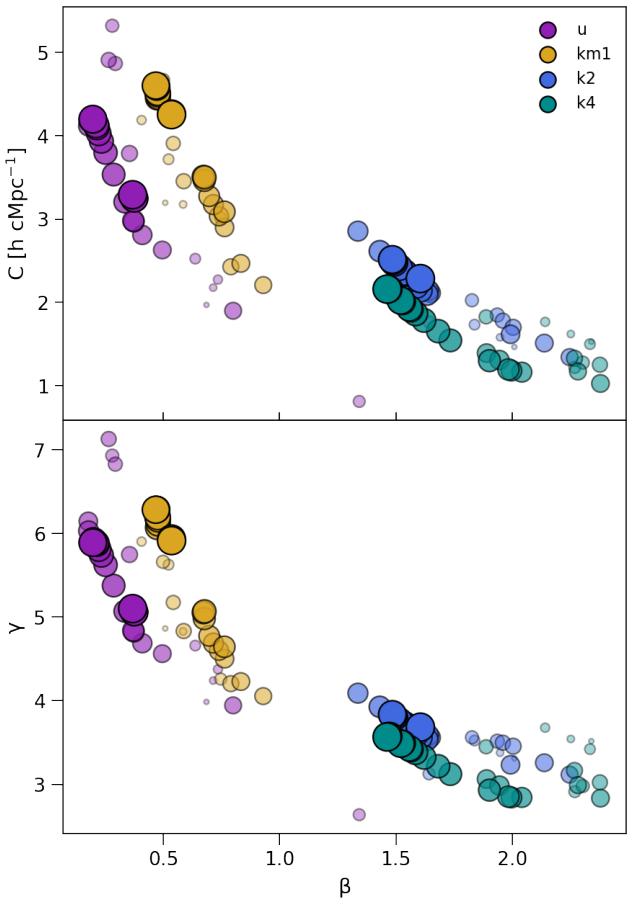

Figure 7.10: Parameter space for the best-fit parameters of our different PMF models considering a $(3.0\,h^{-1}\mathrm{cMpc})^3$ region. Smaller-size markers and lower-opacity colours show the parameters at early times. The top and bottom panels show the results from the fits according to Equations. 7.2,7.3, respectively.

The second fitting function is motivated by the MHD simulations in [24], where a phase-transition-generated magnetic field has a pronounced peak on the scale of the field generation. We adopt the following spectral shape [24, 352]

$$E_B(k) = (1+D)^{1/\alpha} E_\mathrm{m} \frac{(k/k_*)^\beta}{[1+D(k/k_*)^{\alpha(\beta+\gamma)}]^{1/\alpha}}, \tag{7.3}$$

where D controls the peak scale, E_m is the normalisation, k_* is the peak wavenumber, and β and γ are the slopes at large ($k < k_*$) and small scales ($k > k_*$), respectively. The value of α is chosen to be 0.25 to ensure a smooth transition between the spectra on large and small scales. In this case, D, E_m, γ are the best-fit parameters obtained. Figure 7.10 summarises the results of our fitting procedure using Equations (7.2) and (7.3). We only show the most important best-fit parameters for each model in Figure 7.10, while we provide all the parameters at $z = 0$ in Table 7.3.4. In the upper panel we show the $C - \beta$ parameter space (see Equation (7.2)) and in the lower panel we show the $\gamma - \beta$ parameter space (see Equation (7.3)). We show the evolution of the fitting parameters for a time span of 6.1 Gyr in the redshift range of $0.63 \leq z \leq 0$. As it can be seen from Figure 7.9, this period encompasses a major merger event at $z \sim 0.48$ and the relaxing phase of the cluster.

The C–β and γ–β parameter spaces highlight how the spectral characteristics of the

Model	Eq.	A $[\mathrm{G}^2\,h^{-1}\mathrm{cMpc}]$ E_m $[\mathrm{G}^2\,h^{-1}\mathrm{cMpc}]$	B D	C $[h\,\mathrm{cMpc}^{-1}]$ γ
u	(7.2)	8.92×10^{-16}	2.16	3.29
	(7.3)	1.63×10^{-15}	0.03	5.10
km1	(7.2)	2.54×10^{-16}	2.56	4.25
	(7.3)	6.44×10^{-16}	0.095	5.92
k2	(7.2)	8.66×10^{-19}	2.27	2.29
	(7.3)	3.57×10^{-18}	0.403	3.68
k4	(7.2)	4.91×10^{-19}	2.17	2.16
	(7.3)	1.62×10^{-18}	0.427	3.57

Table 7.2: Parameters of the power spectra for different models and for different fitting functions at $z = 0$. The power spectra is fitted with Equations (7.2) and (7.3). The fixed β parameters are: 0.37, 0.54, 1.61, 1.46 for the uniform, scale-invariant, Saffman and Batchelor models correspondingly, and $\alpha = 0.25$.

inflationary cases differ from those of the phase-transitional cases. In the following, we discuss the main points:

(i) The evolution of the C parameter varies between 2–4.5 $h\,\mathrm{cMpc}^{-1}$ for the inflationary models and between 1–2.8 $h\,\mathrm{cMpc}^{-1}$ for the phase transitional models. The ratio between the magnetic correlation length and $1/C$ is ~ 1.4 for the inflationary models and ~ 0.5 for the phase-transitional seedings. That is, $\lambda_B \gtrsim 1/C$ for the former scenarios and $\lambda_B \lesssim 1/C$ for the latter models. This shows that this fitting equation is a good proxy for obtaining a characteristic scale of the magnetic field that can be comparable or of the same order as λ_B.

(ii) The large-scale slope of the magnetic power spectra characterised by β deviates from a Kazantsev slope in the inflationary models where $\beta \lesssim 1$. In contrast, the phase-transitional models are approximately characterised by a Kazantsev slope at late redshifts. These models show a scatter in the range $1.2 \lesssim \beta \lesssim 2.5$, where the slope tends to flatten progressively towards $\sim 3/2$ as the cluster virialized.

(iii) The small-scale slope of the magnetic power spectra characterised by γ varies between 3.9–6.5 in the inflationary models and 2–4.1 in the phase-transitional models. As seen from Figure 7.8, the magnetic energy growth at scales larger than the characteristic scale is more pronounced in the two inflationary cases, therefore, explaining the larger values of γ compared to those from the phase-transitional models.

Finally, we note that we refrain ourselves from claiming that the phase-transitional models can corroborate the 3/2 large-scale slope predicted by the Kazantsev model since, as can be seen from Figures 7.8 and 7.10, throughout the complex evolution of galaxy clusters this slope can vary. Indeed, the multiple merger events that lead to the final formation of a cluster already breaks down one of the most basic assumptions of Kazantsev theory, i.e., a delta correlated (in time) velocity field.

7.4 Rotation Measures

Galaxy cluster RM study can be especially important for the PMF constraining prospects. As we will discuss in Section 8.1 future surveys may enable us to distinguish between

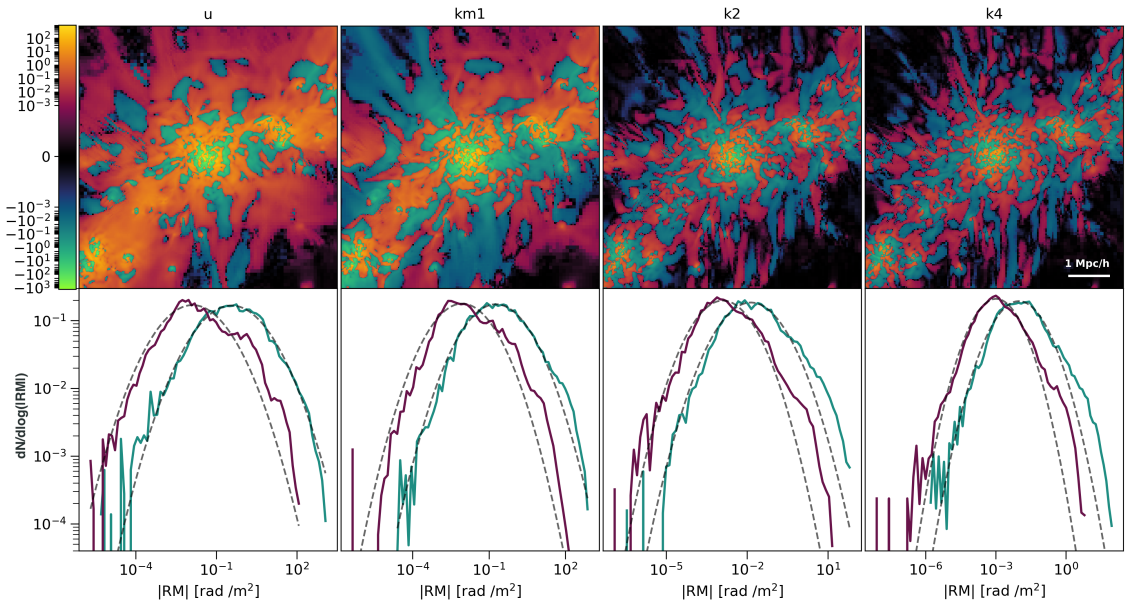

Figure 7.11: Top panel: RM maps [rad/m^2] calculated from a $(3\,h^{-1}\mathrm{Mpc})^3$ box; bottom panel: PDF of the absolute RM in the same box (green color) and in the cluster outskirts (purple): $R_{\rm vir} < r < 2 \times R_{\rm vir}$; $z = 0.1$. The dashed grey lines in each panel show the corresponding lognormal fit for the PDFs.

different magnetogenesis scenarios based on the realistic RM analysis from simulations. In the top panel of Figure 7.11, for illustrative purposes, we show the RM from our simulated galaxy cluster extracted from a $(3\,h^{-1}\mathrm{Mpc})^3$ box at $z = 0.01$. As we can see, in agreement with the RM maps from our cosmic-web study (Section 6.6, see Figure 6.9), the uniform and scale-invariant models show larger RM amplitude and more coherent features compared to the Saffman and Batchelor models. This is a consequence of the larger correlation lengths and field strengths obtained in the former scenarios. While the mean RM from all models is close to zero (with an offset of 0.7 rad/m^2 in the uniform model), the corresponding standard deviations, σ, are $27.53, 20.62, 2.02, 1.62$ rad/m^2 for the uniform, scale-invariant, Saffman and Batchelor models, respectively. We note that the RM differences between the four models in the innermost region of the cluster ($\sim 200\,h^{-1}\mathrm{kpc}$) decreases and become almost indistinguishable. The bottom row of Figure 7.11 complements the discussion above. Here we show the PDF of the absolute RM considering the same region as of the RM maps on the top row (green color) and considering just the outskirts of the cluster, $R_{\rm vir} < r < 2 \times R_{\rm vir}$ (red color). The RM PDFs in the cluster central region peak at 0.564, 0.083, 0.008 and 0.027 rad/m^2 for the uniform, scale-invariant, Batchelor and Saffman models, respectively. In the outskirts' region the PDFs peak at lower values: 0.009, 0.002, 0.0007 and 0.001 rad/m^2 for the uniform, scale-invariant, Batchelor and Saffman models, respectively. All PDFs are generally well fitted by a lognormal function.

7.5 Numerical aspects

The numerical resolution is an important caveat for the analysis conducted in this work. As mentioned earlier (in Chapter 6), magnetic fields tend to be more strongly affected by resolution effects than the velocity field, for example [45, 286]. Therefore, the growth

rates of the seed magnetic fields in galaxy clusters are also resolution-dependent. Within our numerical setup, we assess the convergence of our results by performing extra simulations with different AMR levels. In Appendices 9.3.1 and 9.3.2, we show how the power spectra, the PDFs, and the radial profiles of the magnetic field are already converged at 6 AMR levels (on scales $\gtrsim 50\,h^{-1}\mathrm{ckpc}$).

As in Chapter 6, we relied on the Dedner cleaning algorithm. In Section 6.7 we noted that the intrinsic dissipation of the Dedner scheme by cleaning waves can affect the final magnetic growth of the magnetic field models. Consequently, we cannot entirely rule out that numerics (see also Appendix 9.2.2) can also contribute to the obtained differences between the growth rates of the inflationary and phase-transitional models. In Figure 9.8 of Appendix 9.3.1, we show the radial profile of the magnetic field divergence in our simulated cluster. The densest central region of the cluster exhibits a similar normalised divergence for our four PMF models, whereas some differences between inflationary and phase-transitional cases can be observed only at large radii, $\gtrsim 1.2\,h^{-1}\mathrm{cMpc}$, with the former case showing the lowest values. Nevertheless, the Dedner cleaning method keeps the numerical magnetic field divergence below $\sim 5\%$ ($\sim 8\%$) of the local magnetic field within the cluster volume having $r = R_{500}$ ($r = R_{100}$) radius. This shows that the divergence stays reasonably low in the largest fraction of the simulated cluster volume.

As mentioned in Section 5.1, we did not take into account any additional physics (e.g., radiative cooling) Although, the inclusion of additional physics such as feedback and radiative cooling physics might alter the amplification levels of our PMF models and therefore, may affect the final magnetic fields (see e.g., Refs. [53, 252]). The effect of these processes on distinguishing between different magnetogenesis scenarios will also be studied in our future work.

7.6 Conclusions

In this work we have investigated the evolution of PMFs during the formation of a massive galaxy cluster. We studied seed magnetic fields resembling inflation- and phase-transition-generated non-helical fields. In the former case, we assumed either (i) a uniform, constant magnetic field or (ii) a stochastic field. The stochastic model is motivated by the pre-recombination evolution of an inflationary seed field (initially having a scale-invariant spectrum), while the uniform case corresponds to the Mukohyama model. In the case of phase-transition-generated seed magnetic fields, we studied stochastic models with initial (iii) Batchelor and (iv) Saffman spectra. These magnetic spectra are motivated by the causal generation and evolution of phase-transitional fields until recombination.

The main results of our work can be summarised as follows:

1. *Final amplification*. The amplification of a primordial seed magnetic field in the ICM strongly depends on the initial structure of the magnetic field. In our simulated galaxy cluster, the inflation-generated uniform and scale-invariant models show more efficient amplification compared to the phase-transition-generated Saffman and Batchelor models. We see that in the former cases the magnetic energy density is of the same order of magnitude as the turbulent energy budget of the cluster. In such cases, the magnetic power is concentrated on the largest scales, similarly to the power corresponding to the density and velocity fields. This leads to more efficient turbulent amplification of these large-scale models compared to the small-scale, phase-transitional seed magnetic fields.

2. *Radial profiles*. The radial magnetic field profiles at the final redshift ($z = 0$) reflect the aforementioned differences in the magnetic energy growth. The amplitude of the uniform and scale-invariant models is one order of magnitude larger ($\sim$ 0.8–1 μG, cluster centre) than the amplitude attained by the phase-transition-generated magnetic fields ($\sim$ 0.1 μG). The declining magnetic field profile towards the outskirts reveals the largest differences between the uniform ($r^{-1.19}$) and the Saffman ($r^{-1.5}$) models.
3. *Small-scale dynamo*. All of our models exhibit a degree of small-scale dynamo amplification as hinted at by the lognormality of the magnetic field PDFs and the folded structure of field lines (anticorrelation between the field strength and curvature and ordering of the characteristic wavenumbers). Consistent with the previous works [45–47], we find that cosmological MHD simulations do not exhibit a small-scale dynamo that can be compared one-to-one to the Kazantsev theory.
4. *Coherence lengths*. We find that, throughout the evolution, the magnetic correlation length of the cluster depends on both the initial structure of the seed field and the merger history. We find that the inflationary models (initially large-scale correlated PMFs) will inherently attain larger coherence lengths than the phase-transitional models throughout the evolution of galaxy clusters. This trend is persistent even during merger events, where the correlation length decreases for all models. At the final redshifts, we observe a factor of $\sim$ 1.5 difference in the coherence scales of the uniform and scale-invariant versus Batchelor and Saffman models. The correlation lengths calculated from a $[(1.5\text{–}3)\,h^{-1}\mathrm{cMpc}]^3$ analyzing box span in the range: 260–410, 240–330, 180–230, 170–240 h^{-1}ckpc for the uniform, scale-invariant, Saffman, and Batchelor models, respectively.
6. *Spectral characteristics*. We provide two possible fits for the magnetic energy spectra. The parameterization of the magnetic energy spectra shows how phase-transitional and inflationary models can be differentiated. The large-scale slopes (β parameter; see Section 7.3.4) are smaller ($\lesssim 1$) for the inflationary PMFs, and larger ($1.2 \lesssim \beta \lesssim 2.5$) for the phase-transitional PMFs for a time span of 6.1 Gyr ($0.63 \leq z \leq 0$). The Batchelor and Saffman models have Kazantsev scaling ($\beta = 3/2$) at the final redshifts, even though these fields are amplified to a lesser degree. On the contrary, the small-scale slopes (γ parameter; see Section 7.3.4) are larger for the inflationary models ($\gamma \sim$ 3.9–6.5) than for the phase-transitional seedings ($\gamma \sim$ 3.9–6.5). The $1/C$ scales at the final redshift are: 300 h^{-1}ckpc, 240 h^{-1}ckpc, 440 h^{-1}ckpc, and 460 h^{-1}ckpc for the uniform, scale-invariant, Saffman, and Batchelor models, respectively.
7. *Imprints on RM?*. Galaxy cluster RM maps qualitatively show differences between different PMF seeding models which are better seen in the cluster outskirts. A more realistic galaxy cluster RM analysis is required in order to compare the results of our simulations with radio observations and that we defer to our future work.

In summary, we conclude that the two competing scenarios of primordial magnetogenesis, inflationary and phase-transitional, can indeed be distinguished on galaxy cluster scales. The initial structure of the seed magnetic field affects the efficiency of the dynamo. Thus, PMFs do not only leave unique imprints on scales larger than those of galaxy clusters (Chapter 6), but it can also influence small-scale dynamo action in the ICM. These signatures are reflected in the magnetic energy power spectrum and the coherence scale of different models. An analytical power spectrum of the magnetic field is required for synthetic RM studies (see the method description in, e.g., Ref. [20], giving us the possibility

to constrain the structure of observed galaxy-cluster magnetic fields. We provide two analytical models that can readily be used in observational works (see, e.g., Refs. [19, 34, 93] for such examples).

Finally, since inflationary models show larger field strengths (both in the centre as well as in the outskirts of the simulated cluster) and coherence scales, these may make them better candidates for producing e.g., the central cluster radio diffuse emission in the form of the "megahalos" that have been recently detected with LOFAR [Low-Frequency On the other hand, inflationary magnetogenesis scenarios would be also favoured for obtaining the fast magnetic field amplification needed to explain the observed diffuse radio emission in high redshift galaxy clusters [62]. Deeper observations of megahalos along with detailed RM images obtained by future observations with the SKA and the upgraded LOFAR 2.0, will have the potential of unravelling the origin of large-scale magnetic fields.

Chapter 8

Summary and future directions

The ubiquitous presence of magnetic fields on the largest scales of our Universe has motivated the research on PMFs, presented in this thesis. In the first four chapters, we tried to give the reader an overview of the observational evidence of large-scale magnetic fields and a theoretical framework through which we modelled the evolution of PMFs during large-scale structure formation. We briefly summarised scenarios of the production of PMFs during inflation and phase transitions and their evolutionary trends in the pre-recombination Universe. We also provided a description of the methods used in our cosmological simulations for the reader to better understand the setup, results, and numerical caveats of our works presented in Chapters 6 and 7.

The main result of our work is the distinguishable evolution of PMFs during structure formation. More specifically, we have shown that neither turbulent amplification (on galaxy cluster scales) nor the adiabatic compression of the magnetic field (e.g., filamentary scales) entirely erases the imprints of PMF generation scenarios. Although, this is at odds with the results of pure MHD simulations (i.e., simulations without gravity) we noted that the initial topology of the field should be of notable relevance for the gravity-on simulations where one has preferred scales due to structure formation. We have also studied observational signatures of PMFs on the RM and concluded that future radio surveys should provide valuable insight about the origin of the observed large-scale fields. Our results will have important astrophysical and cosmological implications. In this chapter, we review some of the cosmological implications and future plans motivated by our cosmic web and galaxy-cluster studies.

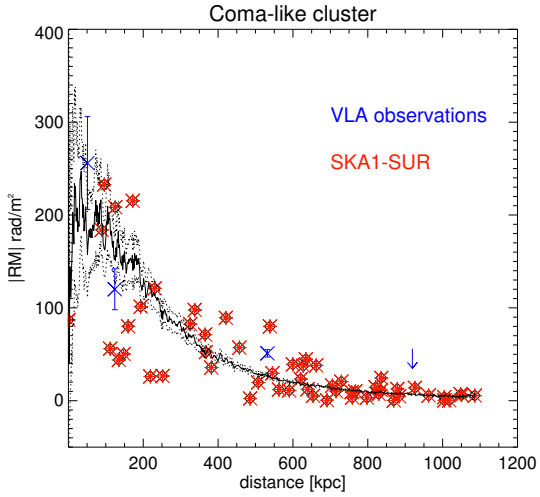

Figure 8.1: RM profile (continuous line) and predictions for the RM observations from future SKA survey for the coma-like galaxy cluster (discrete points; mock RM observations). Observations from Ref. [18] is overplotted in blue colour. Figure credit: Ref. [28].

8.1 Future prospects

PMFs in galaxy clusters: Future RM measurements in galaxy clusters will play a decisive role in understanding the origin of large-scale magnetic fields. The next generation of radio telescopes will have high sensitivity in resolving background polarised sources and therefore, will provide us with a larger number of RM data per galaxy cluster. Figure 8.1 from Ref. [28] shows RM profile for a coma-like galaxy cluster which is obtained by integrating the Equation (1.8) (continuous line). The discrete data in the figure shows RM derived by integrating Equation (1.8) separately for each background source when one assumes the same number of background sources as expected from the SKA observations. Such analysis is usually referred to as mock RM observations and it is done by pre-assuming the shape of the magnetic energy spectrum (along with gas density distribution) which is commonly taken to be a power law [18, 34, 353] (with Kolmogorov scaling). However, recent observational work [20] has also accounted for the power spectrum of the magnetic field obtained from cosmological simulations (although for cluster relic analysis). Our galaxy cluster study and fitting formulae then enable us of conducting a similar analysis when the magnetic power spectrum is set according to inflationary and phase-transitional magnetogenesis scenarios. This will be especially important for future observational surveys since one can potentially distinguish between different PMF models provided a larger number of RM data [28]. In addition, future surveys may enable us to directly link the RM data with the magnetic field structure. For instance, Refs. [35,354] have shown the link between the magnetic energy power spectrum and 2D RM. Our current galaxy-cluster simulations can already be used to probe the relationship between the 2D RM map and magnetic energy spectrum, i.e., whether the results from the simulations match the theoretical expectations [354]. Constraining the magnetic energy spectra from the current or future radio will be another step forward in understanding the nature of the magnetic field.

Finally, It should be mentioned that in our future works we can study the dependence of the turbulent growth of inflationary and phase-transitional PMFs on the field strength and dynamical state of galaxy cluster; i.e., aiming at answering the following questions:

(1) does the dynamical state of galaxy clusters affect the growth rates of different PMF models? (2) Is the overall turbulent amplification of the PMF initial amplitude dependent?

PMFs in IGM: *imprints on the γ-ray spectrum.* Blazar spectra observations are unique probes of magnetogenesis scenarios. Modelling of blazar-induced cascade emission can provide important information on the strength and structure of the large-scale magnetic field. The resulting spectra can be directly compared with the observational data obtained from current/future observations (with the Fermi/CTA telescopes). In such modelling of blazar spectra, the large-scale magnetic fields are usually represented by a monochromatic (peaked at one given scale) spectrum (see Ref. [9] for a review). However, in our work (Chapter 6), we have shown that magnetic field structure in the cosmic web is rather complex and depends on the primordial magnetogenesis scenarios. Therefore, it is interesting to model the propagation of high energy γ-rays while accounting for the realistic distribution of magnetic fields provided from cosmological simulations. Furthermore, our work allows us to study not only the effects of the PMF topology on the cascade spectrum but also the complex interplay of the magnetic field strength and structure on the blazar spectra. Specifically, in future work, we can investigate the effects of the coherence scale and strength of the magnetic field on the low-end tail of the blazar spectrum (see the right panel Figure 1.4); i.e., (1) is the suppression of the GeV emission more effective for the inflationary models which show large coherence scales and large amplitude of the field in the magnetised cosmic web? or (2) is the GeV "halo" more diffused when the magnetised structures (and therewith the void regions) are seeded by the smaller-scale (phase-transitional) PMFs? The increased sensitivity of future CTA telescopes in the 20–$200\,\mathrm{GeV}$ range exactly matches the energy range where the effects from PMFs are expected. Thus, this new survey will be of crucial importance for testing the results of our study and therefore, primordial magnetogenesis scenarios.

Imprints on the γ-ray halo. Studies presented in this thesis can be used for searching the magnetic helicity imprints. Helical magnetic fields lead to unique morphological signatures in γ-ray-induced electromagnetic cascades [9, 111, 112]. The sign of magnetic helicity correlates with the handedness of the halo morphology (see Figure in Ref. [9]). In our cosmic-web study [10], the initial simulation setup for the phase-transitional helical and non-helical fields differs by an initial magnetic energy spectrum (because of more efficient inverse cascade that helical models undergo in the early Universe) as it was shown in Figure 6.1). In the case of inflation-generated PMFs, both inflationary helical and non-helical fields lead to a similar spectrum at the end of the recombination epoch. Then our future work can complement the cosmic web study by simulating the evolution of inflationary helical PMFs in order to understand the signatures on the magnetised cosmic web coming solely from the primordial helicity. This novel approach will be another independent probe of primordial magnetogenesis scenarios. In particular, if the inflationary and phase transitional helical fields lead to distinguishable halo morphology, a comparison of the results of such a study with future observations may enable us to directly settle the issue of the origin of observed large-scale magnetic fields. In Figure 8.2 we summarise the imprints of magnetic fields on the cascade emission. The joint study of the emission using the magnetic field distribution from cosmological simulations and Monte-Carlo simulations for modelling is required in order to analyse the mentioned imprints.

Imprints on the RM. As it was mentioned in Section 6.6 the novel observational approach presented by Ref. [14] can be used to constrain the extragalactic RM variance and

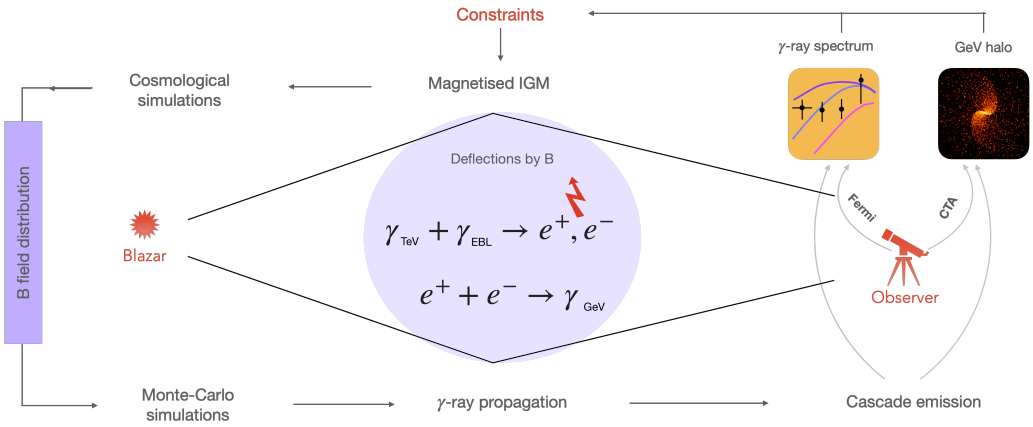

Figure 8.2: Scheme for the illustration of joint cosmological and Monte-Carlo simulations for modelling the blazar spectrum. The magnetic field distribution produced in the cosmological simulations can be provided in the Monte-Carlo simulations of the propagation of high energy γ-rays. Comparison of the simulated and observational spectrum can be used to put constrains on the field strength from different primordial magnetogenesis scenarios. PMF imprints on the halo (if detected) morphology, in turn, can give us a hint on the primordial helicity and magnetogenesis scenarios. The credit for the figures of the γ-ray spectrum and halo: Ref. [9].

thus, the magnetic field strength in the IGM. In Chapter 6 we compared the results of our RM analysis with the constraints obtained from Refs. [14, 15]. However, a more realistic comparison of our simulation results can be done by stacking the cosmological boxes, as we have already discussed. In other words, in order to get a more realistic estimate of $\mathrm{RM_{IGM}}$ one should consider the large LOSs, larger than the simulated box in our cosmic-web study. The cosmic-web study can be used to stack cosmological boxes, construct the light cones at the redshift range relevant for the current/future observations (e.g., for the upcoming, SKA precursor, WEAVE-LOFAR survey [308]) and study the dependence of $\mathrm{RM_{IGM}}$ on redshift. The scatter in $\mathrm{RM_{IGM}}$ values from different magnetogenesis scenarios can give as a hint to whether the studied primordial magnetogenesis is within/above the observational constraints.

PMFs and structure formation. A considerable numerical and theorethical effort is being made for understanding the impact of PMFs on structure formation. The effects of PMFs have been discussed in the context of reionisation [160, 272, 292, 355], first (population III) star [251], direct collapse black hole [356] and dwarf galaxy formation [73]. In connection with reionisation physics, Ref. [272] has shown that the standard picture of the IGM temperature evolution is altered when accounting for the heating processes (through the decaying MHD turbulence and ambipolar diffusion[1]).

Refs. [68, 69, 123] discuss PMF-induced perturbations (sourced by the Lorentz force) that affects the matter power spectrum. This idea has further been explored in cosmological simulations [73, 74] where modification of matter power spectrum due to PMFs increases star formation rate in dwarf galaxies [73] or leads to an unrealistically early

[1]Ambipolar diffusion is a process when the relative velocity between the charged and neutral particles is damped due to ion-neutral collisions; this leads to the dissipation of magnetic energy and heating of the medium.

collapse of first galaxies [74]. On the contrary, Refs. [251, 357] argue in favour of the delayed collapse of population III stars. Thus, currently there is no consensus view on the question. Nevertheless, a more realistic initial conditions that takes into account PMF decay processes in the early Universe might advance our understanding on the impact of PMFs on first structure formation.

PMFs and other physics? PMFs might also serve as indirect probes of DM physics, e.g., to put constraints on the mass of axion-like particles (ALPs; pseudo-scalar fields being candidates for dark matter which have been proposed in the extension of standard model physics), and to advance our knowledge on the ALP-photon mixing, i.e., on the interconversion of photons and ALPs which takes place in the presence of external magnetic field [358–360]. It will be interesting to study how different topology of PMFs would affect the process. For instance, Ref. [361] has studied the impact of the topology of the magnetic field on the ALP-photon conversion and found that helical magnetic field structure is of notable relevance for the process. Ref. [362], on the other hand, has studied the TeV blazar spectrum to search for an excess photon flux that may be due to ALP-photon mixing along the LOS. The authors also considered the ICM magnetic fields (with power law spectra) in their study. The magnetic power spectrum obtained in our galaxy cluster study can be used to study how the realistic distribution of the ICM magnetic fields would affect the process; or how the constraints on the ALP-photon coupling constant are altered when considering the different PMF models.

Finally, it should also be mentioned that recently the North American Nanohertz Observatory for Gravitational Waves (NANOGrav) reported strong evidence for a stochastic gravitational wave (GW) background [363]. Probing primordial magnetogenesis scenarios can help us to bridge constraints on PMFs with GW physics. For instance, if the observed large-scale fields are of a phase-transitional origin then is the amplitude of these fields such that they could induce detectable relic gravitational waves? This might help to constrain GW generation scenarios from the early Universe sources.

Chapter 9

Appendices

9.1 PENCIL CODE Initial Conditions

The uniform magnetic field model which we use in both of our simulations (cosmic web and galaxy cluster studies) is already implemented in in the Enzo code. A stochastic magnetic field models, on the other hand, require a special treatment as it is the result of an MHD simulations with the PENCIL CODE [288]. In this code, we solve the compressible resistive MHD equations [149], in which we advanced the magnetic vector potential. We adopt an ultrarelativistic equation of state, appropriate during the radiation era. The initial condition consists of a Gaussian-distributed spatially random field such that the magnetic energy spectrum has a certain shape, for example: it is proportional to k^{-1} for the scale-invariant spectrum and proportional to k^4 for wavenumbers $k < k_*$ and proportional to $k^{-5/3}$ for $k > k_*$ in the case of a phase-transitional initial magnetic field adopted in the cosmic-web study. In the PENCIL CODE, the simulation domain is triply periodic and normalised such that its volume is $(2\pi)^3$, and so the smallest wavenumber in the domain is then $k_1 = 1$. We choose $k_* = 120$ for the runs with phase-transitional initial magnetic fields. The sound speed, c_s and the mean density are normalised to unity. The rms magnetic field, and thus the initial rms Alfvén speed is $v_\mathrm{A} = 0.1...0.2$. We solve the equations for a time interval Δt such that $c_\mathrm{s} k_1 \Delta t = 10$, corresponding to $v_\mathrm{A} k_* \Delta t \approx 200$.

We generate the magnetic field components as eigenfunctions of the curl operator, but for helical fields the sign of the eigenvalue is the same for all wavevectors; see Equation (23) of [24]. Helical magnetic fields are still random and isotropic, but they have the same systematic swirl of field lines everywhere in the domain, just like a box with randomly oriented screws which all have the same sense of winding.

The use of a stochastic initial magnetic field requires a modification of Enzo where the field is normalised such that for each component $B_{s,i}$, the input (proper) magnetic field is:

$$B_{s,i} = \frac{B_P}{\sigma_P} B_{\mathrm{com},i} \, (1 + z_\mathrm{ini})^2, \tag{9.1}$$

where B_P is the input from the PENCIL CODE, σ_P is its standard deviation, and z_ini is the initial redshift ($z = 50$). We set $B_{\mathrm{com},i} = 1\mathrm{nG}$ and take $B_{u,i} = \mathrm{RMS}[B_{s,i}]$ for the B-field components in the case of a uniform initial field. In this way, we normalise all the initial conditions to have the same magnetic energy, $\int (B^2/8\pi)\, dV$.

9.2 Cosmic web project

9.2.1 Resolution tests

In order to test the convergence of our simulations, we compared our setup with the higher-resolution runs including uniform and helical magnetic seeding only (as the evolution of the power spectrum seems to be similar toward smaller scales in the uniform and scale-invariant cases and helical and nonhelical cases). These runs used the same set of cosmological parameters and the box size as is used in the main paper. Since the initial stochastic magnetic field distributions are obtained from the PENCIL CODE, in the helical case we used the AMR technique of the Enzo code [113] to reach the same resolution ($132h^{-1}\,\mathrm{kpc}$) as in the uniform case with 1024^3 grid points. In Figure 9.1 we show the growth of the magnetic field power spectrum as a function of spatial resolution. As we can see, for our case (i.e., the run with 512^3 grid points, $\Delta x = 132h^{-1}\,\mathrm{kpc}$ resolution), the

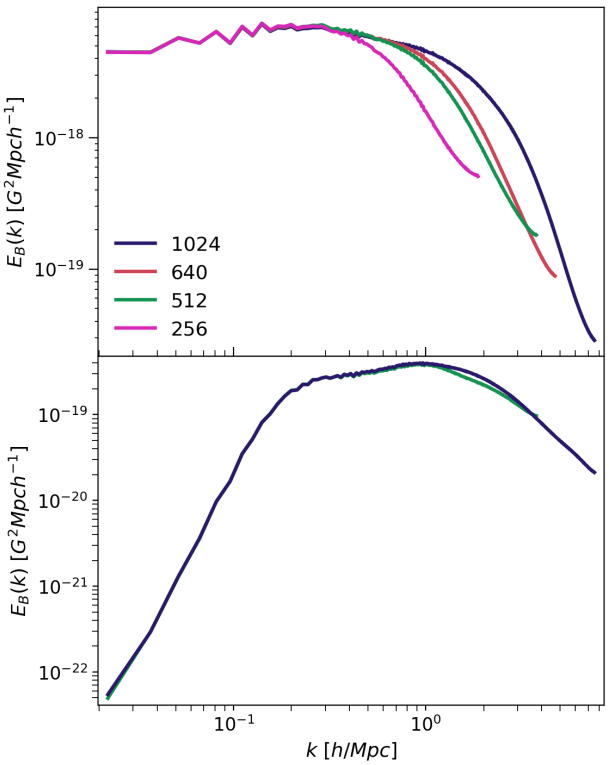

Figure 9.1: Magnetic energy power spectrum with increasing resolutions (comoving: 264 h^{-1}kpc, 132 h^{-1}kpc, 105 h^{-1}kpc, 66 h^{-1}kpc) for the uniform (top panel) and helical cases (bottom panel) at $z = 0.02$.

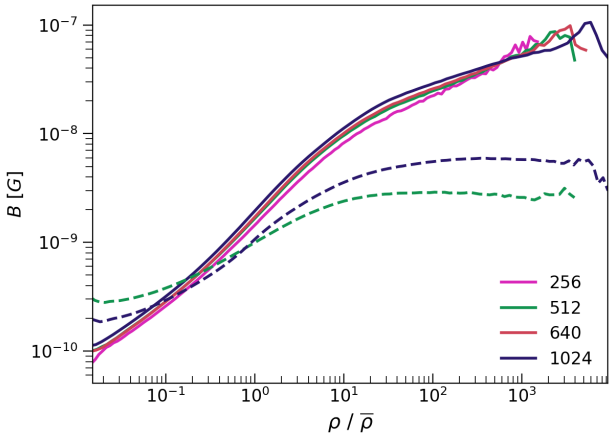

Figure 9.2: The median magnetic field versus overdensity profile for increasing grid points $(256, 512, 640, 1024)$ at $z = 0.02$. Solid lines: uniform seeding case; dashed lines helical case.

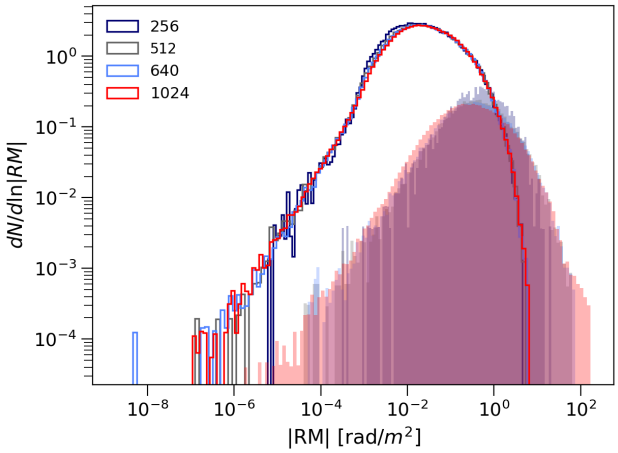

Figure 9.3: |RM| distribution function dependence on resolution (comoving: 264 h^{-1}kpc, 132 h^{-1}kpc, 105 h^{-1}kpc, 66 h^{-1}kpc) at $z = 0.02$ for the uniform seeding. The solid lines represent regions excluding galaxy clusters, while the shaded areas show distributions only for galaxy clusters.

magnetic energy in Fourier space for the uniform seeding (solid lines) would be underestimated on scales $\sim k > 0.5\,h\,\mathrm{Mpc}^{-1}$ (cluster scales), while in the helical case (dashed lines) only the minor difference is expected when doubling the resolution. As we can also see the larger scales $k \lesssim 0.5\,h\,\mathrm{Mpc}^{-1}$ are well converged in our simulations.

Conversely, we can see in Figure 9.2 that the median profiles show no differences in the trends when the higher-resolution simulation is seeded by the uniform magnetic field. On the other hand, in the case of helical seeding (dashed lines), higher magnetic field strength is achieved in the filaments' and clusters' regions and lower strengths in the voids for the higher-resolution run. Therefore, we would expect the differences between the inflationary and phase-transitional models to be decreased in these regions as a result of higher resolution.

In Figure 9.3 we also show the resolution dependence of the PDF of absolute RM. We see that RM values show convergence in the regions where we exclude galaxy clusters, while RMs in galaxy clusters are mostly affected at the high-end and low-end tail of the distribution. This means that our analysis of Sec. 6.6 will be more affected in galaxy-cluster regions.

9.2.2 Testing the Riemann solver

An important aspect of our work is also to determine the dependencies of our results on the adopted numerical methods. As discussed in Section 7.3.1, PMFs are expected to heat the IGM at high redshifts. Nevertheless, the absence of heating and cooling physics in our simulations poses a challenge for the interpretation of large thermal energies observed in the turbulent helical and nonhelical models at redshifts $z > 10$ (see Figure 6.5). In order to check the energy evolution, we have tested our setup with two different Riemann solvers, the LLF and the HLL. Note that the LLF scheme is considerably more diffusive than the HLL scheme. In Figure 9.4 we show the evolution of thermal, kinetic, and magnetic energies obtained from these two setups. Additionally, we show the evolution of thermal and kinetic energies for a $B = 0$ case using the HLL Riemann solver. As we can see, the pure hydrodynamical setup shows the lowest thermal energy at high redshifts

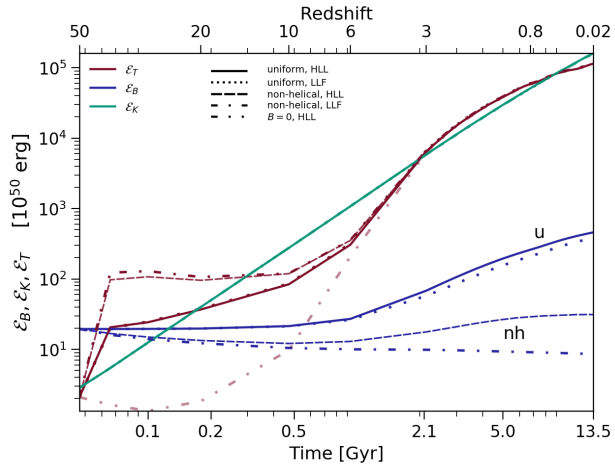

Figure 9.4: Evolution of magnetic, thermal, and kinetic energies for the uniform and nonhelical cases when using HLL (solid, dashed, dashed-dotted lines, where the latter corresponds to the $B = 0$ case) and LLF (dotted and dashed-dotted lines) Riemann solver schemes.

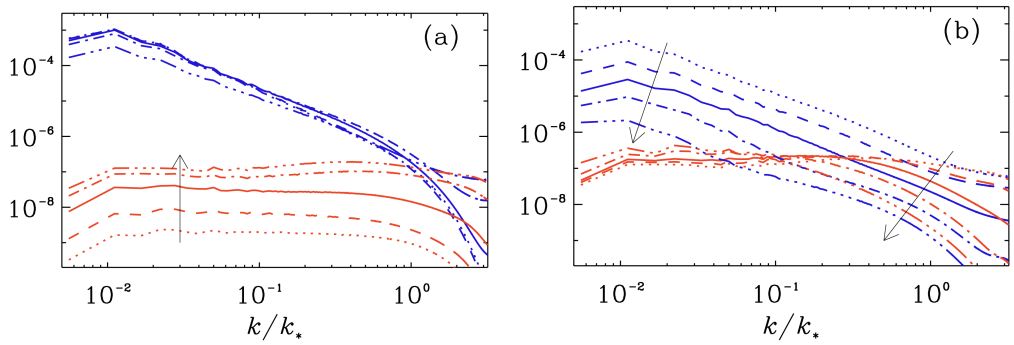

Figure 9.5: MHD simulations with an initial kinetic energy spectrum proportional to k^{-2} in the presence of a weak homogeneous magnetic field. Panels (a) and (b) show the early and late evolution for magnetic energy spectra (red) and kinetic energy spectra (blue).

in comparison to the MHD cases. On the other hand, the evolutionary trends of the thermal and kinetic energies in the MHD cases are not affected by the change of Riemann solvers. This shows that the already observed differences between turbulent, nonhelical and uniform models in thermal energy (see discussion in Section 7.3.1) are not dependent on the selection of the Riemann solver. However, the LLF scheme substantially affects the evolution of the magnetic energy in the nonhelical case. The stronger numerical diffusion completely suppresses the magnetic field amplification at lower redshifts, suggesting that this method may not be optimal for the study of stochastic PMFs.

9.2.3 Tangling of a homogeneous field

In Section 6.5, we noted the rather different response to an imposed (uniform) magnetic field in the present simulations (see the first panel of Figure 6.6) and those of [216], where magnetic fields at the scale of the domain began to grow only after smaller-scale magnetic fields have grown first. An important difference, however, is that our present cosmological simulations always possess a large-scale velocity field, which was not present in the sim-

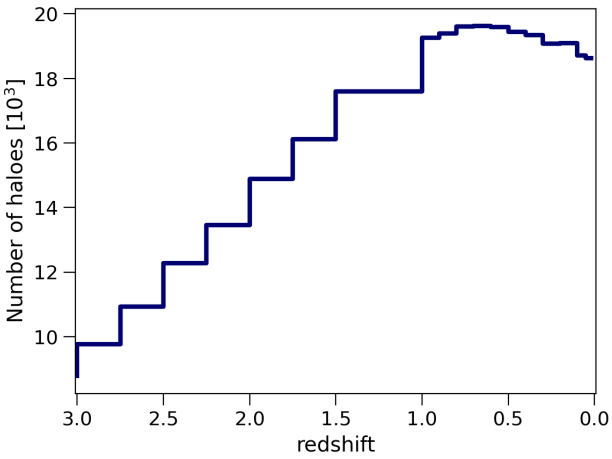

Figure 9.6: Number of virialized objects with baryonic mass range $10^7 M_\odot \leq M \leq 10^{10} M_\odot$ as function of redshift. The masses have been calculated within the sphere enclosing the virial radius of each source. This radius is an output of the *yt* halo finder.

ulations of [216]. The large-scale velocity field in the cosmological simulations leads to tangling of the uniform imposed magnetic field, which leads to the instantaneous growth immediately at the beginning of the simulation.

To verify our reasoning above, we now repeat the simulations presented in Figure 5 of [216] with a weak imposed field, but now with a random initial velocity field with an initial kinetic energy spectrum proportional to k^{-2}. The result is shown in Figure 9.5, where we show the resulting magnetic and kinetic energy spectra. Note the increase of spectral magnetic energy at all wavenumbers already occurs from early times onwards. This is caused by the tangling of the homogeneous magnetic field by the initial large-scale velocity field with a k^{-2} spectrum. This therefore confirms our reasoning in Section 6.5 concerning the rather different response to an imposed magnetic field in the present simulations and those of [216].

9.2.4 RM sources

As we mentioned in Sec. 6.6 our statistical RM analysis does not take into account the spatial distribution of sources at each redshift. Nevertheless, we show the expected redshift distribution of sources in Figure 9.6 for completeness. For this Figure, we used the *yt* halo finder [328], which identifies the groups of linked DM particles based on the [329] algorithm, for each redshift in order to find a selected number of haloes with a baryonic mass range, $10^7 M_\odot \leq M \leq 10^{10} M_\odot$. This range resembles the masses of FRII galaxies, which are the typical type of polarised sources found in large catalogs (see e.g., [364, 365]).

9.3 Galaxy cluster project

9.3.1 Resolution tests & Divergence

In this appendix we discuss the dependence of the results of Chapter 7 on the adopted spatial resolution. We use the same initial conditions and perform different simulations increasing the levels of AMR. We show the results corresponding to a maximum of 5, 6

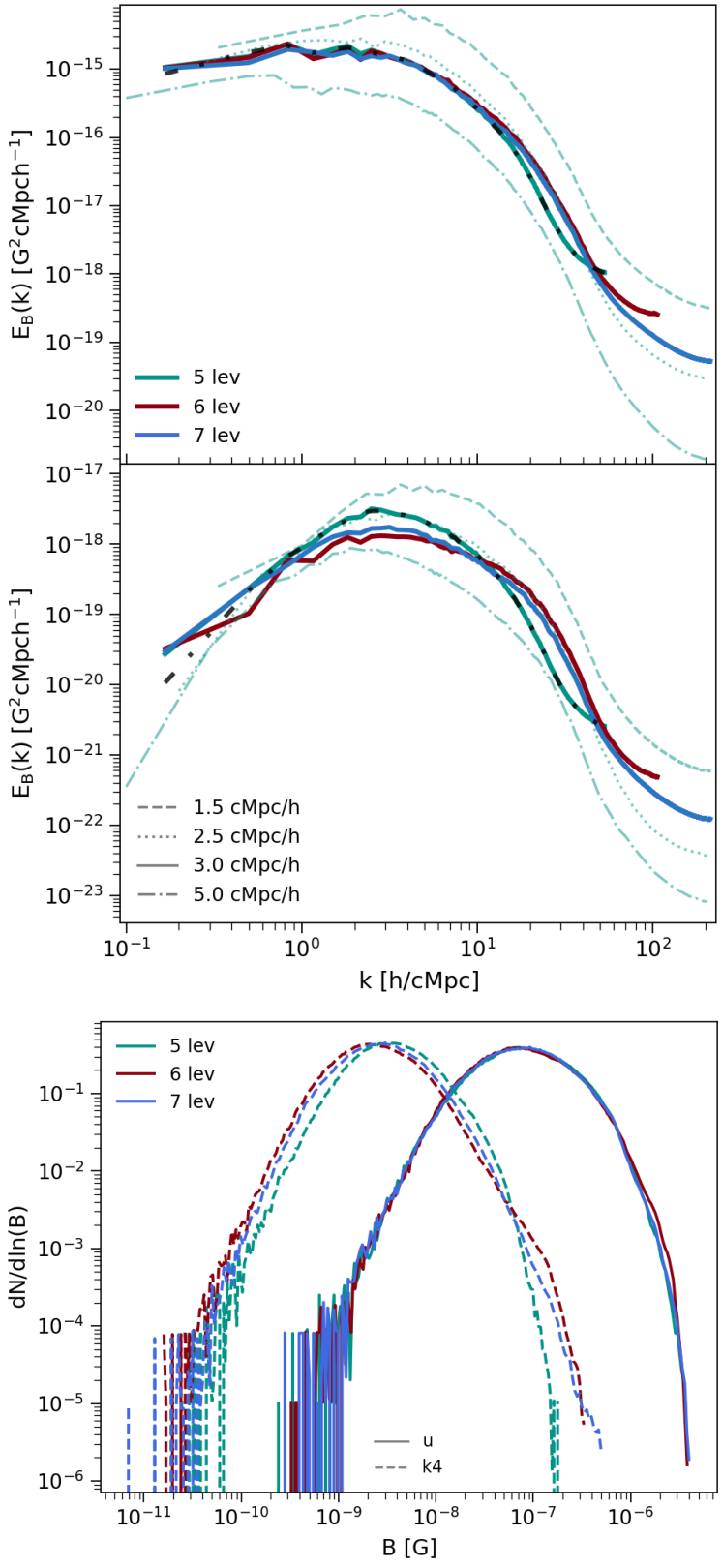

Figure 9.7: *Upper panels*: Magnetic energy power spectrum calculated for different AMR levels and different box sizes at $z = 0$. We show the uniform (top panel) and Batchelor (middle panel) cases. The black, dashed, and dashed-dotted lines in each panel show the power spectrum calculated from a zero-padded array. *Lower panel*: Magnetic field PDFs of the uniform (*solid* lines) and Batchelor (*dashed* lines) models at $z = 0$ at different AMR levels.

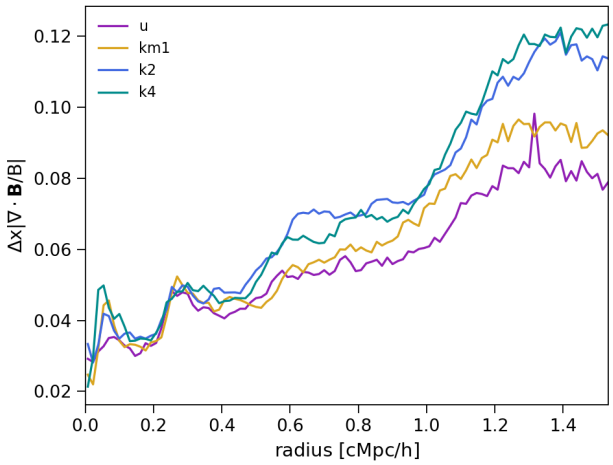

Figure 9.8: Normalized divergence of the magnetic field from the simulation with a maximum of 7 levels of AMR (where Δ is the mesh spacing in the x-direction).

and 7 levels of AMR in Figure 9.7. The dependence on spatial resolution of the magnetic power spectrum and the PDF of the magnetic field is shown with different colors. Even though we see more variation for the Batchelor model (middle panel and dashed lines of bottom panel), we observe convergence of both the uniform and Batchelor models already at the 6th level of AMR and we see no significant change in the shape of the magnetic energy spectra.

The spectral analysis based on Fourier transforms is a common approach to study the scale dependence of the magnetic energy. Nevertheless, some caveats of this approach come from the effects of a limited box size and the non-periodicity of the data. In Figure 9.7 we show the outcome of these effects on the magnetic energy spectra for the simulated uniform and Batchelor models. First, we see that for $k \lesssim 50\,h\,\mathrm{cMpc}^{-1}$, corresponding to scales $\gtrsim 20\,h^{-1}\mathrm{ckpc}$, the spectra are well converged in the uniform model. The shape of the magnetic spectra for both uniform and Batchelor models is also mostly consistent with the spectra calculated in smaller/larger boxes. As expected, the amplitude of the spectrum is more strongly affected by the size of the analysed region. In particular, we see ~ 1 order of magnitude variation on the scales of $\sim 140\,h^{-1}\mathrm{ckpc}$ for the uniform as well as Batchelor model.

We also note that the non-periodic boundary conditions of the selected box may distort the spectrum. In order to check this, we calculated the power spectra from the zero-padded array, extracted for $(3\,h^{-1}\mathrm{cMpc})^3$ volume from the 5-level-AMR simulation (see the black dashed-dotted lines in Figure 9.7). As seen in the figure, the power spectrum calculated using the standard method and zero-padding lead to similar results and show that our results presented in the main text are not significantly affected by the non-periodicity of the data.

Finally, in Figure 9.8 we show the radial profile of the magnetic field divergence in our simulated cluster. The largest differences between the models arise at $r \gtrsim 1\,h^{-1}\mathrm{cMpc}$. with the stochastic models having the largest values of the divergence. Nevertheless, as mentioned in Section 6.7, $\nabla \cdot \mathbf{B}$ stays reasonably low in our four models in the largest fraction of the simulated cluster volume. Quantitatively, we find that the normalised divergence stays below 10%.

9.3.2 Distribution of AMR levels

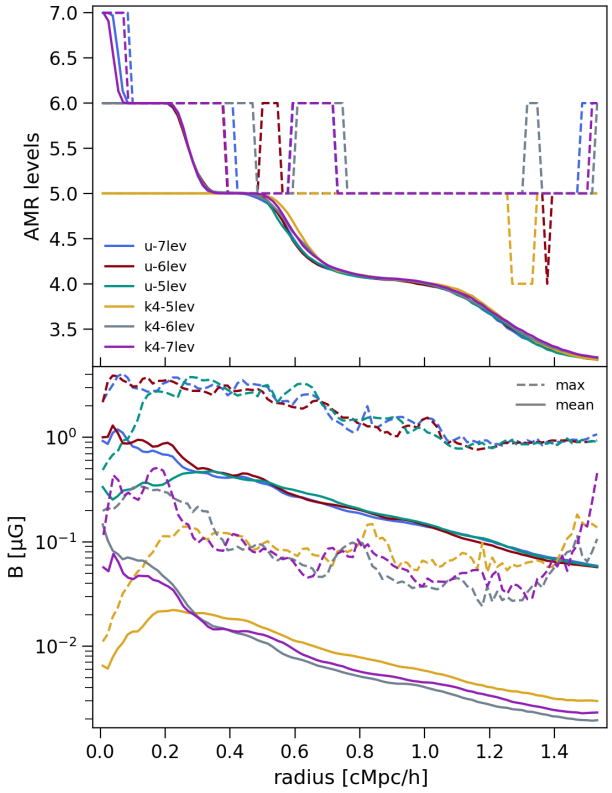

Figure 9.9: Radial distribution of refinement levels and magnetic field. The mean and maximum within each radial bin are shown with solid and dashed lines, respectively. The profiles are shown for the uniform and Batchelor models calculated from a sphere with a $R_{\rm rvir}$ radius.

Similar to [45], we show the radial profile of AMR levels along with the magnetic field profile in Figure 9.9 for the uniform and Batchelor cases from our galaxy cluster study (Chapter 7). In the top panel of Figure 9.9 we see that our simulated cluster is resolved with a maximum of 5 AMR levels (with $9.77\,h^{-1}\mathrm{ckpc}$ resolution) in the $(1.5\ h^{-1}\mathrm{cMpc})^3$ central region while the mean AMR level decreases towards the outskirts. On the other hand, the magnetic field profiles (bottom panel of Figure 9.9) show larger strengths only in the cluster core when the number of the maximum level of AMR is increased from 5 to 7. Our AMR scheme is different from the one used in [45] where the cluster is refined at least up to a 6th AMR level even in the cluster outskirts. An important difference, however, between the simulated clusters used in this work and in [45] is the mass of the cluster which is one order of magnitude larger in the latter work.

In addition, we checked the convergence of our AMR scheme by running an extra simulation with a maximum of 8 levels of AMR (for the Batchelor model, not shown). We do not see an important improvement in the AMR coverage of the cluster region by using higher levels of AMR. Therefore, given our selected refinement parameters, our AMR scheme converges already at 6 AMR levels.

Bibliography

[1] A. Botteon, R. Cassano, R. J. van Weeren, T. W. Shimwell, A. Bonafede, M. Brggen, G. Brunetti, V. Cuciti, D. Dallacasa, F. de Gasperin, G. Di Gennaro, F. Gastaldello, D. N. Hoang, M. Rossetti, and H. J. A. Röttgering, "Discovery of a Radio Halo (and Relic) in a $M_{500}¡2{\times}10^{14}$ $M_{\odot}$ Cluster," ApJ, vol. 914, p. L29, June 2021.

[2] F. Govoni, E. Orrù, A. Bonafede, M. Iacobelli, R. Paladino, F. Vazza, M. Murgia, V. Vacca, G. Giovannini, L. Feretti, F. Loi, G. Bernardi, C. Ferrari, R. F. Pizzo, C. Gheller, S. Manti, M. Brüggen, G. Brunetti, R. Cassano, F. de Gasperin, T. A. Enßlin, M. Hoeft, C. Horellou, H. Junklewitz, H. J. A. Röttgering, A. M. M. Scaife, T. W. Shimwell, R. J. van Weeren, and M. Wise, "A radio ridge connecting two galaxy clusters in a filament of the cosmic web," *Science*, vol. 364, pp. 981–984, June 2019.

[3] C. A. Scharf, D. R. Zurek, and M. Bureau, "The Chandra Fornax Survey. I. The Cluster Environment," ApJ, vol. 633, pp. 154–164, Nov. 2005.

[4] C. Jones, C. Stern, W. Forman, J. Breen, L. David, W. Tucker, and M. Franx, "X-Ray Emission from the Fornax Cluster," ApJ, vol. 482, pp. 143–155, June 1997.

[5] C. S. Anderson, G. H. Heald, J. A. Eilek, E. Lenc, B. M. Gaensler, L. Rudnick, C. L. Van Eck, S. P. O'Sullivan, J. M. Stil, A. Chippendale, C. J. Riseley, E. Carretti, J. West, J. Farnes, L. Harvey-Smith, N. M. McClure-Griffiths, D. C. J. Bock, J. D. Bunton, B. Koribalski, C. D. Tremblay, M. A. Voronkov, and K. Warhurst, "Early Science from POSSUM: Shocks, turbulence, and a massive new reservoir of ionised gas in the Fornax cluster," PASA, vol. 38, p. e020, Apr. 2021.

[6] T. Vachaspati, "Progress on cosmological magnetic fields," *Reports on Progress in Physics*, vol. 84, p. 074901, July 2021.

[7] M. Ackermann, M. Ajello, L. Baldini, J. Ballet, G. Barbiellini, D. Bastieri, R. Bellazzini, E. Bissaldi, R. D. Blandford, E. D. Bloom, R. Bonino, E. Bottacini, T. J. Brandt, J. Bregeon, P. Bruel, R. Buehler, R. A. Cameron, R. Caputo, P. A. Caraveo, D. Castro, E. Cavazzuti, E. Charles, C. C. Cheung, G. Chiaro, S. Ciprini, J. Cohen-Tanugi, D. Costantin, S. Cutini, F. D'Ammand o, F. de Palma, A. Desai, N. Di Lalla, M. Di Mauro, L. Di Venere, C. Favuzzi, J. Finke, A. Franckowiak, Y. Fukazawa, S. Funk, P. Fusco, F. Gargano, D. Gasparrini, N. Giglietto, F. Giordano, M. Giroletti, D. Green, I. A. Grenier, L. Guillemot, S. Guiriec, E. Hays, J. W. Hewitt, D. Horan, G. Jóhannesson, S. Kensei, M. Kuss, S. Larsson, L. Latronico, M. Lemoine-Goumard, J. Li, F. Longo, F. Loparco, M. N. Lovellette, P. Lubrano, J. D. Magill, S. Maldera, A. Manfreda, M. N. Mazziotta, J. E. McEnery,

M. Meyer, T. Mizuno, M. E. Monzani, A. Morselli, I. V. Moskalenko, M. Negro, E. Nuss, N. Omodei, M. Orienti, E. Orlando, J. F. Ormes, M. Palatiello, V. S. Paliya, D. Paneque, J. S. Perkins, M. Persic, M. Pesce-Rollins, F. Piron, T. A. Porter, G. Principe, S. Rainò, R. Rando, B. Rani, S. Razzaque, A. Reimer, O. Reimer, T. Reposeur, C. Sgrò, E. J. Siskind, G. Spandre, P. Spinelli, D. J. Suson, H. Tajima, J. B. Thayer, L. Tibaldo, D. F. Torres, G. Tosti, J. Valverde, T. M. Venters, M. Vogel, K. Wood, M. Wood, G. Zaharijas, Fermi-LAT Collaboration, and J. Biteau, "The Search for Spatial Extension in High-latitude Sources Detected by the Fermi Large Area Telescope," ApJS, vol. 237, p. 32, Aug. 2018.

[8] F. Aharonian *et al.*, "New constraints on the mid-IR EBL from the HESS discovery of VHE γ-rays from 1ES 0229+200," A&A, vol. 475, pp. L9–L13, Nov. 2007.

[9] R. Alves Batista and A. Saveliev, "The Gamma-Ray Window to Intergalactic Magnetism," *Universe*, vol. 7, p. 223, July 2021.

[10] S. Mtchedlidze, P. Domínguez-Fernández, X. Du, A. Brandenburg, T. Kahniashvili, S. O'Sullivan, W. Schmidt, and M. Brüggen, "Evolution of primordial magnetic fields during large-scale structure formation," *The Astrophysical Journal*, vol. 929, p. 127, apr 2022.

[11] S. Mtchedlidze, P. Domínguez-Fernández, X. Du, W. Schmidt, A. Brandenburg, J. Niemeyer, and T. Kahniashvili, "Inflationary and phase-transitional primordial magnetic fields in galaxy clusters," *arXiv e-prints*, p. arXiv:2210.10183, Oct. 2022.

[12] E. G. Blackman, "Magnetic Helicity and Large Scale Magnetic Fields: A Primer," Space Sci. Rev., vol. 188, pp. 59–91, May 2015.

[13] M. S. Pshirkov, P. G. Tinyakov, and F. R. Urban, "New Limits on Extragalactic Magnetic Fields from Rotation Measures," Phys. Rev. Lett., vol. 116, p. 191302, May 2016.

[14] T. Vernstrom, B. M. Gaensler, L. Rudnick, and H. Andernach, "Differences in Faraday Rotation between Adjacent Extragalactic Radio Sources as a Probe of Cosmic Magnetic Fields," ApJ, vol. 878, p. 92, June 2019.

[15] S. P. O'Sullivan, M. Brüggen, F. Vazza, E. Carretti, N. T. Locatelli, C. Stuardi, V. Vacca, T. Vernstrom, G. Heald, C. Horellou, T. W. Shimwell, M. J. Hardcastle, C. Tasse, and H. Röttgering, "New constraints on the magnetization of the cosmic web using LOFAR Faraday rotation observations," MNRAS, vol. 495, pp. 2607–2619, July 2020.

[16] M. Brüggen, T. H. Reiprich, E. Bulbul, B. S. Koribalski, H. Andernach, L. Rudnick, D. N. Hoang, A. G. Wilber, S. W. Duchesne, A. Veronica, F. Pacaud, A. M. Hopkins, R. P. Norris, M. Johnston-Hollitt, M. J. I. Brown, A. Bonafede, G. Brunetti, J. D. Collier, J. S. Sanders, E. Vardoulaki, T. Venturi, A. D. Kapinska, and J. Marvil, "Radio observations of the merging galaxy cluster system Abell 3391-Abell 3395," A&A, vol. 647, p. A3, Mar. 2021.

[17] T. Vernstrom, G. Heald, F. Vazza, T. Galvin, J. West, N. Locatelli, N. Fornengo, and E. Pinetti, "Discovery of Magnetic Fields Along Stacked Cosmic Filaments

as Revealed by Radio and X-Ray Emission," *arXiv e-prints*, p. arXiv:2101.09331, Jan. 2021.

[18] A. Bonafede, L. Feretti, M. Murgia, F. Govoni, G. Giovannini, D. Dallacasa, K. Dolag, and G. B. Taylor, "The Coma cluster magnetic field from Faraday rotation measures," A&A, vol. 513, p. A30, Apr. 2010.

[19] F. Govoni, M. Murgia, V. Vacca, F. Loi, M. Girardi, F. Gastaldello, G. Giovannini, L. Feretti, R. Paladino, E. Carretti, R. Concu, A. Melis, S. Poppi, G. Valente, G. Bernardi, A. Bonafede, W. Boschin, M. Brienza, T. E. Clarke, S. Colafrancesco, F. de Gasperin, D. Eckert, T. A. Enßlin, C. Ferrari, L. Gregorini, M. Johnston-Hollitt, H. Junklewitz, E. Orrù, P. Parma, R. Perley, M. Rossetti, G. B Taylor, and F. Vazza, "Sardinia Radio Telescope observations of Abell 194. The intra-cluster magnetic field power spectrum," A&A, vol. 603, p. A122, July 2017.

[20] C. Stuardi, A. Bonafede, L. Lovisari, P. Domínguez-Fernández, F. Vazza, M. Brüggen, R. J. van Weeren, and F. de Gasperin, "The intracluster magnetic field in the double relic galaxy cluster Abell 2345," MNRAS, vol. 502, pp. 2518–2535, Apr. 2021.

[21] Planck Collaboration, P. A. R. Ade, N. Aghanim, M. Arnaud, F. Arroja, M. Ashdown, J. Aumont, C. Baccigalupi, M. Ballardini, A. J. Banday, R. B. Barreiro, N. Bartolo, E. Battaner, K. Benabed, A. Benoît, A. Benoit-Lévy, J. P. Bernard, M. Bersanelli, P. Bielewicz, J. J. Bock, A. Bonaldi, L. Bonavera, J. R. Bond, J. Borrill, F. R. Bouchet, M. Bucher, C. Burigana, R. C. Butler, E. Calabrese, J. F. Cardoso, A. Catalano, A. Chamballu, H. C. Chiang, J. Chluba, P. R. Christensen, S. Church, D. L. Clements, S. Colombi, L. P. L. Colombo, C. Combet, F. Couchot, A. Coulais, B. P. Crill, A. Curto, F. Cuttaia, L. Danese, R. D. Davies, R. J. Davis, P. de Bernardis, A. de Rosa, G. de Zotti, J. Delabrouille, F. X. Désert, J. M. Diego, K. Dolag, H. Dole, S. Donzelli, O. Doré, M. Douspis, A. Ducout, X. Dupac, G. Efstathiou, F. Elsner, T. A. Enßlin, H. K. Eriksen, J. Fergusson, F. Finelli, E. Florido, O. Forni, M. Frailis, A. A. Fraisse, E. Franceschi, A. Frejsel, S. Galeotta, S. Galli, K. Ganga, M. Giard, Y. Giraud-Héraud, E. Gjerløw, J. González-Nuevo, K. M. Górski, S. Gratton, A. Gregorio, A. Gruppuso, J. E. Gudmundsson, F. K. Hansen, D. Hanson, D. L. Harrison, G. Helou, S. Henrot-Versillé, C. Hernández-Monteagudo, D. Herranz, S. R. Hildebrand t, E. Hivon, M. Hobson, W. A. Holmes, A. Hornstrup, W. Hovest, K. M. Huffenberger, G. Hurier, A. H. Jaffe, T. R. Jaffe, W. C. Jones, M. Juvela, E. Keihänen, R. Keskitalo, J. Kim, T. S. Kisner, J. Knoche, M. Kunz, H. Kurki-Suonio, G. Lagache, A. Lähteenmäki, J. M. Lamarre, A. Lasenby, M. Lattanzi, C. R. Lawrence, J. P. Leahy, R. Leonardi, J. Lesgourgues, F. Levrier, M. Liguori, P. B. Lilje, M. Linden-Vørnle, M. López-Caniego, P. M. Lubin, J. F. Macías-Pérez, G. Maggio, D. Maino, N. Mand olesi, A. Mangilli, M. Maris, P. G. Martin, E. Martínez-González, S. Masi, S. Matarrese, P. McGehee, P. R. Meinhold, A. Melchiorri, L. Mendes, A. Mennella, M. Migliaccio, S. Mitra, M. A. Miville-Deschênes, D. Molinari, A. Moneti, L. Montier, G. Morgante, D. Mortlock, A. Moss, D. Munshi, J. A. Murphy, P. Naselsky, F. Nati, P. Natoli, C. B. Netterfield, H. U. Nørgaard-Nielsen, F. Noviello, D. Novikov, I. Novikov, N. Oppermann, C. A. Oxborrow, F. Paci, L. Pagano, F. Pajot, D. Paoletti, F. Pasian, G. Patanchon, O. Perdereau, L. Perotto, F. Perrotta, V. Pettorino,

F. Piacentini, M. Piat, E. Pierpaoli, D. Pietrobon, S. Plaszczynski, E. Pointecouteau, G. Polenta, L. Popa, G. W. Pratt, G. Prézeau, S. Prunet, J. L. Puget, J. P. Rachen, R. Rebolo, M. Reinecke, M. Remazeilles, C. Renault, A. Renzi, I. Ristorcelli, G. Rocha, C. Rosset, M. Rossetti, G. Roudier, J. A. Rubiño-Martín, B. Ruiz-Granados, B. Rusholme, M. Sandri, D. Santos, M. Savelainen, G. Savini, D. Scott, M. D. Seiffert, E. P. S. Shellard, M. Shiraishi, L. D. Spencer, V. Stolyarov, R. Stompor, R. Sudiwala, R. Sunyaev, D. Sutton, A. S. Suur-Uski, J. F. Sygnet, J. A. Tauber, L. Terenzi, L. Toffolatti, M. Tomasi, M. Tristram, M. Tucci, J. Tuovinen, G. Umana, L. Valenziano, J. Valiviita, B. Van Tent, P. Vielva, F. Villa, L. A. Wade, B. D. Wandelt, I. K. Wehus, D. Yvon, A. Zacchei, and A. Zonca, "Planck 2015 results. XIX. Constraints on primordial magnetic fields," A&A, vol. 594, p. A19, Sept. 2016.

[22] A. Brandenburg and T. Kahniashvili, "Classes of Hydrodynamic and Magnetohydrodynamic Turbulent Decay," Phys. Rev. Lett., vol. 118, p. 055102, Feb. 2017.

[23] R. Durrer and A. Neronov, "Cosmological magnetic fields: their generation, evolution and observation," A&A Rev., vol. 21, p. 62, June 2013.

[24] A. Brandenburg, T. Kahniashvili, S. Mandal, A. R. Pol, A. G. Tevzadze, and T. Vachaspati, "Evolution of hydromagnetic turbulence from the electroweak phase transition," Phys. Rev. D, vol. 96, p. 123528, Dec. 2017.

[25] P. MacNeice, K. M. Olson, C. Mobarry, R. de Fainchtein, and C. Packer, "PARAMESH: A parallel adaptive mesh refinement community toolkit," *Computer Physics Communications*, vol. 126, pp. 330–354, Apr. 2000.

[26] A. A. Schekochihin, S. C. Cowley, S. F. Taylor, J. L. Maron, and J. C. McWilliams, "Simulations of the Small-Scale Turbulent Dynamo," ApJ, vol. 612, pp. 276–307, Sept. 2004.

[27] M. J. Turk, B. D. Smith, J. S. Oishi, S. Skory, S. W. Skillman, T. Abel, and M. L. Norman, "yt: A Multi-code Analysis Toolkit for Astrophysical Simulation Data," *The Astrophysical Journal Supplement Series*, vol. 192, p. 9, Jan. 2011.

[28] A. Bonafede, F. Vazza, M. Brüggen, T. Akahori, E. Carretti, S. Colafrancesco, L. Feretti, C. Ferrari, G. Giovannini, F. Govoni, M. Johnston-Hollitt, M. Murgia, A. Scaife, V. Vacca, F. Govoni, L. Rudnick, and A. Scaife, "Unravelling the origin of large-scale magnetic fields in galaxy clusters and beyond through Faraday Rotation Measures with the SKA," in *Advancing Astrophysics with the Square Kilometre Array (AASKA14)*, p. 95, Apr. 2015.

[29] A. Brandenburg, H. Zhou, and R. Sharma, "Batchelor, Saffman, and Kazantsev spectra in galactic small-scale dynamos," *arXiv e-prints*, p. arXiv:2207.09414, July 2022.

[30] D. J. Stevenson, "Planetary Magnetic Fields: Achievements and Prospects," Space Sci. Rev., vol. 152, pp. 651–664, May 2010.

[31] G. Schubert and K. M. Soderlund, "Planetary magnetic fields: Observations and models," *Physics of the Earth and Planetary Interiors*, vol. 187, pp. 92–108, Aug. 2011.

[32] R. Beck, "Galactic and Extragalactic Magnetic Fields," Space Sci. Rev., vol. 99, pp. 243–260, Oct. 2001.

[33] R. Beck and R. Wielebinski, *Magnetic Fields in Galaxies*, vol. 5, p. 641. 2013.

[34] M. Murgia, F. Govoni, L. Feretti, G. Giovannini, D. Dallacasa, R. Fanti, G. B. Taylor, and K. Dolag, "Magnetic fields and Faraday rotation in clusters of galaxies," A&A, vol. 424, pp. 429–446, Sept. 2004.

[35] C. Vogt and T. A. Enßlin, "A Bayesian view on Faraday rotation maps Seeing the magnetic power spectra in galaxy clusters," A&A, vol. 434, pp. 67–76, Apr. 2005.

[36] A. Botteon, T. W. Shimwell, A. Bonafede, D. Dallacasa, G. Brunetti, S. Mandal, R. J. van Weeren, M. Brüggen, R. Cassano, F. de Gasperin, D. N. Hoang, M. Hoeft, H. J. A. Röttgering, F. Savini, G. J. White, A. Wilber, and T. Venturi, "LOFAR discovery of a double radio halo system in Abell 1758 and radio/X-ray study of the cluster pair," MNRAS, vol. 478, pp. 885–898, July 2018.

[37] A. Botteon, R. Cassano, D. Eckert, G. Brunetti, D. Dallacasa, T. W. Shimwell, R. J. van Weeren, F. Gastaldello, A. Bonafede, M. Brüggen, L. Bîrzan, S. Clavico, V. Cuciti, F. de Gasperin, S. De Grandi, S. Ettori, S. Ghizzardi, M. Rossetti, H. J. A. Röttgering, and M. Sereno, "Particle acceleration in a nearby galaxy cluster pair: the role of cluster dynamics," A&A, vol. 630, p. A77, Oct. 2019.

[38] R. M. Kulsrud and E. G. Zweibel, "The Origin of Astrophysical Magnetic Fields," *Rept. Prog. Phys.*, vol. 71, p. 0046091, 2008.

[39] D. Ryu, H. Kang, J. Cho, and S. Das, "Turbulence and Magnetic Fields in the Large-Scale Structure of the Universe," *Science*, vol. 320, p. 909, May 2008.

[40] A. Kandus, K. E. Kunze, and C. G. Tsagas, "Primordial magnetogenesis," Phys. Rep., vol. 505, pp. 1–58, Aug. 2011.

[41] R. Pakmor, F. A. Gómez, R. J. J. Grand, F. Marinacci, C. M. Simpson, V. Springel, D. J. R. Campbell, C. S. Frenk, T. Guillet, C. Pfrommer, and S. D. M. White, "Magnetic field formation in the Milky Way like disc galaxies of the Auriga project," MNRAS, vol. 469, pp. 3185–3199, Aug. 2017.

[42] M. Rieder and R. Teyssier, "A small-scale dynamo in feedback-dominated galaxies - II. The saturation phase and the final magnetic configuration," MNRAS, vol. 471, pp. 2674–2686, Nov. 2017.

[43] U. P. Steinwandel, K. Dolag, H. Lesch, B. P. Moster, A. Burkert, and A. Prieto, "On the origin of magnetic driven winds and the structure of the galactic dynamo in isolated galaxies," MNRAS, vol. 494, pp. 4393–4412, May 2020.

[44] H. Xu, H. Li, D. C. Collins, S. Li, and M. L. Norman, "Turbulence and Dynamo in Galaxy Cluster Medium: Implications on the Origin of Cluster Magnetic Fields," ApJ, vol. 698, pp. L14–L17, June 2009.

[45] F. Vazza, G. Brunetti, M. Brüggen, and A. Bonafede, "Resolved magnetic dynamo action in the simulated intracluster medium," MNRAS, vol. 474, pp. 1672–1687, Feb. 2018.

[46] P. Domínguez-Fernández, F. Vazza, M. Brüggen, and G. Brunetti, "Dynamical evolution of magnetic fields in the intracluster medium," MNRAS, vol. 486, pp. 623–638, June 2019.

[47] U. P. Steinwandel, L. M. Boess, K. Dolag, and H. Lesch, "On the small scale turbulent dynamo in the intracluster medium: A comparison to dynamo theory," *arXiv e-prints*, p. arXiv:2108.07822, Aug. 2021.

[48] L. Biermann, "Über den Ursprung der Magnetfelder auf Sternen und im interstellaren Raum (miteinem Anhang von A. Schlüter)," *Zeitschrift Naturforschung Teil A*, vol. 5, p. 65, Jan. 1950.

[49] E. R. Harrison, "Generation of magnetic fields in the radiation ERA," MNRAS, vol. 147, p. 279, Jan. 1970.

[50] S. Bertone, C. Vogt, and T. Enßlin, "Magnetic field seeding by galactic winds," MNRAS, vol. 370, pp. 319–330, July 2006.

[51] J. Donnert, K. Dolag, H. Lesch, and E. Müller, "Cluster magnetic fields from galactic outflows," *Mon. Not. Roy. Astron. Soc.*, vol. 392, pp. 1008–1021, Jan. 2009.

[52] H. Xu, H. Li, D. C. Collins, S. Li, and M. L. Norman, "Evolution and Distribution of Magnetic Fields from Active Galactic Nuclei in Galaxy Clusters. II. The Effects of Cluster Size and Dynamical State," ApJ, vol. 739, p. 77, Oct. 2011.

[53] F. Vazza, M. Brüggen, C. Gheller, S. Hackstein, D. Wittor, and P. M. Hinz, "Simulations of extragalactic magnetic fields and of their observables," *Classical and Quantum Gravity*, vol. 34, p. 234001, Dec. 2017.

[54] M. S. Turner and L. M. Widrow, "Inflation-produced, large-scale magnetic fields," *Phys. Rev. D*, vol. 37, pp. 2743–2754, May 1988.

[55] B. Ratra, "Cosmological "Seed" Magnetic Field from Inflation," ApJ, vol. 391, p. L1, May 1992.

[56] S. Mukohyama, "Stealth magnetic field in de Sitter spacetime," Phys. Rev. D, vol. 94, p. 121302, Dec. 2016.

[57] T. Kahniashvili, A. Brandenburg, A. e. G. Tevzadze, and B. Ratra, "Numerical simulations of the decay of primordial magnetic turbulence," Phys. Rev. D, vol. 81, p. 123002, June 2010.

[58] J. M. Cornwall, "Speculations on primordial magnetic helicity," Phys. Rev. D, vol. 56, pp. 6146–6154, Nov. 1997.

[59] M. Giovannini and M. E. Shaposhnikov, "Primordial magnetic fields, anomalous isocurvature fluctuations and big bang nucleosynthesis," *Phys. Rev. Lett.*, vol. 80, pp. 22–25, 1998.

[60] T. Vachaspati, "Estimate of the Primordial Magnetic Field Helicity," Phys. Rev. Lett., vol. 87, p. 251302, Dec. 2001.

[61] M. L. Bernet, F. Miniati, S. J. Lilly, P. P. Kronberg, and M. Dessauges-Zavadsky, "Strong magnetic fields in normal galaxies at high redshift," Nature, vol. 454, pp. 302–304, July 2008.

[62] G. Di Gennaro, R. J. van Weeren, G. Brunetti, R. Cassano, M. Brüggen, M. Hoeft, T. W. Shimwell, H. J. A. Röttgering, A. Bonafede, A. Botteon, V. Cuciti, D. Dallacasa, F. de Gasperin, P. Domínguez-Fernández, T. A. Enßlin, F. Gastaldello, S. Mandal, M. Rossetti, and A. Simionescu, "Fast magnetic field amplification in distant galaxy clusters," *Nature Astronomy*, vol. 5, pp. 268–275, Jan. 2021.

[63] Y. Luo, T. Kajino, M. Kusakabe, and G. J. Mathews, "Big Bang Nucleosynthesis with an Inhomogeneous Primordial Magnetic Field Strength," ApJ, vol. 872, p. 172, Feb. 2019.

[64] R. Durrer, P. G. Ferreira, and T. Kahniashvili, "Tensor microwave anisotropies from a stochastic magnetic field," Phys. Rev. D, vol. 61, p. 043001, Feb. 2000.

[65] A. Mack, T. Kahniashvili, and A. Kosowsky, "Microwave background signatures of a primordial stochastic magnetic field," *Phys. Rev. D*, vol. 65, p. 123004, Jun 2002.

[66] J. R. Shaw and A. Lewis, "Massive neutrinos and magnetic fields in the early universe," Phys. Rev. D, vol. 81, p. 043517, Feb. 2010.

[67] K. Jedamzik and A. Saveliev, "Stringent Limit on Primordial Magnetic Fields from the Cosmic Microwave Background Radiation," *Phys. Rev. Lett.*, vol. 123, no. 2, p. 021301, 2019.

[68] I. Wasserman, "On the origins of galaxies, galactic angular momenta, and galactic magnetic fields.," ApJ, vol. 224, pp. 337–343, Sept. 1978.

[69] E.-J. Kim, A. V. Olinto, and R. Rosner, "Generation of Density Perturbations by Primordial Magnetic Fields," ApJ, vol. 468, p. 28, Sept. 1996.

[70] R. Gopal and S. K. Sethi, "Large Scale Magnetic Fields: Density Power Spectrum in Redshift Space," *Journal of Astrophysics and Astronomy*, vol. 24, pp. 51–68, Dec. 2003.

[71] C. Fedeli and L. Moscardini, "Constraining primordial magnetic fields with future cosmic shear surveys," J. Cosmology Astropart. Phys., vol. 2012, p. 055, Nov. 2012.

[72] T. Kahniashvili, Y. Maravin, A. Natarajan, N. Battaglia, and A. G. Tevzadze, "Constraining Primordial Magnetic Fields through Large-scale Structure," ApJ, vol. 770, p. 47, June 2013.

[73] M. Sanati, Y. Revaz, J. Schober, K. E. Kunze, and P. Jablonka, "Constraining the primordial magnetic field with dwarf galaxy simulations," *arXiv e-prints*, p. arXiv:2005.05401, May 2020.

[74] H. Katz, S. Martin-Alvarez, J. Rosdahl, T. Kimm, J. Blaizot, M. G. Haehnelt, L. Michel-Dansac, T. Garel, J. Oñorbe, J. Devriendt, A. Slyz, O. Attia, and

R. Teyssier, "Introducing SPHINX-MHD: The Impact of Primordial Magnetic Fields on the First Galaxies, Reionization, and the Global 21cm Signal," *arXiv e-prints*, p. arXiv:2101.11624, Jan. 2021.

[75] K. Jedamzik and L. Pogosian, "Relieving the Hubble tension with primordial magnetic fields," *Phys. Rev. Lett.*, vol. 125, no. 18, p. 181302, 2020.

[76] R. Banerjee and K. Jedamzik, "Evolution of cosmic magnetic fields: From the very early Universe, to recombination, to the present," Phys. Rev. D, vol. 70, p. 123003, Dec. 2004.

[77] P. Trivedi, J. Reppin, J. Chluba, and R. Banerjee, "Magnetic heating across the cosmological recombination era: results from 3D MHD simulations," MNRAS, vol. 481, pp. 3401–3422, Dec. 2018.

[78] J. Donnert, F. Vazza, M. Brüggen, and J. ZuHone, "Magnetic Field Amplification in Galaxy Clusters and Its Simulation," Space Sci. Rev., vol. 214, p. 122, Dec. 2018.

[79] F. Marinacci, M. Vogelsberger, R. Pakmor, P. Torrey, V. Springel, L. Hernquist, D. Nelson, R. Weinberger, A. Pillepich, J. Naiman, and S. Genel, "First results from the IllustrisTNG simulations: radio haloes and magnetic fields," *Mon. Not. Roy. Astron. Soc.*, vol. 480, pp. 5113–5139, Nov. 2018.

[80] F. Miniati and A. Beresnyak, "Self-similar energetics in large clusters of galaxies," Nature, vol. 523, pp. 59–62, July 2015.

[81] B. M. Gaensler, R. Beck, and L. Feretti, "The origin and evolution of cosmic magnetism," New A Rev., vol. 48, pp. 1003–1012, Dec. 2004.

[82] R. Beck, "Future Observations of Cosmic Magnetic Fields with LOFAR, SKA and Its Precursors," in *Magnetic Fields in Diffuse Media* (A. Lazarian, E. M. de Gouveia Dal Pino, and C. Melioli, eds.), vol. 407 of *Astrophysics and Space Science Library*, p. 3, Jan. 2015.

[83] G. Heald, S. Mao, V. Vacca, T. Akahori, A. Damas-Segovia, B. Gaensler, M. Hoeft, I. Agudo, A. Basu, R. Beck, M. Birkinshaw, A. Bonafede, T. Bourke, A. Bracco, E. Carretti, L. Feretti, J. Girart, F. Govoni, J. Green, J. Han, M. Haverkorn, C. Horellou, M. Johnston-Hollitt, R. Kothes, T. Landecker, B. Nikiel-Wroczyński, S. O'Sullivan, M. Padovani, F. Poidevin, L. Pratley, M. Regis, C. Riseley, T. Robishaw, L. Rudnick, C. Sobey, J. Stil, X. Sun, S. Sur, A. Taylor, A. Thomson, C. Van Eck, F. Vazza, J. West, and SKA Magnetism Science Working Group, "Magnetism Science with the Square Kilometre Array," *Galaxies*, vol. 8, p. 53, July 2020.

[84] V. Parekh, K. van der Heyden, C. Ferrari, G. Angus, and B. Holwerda, "Morphology parameters: substructure identification in X-ray galaxy clusters," A&A, vol. 575, p. A127, Mar. 2015.

[85] R. J. van Weeren, F. de Gasperin, H. Akamatsu, M. Brüggen, L. Feretti, H. Kang, A. Stroe, and F. Zandanel, "Diffuse Radio Emission from Galaxy Clusters," Space Sci. Rev., vol. 215, p. 16, Feb. 2019.

[86] Planck Collaboration, P. A. R. Ade, N. Aghanim, M. Arnaud, M. Ashdown, F. Atrio-Barandela, J. Aumont, C. Baccigalupi, A. Balbi, A. J. Banday, R. B. Barreiro, J. G. B. E. Battaner, K. Benabed, A. Benoît, J. P. Bernard, M. Bersanelli, R. Bhatia, I. Bikmaev, H. Böhringer, A. Bonaldi, J. R. Bond, J. Borrill, F. R. Bouchet, H. Bourdin, R. Burenin, C. Burigana, P. Cabella, J. F. Cardoso, G. Castex, A. Catalano, L. Cayón, A. Chamballu, R. R. Chary, L. Y. Chiang, G. Chon, P. R. Christensen, D. L. Clements, S. Colafrancesco, L. P. L. Colombo, B. Comis, A. Coulais, B. P. Crill, F. Cuttaia, L. Danese, R. J. Davis, P. de Bernardis, G. de Gasperis, G. de Zotti, J. Delabrouille, J. Démoclès, F. X. Désert, J. M. Diego, K. Dolag, H. Dole, S. Donzelli, O. Doré, U. Dörl, M. Douspis, X. Dupac, G. Efstathiou, T. A. Enßlin, H. K. Eriksen, F. Finelli, I. Flores-Cacho, O. Forni, M. Frailis, E. Franceschi, M. Frommert, K. Ganga, T. Génova-Santos, M. Giard, M. Gilfanov, Y. Giraud-Héraud, J. González-Nuevo, K. M. Górski, A. Gregorio, A. Gruppuso, F. K. Hansen, D. Harrison, A. Hempel, S. Henrot-Versillé, C. Hernández-Monteagudo, D. Herranz, S. R. Hildebrandt, E. Hivon, M. Hobson, W. A. Holmes, W. Hovest, G. Hurier, T. R. Jaffe, A. H. Jaffe, T. Jagemann, W. C. Jones, M. Juvela, I. Khamitov, T. S. Kisner, R. Kneissl, J. Knoche, L. Knox, M. Kunz, H. Kurki-Suonio, G. Lagache, J. M. Lamarre, A. Lasenby, C. R. Lawrence, M. Le Jeune, R. Leonardi, P. B. Lilje, M. Linden-Vørnle, M. López-Caniego, P. M. Lubin, G. Luzzi, J. F. Macías-Pérez, B. Maffei, D. Maino, N. Mandolesi, M. Maris, F. Marleau, D. J. Marshall, E. Martínez-González, S. Masi, M. Massardi, S. Matarrese, F. Matthai, P. Mazzotta, S. Mei, A. Melchiorri, J. B. Melin, L. Mendes, A. Mennella, S. Mitra, M. A. Miville-Deschènes, A. Moneti, L. Montier, G. Morgante, D. Munshi, J. A. Murphy, P. Naselsky, F. Nati, P. Natoli, H. U. Nørgaard-Nielsen, F. Noviello, D. Novikov, I. Novikov, S. Osborne, F. Pajot, D. Paoletti, F. Pasian, G. Patanchon, O. Perdereau, L. Perotto, F. Perrotta, F. Piacentini, M. Piat, E. Pierpaoli, R. Piffaretti, S. Plaszczynski, E. Pointecouteau, G. Polenta, N. Ponthieu, L. Popa, T. Poutanen, G. W. Pratt, S. Prunet, J. L. Puget, J. P. Rachen, R. Rebolo, M. Reinecke, M. Remazeilles, C. Renault, S. Ricciardi, T. Riller, I. Ristorcelli, G. Rocha, M. Roman, C. Rosset, M. Rossetti, J. A. Rubiño-Martín, B. Rusholme, M. Sandri, G. Savini, B. M. Schaefer, D. Scott, G. F. Smoot, J. L. Starck, R. Sudiwala, R. Sunyaev, D. Sutton, A. S. Suur-Uski, J. F. Sygnet, J. A. Tauber, L. Terenzi, L. Toffolatti, M. Tomasi, M. Tristram, M. Tucci, L. Valenziano, B. Van Tent, P. Vielva, F. Villa, N. Vittorio, L. A. Wade, B. D. Wandelt, N. Welikala, S. D. M. White, D. Yvon, A. Zacchei, and A. Zonca, "Planck intermediate results. VIII. Filaments between interacting clusters," A&A, vol. 550, p. A134, Feb. 2013.

[87] F. Govoni and L. Feretti, "Magnetic Fields in Clusters of Galaxies," *International Journal of Modern Physics D*, vol. 13, pp. 1549–1594, Jan. 2004.

[88] A. Bonafede, L. Feretti, G. Giovannini, F. Govoni, M. Murgia, G. B. Taylor, H. Ebeling, S. Allen, G. Gentile, and Y. Pihlström, "Revealing the magnetic field in a distant galaxy cluster: discovery of the complex radio emission from MACS J0717.5 +3745," A&A, vol. 503, pp. 707–720, Sept. 2009.

[89] C. Pfrommer and T. A. Enßlin, "Estimating galaxy cluster magnetic fields by the classical and hadronic minimum energy criterion," MNRAS, vol. 352, pp. 76–90, July 2004.

[90] K. Ferrière, J. L. West, and T. R. Jaffe, "The correct sense of Faraday rotation," MNRAS, vol. 507, pp. 4968–4982, Nov. 2021.

[91] B. J. Burn, "On the depolarization of discrete radio sources by Faraday dispersion," MNRAS, vol. 133, p. 67, Jan. 1966.

[92] A. G. de Bruyn and M. A. Brentjens, "Diffuse polarized emission associated with the Perseus cluster," A&A, vol. 441, pp. 931–947, Oct. 2005.

[93] A. Bonafede, F. Vazza, M. Brüggen, M. Murgia, F. Govoni, L. Feretti, G. Giovannini, and G. Ogrean, "Measurements and simulation of Faraday rotation across the Coma radio relic," MNRAS, vol. 433, pp. 3208–3226, Aug. 2013.

[94] S. Ideguchi, Y. Miyashita, and G. Heald, "Faraday Tomography Tutorial," *Galaxies*, vol. 6, p. 140, Dec. 2018.

[95] P. P. Kronberg and J. J. Perry, "Absorption lines, Faraday rotation, and magnetic field estimates for QSO absorption-line clouds," ApJ, vol. 263, pp. 518–532, Dec. 1982.

[96] R. Plaga, "Detecting intergalactic magnetic fields using time delays in pulses of γ-rays," Nature, vol. 374, pp. 430–432, Mar. 1995.

[97] F. A. Aharonian, P. S. Coppi, and H. J. Voelk, "Very High Energy Gamma Rays from Active Galactic Nuclei: Cascading on the Cosmic Background Radiation Fields and the Formation of Pair Halos," ApJ, vol. 423, p. L5, Mar. 1994.

[98] A. Neronov and D. V. Semikoz, "Sensitivity of γ-ray telescopes for detection of magnetic fields in the intergalactic medium," Phys. Rev. D, vol. 80, p. 123012, Dec. 2009.

[99] A. Neronov, "Large-scale, intergalactic magnetic and radiation fields," in *25th Texas Symposium on Relativistic Astrophysics* (F. M. Rieger, C. van Eldik, and W. Hofmann, eds.), p. 221, Jan. 2010.

[100] A. M. Taylor, I. Vovk, and A. Neronov, "Extragalactic magnetic fields constraints from simultaneous GeV-TeV observations of blazars," A&A, vol. 529, p. A144, May 2011.

[101] A. Neronov and I. Vovk, "Evidence for Strong Extragalactic Magnetic Fields from Fermi Observations of TeV Blazars," *Science*, vol. 328, p. 73, Apr. 2010.

[102] K. Dolag, M. Kachelriess, S. Ostapchenko, and R. Tomàs, "Lower Limit on the Strength and Filling Factor of Extragalactic Magnetic Fields," ApJ, vol. 727, p. L4, Jan. 2011.

[103] K. Bondarenko, A. Boyarsky, A. Korochkin, A. Neronov, D. Semikoz, and A. Sokolenko, "Account of baryonic feedback effect in the gamma-ray measurements of intergalactic magnetic fields," *arXiv e-prints*, p. arXiv:2106.02690, June 2021.

[104] A. E. Broderick, P. Chang, and C. Pfrommer, "The Cosmological Impact of Luminous TeV Blazars. I. Implications of Plasma Instabilities for the Intergalactic Magnetic Field and Extragalactic Gamma-Ray Background," ApJ, vol. 752, p. 22, June 2012.

[105] R. Alves Batista, A. Saveliev, and E. M. de Gouveia Dal Pino, "The impact of plasma instabilities on the spectra of TeV blazars," MNRAS, vol. 489, pp. 3836–3849, Nov. 2019.

[106] R. Schlickeiser, D. Ibscher, and M. Supsar, "Plasma Effects on Fast Pair Beams in Cosmic Voids," ApJ, vol. 758, p. 102, Oct. 2012.

[107] R. Perry and Y. Lyubarsky, "The role of resonant plasma instabilities in the evolution of blazar-induced pair beams," MNRAS, vol. 503, pp. 2215–2228, May 2021.

[108] A. Kempf, P. Kilian, and F. Spanier, "Energy loss in intergalactic pair beams: Particle-in-cell simulation," A&A, vol. 585, p. A132, Jan. 2016.

[109] M. Alawashra, "Suppression of the TeV Pair-beam–Plasma Instability by a Tangled Weak Intergalactic Magnetic Field," in *31st Texas Symposium on Relativistic Astrophysics*, p. 3, Sept. 2022.

[110] M. Alawashra and M. Pohl, "Suppression of the TeV Pair-beam-Plasma Instability by a Tangled Weak Intergalactic Magnetic Field," ApJ, vol. 929, p. 67, Apr. 2022.

[111] A. J. Long and T. Vachaspati, "Morphology of blazar-induced gamma ray halos due to a helical intergalactic magnetic field," *Journal of Cosmology and Astroparticle Physics*, vol. 2015, pp. 065–065, sep 2015.

[112] R. Alves Batista, A. Saveliev, G. Sigl, and T. Vachaspati, "Probing intergalactic magnetic fields with simulations of electromagnetic cascades," Phys. Rev. D, vol. 94, p. 083005, Oct. 2016.

[113] G. L. Bryan, M. L. Norman, B. W. O'Shea, T. Abel, J. H. Wise, M. J. Turk, D. R. Reynolds, D. C. Collins, P. Wang, S. W. Skillman, B. Smith, R. P. Harkness, J. Bordner, J.-h. Kim, M. Kuhlen, H. Xu, N. Goldbaum, C. Hummels, A. G. Kritsuk, E. Tasker, S. Skory, C. M. Simpson, O. Hahn, J. S. Oishi, G. C. So, F. Zhao, R. Cen, Y. Li, and Enzo Collaboration, "ENZO: An Adaptive Mesh Refinement Code for Astrophysics," ApJS, vol. 211, p. 19, Apr. 2014.

[114] S. Dodelson, *Modern Cosmology*. 2003.

[115] V. Mukhanov, *Physical Foundations of Cosmology*. 2005.

[116] H. Mo, F. C. van den Bosch, and S. White, *Galaxy Formation and Evolution*. 2010.

[117] E. Hubble, "A Relation between Distance and Radial Velocity among Extra-Galactic Nebulae," *Proceedings of the National Academy of Science*, vol. 15, pp. 168–173, Mar. 1929.

[118] A. Friedmann, "Über die Möglichkeit einer Welt mit konstanter negativer Krümmung des Raumes," *Zeitschrift fur Physik*, vol. 21, pp. 326–332, Dec. 1924.

[119] G. Lemaître, "Un Univers homogène de masse constante et de rayon croissant rendant compte de la vitesse radiale des nébuleuses extra-galactiques," *Annales de la Société Scientifique de Bruxelles*, vol. 47, pp. 49–59, Jan. 1927.

[120] H. P. Robertson, "Kinematics and World-Structure," ApJ, vol. 82, p. 284, Nov. 1935.

[121] A. G. Walker, "On Milne's Theory of World-Structure," *Proceedings of the London Mathematical Society*, vol. 42, pp. 90–127, Jan. 1937.

[122] Planck Collaboration, N. Aghanim, Y. Akrami, M. Ashdown, J. Aumont, C. Baccigalupi, M. Ballardini, A. J. Banday, R. B. Barreiro, N. Bartolo, S. Basak, R. Battye, K. Benabed, J. P. Bernard, M. Bersanelli, P. Bielewicz, J. J. Bock, J. R. Bond, J. Borrill, F. R. Bouchet, F. Boulanger, M. Bucher, C. Burigana, R. C. Butler, E. Calabrese, J. F. Cardoso, J. Carron, A. Challinor, H. C. Chiang, J. Chluba, L. P. L. Colombo, C. Combet, D. Contreras, B. P. Crill, F. Cuttaia, P. de Bernardis, G. de Zotti, J. Delabrouille, J. M. Delouis, E. Di Valentino, J. M. Diego, O. Doré, M. Douspis, A. Ducout, X. Dupac, S. Dusini, G. Efstathiou, F. Elsner, T. A. Enßlin, H. K. Eriksen, Y. Fantaye, M. Farhang, J. Fergusson, R. Fernandez-Cobos, F. Finelli, F. Forastieri, M. Frailis, A. A. Fraisse, E. Franceschi, A. Frolov, S. Galeotta, S. Galli, K. Ganga, R. T. Génova-Santos, M. Gerbino, T. Ghosh, J. González-Nuevo, K. M. Górski, S. Gratton, A. Gruppuso, J. E. Gudmundsson, J. Hamann, W. Handley, F. K. Hansen, D. Herranz, S. R. Hildebrandt, E. Hivon, Z. Huang, A. H. Jaffe, W. C. Jones, A. Karakci, E. Keihänen, R. Keskitalo, K. Kiiveri, J. Kim, T. S. Kisner, L. Knox, N. Krachmalnicoff, M. Kunz, H. Kurki-Suonio, G. Lagache, J. M. Lamarre, A. Lasenby, M. Lattanzi, C. R. Lawrence, M. Le Jeune, P. Lemos, J. Lesgourgues, F. Levrier, A. Lewis, M. Liguori, P. B. Lilje, M. Lilley, V. Lindholm, M. López-Caniego, P. M. Lubin, Y. Z. Ma, J. F. Macías-Pérez, G. Maggio, D. Maino, N. Mandolesi, A. Mangilli, A. Marcos-Caballero, M. Maris, P. G. Martin, M. Martinelli, E. Martínez-González, S. Matarrese, N. Mauri, J. D. McEwen, P. R. Meinhold, A. Melchiorri, A. Mennella, M. Migliaccio, M. Millea, S. Mitra, M. A. Miville-Deschênes, D. Molinari, L. Montier, G. Morgante, A. Moss, P. Natoli, H. U. Nørgaard-Nielsen, L. Pagano, D. Paoletti, B. Partridge, G. Patanchon, H. V. Peiris, F. Perrotta, V. Pettorino, F. Piacentini, L. Polastri, G. Polenta, J. L. Puget, J. P. Rachen, M. Reinecke, M. Remazeilles, A. Renzi, G. Rocha, C. Rosset, G. Roudier, J. A. Rubiño-Martín, B. Ruiz-Granados, L. Salvati, M. Sandri, M. Savelainen, D. Scott, E. P. S. Shellard, C. Sirignano, G. Sirri, L. D. Spencer, R. Sunyaev, A. S. Suur-Uski, J. A. Tauber, D. Tavagnacco, M. Tenti, L. Toffolatti, M. Tomasi, T. Trombetti, L. Valenziano, J. Valiviita, B. Van Tent, L. Vibert, P. Vielva, F. Villa, N. Vittorio, B. D. Wandelt, I. K. Wehus, M. White, S. D. M. White, A. Zacchei, and A. Zonca, "Planck 2018 results. VI. Cosmological parameters," A&A, vol. 641, p. A6, Sept. 2020.

[123] K. Subramanian and J. D. Barrow, "Microwave Background Signals from Tangled Magnetic Fields," Phys. Rev. Lett., vol. 81, pp. 3575–3578, Oct. 1998.

[124] L. D. Landau and E. M. Lifshitz, *The classical theory of fields*. 1975.

[125] D. W. Hogg, "Distance measures in cosmology," *arXiv e-prints*, pp. astro–ph/9905116, May 1999.

[126] S. Capozziello, M. De Laurentis, O. Luongo, and A. Ruggeri, "Cosmographic Constraints and Cosmic Fluids," *Galaxies*, vol. 1, pp. 216–260, Dec. 2013.

[127] S. H. Suyu, T.-C. Chang, F. Courbin, and T. Okumura, "Cosmological Distance Indicators," Space Sci. Rev., vol. 214, p. 91, Aug. 2018.

[128] E.-K. Li, M. Du, and L. Xu, "General cosmography model with spatial curvature," MNRAS, vol. 491, pp. 4960–4972, Feb. 2020.

[129] S. M. Carroll, "The Cosmological Constant," *Living Reviews in Relativity*, vol. 4, p. 1, Feb. 2001.

[130] A. G. Riess, A. V. Filippenko, P. Challis, A. Clocchiatti, A. Diercks, P. M. Garnavich, R. L. Gilliland, C. J. Hogan, S. Jha, R. P. Kirshner, B. Leibundgut, M. M. Phillips, D. Reiss, B. P. Schmidt, R. A. Schommer, R. C. Smith, J. Spyromilio, C. Stubbs, N. B. Suntzeff, and J. Tonry, "Observational Evidence from Supernovae for an Accelerating Universe and a Cosmological Constant," AJ, vol. 116, pp. 1009–1038, Sept. 1998.

[131] S. Perlmutter, G. Aldering, G. Goldhaber, R. A. Knop, P. Nugent, P. G. Castro, S. Deustua, S. Fabbro, A. Goobar, D. E. Groom, I. M. Hook, A. G. Kim, M. Y. Kim, J. C. Lee, N. J. Nunes, R. Pain, C. R. Pennypacker, R. Quimby, C. Lidman, R. S. Ellis, M. Irwin, R. G. McMahon, P. Ruiz-Lapuente, N. Walton, B. Schaefer, B. J. Boyle, A. V. Filippenko, T. Matheson, A. S. Fruchter, N. Panagia, H. J. M. Newberg, W. J. Couch, and T. S. C. Project, "Measurements of Ω and Λ from 42 High-Redshift Supernovae," ApJ, vol. 517, pp. 565–586, June 1999.

[132] G. F. Smoot, C. L. Bennett, A. Kogut, E. L. Wright, J. Aymon, N. W. Boggess, E. S. Cheng, G. de Amici, S. Gulkis, M. G. Hauser, G. Hinshaw, P. D. Jackson, M. Janssen, E. Kaita, T. Kelsall, P. Keegstra, C. Lineweaver, K. Loewenstein, P. Lubin, J. Mather, S. S. Meyer, S. H. Moseley, T. Murdock, L. Rokke, R. F. Silverberg, L. Tenorio, R. Weiss, and D. T. Wilkinson, "Structure in the COBE Differential Microwave Radiometer First-Year Maps," ApJ, vol. 396, p. L1, Sept. 1992.

[133] A. H. Guth, "Inflationary universe: A possible solution to the horizon and flatness problems," Phys. Rev. D, vol. 23, pp. 347–356, Jan. 1981.

[134] P. W. Higgs, "Broken symmetries, massless particlees and gauge fields," *Physics Letters*, vol. 12, pp. 132–133, Sept. 1964.

[135] P. W. Higgs, "Broken Symmetries and the Masses of Gauge Bosons," Phys. Rev. Lett., vol. 13, pp. 508–509, Oct. 1964.

[136] D. Boyanovsky, H. J. de Vega, and D. J. Schwarz, "Phase Transitions in the Early and Present Universe," *Annual Review of Nuclear and Particle Science*, vol. 56, pp. 441–500, Nov. 2006.

[137] C. J. Copi, D. N. Schramm, and M. S. Turner, "Big-Bang Nucleosynthesis and the Baryon Density of the Universe," *Science*, vol. 267, pp. 192–199, Jan. 1995.

[138] A. Riotto and M. Trodden, "Recent Progress in Baryogenesis," *Annual Review of Nuclear and Particle Science*, vol. 49, pp. 35–75, Jan. 1999.

[139] M. McQuinn, "The Evolution of the Intergalactic Medium," ARA&A, vol. 54, pp. 313–362, Sept. 2016.

[140] K. S. Thorne, "Primordial Element Formation, Primordial Magnetic Fields, and the Isotropy of the Universe," ApJ, vol. 148, p. 51, Apr. 1967.

[141] C. G. Tsagas, "Electromagnetic fields in curved spacetimes," *Classical and Quantum Gravity*, vol. 22, pp. 393–407, Jan. 2005.

[142] T. Kahniashvili, A. G. Tevzadze, S. K. Sethi, K. Pandey, and B. Ratra, "Primordial magnetic field limits from cosmological data," Phys. Rev. D, vol. 82, p. 083005, Oct. 2010.

[143] C. G. Tsagas and R. Maartens, "Magnetized cosmological perturbations," Phys. Rev. D, vol. 61, p. 083519, Apr. 2000.

[144] M. Giovannini, "The Magnetized Universe," *International Journal of Modern Physics D*, vol. 13, pp. 391–502, Jan. 2004.

[145] I. A. Brown, *Primordial Magnetic Fields in Cosmology*. PhD thesis, -, Dec. 2008.

[146] K. Subramanian, "The origin, evolution and signatures of primordial magnetic fields," *Reports on Progress in Physics*, vol. 79, p. 076901, July 2016.

[147] A. Lewis, "Cmb anisotropies from primordial inhomogeneous magnetic fields," *Phys. Rev. D*, vol. 70, p. 043011, Aug 2004.

[148] K. Subramanian, "Magnetic fields in the early Universe," *Astronomische Nachrichten*, vol. 331, p. 110, Jan. 2010.

[149] A. Brandenburg, K. Enqvist, and P. Olesen, "Large-scale magnetic fields from hydromagnetic turbulence in the very early universe," Phys. Rev. D, vol. 54, pp. 1291–1300, July 1996.

[150] A. A. Schekochihin and S. C. Cowley, "Turbulence, magnetic fields, and plasma physics in clusters of galaxies," *Physics of Plasmas*, vol. 13, pp. 056501–056501, May 2006.

[151] A. Schekochihin, S. Cowley, G. Hammett, J. Maron, J. McWilliams, and S. Taylor, "MHD turbulence in galaxies and clusters," in *APS Division of Plasma Physics Meeting Abstracts*, vol. 46 of *APS Meeting Abstracts*, p. JO2.008, Nov. 2004.

[152] J. M. Cornwall, "Exact zero-momentum sum rules in d = 3 gauge theory," *Nuclear Physics B*, vol. 416, pp. 335–347, Mar. 1994.

[153] T. Vachaspati and G. B. Field, "Electroweak String Configurations with Baryon Number[Phys. Rev. Lett. 73, 373 (1994)]," Phys. Rev. Lett., vol. 74, p. 1258, Feb. 1995.

[154] T. Vachaspati, "Electroweak Strings, Sphalerons and Magnetic Fields," in *Electroweak Physics and the Early Universe*, vol. 338 of *NATO Advanced Study Institute (ASI) Series B*, p. 171, Jan. 1994.

[155] A. Brandenburg and K. Subramanian, "Astrophysical magnetic fields and nonlinear dynamo theory," Phys. Rep., vol. 417, pp. 1–209, Oct. 2005.

[156] U. Frisch, A. Pouquet, J. Leorat, and A. Mazure, "Possibility of an inverse cascade of magnetic helicity in magnetohydrodynamic turbulence," *Journal of Fluid Mechanics*, vol. 68, pp. 769–778, Apr. 1975.

[157] H. K. Moffatt, *Magnetic field generation in electrically conducting fluids*. 1978.

[158] M. A. Berger and G. B. Field, "The topological properties of magnetic helicity," *Journal of Fluid Mechanics*, vol. 147, pp. 133–148, Oct. 1984.

[159] D. Biskamp, *Nonlinear magnetohydrodynamics*. 1993.

[160] K. Jedamzik, V. Katalinić, and A. V. Olinto, "Damping of cosmic magnetic fields," Phys. Rev. D, vol. 57, pp. 3264–3284, Mar. 1998.

[161] D. H. Lyth and A. R. Liddle, *The Primordial Density Perturbation*. 2009.

[162] A. S. Monin and A. M. I'Aglom, *Statistical fluid mechanics; mechanics of turbulence*. 1971.

[163] A. Brandenburg, R. Durrer, T. Kahniashvili, S. Mand al, and W. W. Yin, "Statistical properties of scale-invariant helical magnetic fields and applications to cosmology," J. Cosmology Astropart. Phys., vol. 2018, p. 034, Aug. 2018.

[164] K. Subramanian, "From Primordial Seed Magnetic Fields to the Galactic Dynamo," *Galaxies*, vol. 7, p. 47, Apr. 2019.

[165] C. J. Hogan, "Magnetohydrodynamic Effects of a First-Order Cosmological Phase Transition," Phys. Rev. Lett., vol. 51, pp. 1488–1491, Oct. 1983.

[166] R. Durrer and C. Caprini, "Primordial magnetic fields and causality," J. Cosmology Astropart. Phys., vol. 2003, p. 010, Nov. 2003.

[167] J. Cho and D. Ryu, "Characteristic Lengths of Magnetic Field in Magnetohydrodynamic Turbulence," ApJ, vol. 705, pp. L90–L94, Nov. 2009.

[168] A. Schekochihin, S. Cowley, J. Maron, and L. Malyshkin, "Structure of small-scale magnetic fields in the kinematic dynamo theory," Phys. Rev. E, vol. 65, p. 016305, Dec. 2001.

[169] D. Grasso and H. R. Rubinstein, "Magnetic fields in the early Universe," Phys. Rep., vol. 348, pp. 163–266, July 2001.

[170] L. M. Widrow, "Origin of galactic and extragalactic magnetic fields," *Reviews of Modern Physics*, vol. 74, pp. 775–823, Jan. 2002.

[171] D. G. Yamazaki, K. Ichiki, K.-I. Umezu, and H. Hanayama, "Effect of primordial magnetic field on seeds for large scale structure," Phys. Rev. D, vol. 74, p. 123518, Dec. 2006.

[172] B. Cheng, A. V. Olinto, D. N. Schramm, and J. W. Truran, "Constraints on the strength of primordial magnetic fields from big bang nucleosynthesis reexamined," Phys. Rev. D, vol. 54, pp. 4714–4718, Oct. 1996.

[173] D. Grasso and H. R. Rubinstein, "Revisiting nucleosynthesis constraints on primordial magnetic fields," *Physics Letters B*, vol. 379, pp. 73–79, Feb. 1996.

[174] P. J. Kernan, G. D. Starkman, and T. Vachaspati, "Big bang nucleosynthesis constraints on primordial magnetic fields," Phys. Rev. D, vol. 54, pp. 7207–7214, Dec. 1996.

[175] M. Kawasaki and M. Kusakabe, "Updated constraint on a primordial magnetic field during big bang nucleosynthesis and a formulation of field effects," Phys. Rev. D, vol. 86, p. 063003, Sept. 2012.

[176] D. G. Yamazaki and M. Kusakabe, "Effects of power law primordial magnetic field on big bang nucleosynthesis," Phys. Rev. D, vol. 86, p. 123006, Dec. 2012.

[177] M. Kawasaki and M. Kusakabe, "Updated constraint on a primordial magnetic field during big bang nucleosynthesis and a formulation of field effects," Phys. Rev. D, vol. 86, p. 063003, Sept. 2012.

[178] J. J. Matese and R. F. O'Connell, "Production of Helium in the Big-Bang Expansion of a Magnetic Universe," ApJ, vol. 160, p. 451, May 1970.

[179] A. N. Kolmogorov, "Dissipation of Energy in Locally Isotropic Turbulence," *Akademiia Nauk SSSR Doklady*, vol. 32, p. 16, Apr. 1941.

[180] G. K. Batchelor, "On the Spontaneous Magnetic Field in a Conducting Liquid in Turbulent Motion," *Proceedings of the Royal Society of London Series A*, vol. 201, pp. 405–416, Apr. 1950.

[181] Y. B. Zel'dovich, A. A. Ruzmaikin, S. A. Molchanov, and D. D. Sokolov, "Kinematic dynamo problem in a linear velocity field," *Journal of Fluid Mechanics*, vol. 144, pp. 1–11, Jan. 1984.

[182] S. Childress and A. D. Gilbert, *Stretch, Twist, Fold*. 1995.

[183] A. Brandenburg and E. Ntormousi, "Dynamo effect in unstirred self-gravitating turbulence," MNRAS, vol. 513, pp. 2136–2151, June 2022.

[184] A. P. Kazantsev, "Enhancement of a Magnetic Field by a Conducting Fluid," *Soviet Journal of Experimental and Theoretical Physics*, vol. 26, p. 1031, May 1968.

[185] R. M. Kulsrud and S. W. Anderson, "The Spectrum of Random Magnetic Fields in the Mean Field Dynamo Theory of the Galactic Magnetic Field," ApJ, vol. 396, p. 606, Sept. 1992.

[186] A. A. Schekochihin, S. C. Cowley, G. W. Hammett, J. L. Maron, and J. C. McWilliams, "A model of nonlinear evolution and saturation of the turbulent MHD dynamo," *New Journal of Physics*, vol. 4, p. 84, Oct. 2002.

[187] K. Subramanian, "Dynamics of fluctuating magnetic fields in turbulent dynamos incorporating ambipolar drifts," *arXiv e-prints*, pp. astro–ph/9708216, Aug. 1997.

[188] N. E. Haugen, A. Brandenburg, and W. Dobler, "Simulations of nonhelical hydromagnetic turbulence," Phys. Rev. E, vol. 70, p. 016308, July 2004.

[189] C. Federrath, G. Chabrier, J. Schober, R. Banerjee, R. S. Klessen, and D. R. G. Schleicher, "Mach Number Dependence of Turbulent Magnetic Field Amplification: Solenoidal versus Compressive Flows," Phys. Rev. Lett., vol. 107, p. 114504, Sept. 2011.

[190] J. Schober, D. Schleicher, S. Bovino, and R. S. Klessen, "Small-scale dynamo at low magnetic Prandtl numbers," Phys. Rev. E, vol. 86, p. 066412, Dec. 2012.

[191] J. Schober, D. R. G. Schleicher, C. Federrath, S. Bovino, and R. S. Klessen, "Saturation of the turbulent dynamo," Phys. Rev. E, vol. 92, p. 023010, Aug. 2015.

[192] R. Achikanath Chirakkara, C. Federrath, P. Trivedi, and R. Banerjee, "Efficient Highly Subsonic Turbulent Dynamo and Growth of Primordial Magnetic Fields," Phys. Rev. Lett., vol. 126, p. 091103, Mar. 2021.

[193] C. Federrath, "Magnetic field amplification in turbulent astrophysical plasmas," *Journal of Plasma Physics*, vol. 82, p. 535820601, Dec. 2016.

[194] S. Xu and A. Lazarian, "Small-scale turbulent dynamo in astrophysical environments: nonlinear dynamo and dynamo in a partially ionized plasma," *Reviews of Modern Plasma Physics*, vol. 5, p. 2, Dec. 2021.

[195] C. Federrath, S. Sur, D. R. G. Schleicher, R. Banerjee, and R. S. Klessen, "A New Jeans Resolution Criterion for (M)HD Simulations of Self-gravitating Gas: Application to Magnetic Field Amplification by Gravity-driven Turbulence," ApJ, vol. 731, p. 62, Apr. 2011.

[196] S. Martin-Alvarez, H. Katz, D. Sijacki, J. Devriendt, and A. Slyz, "Unravelling the origin of magnetic fields in galaxies," MNRAS, vol. 504, pp. 2517–2534, June 2021.

[197] S. Martin-Alvarez, J. Devriendt, A. Slyz, D. Sijacki, M. L. A. Richardson, and H. Katz, "Towards convergence of turbulent dynamo amplification in cosmological simulations of galaxies," MNRAS, vol. 513, pp. 3326–3344, July 2022.

[198] K. Subramanian, "Can the turbulent galactic dynamo generate large-scale magnetic fields?," MNRAS, vol. 294, pp. 718–728, Mar. 1998.

[199] K. Enqvist, "Primordial Magnetic Fields," *International Journal of Modern Physics D*, vol. 7, pp. 331–349, Jan. 1998.

[200] A. Lazarian, "Diffusion-generated electromotive force and seed magnetic field problem," A&A, vol. 264, pp. 326–330, Oct. 1992.

[201] K. Subramanian, D. Narasimha, and S. M. Chitre, "Thermal generation of cosmological seed magnetic fields in ionization fronts," MNRAS, vol. 271, p. L15, Nov. 1994.

[202] T. Kobayashi, R. Maartens, T. Shiromizu, and K. Takahashi, "Cosmological magnetic fields from nonlinear effects," Phys. Rev. D, vol. 75, p. 103501, May 2007.

[203] O. Savchenko and Y. Shtanov, "Magnetogenesis by non-minimal coupling to gravity in the Starobinsky inflationary model," J. Cosmology Astropart. Phys., vol. 2018, p. 040, Oct. 2018.

[204] M. Banyeres, G. Domènech, and J. Garriga, "Vacuum birefringence and the Schwinger effect in (3+1) de Sitter," J. Cosmology Astropart. Phys., vol. 2018, p. 023, Oct. 2018.

[205] D. Green and T. Kobayashi, "Constraints on primordial magnetic fields from inflation," J. Cosmology Astropart. Phys., vol. 2016, p. 010, Mar. 2016.

[206] L. M. Widrow, D. Ryu, D. R. G. Schleicher, K. Subramanian, C. G. Tsagas, and R. A. Treumann, "The First Magnetic Fields," Space Sci. Rev., vol. 166, pp. 37–70, May 2012.

[207] J. Martin and J. Yokoyama, "Generation of large scale magnetic fields in single-field inflation," J. Cosmology Astropart. Phys., vol. 2008, p. 025, Jan. 2008.

[208] S. Kanno, J. Soda, and M.-a. Watanabe, "Cosmological magnetic fields from inflation and backreaction," J. Cosmology Astropart. Phys., vol. 2009, p. 009, Dec. 2009.

[209] R. Emami, H. Firouzjahi, and M. S. Movahed, "Inflation from charged scalar and primordial magnetic fields?," Phys. Rev. D, vol. 81, p. 083526, Apr. 2010.

[210] T. Fujita and S. Mukohyama, "Universal upper limit on inflation energy scale from cosmic magnetic field," J. Cosmology Astropart. Phys., vol. 2012, p. 034, Oct. 2012.

[211] V. Demozzi, V. Mukhanov, and H. Rubinstein, "Magnetic fields from inflation?," J. Cosmology Astropart. Phys., vol. 2009, p. 025, Aug. 2009.

[212] R. J. Z. Ferreira, R. K. Jain, and M. S. Sloth, "Inflationary magnetogenesis without the strong coupling problem," J. Cosmology Astropart. Phys., vol. 2013, p. 004, Oct. 2013.

[213] G. Tasinato, "A scenario for inflationary magnetogenesis without strong coupling problem," J. Cosmology Astropart. Phys., vol. 2015, pp. 040–040, Mar. 2015.

[214] A. Talebian, A. Nassiri-Rad, and H. Firouzjahi, "Revisiting magnetogenesis during inflation," Phys. Rev. D, vol. 102, p. 103508, Nov. 2020.

[215] T. Fujita, R. Namba, Y. Tada, N. Takeda, and H. Tashiro, "Consistent generation of magnetic fields in axion inflation models," J. Cosmology Astropart. Phys., vol. 2015, pp. 054–054, May 2015.

[216] A. Brandenburg, R. Durrer, Y. Huang, T. Kahniashvili, S. Mandal, and S. Mukohyama, "Primordial magnetic helicity evolution with homogeneous magnetic field from inflation," *arXiv e-prints*, p. arXiv:2005.06449, May 2020.

[217] R. Durrer, L. Hollenstein, and R. K. Jain, "Can slow roll inflation induce relevant helical magnetic fields?," J. Cosmology Astropart. Phys., vol. 2011, p. 037, Mar. 2011.

[218] R. K. Jain, R. Durrer, and L. Hollenstein, "Generation of helical magnetic fields from inflation," *arXiv e-prints*, p. arXiv:1204.2409, Apr. 2012.

[219] T. Fujita and R. Durrer, "Scale-invariant helical magnetic fields from inflation," J. Cosmology Astropart. Phys., vol. 2019, p. 008, Sept. 2019.

[220] A. Kushwaha and S. Shankaranarayanan, "Helical magnetic fields from Riemann coupling lead to baryogenesis," Phys. Rev. D, vol. 104, p. 063502, Sept. 2021.

[221] A. Talebian, A. Nassiri-Rad, and H. Firouzjahi, "Primordial helical magnetic fields from inflation?," Phys. Rev. D, vol. 105, p. 023528, Jan. 2022.

[222] K. Kajantie, M. Laine, K. Rummukainen, and M. Shaposhnikov, "Is There a Hot Electroweak Phase Transition at m_H ¿~m_W?," Phys. Rev. Lett., vol. 77, pp. 2887–2890, Sept. 1996.

[223] F. Csikor, Z. Fodor, and J. Heitger, "The electroweak phase transition at m_H 80 GeV from L_t = 2 lattices," *Nuclear Physics B Proceedings Supplements*, vol. 63, pp. 569–571, Apr. 1998.

[224] Y. Aoki, G. Endrődi, Z. Fodor, S. D. Katz, and K. K. Szabó, "The order of the quantum chromodynamics transition predicted by the standard model of particle physics," Nature, vol. 443, pp. 675–678, Oct. 2006.

[225] K. Fukushima and T. Hatsuda, "The phase diagram of dense QCD," *Reports on Progress in Physics*, vol. 74, p. 014001, dec 2010.

[226] C. Grojean, G. Servant, and J. D. Wells, "First-order electroweak phase transition in the standard model with a low cutoff," Phys. Rev. D, vol. 71, p. 036001, Feb. 2005.

[227] S. J. Huber, T. Konstandin, T. Prokopec, and M. G. Schmidt, "Baryogenesis in the MSSM, nMSSM and NMSSM," Nucl. Phys. A, vol. 785, pp. 206–209, Mar. 2007.

[228] D. J. Schwarz and M. Stuke, "Lepton asymmetry and the cosmic QCD transition," J. Cosmology Astropart. Phys., vol. 2009, p. 025, Nov. 2009.

[229] J. M. Quashnock, A. Loeb, and D. N. Spergel, "Magnetic Field Generation during the Cosmological QCD Phase Transition," ApJ, vol. 344, p. L49, Sept. 1989.

[230] G. Baym, D. Bödeker, and L. McLerran, "Magnetic fields produced by phase transition bubbles in the electroweak phase transition," Phys. Rev. D, vol. 53, pp. 662–667, Jan. 1996.

[231] B. Cheng and A. V. Olinto, "Primordial magnetic fields generated in the quark-hadron transition," Phys. Rev. D, vol. 50, pp. 2421–2424, Aug. 1994.

[232] G. Sigl, A. V. Olinto, and K. Jedamzik, "Primordial magnetic fields from cosmological first order phase transitions," Phys. Rev. D, vol. 55, pp. 4582–4590, Apr. 1997.

[233] E. W. Kolb and M. S. Turner, *The early universe*, vol. 69. 1990.

[234] T. Vachaspati, "Magnetic fields from cosmological phase transitions," *Physics Letters B*, vol. 265, pp. 258–261, Aug. 1991.

[235] K. Enqvist and P. Olesen, "On primordial magnetic fields of electroweak origin," *Physics Letters B*, vol. 319, pp. 178–185, Dec. 1993.

[236] T. W. B. Kibble and A. Vilenkin, "Phase equilibration in bubble collisions," Phys. Rev. D, vol. 52, pp. 679–688, July 1995.

[237] A. Díaz-Gil, J. García-Bellido, M. García Pérez, and A. González-Arroyo, "Magnetic Field Production during Preheating at the Electroweak Scale," Phys. Rev. Lett., vol. 100, p. 241301, June 2008.

[238] Y. Zhang, T. Vachaspati, and F. Ferrer, "Magnetic field production at a first-order electroweak phase transition," Phys. Rev. D, vol. 100, p. 083006, Oct. 2019.

[239] Z.-G. Mou, P. M. Saffin, and A. Tranberg, "Simulations of Cold Electroweak Baryogenesis: hypercharge U(1) and the creation of helical magnetic fields," *Journal of High Energy Physics*, vol. 2017, p. 75, June 2017.

[240] L. Campanelli and M. Giannotti, "Magnetic helicity generation from the cosmic axion field," Phys. Rev. D, vol. 72, p. 123001, Dec. 2005.

[241] F. Miniati, G. Gregori, B. Reville, and S. Sarkar, "Axion-Driven Cosmic Magnetogenesis during the QCD Crossover," Phys. Rev. Lett., vol. 121, p. 021301, July 2018.

[242] J. García-Bellido, M. García Pérez, and A. González-Arroyo, "Chern-Simons production during preheating in hybrid inflation models," Phys. Rev. D, vol. 69, p. 023504, Jan. 2004.

[243] A. G. Tevzadze, L. Kisslinger, A. Brandenburg, and T. Kahniashvili, "Magnetic Fields from QCD Phase Transitions," ApJ, vol. 759, p. 54, Nov. 2012.

[244] T. Kahniashvili, A. G. Tevzadze, A. Brandenburg, and A. Neronov, "Evolution of primordial magnetic fields from phase transitions," Phys. Rev. D, vol. 87, p. 083007, Apr. 2013.

[245] L. S. Kisslinger, "Magnetic Wall From Chiral Phase Transitiion and CMBR Correlations," in *APS Ohio Sections Fall Meeting Abstracts*, APS Meeting Abstracts, p. C2.006, Oct. 2003.

[246] A. Pouquet, U. Frisch, and J. Léorat *J. Fluid Mech.*, vol. 77, pp. 321–354, 1976.

[247] D. Biskamp and W.-C. Müller, "Decay Laws for Three-Dimensional Magnetohydrodynamic Turbulence," Phys. Rev. Lett., vol. 83, pp. 2195–2198, Sept. 1999.

[248] M. Christensson, M. Hindmarsh, and A. Brandenburg, "Inverse cascade in decaying three-dimensional magnetohydrodynamic turbulence," Phys. Rev. E, vol. 64, p. 056405, Nov. 2001.

[249] T. Kahniashvili, A. Brandenburg, and A. e. G. Tevzadze, "The evolution of primordial magnetic fields since their generation," Phys. Scr, vol. 91, p. 104008, Oct. 2016.

[250] T. Kahniashvili, E. Clarke, J. Stepp, and A. Brandenburg, "Big Bang Nucleosynthesis Limits and Relic Gravitational-Wave Detection Prospects," Phys. Rev. Lett., vol. 128, p. 221301, June 2022.

[251] D. Koh, T. Abel, and K. Jedamzik, "First Star Formation in the Presence of Primordial Magnetic Fields," ApJ, vol. 909, p. L21, Mar. 2021.

[252] F. Marinacci, M. Vogelsberger, P. Mocz, and R. Pakmor, "The large-scale properties of simulated cosmological magnetic fields," *Mon. Not. Roy. Astron. Soc.*, vol. 453, pp. 3999–4019, Nov. 2015.

[253] F. Vazza, D. Paoletti, S. Banfi, F. Finelli, C. Gheller, S. O'Sullivan, and M. Brüggen, "Simulations and observational tests of primordial magnetic fields from Cosmic Microwave Background constraints," *arXiv e-prints*, p. arXiv:2009.01539, Sept. 2020.

[254] K. Dolag, M. Bartelmann, and H. Lesch, "SPH simulations of magnetic fields in galaxy clusters," *arXiv e-prints*, pp. astro–ph/9906329, June 1999.

[255] V. Springel, "The cosmological simulation code GADGET-2," MNRAS, vol. 364, pp. 1105–1134, Dec. 2005.

[256] S. Fromang, P. Hennebelle, and R. Teyssier, "A high order Godunov scheme with constrained transport and adaptive mesh refinement for astrophysical magnetohydrodynamics," A&A, vol. 457, pp. 371–384, Oct. 2006.

[257] R. Teyssier, S. Fromang, and E. Dormy, "Kinematic dynamos using constrained transport with high order Godunov schemes and adaptive mesh refinement," *Journal of Computational Physics*, vol. 218, pp. 44–67, Oct. 2006.

[258] J. M. Stone, T. A. Gardiner, P. Teuben, J. F. Hawley, and J. B. Simon, "Athena: A New Code for Astrophysical MHD," ApJS, vol. 178, pp. 137–177, Sept. 2008.

[259] R. Weinberger, V. Springel, and R. Pakmor, "The AREPO Public Code Release," ApJS, vol. 248, p. 32, June 2020.

[260] V. Quilis, J.-M. Martí, and S. Planelles, "Cosmic magnetic fields with masclet: an application to galaxy clusters," MNRAS, vol. 494, pp. 2706–2717, May 2020.

[261] B. W. O'Shea, K. Nagamine, V. Springel, L. Hernquist, and M. L. Norman, "Comparing AMR and SPH Cosmological Simulations. I. Dark Matter and Adiabatic Simulations," ApJS, vol. 160, pp. 1–27, Sept. 2005.

[262] F. Vazza, K. Dolag, D. Ryu, G. Brunetti, C. Gheller, H. Kang, and C. Pfrommer, "A comparison of cosmological codes: properties of thermal gas and shock waves in large-scale structures," MNRAS, vol. 418, pp. 960–985, Dec. 2011.

[263] B. van Leer, "Towards the Ultimate Conservative Difference Scheme. V. A Second-Order Sequel to Godunov's Method," *Journal of Computational Physics*, vol. 32, pp. 101–136, July 1979.

[264] A. Dedner, F. Kemm, D. Kröner, C. D. Munz, T. Schnitzer, and M. Wesenberg, "Hyperbolic Divergence Cleaning for the MHD Equations," *Journal of Computational Physics*, vol. 175, pp. 645–673, Jan. 2002.

[265] C.-W. Shu and S. Osher, "Efficient implementation of essentially non-oscillatory shock-capturing schemes," *Journal of Computational Physics*, vol. 77, no. 2, pp. 439–471, 1988.

[266] A. Kurganov and E. Tadmor, "New High-Resolution Central Schemes for Nonlinear Conservation Laws and Convection-Diffusion Equations," *Journal of Computational Physics*, vol. 160, pp. 241–282, May 2000.

[267] J. U. Brackbill and D. C. Barnes, "The Effect of Nonzero $\nabla \cdot$ B on the numerical solution of the magnetohydrodynamic equations," *Journal of Computational Physics*, vol. 35, pp. 426–430, May 1980.

[268] Vides, J., Audit, E., Guillard, H., and Nkonga, B., "Divergence-free mhd simulations with the heracles code," *ESAIM: Proc.*, vol. 43, pp. 180–194, 2013.

[269] C. R. Evans and J. F. Hawley, "Simulation of Magnetohydrodynamic Flows: A Constrained Transport Model," ApJ, vol. 332, p. 659, Sept. 1988.

[270] D. J. Eisenstein and W. Hu, "Baryonic Features in the Matter Transfer Function," ApJ, vol. 496, pp. 605–614, Mar. 1998.

[271] E. Bertschinger, "Simulations of Structure Formation in the Universe," ARA&A, vol. 36, pp. 599–654, Jan. 1998.

[272] S. K. Sethi and K. Subramanian, "Primordial magnetic fields in the post-recombination era and early reionization," MNRAS, vol. 356, pp. 778–788, Jan. 2005.

[273] T. Kahniashvili, Y. Maravin, A. Natarajan, N. Battaglia, and A. G. Tevzadze, "Constraining Primordial Magnetic Fields through Large-scale Structure," ApJ, vol. 770, p. 47, June 2013.

[274] R. A. Gingold and J. J. Monaghan, "Smoothed particle hydrodynamics: theory and application to non-spherical stars.," MNRAS, vol. 181, pp. 375–389, Nov. 1977.

[275] L. B. Lucy, "A numerical approach to the testing of the fission hypothesis.," AJ, vol. 82, pp. 1013–1024, Dec. 1977.

[276] J. J. Monaghan, "Smoothed particle hydrodynamics.," ARA&A, vol. 30, pp. 543–574, Jan. 1992.

[277] M. J. Berger and P. Colella, "Local Adaptive Mesh Refinement for Shock Hydrodynamics," *Journal of Computational Physics*, vol. 82, pp. 64–84, May 1989.

[278] G. L. Bryan and M. L. Norman, "Simulating X-Ray Clusters with Adaptive Mesh Refinement," in *Computational Astrophysics; 12th Kingston Meeting on Theoretical Astrophysics* (D. A. Clarke and M. J. West, eds.), vol. 12 of *Astronomical Society of the Pacific Conference Series*, p. 363, Jan. 1997.

[279] D. C. Collins, H. Xu, M. L. Norman, H. Li, and S. Li, "Cosmological Adaptive Mesh Refinement Magnetohydrodynamics with Enzo," ApJS, vol. 186, pp. 308–333, Feb. 2010.

[280] L. Iapichino and J. C. Niemeyer, "Hydrodynamical adaptive mesh refinement simulations of turbulent flows - II. Cosmological simulations of galaxy clusters," MNRAS, vol. 388, pp. 1089–1100, Aug. 2008.

[281] F. Vazza, G. Brunetti, A. Kritsuk, R. Wagner, C. Gheller, and M. Norman, "Turbulent motions and shocks waves in galaxy clusters simulated with adaptive mesh refinement," A&A, vol. 504, pp. 33–43, Sept. 2009.

[282] L. Iapichino, C. Federrath, and R. S. Klessen, "Adaptive mesh refinement simulations of a galaxy cluster merger - I. Resolving and modelling the turbulent flow in the cluster outskirts," MNRAS, vol. 469, pp. 3641–3655, Aug. 2017.

[283] D. J. Schwarz, "The first second of the Universe," *Annalen der Physik*, vol. 12, pp. 220–270, June 2003.

[284] T. Kahniashvili, A. Brandenburg, R. Durrer, A. G. Tevzadze, and W. Yin, "Scale-invariant helical magnetic field evolution and the duration of inflation," J. Cosmology Astropart. Phys., vol. 2017, p. 002, Dec. 2017.

[285] T. Kahniashvili, A. Brandenburg, G. Gogoberidze, S. Mandal, and A. Roper Pol, "Circular Polarization of Gravitational Waves from Early-Universe Helical Turbulence," *arXiv e-prints*, p. arXiv:2011.05556, Nov. 2020.

[286] F. Vazza, M. Brüggen, C. Gheller, and P. Wang, "On the amplification of magnetic fields in cosmic filaments and galaxy clusters," *Mon. Not. Roy. Astron. Soc.*, vol. 445, pp. 3706–3722, Dec. 2014.

[287] A. Bera, K. K. Datta, and S. Samui, "Primordial magnetic fields during the cosmic dawn in light of EDGES 21-cm signal," MNRAS, vol. 498, pp. 918–925, Oct. 2020.

[288] Pencil Code Collaboration, A. Brandenburg, A. Johansen, P. Bourdin, W. Dobler, W. Lyra, M. Rheinhardt, S. Bingert, N. Haugen, A. Mee, F. Gent, N. Babkovskaia, C.-C. Yang, T. Heinemann, B. Dintrans, D. Mitra, S. Candelaresi, J. Warnecke, P. Käpylä, A. Schreiber, P. Chatterjee, M. Käpylä, X.-Y. Li, J. Krüger, J. Aarnes, G. Sarson, J. Oishi, J. Schober, R. Plasson, C. Sandin, E. Karchniwy, L. Rodrigues, A. Hubbard, G. Guerrero, A. Snodin, I. Losada, J. Pekkilä, and C. Qian, "The Pencil Code, a modular MPI code for partial differential equations and particles: multipurpose and multiuser-maintained," *The Journal of Open Source Software*, vol. 6, p. 2807, Feb. 2021.

[289] T. H. Reiprich, A. Veronica, F. Pacaud, M. E. Ramos-Ceja, N. Ota, J. Sanders, M. Kara, T. Erben, M. Klein, J. Erler, J. Kerp, D. N. Hoang, M. Brüggen, J. Marvil, L. Rudnick, V. Biffi, K. Dolag, J. Aschersleben, K. Basu, H. Brunner, E. Bulbul, K. Dennerl, D. Eckert, M. Freyberg, E. Gatuzz, V. Ghirardini, F. Käfer, A. Merloni, K. Migkas, K. Nandra, P. Predehl, J. Robrade, M. Salvato, B. Whelan, A. Diaz-Ocampo, D. Hernandez-Lang, A. Zenteno, M. J. I. Brown, J. D. Collier, J. M. Diego, A. M. Hopkins, A. Kapinska, B. Koribalski, T. Mroczkowski, R. P. Norris, A. O'Brien, and E. Vardoulaki, "The Abell 3391/95 galaxy cluster system. A 15 Mpc intergalactic medium emission filament, a warm gas bridge, infalling matter clumps, and (re-) accelerated plasma discovered by combining SRG/eROSITA data with ASKAP/EMU and DECam data," A&A, vol. 647, p. A2, Mar. 2021.

[290] C. Gheller and F. Vazza, "A survey of the thermal and non-thermal properties of cosmic filaments," MNRAS, vol. 486, pp. 981–1002, June 2019.

[291] Y. Dubois and R. Teyssier, "Cosmological MHD simulation of a cooling flow cluster," A&A, vol. 482, pp. L13–L16, May 2008.

[292] T. Minoda, K. Hasegawa, H. Tashiro, K. Ichiki, and N. Sugiyama, "Thermal Sunyaev-Zel'dovich effect in the intergalactic medium with primordial magnetic fields," Phys. Rev. D, vol. 96, p. 123525, Dec. 2017.

[293] S. K. Sethi, "HI signal from re-ionization epoch," MNRAS, vol. 363, pp. 818–830, Nov. 2005.

[294] T. Minoda, H. Tashiro, and T. Takahashi, "Insight into primordial magnetic fields from 21-cm line observation with EDGES experiment," MNRAS, vol. 488, pp. 2001–2005, Sept. 2019.

[295] P. K. Natwariya, "Constraint on primordial magnetic fields in the light of ARCADE 2 and EDGES observations," *European Physical Journal C*, vol. 81, p. 394, May 2021.

[296] J. D. Bowman, A. E. E. Rogers, R. A. Monsalve, T. J. Mozdzen, and N. Mahesh, "An absorption profile centred at 78 megahertz in the sky-averaged spectrum," Nature, vol. 555, pp. 67–70, Mar. 2018.

[297] R. Barkana, "Possible interaction between baryons and dark-matter particles revealed by the first stars," Nature, vol. 555, pp. 71–74, Mar. 2018.

[298] R. Fusco-Femiano, D. Dal Fiume, M. Orlandini, G. Brunetti, L. Feretti, and G. Giovannini, "Hard X-Ray Emission from the Galaxy Cluster A3667," ApJ, vol. 552, pp. L97–L100, May 2001.

[299] R. Fusco-Femiano, M. Orlandini, G. Brunetti, L. Feretti, G. Giovannini, P. Grandi, and G. Setti, "Confirmation of Nonthermal Hard X-Ray Excess in the Coma Cluster from Two Epoch Observations," ApJ, vol. 602, pp. L73–L76, Feb. 2004.

[300] M. S. Väisälä, J. Pekkilä, M. J. Käpylä, M. Rheinhardt, H. Shang, and R. Krasnopolsky, "Interaction of large- and small-scale dynamos in isotropic turbulent flows from GPU-accelerated simulations," *arXiv e-prints*, p. arXiv:2012.08758, Dec. 2020.

[301] A. Brandenburg, T. Kahniashvili, and A. G. Tevzadze, "Nonhelical Inverse Transfer of a Decaying Turbulent Magnetic Field," Phys. Rev. Lett., vol. 114, p. 075001, Feb. 2015.

[302] A. Seta and C. Federrath, "Seed magnetic fields in turbulent small-scale dynamos," MNRAS, vol. 499, pp. 2076–2086, Dec. 2020.

[303] A. Seta, A. Shukurov, T. S. Wood, P. J. Bushby, and A. P. Snodin, "Relative distribution of cosmic rays and magnetic fields," MNRAS, vol. 473, pp. 4544–4557, Feb. 2018.

[304] O. Hahn and T. Abel, "Multi-scale initial conditions for cosmological simulations," MNRAS, vol. 415, pp. 2101–2121, Aug. 2011.

[305] D. H. F. M. Schnitzeler, "The latitude dependence of the rotation measures of NVSS sources," MNRAS, vol. 409, pp. L99–L103, Nov. 2010.

[306] N. Oppermann, H. Junklewitz, M. Greiner, T. A. Enßlin, T. Akahori, E. Carretti, B. M. Gaensler, A. Goobar, L. Harvey-Smith, M. Johnston-Hollitt, L. Pratley, D. H. F. M. Schnitzeler, J. M. Stil, and V. Vacca, "Estimating extragalactic Faraday rotation," A&A, vol. 575, p. A118, Mar. 2015.

[307] S. Hutschenreuter, C. S. Anderson, S. Betti, G. C. Bower, J.-A. Brown, M. Brüggen, E. Carretti, T. Clarke, A. Clegg, A. Costa, S. Croft, C. Van Eck, B. M. Gaensler, F. de Gasperin, M. Haverkorn, G. Heald, C. L. H. Hull, M. Inoue, M. Johnston-Hollitt, J. Kaczmarek, C. Law, Y. K. Ma, D. MacMahon, S. A. Mao, C. Riseley, S. Roy, R. Shanahan, T. Shimwell, J. Stil, C. Sobey, S. O'Sullivan, C. Tasse, V. Vacca, T. Vernstrom, P. K. G. Williams, M. Wright, and T. A. Enßlin, "The Galactic Faraday rotation sky 2020," *arXiv e-prints*, p. arXiv:2102.01709, Feb. 2021.

[308] D. J. B. Smith, P. N. Best, K. J. Duncan, N. A. Hatch, M. J. Jarvis, H. J. A. Röttgering, C. J. Simpson, J. P. Stott, R. K. Cochrane, K. E. Coppin, H. Dannerbauer, T. A. Davis, J. E. Geach, C. L. Hale, M. J. Hardcastle, P. W. Hatfield, R. C. W. Houghton, N. Maddox, S. L. McGee, L. Morabito, D. Nisbet, M. Pandey-Pommier, I. Prandoni, A. Saxena, T. W. Shimwell, M. Tarr, I. van Bemmel, A. Verma, G. J. White, and W. L. Williams, "The WEAVE-LOFAR Survey," in *SF2A-2016: Proceedings of the Annual meeting of the French Society of Astronomy and Astrophysics* (C. Reylé, J. Richard, L. Cambrésy, M. Deleuil, E. Pécontal, L. Tresse, and I. Vauglin, eds.), pp. 271–280, Dec. 2016.

[309] T. W. Shimwell, C. Tasse, M. J. Hardcastle, A. P. Mechev, W. L. Williams, P. N. Best, H. J. A. Röttgering, J. R. Callingham, T. J. Dijkema, F. de Gasperin, D. N. Hoang, B. Hugo, M. Mirmont, J. B. R. Oonk, I. Prandoni, D. Rafferty, J. Sabater, O. Smirnov, R. J. van Weeren, G. J. White, M. Atemkeng, L. Bester, E. Bonnassieux, M. Brüggen, G. Brunetti, K. T. Chyży, R. Cochrane, J. E. Conway, J. H. Croston, A. Danezi, K. Duncan, M. Haverkorn, G. H. Heald, M. Iacobelli, H. T. Intema, N. Jackson, M. Jamrozy, M. J. Jarvis, R. Lakhoo, M. Mevius, G. K. Miley, L. Morabito, R. Morganti, D. Nisbet, E. Orrú, S. Perkins, R. F. Pizzo, C. Schrijvers, D. J. B. Smith, R. Vermeulen, M. W. Wise, L. Alegre, D. J. Bacon, I. M. van Bemmel, R. J. Beswick, A. Bonafede, A. Botteon, S. Bourke, M. Brienza, G. Calistro Rivera, R. Cassano, A. O. Clarke, C. J. Conselice, R. J. Dettmar, A. Drabent, C. Dumba, K. L. Emig, T. A. Enßlin, C. Ferrari, M. A. Garrett, R. T. Génova-Santos, A. Goyal, G. Gürkan, C. Hale, J. J. Harwood, V. Heesen, M. Hoeft, C. Horellou, C. Jackson, G. Kokotanekov, R. Kondapally, M. Kunert-Bajraszewska, V. Mahatma, E. K. Mahony, S. Mandal, J. P. McKean, A. Merloni, B. Mingo, A. Miskolczi, S. Mooney, B. Nikiel-Wroczyński, S. P. O'Sullivan, J. Quinn, W. Reich, C. Roskowiński, A. Rowlinson, F. Savini, A. Saxena, D. J. Schwarz, A. Shulevski, S. S. Sridhar, H. R. Stacey, S. Urquhart, M. H. D. van der Wiel, E. Varenius, B. Webster, and A. Wilber, "The LOFAR Two-metre Sky Survey. II. First data release," A&A, vol. 622, p. A1, Feb. 2019.

[310] T. Akahori and D. Ryu, "Faraday Rotation Measure Due to the Intergalactic Magnetic Field," ApJ, vol. 723, pp. 476–481, Nov. 2010.

[311] T. Akahori and D. Ryu, "Faraday Rotation Measure due to the Intergalactic Magnetic Field. II. The Cosmological Contribution," ApJ, vol. 738, p. 134, Sept. 2011.

[312] H. Böhringer, G. Chon, and P. P. Kronberg, "The Cosmic Large-Scale Structure in X-rays (CLASSIX) Cluster Survey. I. Probing galaxy cluster magnetic fields with line of sight rotation measures," A&A, vol. 596, p. A22, Nov. 2016.

[313] P. Thomas and R. G. Carlberg, "Hot gas in a cosmological N-body simulation," MNRAS, vol. 240, pp. 1009–1023, Oct. 1989.

[314] R. Scaramella, R. Cen, and J. P. Ostriker, "A Hydrodynamic Approach to Cosmology: Nonlinear Effects on Cosmic Backgrounds in the Cold Dark Matter Model," ApJ, vol. 416, p. 399, Oct. 1993.

[315] C. Stuardi, S. P. O'Sullivan, A. Bonafede, M. Brüggen, P. Dabhade, C. Horellou, R. Morganti, E. Carretti, G. Heald, M. Iacobelli, and V. Vacca, "The LOFAR view of intergalactic magnetic fields with giant radio galaxies," A&A, vol. 638, p. A48, June 2020.

[316] S. Galli, L. Pogosian, K. Jedamzik, and L. Balkenhol, "Consistency of planck, act and spt constraints on magnetically assisted recombination and forecasts for future experiments," 2021.

[317] C. Sotomayor-Beltran, C. Sobey, J. W. T. Hessels, G. de Bruyn, A. Noutsos, A. Alexov, J. Anderson, A. Asgekar, I. M. Avruch, R. Beck, M. E. Bell, M. R. Bell, M. J. Bentum, G. Bernardi, P. Best, L. Birzan, A. Bonafede, F. Breitling, J. Broderick, W. N. Brouw, M. Brüggen, B. Ciardi, F. de Gasperin, R. J. Dettmar, A. van Duin, S. Duscha, J. Eislöffel, H. Falcke, R. A. Fallows, R. Fender, C. Ferrari, W. Frieswijk, M. A. Garrett, J. Grießmeier, T. Grit, A. W. Gunst, T. E. Hassall, G. Heald, M. Hoeft, A. Horneffer, M. Iacobelli, E. Juette, A. Karastergiou, E. Keane, J. Kohler, M. Kramer, V. I. Kondratiev, L. V. E. Koopmans, M. Kuniyoshi, G. Kuper, J. van Leeuwen, P. Maat, G. Macario, S. Markoff, J. P. McKean, D. D. Mulcahy, H. Munk, E. Orru, H. Paas, M. Pandey-Pommier, M. Pilia, R. Pizzo, A. G. Polatidis, W. Reich, H. Röttgering, M. Serylak, J. Sluman, B. W. Stappers, M. Tagger, Y. Tang, C. Tasse, S. ter Veen, R. Vermeulen, R. J. van Weeren, R. A. M. J. Wijers, S. J. Wijnholds, M. W. Wise, O. Wucknitz, S. Yatawatta, and P. Zarka, "Calibrating high-precision Faraday rotation measurements for LOFAR and the next generation of low-frequency radio telescopes," A&A, vol. 552, p. A58, Apr. 2013.

[318] R. Braun, "The Square Kilometre Array: Current Status and Science Prospects," in *IAU General Assembly*, vol. 29, p. 2252814, Aug. 2015.

[319] A. G. Kritsuk, Å. Nordlund, D. Collins, P. Padoan, M. L. Norman, T. Abel, R. Banerjee, C. Federrath, M. Flock, D. Lee, P. S. Li, W.-C. Müller, R. Teyssier, S. D. Ustyugov, C. Vogel, and H. Xu, "Comparing Numerical Methods for Isothermal Magnetized Supersonic Turbulence," ApJ, vol. 737, p. 13, Aug. 2011.

[320] P. Wang and T. Abel, "Magnetohydrodynamic Simulations of Disk Galaxy Formation: The Magnetization of the Cold and Warm Medium," ApJ, vol. 696, pp. 96–109, May 2009.

[321] P. Wang, T. Abel, and R. Kaehler, "Adaptive mesh fluid simulations on GPU," New A, vol. 15, pp. 581–589, Oct. 2010.

[322] P. F. Hopkins and M. J. Raives, "Accurate, meshless methods for magnetohydrodynamics," MNRAS, vol. 455, pp. 51–88, Jan. 2016.

[323] T. S. Tricco, D. J. Price, and C. Federrath, "A comparison between grid and particle methods on the small-scale dynamo in magnetized supersonic turbulence," MNRAS, vol. 461, pp. 1260–1275, Sept. 2016.

[324] D. J. Barnes, A. Y. L. On, K. Wu, and D. Kawata, "SPMHD simulations of structure formation," MNRAS, vol. 476, pp. 2890–2904, May 2018.

[325] A. Schekochihin, S. Cowley, G. Hammett, J. Maron, J. McWilliams, and S. Taylor, "MHD turbulence in galaxies and clusters," in *APS Division of Plasma Physics Meeting Abstracts*, vol. 46 of *APS Meeting Abstracts*, p. JO2.008, Nov. 2004.

[326] A. Beresnyak and F. Miniati, "Turbulent Amplification and Structure of the Intracluster Magnetic Field," ApJ, vol. 817, p. 127, Feb. 2016.

[327] R. Alves Batista, M.-S. Shin, J. Devriendt, D. Semikoz, and G. Sigl, "Implications of strong intergalactic magnetic fields for ultrahigh-energy cosmic-ray astronomy," Phys. Rev. D, vol. 96, p. 023010, July 2017.

[328] S. Skory, M. J. Turk, M. L. Norman, and A. L. Coil, "Parallel HOP: A Scalable Halo Finder for Massive Cosmological Data Sets," Mar. 2011.

[329] D. J. Eisenstein and P. Hut, "HOP: A New Group-Finding Algorithm for N-Body Simulations," ApJ, vol. 498, pp. 137–142, May 1998.

[330] F. de Gasperin, H. T. Intema, J. Ridl, M. Salvato, R. van Weeren, A. Bonafede, J. Greiner, R. Cassano, and M. Brüggen, "Tracing low-mass galaxy clusters using radio relics: the discovery of Abell 3527-bis," A&A, vol. 597, p. A15, Jan. 2017.

[331] H. Kang, D. Ryu, R. Cen, and J. P. Ostriker, "Cosmological Shock Waves in the Large-Scale Structure of the Universe: Nongravitational Effects," ApJ, vol. 669, pp. 729–740, Nov. 2007.

[332] M. Germano, "Turbulence - The filtering approach," *JFM*, vol. 238, pp. 325–336, May 1992.

[333] W. Schmidt, J. C. Niemeyer, and W. Hillebrandt, "A localised subgrid scale model for fluid dynamical simulations in astrophysics. I. Theory and numerical tests," A&A, vol. 450, pp. 265–281, Apr. 2006.

[334] F. Vazza, E. Roediger, and M. Brüggen, "Turbulence in the ICM from mergers, cool-core sloshing, and jets: results from a new multi-scale filtering approach," A&A, vol. 544, p. A103, Aug. 2012.

[335] J. M. Kubo, A. Stebbins, J. Annis, I. P. Dell'Antonio, H. Lin, H. Khiabanian, and J. A. Frieman, "The Mass of the Coma Cluster from Weak Lensing in the Sloan Digital Sky Survey," ApJ, vol. 671, pp. 1466–1470, Dec. 2007.

[336] M. Girardi, G. Giuricin, F. Mardirossian, M. Mezzetti, and W. Boschin, "Optical Mass Estimates of Galaxy Clusters," ApJ, vol. 505, pp. 74–95, Sept. 1998.

[337] A. A. Schekochihin, J. L. Maron, S. C. Cowley, and J. C. McWilliams, "The Small-Scale Structure of Magnetohydrodynamic Turbulence with Large Magnetic Prandtl Numbers," ApJ, vol. 576, pp. 806–813, Sept. 2002.

[338] J. Cho, A. Lazarian, and E. T. Vishniac, "New Regime of Magnetohydrodynamic Turbulence: Cascade below the Viscous Cutoff," ApJ, vol. 566, pp. L49–L52, Feb. 2002.

[339] R. H. Kraichnan and S. Nagarajan, "Growth of Turbulent Magnetic Fields," *Physics of Fluids*, vol. 10, pp. 859–870, Apr. 1967.

[340] A. Beresnyak and A. Lazarian, *Turbulence in Magnetohydrodynamics*. 2019.

[341] S. Sur, D. R. G. Schleicher, R. Banerjee, C. Federrath, and R. S. Klessen, "The Generation of Strong Magnetic Fields During the Formation of the First Stars," ApJ, vol. 721, pp. L134–L138, Oct. 2010.

[342] S. Sur, C. Federrath, D. R. G. Schleicher, R. Banerjee, and R. S. Klessen, "Magnetic field amplification during gravitational collapse - influence of turbulence, rotation and gravitational compression," MNRAS, vol. 423, pp. 3148–3162, July 2012.

[343] J. Schober, D. Schleicher, C. Federrath, S. Glover, R. S. Klessen, and R. Banerjee, "The Small-scale Dynamo and Non-ideal Magnetohydrodynamics in Primordial Star Formation," ApJ, vol. 754, p. 99, Aug. 2012.

[344] C. F. McKee, A. Stacy, and P. S. Li, "Magnetic fields in the formation of the first stars - I. Theory versus simulation," MNRAS, vol. 496, pp. 5528–5551, Aug. 2020.

[345] S. Xu and A. Lazarian, "Nonlinear Turbulent Dynamo during Gravitational Collapse," ApJ, vol. 899, p. 115, Aug. 2020.

[346] A. Brandenburg, I. Procaccia, and D. Segel, "The size and dynamics of magnetic flux structures in magnetohydrodynamic turbulence," *Phys. Plasmas*, vol. 2, pp. 1148–1156, Apr. 1995.

[347] F. Govoni, M. Murgia, L. Feretti, G. Giovannini, K. Dolag, and G. B. Taylor, "The intracluster magnetic field power spectrum in Abell 2255," A&A, vol. 460, pp. 425–438, Dec. 2006.

[348] J. Cho, E. T. Vishniac, A. Beresnyak, A. Lazarian, and D. Ryu, "Growth of Magnetic Fields Induced by Turbulent Motions," ApJ, vol. 693, pp. 1449–1461, Mar. 2009.

[349] N. Kriel, J. R. Beattie, A. Seta, and C. Federrath, "Fundamental scales in the kinematic phase of the turbulent dynamo," MNRAS, vol. 513, pp. 2457–2470, June 2022.

[350] A. Brandenburg, I. Rogachevskii, and J. Schober, "Dissipative magnetic structures and scales in small-scale dynamos," MNRAS, vol. 518, pp. 6367–6375, Feb. 2023.

[351] D. A. St-Onge and M. W. Kunz, "Fluctuation Dynamo in a Collisionless, Weakly Magnetized Plasma," ApJ, vol. 863, p. L25, Aug. 2018.

[352] A. Roper Pol, C. Caprini, A. Neronov, and D. Semikoz, "The gravitational wave signal from primordial magnetic fields in the Pulsar Timing Array frequency band," *arXiv e-prints*, p. arXiv:2201.05630, Jan. 2022.

[353] F. Govoni, K. Dolag, M. Murgia, L. Feretti, S. Schindler, G. Giovannini, W. Boschin, V. Vacca, and A. Bonafede, "Rotation measures of radio sources in hot galaxy clusters," A&A, vol. 522, p. A105, Nov. 2010.

[354] T. A. Enßlin and C. Vogt, "The magnetic power spectrum in Faraday rotation screens," A&A, vol. 401, pp. 835–848, Apr. 2003.

[355] S. K. Sethi and K. Subramanian, "Primordial magnetic fields and the HI signal from the epoch of reionization," J. Cosmology Astropart. Phys., vol. 2009, p. 021, Nov. 2009.

[356] K. L. Pandey, S. K. Sethi, and B. Ratra, "Cosmological magnetic braking and the formation of high-redshift, super-massive black holes," MNRAS, vol. 486, pp. 1629–1640, June 2019.

[357] C. R. Saad, V. Bromm, and M. El Eid, "Impact of magnetic fields on Population III star formation," MNRAS, vol. 516, pp. 3130–3143, Nov. 2022.

[358] P. Sikivie, "Experimental Tests of the "INVISIBLE" Axion," Phys. Rev. Lett., vol. 52, p. 695, Feb. 1984.

[359] G. Raffelt and L. Stodolsky, "Mixing of the photon with low-mass particles," Phys. Rev. D, vol. 37, pp. 1237–1249, Mar. 1988.

[360] A. A. Anselm, "Experimental test for arion photon oscillations in a homogeneous constant magnetic field," Phys. Rev. D, vol. 37, pp. 2001–2004, Apr. 1988.

[361] E. Masaki, A. Aoki, and J. Soda, "Photon-axion conversion, magnetic field configuration, and polarization of photons," Phys. Rev. D, vol. 96, p. 043519, Aug. 2017.

[362] S. Jacobsen, T. Linden, and K. Freese, "Constraining Axion-Like Particles with HAWC Observations of TeV Blazars," *arXiv e-prints*, p. arXiv:2203.04332, Mar. 2022.

[363] Z. Arzoumanian, P. T. Baker, H. Blumer, B. Bécsy, A. Brazier, P. R. Brook, S. Burke-Spolaor, S. Chatterjee, S. Chen, J. M. Cordes, N. J. Cornish, F. Crawford, H. T. Cromartie, M. E. Decesar, P. B. Demorest, T. Dolch, J. A. Ellis, E. C. Ferrara, W. Fiore, E. Fonseca, N. Garver-Daniels, P. A. Gentile, D. C. Good, J. S. Hazboun, A. M. Holgado, K. Islo, R. J. Jennings, M. L. Jones, A. R. Kaiser, D. L. Kaplan, L. Z. Kelley, J. S. Key, N. Laal, M. T. Lam, T. J. W. Lazio, D. R. Lorimer, J. Luo, R. S. Lynch, D. R. Madison, M. A. McLaughlin, C. M. F. Mingarelli, C. Ng,

D. J. Nice, T. T. Pennucci, N. S. Pol, S. M. Ransom, P. S. Ray, B. J. Shapiro-Albert, X. Siemens, J. Simon, R. Spiewak, I. H. Stairs, D. R. Stinebring, K. Stovall, J. P. Sun, J. K. Swiggum, S. R. Taylor, J. E. Turner, M. Vallisneri, S. J. Vigeland, C. A. Witt, and Nanograv Collaboration, "The NANOGrav 12.5 yr Data Set: Search for an Isotropic Stochastic Gravitational-wave Background," ApJ, vol. 905, p. L34, Dec. 2020.

[364] A. R. Taylor, J. M. Stil, and C. Sunstrum, "A Rotation Measure Image of the Sky," ApJ, vol. 702, pp. 1230–1236, Sept. 2009.

[365] C. L. Van Eck, M. Haverkorn, M. I. R. Alves, R. Beck, P. Best, E. Carretti, K. T. Chyży, J. S. Farnes, K. Ferrière, M. J. Hardcastle, G. Heald, C. Horellou, M. Iacobelli, V. Jelić, D. D. Mulcahy, S. P. O'Sullivan, I. M. Polderman, W. Reich, C. J. Riseley, H. Röttgering, D. H. F. M. Schnitzeler, T. W. Shimwell, V. Vacca, J. Vink, and G. J. White, "Polarized point sources in the LOFAR Two-meter Sky Survey: A preliminary catalog," A&A, vol. 613, p. A58, June 2018.